Journal of Fluids Engineering

Published Monthly by ASME

VOLUME 129 • NUMBER 1 • JANUARY 2007

FLUIDS ENGINEERING DIVISION
Editor
J. KATZ (2008)
Assistant to the Editor
L. MURPHY (2008)
Associate Editors
M. J. ANDREWS (2009)
S. BALACHANDAR (2008)
A. BESKOK (2008)
S. L. CECCIO (2009)
D. DRIKAKIS (2008)
P. A. DURBIN (2008)
A. GOTO (2007)
C. HAH (2009)
T. J. HEINDEL (2007)
H. JOHARI (2009)
J. KOMPENHANS (2009)
Y. T. LEE (2007)
J. A. LIBURDY (2007)
P. LIGRANI (2008)
R. MITTAL (2009)
T. J. O'HERN (2008)
U. PIOMELLI (2007)
S. ROY (2007)
D. SIGINER (2008)
S. P. VANKA (2007)
Y. ZHOU (2008)

PUBLICATIONS COMMITTEE
Chair, **B. RAVANI**

OFFICERS OF THE ASME
President, **T. E. SHOUP**
Executive Director, **V. R. CARTER**
Treasurer, **T. D. PESTORIUS**

PUBLISHING STAFF
Managing Director, Publishing
P. DI VIETRO
Manager, Journals
C. MCATEER
Production Assistant
M. ANDINO

TECHNICAL PAPERS

Transactions of the ASME, Journal of Fluids Engineering
(ISSN 0098-2202) is published monthly by
The American Society of Mechanical Engineers,
Three Park Avenue, New York, NY 10016.
Periodicals postage paid at New York, NY
and additional mailing offices.
POSTMASTER: Send address changes to Transactions of the
ASME, Journal of Fluids Engineering, c/o THE AMERICAN
SOCIETY OF MECHANICAL ENGINEERS,
22 Law Drive, Box 2300, Fairfield, NJ 07007-2300.
CHANGES OF ADDRESS must be received at Society
headquarters seven weeks before they are to be effective.
Please send old label and new address.
STATEMENT from By-Laws. The Society shall not be
responsible for statements or opinions advanced in papers
or ... printed in its publications (B7.1, Par. 3).
COPYRIGHT © 2007 by the American Society of
Mechanical Engineers. Authorization to photocopy material for
internal or personal use under those circumstances not falling
within the fair use provisions of the Copyright Act, contact
the Copyright Clearance Center (CCC), 222 Rosewood Drive,
Danvers, MA 01923, tel: 978-750-8400, www.copyright.com.
Request for special permission or bulk copying should be
addressed to Reprints/Permission Department.
Canadian Goods & Services Tax Registration #126148048.

(Contents continued on inside back cover)

This journal is printed on acid-free paper, which exceeds the ANSI Z39.48-1992 specification for permanence of paper and library materials. ∞™
♲ 85% recycled content, including 10% post-consumer fibers.

Downloaded 03 Jun 2010 to 171.66.16.159. Redistribution subject to ASME license or copyright; see http://www.asme.org/terms/Terms_Use.cfm

Journal of Fluids Engineering **Volume 129, Number 1** **JANUARY 2007**

TECHNICAL BRIEF

The ASME Journal of Fluids Engineering is abstracted and indexed in the following:

Applied Science & Technology Index, Chemical Abstracts, Chemical Engineering and Biotechnology Abstracts (Electronic equivalent of Process and Chemical Engineering), Civil Engineering Abstracts, Computer & Information Systems Abstracts, Corrosion Abstracts, Current Contents, Ei EncompassLit, Electronics & Communications Abstracts, Engineered Materials Abstracts, Engineering Index, Environmental Engineering Abstracts, Environmental Science and Pollution Management, Excerpta Medica, Fluidex, Index to Scientific Reviews, INSPEC, International Building Services Abstracts, Mechanical & Transportation Engineering Abstracts, Mechanical Engineering Abstracts, METADEX (The electronic equivalent of Metals Abstracts and Alloys Index), Petroleum Abstracts, Process and Chemical Engineering, Referativnyi Zhurnal, Science Citation Index, SciSearch (The electronic equivalent of Science Citation Index), Shock and Vibration Digest, Solid State and Superconductivity Abstracts, Theoretical Chemical Engineering

Fluctuation of Air-Water Two-Phase Flow in Horizontal and Inclined Water Pipelines

A. R. Kabiri-Samani[1]
Assistant Professor
School of Engineering,
Civil Engineering Division,
ShahreKord University,
ShahreKord, Iran
e-mail: kabiri@eng.sku.ac.ir

S. M. Borghei
Associate Professor
Civil Engineering Department,
Sharif University of Technology,
P.O. Box 11365-9313,
Azadi Avenue,
Tehran, Iran
e-mail: mahmood@sharif.edu

M. H. Saidi
Associate Professor
Mechanical Engineering Department,
Sharif University of Technology,
P.O. Box 11365-9313,
Azadi Avenue,
Tehran, Iran
e-mail: saman@sharif.edu

*Air in water flow is a frequent phenomenon in hydraulic structures. The main reason for air entrainment is vortices at water intakes, pumping stations, tunnel inlets, and so on. The accumulated air, in a conduit, can evolve to a different flow pattern, from stratified to pressurized. Among different patterns, slug is most complex with extreme pressure variations. Due to lack of firm relations between pressure and influential parameters, study of slug flow is very important. Based on an experimental model, pressure fluctuations inside a circular, horizontal, and inclined pipe (*90 mm *inside diameter and* 10 m *long) carrying tow-phase air-water slug flow has been studied. Pressure fluctuations were sampled simultaneously at different sections, and longitudinal positions. The pressure fluctuations were measured using differential pressure transducers (DPT), while behavior of the air slug was studied using a digital camera. The objective of the paper is to predict the pressure variation in a pipeline or tunnel, involving resonance and shock waves experimentally. The results show that the more intensive phase interaction commences stronger fluctuations. It is shown, that the air-water mixture entering the pipe during rapid filling of surcharging can cause a tremendous pressure surge in the system and may eventually cause failure of the system (e.g., the maximum pressure inside the pipe would reach up to 10 times of upstream hydrostatic pressure as suggested by others too). Relations for forecasting pressure in these situations are presented as a function of flow characteristics, pipe geometry, longitudinal, and cross-sectional positions and head water.*
[DOI: 10.1115/1.2375134]

Keywords: two-phase flow, water tunnel, pressure fluctuation, experimental model, slug flow

1 Introduction

In the context of the multiphase system, two-phase flow considered here, consists of a mixture of water existing in a liquid state or "phase," and air which exists in a gaseous state or "phase." Although two-phase flow obeys all the basic laws of fluid mechanics, it is quite complex, in a way that even one-dimensional flow in a pipe with many simplifications is much more complicated than single-phase flow. In an attempt to overcome these complexities, researchers have conducted experiments to develop correlations which can be used by a design engineer to utilize practical problems.

Two-phase gas-liquid flows occur in a wide variety of situations, i.e., in chemical processing, power generation, water supply systems, petroleum industry, and energy production facilities [1]. Two-phase flows can be grouped into a number of different flow patterns. These are based on the spatial distribution of the gas and liquid phases. The flow patterns that are attainable with the available air and water supplies in horizontal and small inclined pipes include stratified, wavy, and slug flow (Fig. 1) which will be discussed in the next section.

In recent years, extensive work has been carried out for more reliable analysis and application of two-phase flow detection systems. Depending on the application, prediction methods for two-phase gas/liquid flow requires information about flow rates to pressure drop relationships in more detail such as, frequency of the slug flow, void fraction, pipe inclination, and air concentration. The general equations for two-phase flow derived from different approaches, such as homogeneous and separate air-water mixture. Lockhart and Martinelli [2] have found correlations for each phase of flow path. Their approach is based on the assumption of conventional friction pressure drop equations which can be applied to each phase of the flow path. Hamam and McCorquodal [3] proposed a rigid water column approach to model the mixed flow pressure transients. The model assumes a water column as incompressible and the flow is uniform, but unsteady and that the air bubble is trapped inside the water after the occurrence of interfacial instability between air-water flows. Zhou et al. [4] have investigated flow transients in a rapid filling horizontal pipe containing trapped air in sewer pipes. Azzopardi and Baker [5] studied the characteristics of periodic structures in gas/liquid two-phase flow. They concluded that data from most flow patterns can be broadly correlated if plotted as a Strouhal number against the Lockhart-Martinelli parameter. Zhang et al. [6] have developed a unified mechanistic model for slug liquid holdup and transition between slug and dispersed bubble flows. Issa and Kempf [7] simulated the slug flow in horizontal and nearly horizontal pipes with the two-fluid model. They concluded that when the two-fluid model is invoked within the confines of the conditions under which it is mathematically well-posed, it is capable of capturing the growth of instabilities in stratified flow leading to the generation of slugs.

One of the major concerns of engineers is the pressure of the two-phase flow at different stages (Fig. 1). Rapid approximations of pressure drop can be calculated using the relation presented by Lockhart and Martinelli [2]. This correlation is empirically derived and has a predictive capability within ±50%, with a great majority of the predictions within 25%. The correlation is more precise for certain flow patterns while it is high for stratified, wavy, and slug flows. This correlation is meant to predict friction losses only, as there is no hydrostatic component without a change

---

[1] Corresponding author.

Contributed by the Fluids Engineering Division of ASME for publication in the JOURNAL OF FLUIDS ENGINEERING. Manuscript received May 24, 2006; final manuscript received June 17, 2005. Assoc. Editor: Theodore Heindel.

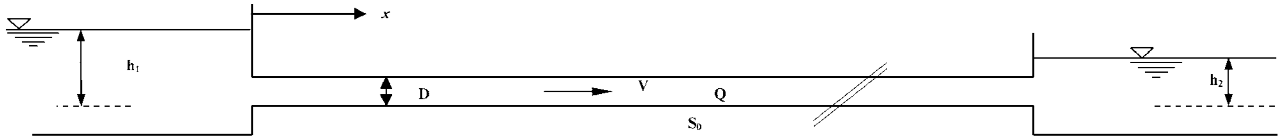

(a) Pressurized flow

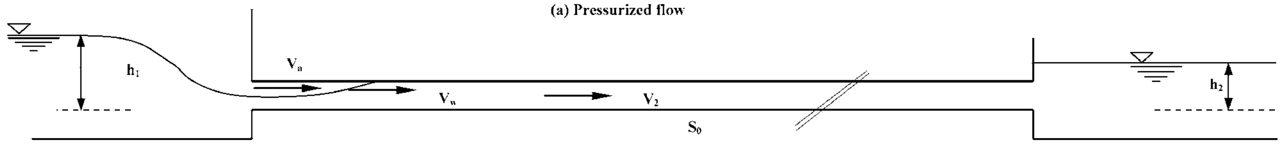

(b) Releasing trapped air or slug flow initiation

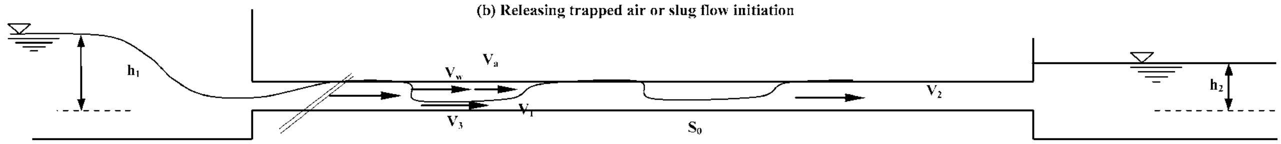

(c) Fully developed slug flow

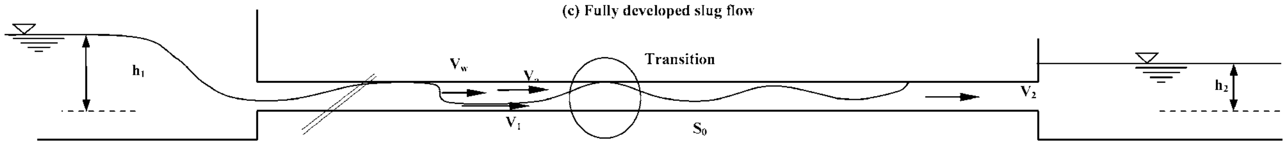

(d) Transition to wavy stratified flow from slug flow

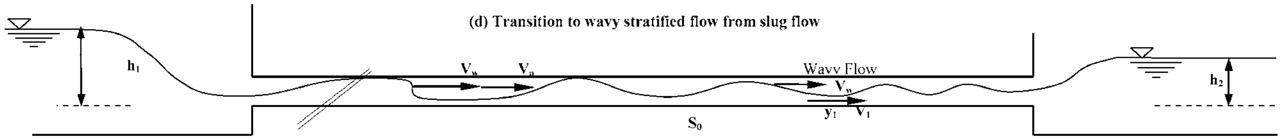

(e) Wavy stratified flow

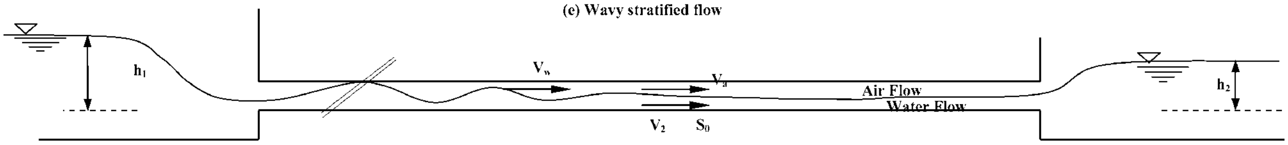

(f) Stratified flow regime

Fig. 1 Stages of flow from pressurized to free-surface

in elevation. Chenoweth and Martin [8] utilized 38.1–76.2 mm diameter galvanized steel pipe for isothermal air-water mixtures at different pressures to derive their relation. Pressure oscillations in a pipeline occur when the gas-phase is discontinuous, or the flow rates are changed, or in a case of rupture. Predicting of pressure pulses are also an important design criteria to prevent rupture [9]. Since a slug flow is a periodic phenomenon, if the frequency of the wave is near to the frequency of the structure, then it can yield to resonance and can increase damage risk to the conduit. From the pressure pulses it is possible to extract information about flow properties like average density and flow velocity [10]. Pressure fluctuations might be used to discover and locate leaks in long water tunnels and offshore pipelines [11]. It can also be used for flow regime prediction in combination with transient void fraction. Flow control is the other area that requires knowledge about pressure waves. A large amount of work has been devoted to the study of pressure propagation in two-phase flow. Experimental work has shown that the pressure pulses could be approximated by the Woods equation for low frequencies [12,13] and that the velocity and attenuation of the pressure waves were a function of the frequency and bubble radius [14].

Semenov [15] carried out tests for both horizontal and vertical flows and concluded that the pressure fluctuations were higher than predicted by homogenous theory. However, experiments in vertical slug flow showed that the pressure pulse velocity approached the homogeneous velocity as the number of slugs increased [16,17].

Lack of solid and comprehensive design methods for predicting and calculating the pressure variation in two-phase air/water flow situations has left engineers without essential information for proper design of two-phase systems, especially in hydraulic structures, such as, pipelines, tunnels, and culverts. No doubt that much more field and laboratory investigations are needed to increase the knowledge in this area of science. Hence, this paper is another experimental study on two-phase air-water flow. The equipments such as differential pressure transducer (DPT) and digital camera for image processing and transparent pipe with 90 mm inside diameter and 10 m long were used. The variables and measurements are, air flow rate, water flow rate, pipe inclination, head water, pressure, and pressure drop at different locations and levels in the conduit. The results are presented in dimensionless forms as normalized pressure related to other dimensionless variables. The hydraulic system has been scaled down, while considering all key variables of two-phase flow such as, void fraction, concentration, longitudinal slope, frequency, etc., which has not been seen by many other investigators all together. Also, another unique situation is that, the model of circular pipe having 90 mm inside diameter is large enough to minimize scale effects. In this respect, this paper is a comprehensive experimental study for two-phase air/water flow, for forecasting pressure variation in slug flow situation.

2 Two-Phase Flow Formation and Important Parameters

Hydraulic instability may occur during the transition from free-surface to pressurized flow in a closed conduit. In a certain range of headwater (h_1), between free-surface and pressurized flow conditions, the sudden change of boundary conditions induce air-water mixture flow in the conduit. Air entrainment can cause severe pressure fluctuations, which may damage the pipeline and cause other related problems.

Transition from pressurized to free-surface flow, which occasionally happens in long water conduits such as, tunnels and cul-

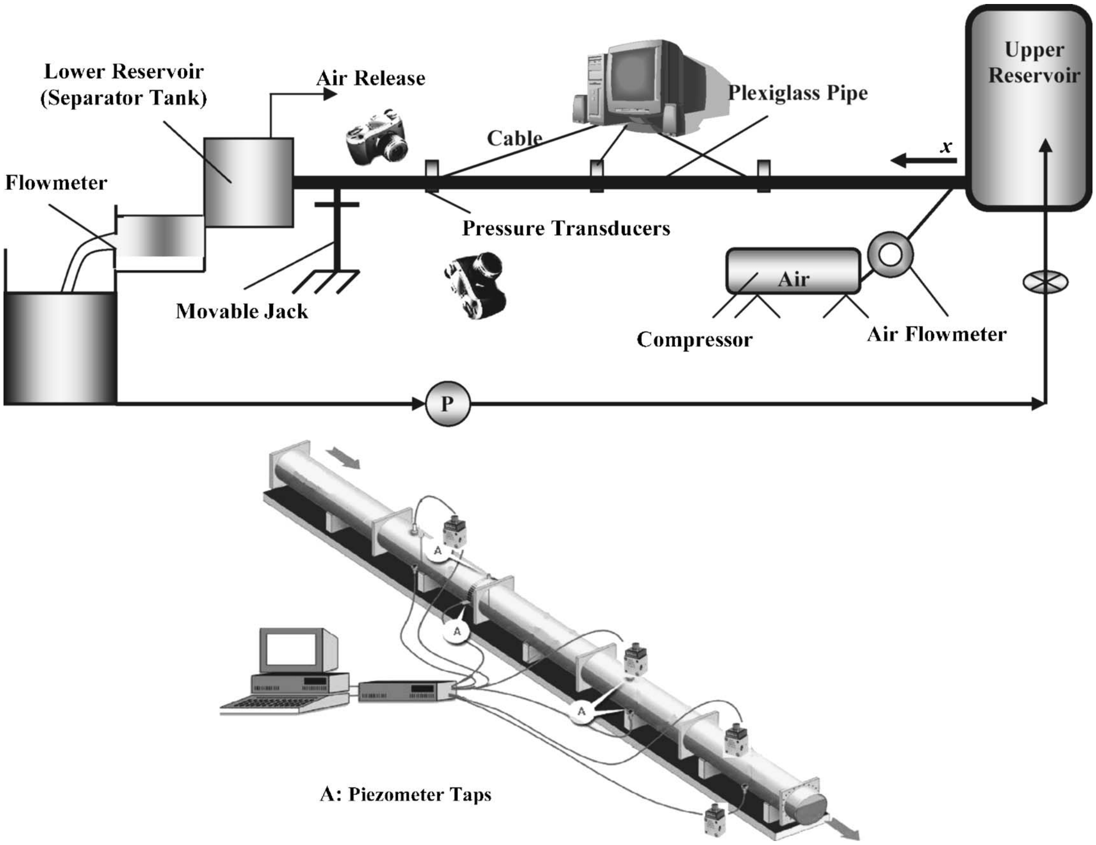

Fig. 2 Schematic view of the experimental setup

verts, is classified into six stages, as shown in Fig. 1. Stage a indicates completely pressurized flow and usually occurs when $h_1/D \geqslant 1.5$ (D is the conduit inside diameter or height) and the conventional pressurized flow equation is used [18]. At stage b the sudden filling of a partially full conduit, or the falling down of water level in an upstream reservoir, could result in the release of air into the water. In order for the trapped air to escape into the atmosphere, the pressure inside the bubble has to exceed a certain threshold value. After partial release of air, the pressure inside the bubble drops below the threshold value and the remaining air undergoes compression and expansion. The next release of the air-water mixture occurs when the pressure inside the air bubble drops below the threshold value again, which is the start of slug flow. Stage c implies fully developed slug flow, which is the most complicated pattern in a two-phase flow and includes extreme conditions. At this stage, the flow contains compressible air bubbles translating in a velocity different from the water velocity. Stage d includes the initiation of instability inside the fluid and refers to the tendency of the flow to return to its original state after being perturbed. Due to the hydraulic properties of flow and fluids, after the occurrence of instability the flow begins to make and develop regular and irregular waves which yield to stage e. For stage f, the flow is almost uniform and the fluid interface is close to a straight line and the flow is stratified smooth. Therefore, the "two-fluid model" can be used for this stage [19].

In the two-phase flow, traditional dimensionless groups have very limited use in correlating data. Among many parameters and forces which affect the two-phase flow, turbulent diffusivity and buoyant force are the most important. Therefore, the pressure which relates to gravity, Reynolds shear stress, interfacial forces, and fluid properties are important functions and can be obtained from

$$P = \xi(Q_a, V_w, D, g, \mu_a, \mu_w, \rho_a, \rho_w, \sigma, \tau_0, f, \varphi) \tag{1}$$

where P, Q_a, V_w, D, g, μ, ρ, σ, τ_0, f, φ, are pressure inside the pipe, air discharge, water velocity, pipe inner diameter, acceleration due to gravity, viscosity, density, surface tension, shear stress, wave frequency, and pipe inclination, respectively, ξ is a functional symbol and subscripts a and w denote air and water.

Applying dimensional analysis and using V_w, ρ_w, and g as basic dimensional independent variables, leads to the following relation among the dimensionless parameters:

$$\frac{P}{\rho_w V_w^2} = \xi\left(\frac{Q_a}{V_w D^2}, \frac{\tau_0}{\rho_w V_w^2}, \frac{\sigma}{\rho_w D V_w^2}, \frac{\rho_a}{\rho_w}, \frac{\mu_a}{\mu_w}, \frac{\mu_w}{\rho_w D V_w}, \frac{gD}{V_w^2}, \frac{Df}{V_w}, \sin\varphi\right) \tag{2}$$

or with convectional form of dimensionless variables

$$\frac{P}{\rho_w V_w^2} = \xi\left(\frac{Q_a}{Q_w}, K_f, \mathrm{We}, \alpha, \frac{\mu_a}{\mu_w}, \mathrm{Re}, \mathrm{Fr}, \mathrm{Sh}, \sin\varphi\right) \tag{3}$$

where Q, K_f, We, α, Re, Fr, and Sh are discharge, friction factor ($K_f = f_{TP} L/D$, L is the characteristic length), Weber number, void fraction, Reynolds number, Froude number, and Strouhal number, respectively. Applying the incomplete-self-similarity approach [20], and introducing $\beta = Q_a/Q_w$, $\bar{C} = \beta/(1+\beta)$, $P_h = P/(\rho_w g)$, $h = kV_w^2/2g$, $\sin\varphi = S_0$ and also by simplifying and substituting into Eq. (3) the result would be

$$\frac{P_h}{h} = \xi\left(\bar{C}, K_f, \alpha, \frac{\mu_a}{\mu_w}, \mathrm{Re}, \mathrm{Fr}, \mathrm{Sh}, \frac{\mathrm{We}}{\mathrm{Fr}\sqrt{1 - S_0}}\right) \tag{4}$$

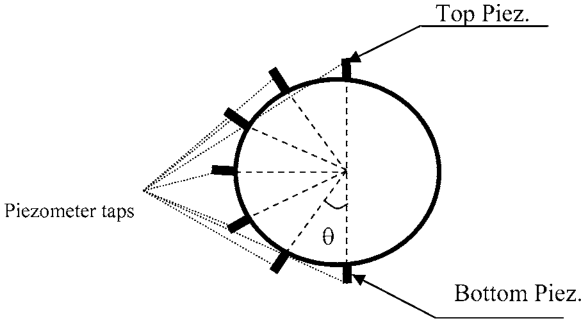

Fig. 3 The arrangement of sensors at a pipe section

Zielinski and Willemonte [21] showed that when Reynolds number is greater than 10^4, the effects of viscosity could be neglected (same as single-phase flow in pressurized pipe), then

$$\frac{P_h}{h} = \xi(\bar{C}, K_f, \alpha, \mathrm{Fr}, \mathrm{Sh}, wfs) \qquad (5)$$

where $wfs = \mathrm{We}/(\mathrm{Fr}(1-S_0)^{0.5})$.

Using the above dimensionless parameters, the experimental tests have been carried out and analyzed based on the achieved data.

3 Test Facility and Experimental Description

The experimental apparatus was designed and constructed to obtain two-phase air-water flow in horizontal and inclined pipes. The pipe was 10 m long, with an inner diameter of 90 mm using transparent plexiglass material in order to permit visual observation of the flow phenomenon. The tests were done at room temperature and pressure. The temperature of the water was held constant for each test, between 18 and 25°C. The experimental equipment consisted of a closed water circuit, an open gas circuit, and test sections. The entrained air was released directly to the atmosphere at the end of the main pipe from the lower reservoir. The mechanical support of the loop was specially constructed to absorb the vibrations generated by the flow. A schematic representation of the experimental setup is shown in Fig. 2.

About 300 piezometer taps were set to connect the pressure sensors to the pipe. Digital cameras, scales, and rulers were used for measuring the water surface level, wavelength, and void fraction. A PC coupled with cameras and data acquisition system was employed for visualizing the flow phenomena and data recording. Experiments were conducted with deionized water as a working fluid at an atmospheric pressure condition. The pressure sensors used, were variable reluctance differential pressure transducers, which could measure the pressure from 88 to 350 cm H_2O.

For each test, 8 pressure transducers were used, 7 were arranged on half of the pipe perimeter at different angles ($\theta = 30$ deg, 60 deg, 90 deg, 120 deg, 150 deg, 180 deg) as shown in Fig. 3, while the last one was used to measure the pressure inside the separator tank. About 455 tests were done, and 2730 data were recorded. Table 1 shows the range of variables such as air and water discharge and other variables including pipe inclinations, longitudinal ($x = 1.61$, 2.82, 4.02, 5.22, 7.12, 8.92 m, x direction is shown in Fig. 2) and lateral measurement points and the minimum time for data recording.

4 Results and Analysis

Figure 4(*a*) shows an example of pressure fluctuation signals measured at different positions (x). For choosing the right test period, one directional variance analysis for up to 12 h has been used [22]. It was shown that 150 s is an optimum time for all variable test requirements including extreme values. From the observed time shifts and knowing the distance between the pressure transducers, the velocity of the two-phase flow can be calculated. In Figs. 4(*b*) and 4(*c*) pressure signals are shown for the same geometrical and test conditions as in Fig. 4(*a*), but with different air and water flow rates.

As shown, pressure fluctuation has a periodic character. Figure 4(*d*) shows an example of pressure fluctuation signals measured at different pipe depth or sectional position (angles, 0 deg, 30 deg, 60 deg, 90 deg, 120 deg, 150 deg, 180 deg). As is expected, there is no time lag among the results and the pressure decreases from the bottom to the top of the pipe or, to the air bubble pressure at the top. Figure 5 shows sectional nondimensional or normalized mean pressure (or P_h/h when $P_h = P/(\rho_w g)$) distribution in a horizontal pipe at $x = 1.61$ m.

Figure 6 shows the variation of normalized maximum and minimum pressure with the normalized mean pressure for different Q_a/Q_w. The relations between the parameters can be presented as

$$\left(\frac{P_h}{h}\right)_{\max} = 0.6e^{-4.8S_0}\left(1.2\left(\frac{P_h}{h}\right)^2 + 2.4\left(\frac{Q_a}{Q_w}\right)^{0.75}\right) \qquad (6a)$$

$$\left(\frac{P_h}{h}\right)_{\min} = 0.6e^{1.25S_0}\left(0.95\left(\frac{P_h}{h}\right)^{1.1} + 0.45\left(\frac{Q_a}{Q_w}\right)^{0.85}\right) \qquad (6b)$$

The rest of the results can be represented by mean pressure and convert to minimum or maximum pressure using the equations, if required. Normalized average pressure plotted against nondimensional distance along the pipe is shown in Fig. 7. Each set represents constant air and water flow rates and piezometer levels. An interesting result is that the pressure decreases with increasing

Table 1 The test variables

Pipe Inclination (%)	Air Discharge (lit/min)	Water Discharge Range (lit/sec)	Longitudinal Position of Test Sections (x) (m)	Lateral Meas. Points (Deg.)	Data Recording Time (sec)
0, 0.5, 1, 2, 3, 4	67, 100,120, 150, 180, 210, 240, 270, 300, 330, 360, 400	4-25	1.61, 2.82, 4.02, 5.22, 7.12, 8.92	0, 30, 60, 90, 120, 150, 180 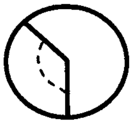	Minimum 150

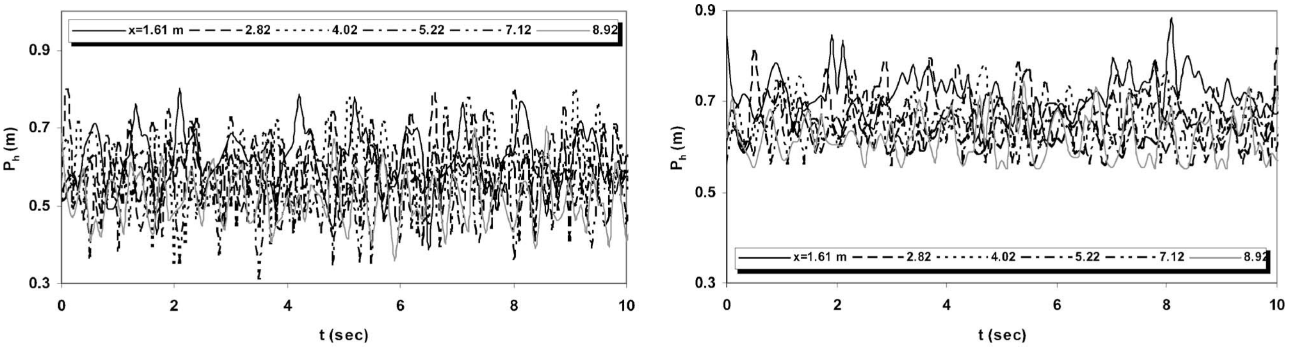

a: Q_a=1.11 lit/sec, Q_w=4.74 lit/sec and h_l=0.337 m

b: Q_a=1.67 lit/sec, Q_w=4.74 lit/sec and h_l=0.302 m

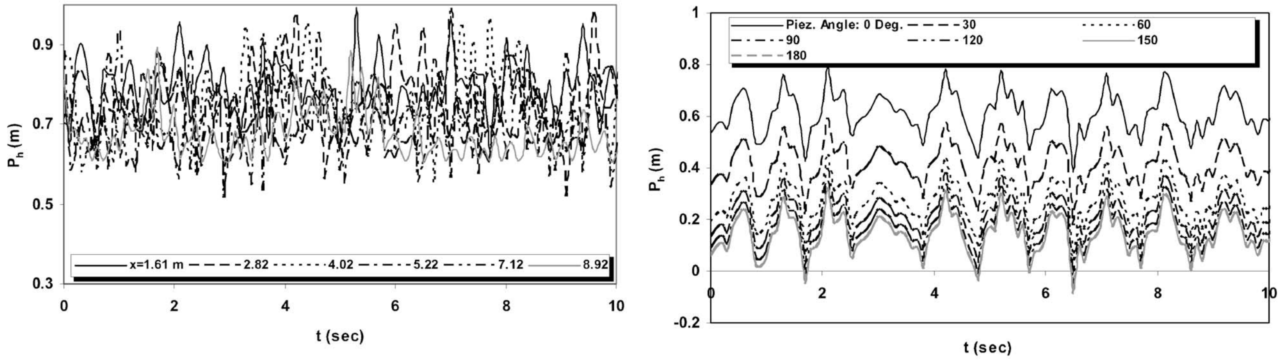

c: Q_a=1.11 lit/sec, Q_w=6.42 lit/sec and h_l=0.434 m

d: Q_a=1.11 lit/sec, Q_w=4.74 lit/sec and h_l=0.337 m

Fig. 4 Examples of pressure fluctuation pulses for different conditions in slug flow at different longitudinal positions (*x*)

height (or θ from 0 deg to 180 deg) and the pressure loss of water flow (the lowest piezometer at 0 deg) is more than that of air flow (the highest piezometer at 180 deg). From this figure the following correlation is reached for the pressure gradient (dP_h/dx), which remarks on the effect of the piezometer angle (in rad), or water depth in the pipe and the pipe length to the diameter,

$$\frac{dP_h}{dx} = 2.7 \times 10^{-4} e^{-0.52\theta} \frac{x}{D} + (-0.003\theta^2 + 0.017\theta - 0.028) \quad (7)$$

Pressure drop per unit length is plotted versus Q_w and Q_a/Q_w in Figs. 8(*a*) and 8(*b*), respectively. Each curve represents constant air flow while, water flow rate was changed. As is expected, the pressure drop increases with both water and air flow rates. It must be noted that for high values of water flow and low values of air flow, the increase in pressure gradient is stronger. Also, when the gas flow rate is increased, the rate of the pressure drop is decreased. The result can have the following relationship in order to predict pressure drop:

$$\frac{\Delta P_h}{L} = a e^{b(Q_a/Q_w)} \quad (8)$$

The coefficients a and b are obtained by optimizing the mean relative error among the measured statistical package for the social sciences (SPSS) as

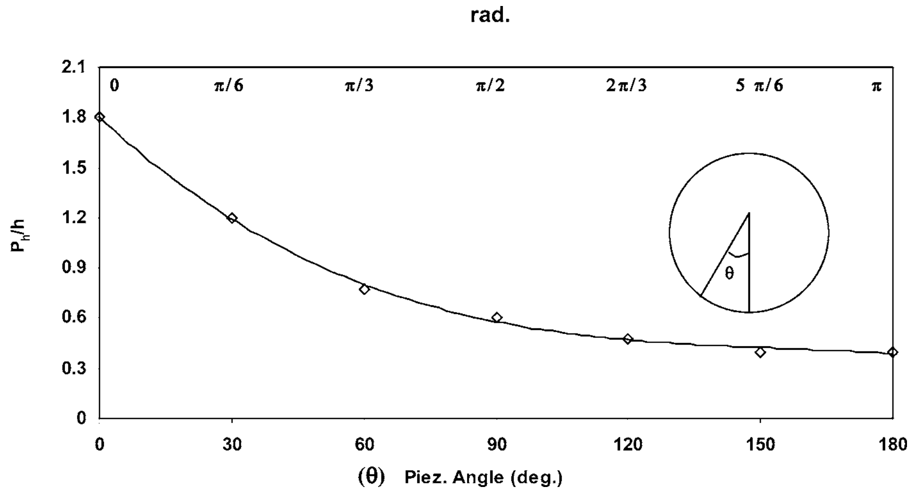

Fig. 5 Typical mean pressure distribution on the pipe wall in a horizontal pipe (at *x* =1.61 m)

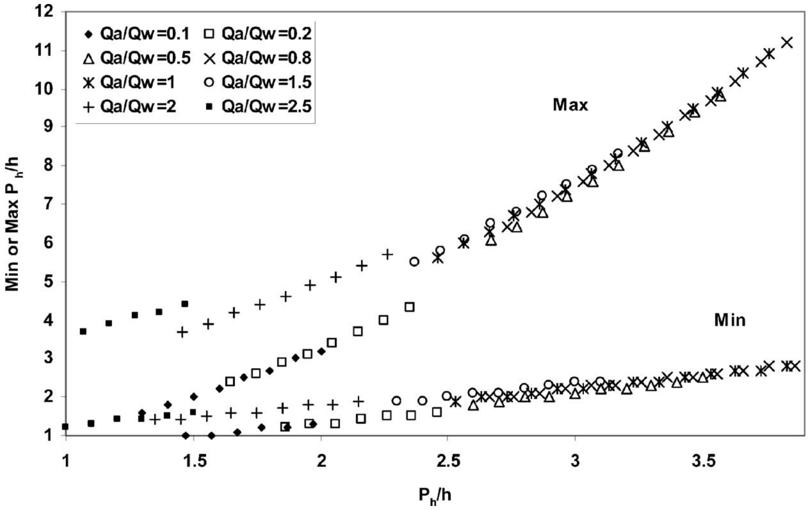

Fig. 6 Normalized maximum and minimum instantaneous pressure versus mean pressure

$$a = 0.003Q_a^2 + 0.006Q_a + 0.07 \tag{9a}$$

$$b = 0.18Q_a^3 - 2.45Q_a^2 + 11.55Q_a - 19.7 \tag{9b}$$

The influence of air/water flow rates and the positive pipe slope or downward flow (0%, 0.5%, 1%, 2%, 3%, and 4%) on the mean pressure is presented in Fig. 9(*a*). The figure includes all data points for different setup conditions. It is clear that the normalized mean pressure increases with air/water rate ratios up to a certain value between 0.7 and 0.9, then decreases with the increase of air/water rates. Also, the pressure peak value increases with the pipe inclination too. The increased pressure causes awful effects on the pipeline, depending on the pipe properties and geometry, and its support structure and hydraulic operation. Best fitted curves among data points of normalized mean pressure and air/water rates are plotted for different pipe inclinations (Fig. 9(*b*)). This interesting result clearly shows the effect of pipe slope as well as air/water discharge ratio on pressure and, hence, should be considered in the design problems.

To investigate the effect of dimensionless parameters given in Eq. (5), i.e., Froude number, pipe inclination, void fraction, and concentration, the results of normalized mean pressure are plotted against each parameter. First of all, the pressure is plotted as a function of Strouhal number (Sh) for different pipe inclinations in Fig. 10. The mean pressure increases with Sh up to about 0.05 and then decreases with increasing Sh. Also, for a constant Sh, the normalized mean pressure increases with the pipe inclination.

Figure 11 shows the variation of the dimensionless parameter $\mathrm{Fr}_{ah}/\mathrm{Fr}$ versus the normalized mean pressure, while

$$\mathrm{Fr}_{ah} = \frac{Q_a}{\sqrt{gh^5}} \quad \mathrm{Fr} = \frac{Q_a + Q_w}{\sqrt{gD^5}} \tag{10}$$

The plotted points implicate that the fitted relation between P_h/h and $\mathrm{Fr}_{ah}/\mathrm{Fr}$ can be represented by second order polynomial equations as drawn.

The relation between pipe inclination and mean pressure relative to the mean pressure in the horizontal pipe is illustrated in Fig. 12. The results show that by increasing the pipe inclination the mean pressure increases. The best correlation yields to be

$$\frac{P_h}{P_{h0}} = \frac{(1 + 2S_0)^4}{(1 - S_0^2)^2} \tag{11}$$

where, P_{h0} is the mean pressure in the horizontal pipe. Figure 13 shows the effect of the dimensionless parameter $K_f = f_{\mathrm{TP}}L/D$ against the normalized mean pressure for different pipe inclinations (L is taken as the slug wavelength). The parameter f_{TP} is the two-phase flow friction factor and defined as [19]

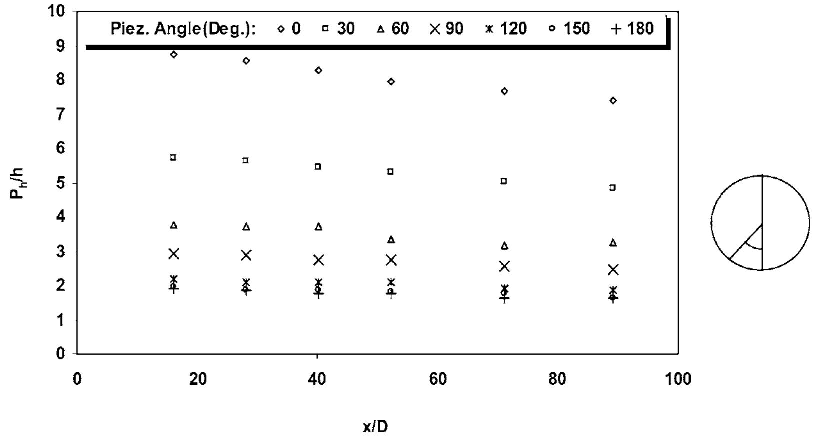

Fig. 7 Normalized mean pressure versus the pipe distance

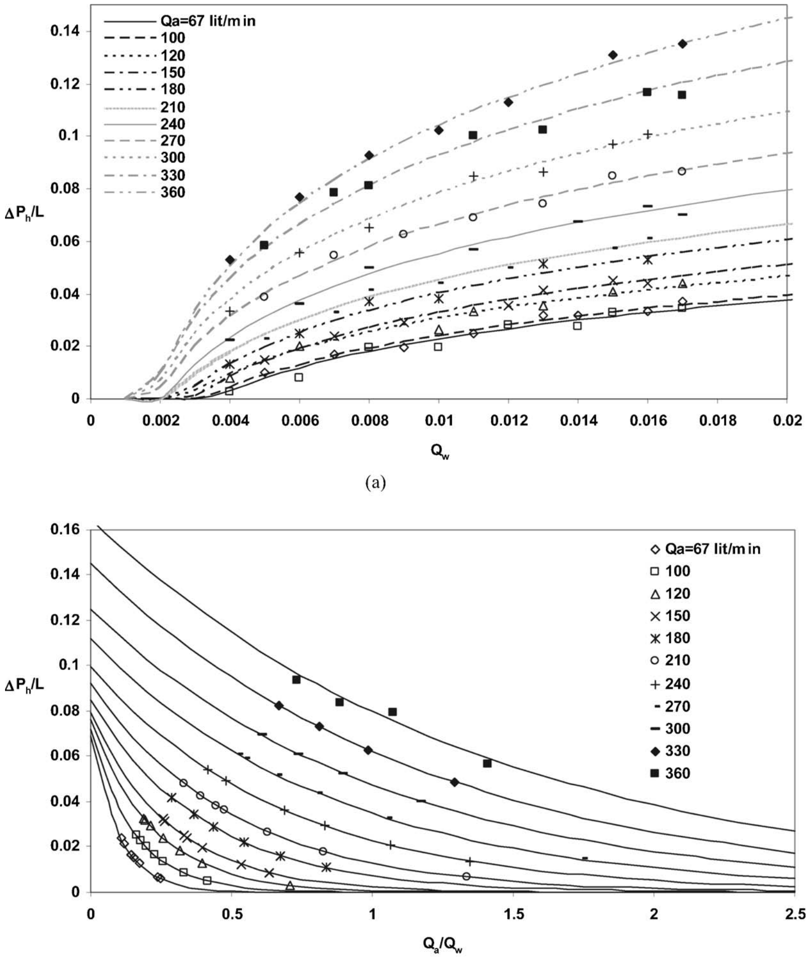

(a)

(b)

Fig. 8 Dimensionless pressure gradient as a function of (*a*) Q_w/Q_c, and (*b*) Q_a/Q_w

$$f_{\mathrm{TP}} = 0.079\left(\frac{GD}{x_m\mu_a + (1-x_m)\mu_w}\right)^{-0.25} \tag{12}$$

where, G, x_m, and μ are mass velocity, mass quality, and viscosity, respectively. Equation (12) is a kind of well-known Blasius formula. It is clearly seen that there is a peak for normalized mean pressure at $K_f=200$. Also, for a constant K_f, pipe inclination increases the value of pressure.

Figure 14 shows the relation of P_h/h versus *wfs* for all data. It can be seen that increasing pipe inclination, for a given *wfs*, increases the normalized mean pressure. Also, at a certain value for *wfs* of about 1700, the curves have a peak from 2.7 for the horizontal pipe to 4 for 4% pipe slope. Figure 15 shows the effect of void fraction on the normalized mean pressure.

Void fraction (α) is an important parameter of two-phase flow which is the ratio of volume of air or gaseous phase to the total volume of two-phase flow, or

$$\alpha = \frac{v_a}{v_a + v_w} = \frac{L_a A_a}{\lambda A} \tag{13}$$

where, L_a, A_a, λ, and A are the air bubble length, air bubble sectional area, wavelength, and the pipe sectional area, respectively. It can be seen that increase of pipe slope for a constant void fraction decreases the normalized mean pressure for α up to 0.45 while after this value pressure increases with pipe slope. Also, there is a peak value for the pressure at different inclinations which varies from 2.7 to 3.8 for this study. Figure 16 illustrates the variation of normalized mean pressure against wave Froude number ($\mathrm{Fr}_c = c/\sqrt{\lambda g}$) for different pipe inclinations, where c is the wave celerity or the velocity of the slug front.

An interesting result is that, for $\mathrm{Fr}_c < 0.14$ increasing the pipe slope, decreases the normalized mean pressure while for $\mathrm{Fr}_c > 0.14$ the pressure increases with pipe slope. As seen, at $\mathrm{Fr}_c = 0.14$ the lines intersect and a singular point is obtained at a value of 3.3 for P_h/h. Applying the trial and error procedures, the following expression is obtained:

$$\frac{P_h}{h} = a\,\mathrm{Fr}_c^2 + b\,\mathrm{Fr}_c + c \tag{14}$$

where

$$a = -1437S_0 - 42.15 \tag{15a}$$

$$b = 1946.9S_0 - 21.13 \tag{15b}$$

$$c = -243S_0 + 10.24 \tag{15c}$$

Figure 17 includes the entire data and fitted curves for normalized mean pressure versus air concentration ($\bar{C}$) for different pipe inclinations. As the concentration increases up to about 0.4, the value of P_h/h increases, while for higher values of concentration, P_h/h decreases. Figures 18–20 compare the results of present experimental model with the theoretical and available experimental results of previous researches. Figure 18(*a*) illustrates the varia-

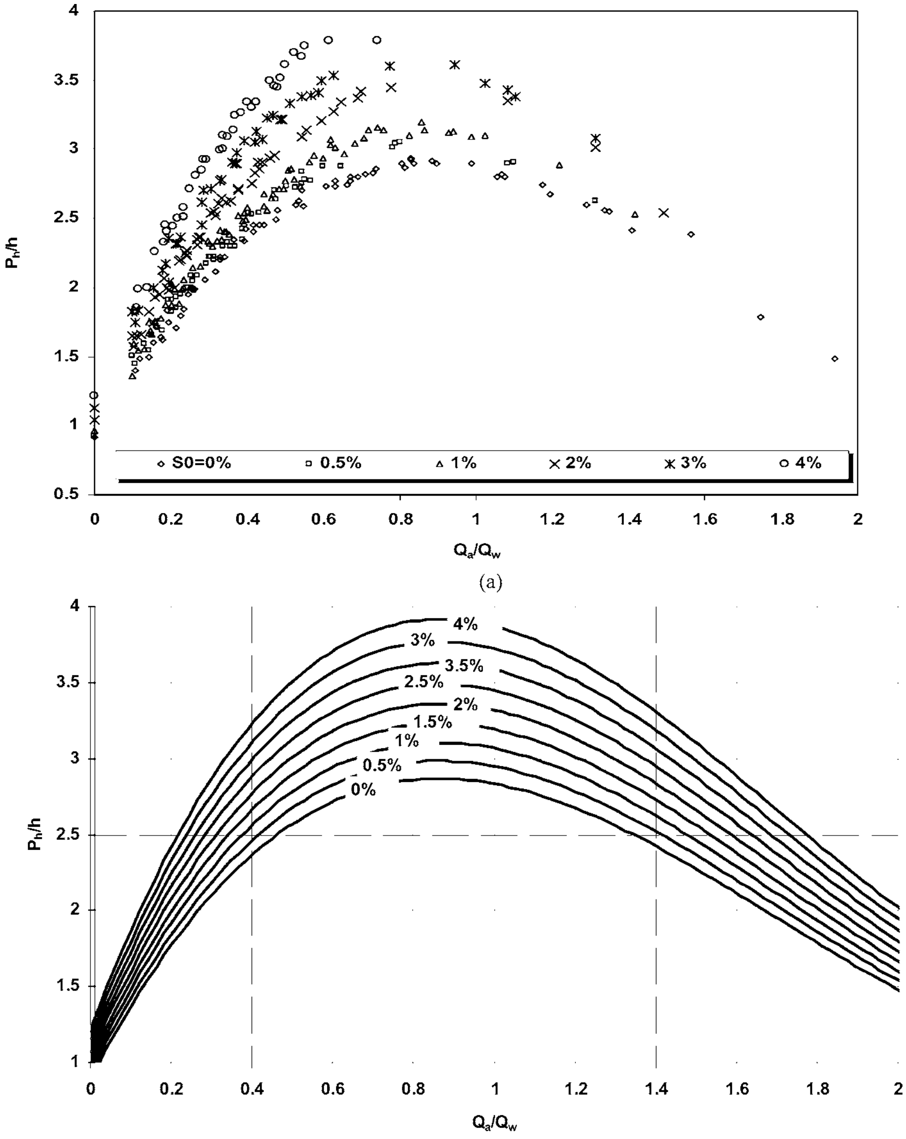

(a)

(b)

Fig. 9 Dimensionless mean pressure versus air/water flow rates ratio for different pipe inclinations: (*a*) data; (*b*) best fit curves

tion of pressure loss versus water flow rate for $Q_a=2$ l/s. The zero slope pipeline which was used by Yakubov [23] was 2.54 cm diameter and 3.5 m long. The dimensionless parameter Q_w/Q_c ($Q_c=V_cA_p$ and $V_c=(gD)^{0.5}$, D is the pipe diameter) was used to have a better criterion for comparison. Figure 18(*b*) compares the normalized mean pressure from the present study and the same reference. Despite the significant difference between the results, the close behavior and trend can be seen between the results. It should be noticed that for the pipe diameter of 2.54 cm the effects of surface tension and viscosity are more significant. Figure 19 compares the present results with Gonçalves et al. experimental data [24], Boll's model, Calvert's formula, and the Yung et al. expression (all data are taken from Gonçalves et al.). Good agreement exists between the results of present model and those of previous researches, especially Boll's and Gonçalves et al. Figure 20 shows the results of the present data with the numerical model of Tarasevich [25]. Tarasevich presented a method of calculation for the two-phase flows based on the method of characteristics. This method uses the two-scale joint grid: one for liquid phase and other for gas phase. The majority of the points are within ±15% bound, which show fair agreement between the present data and numerical results of Tarasevich.

As shown, P_h/h has significant relations with each dimensionless parameter, developed in Eq. (5). However, in order to show the multivariation equation between the results, the general statistical package SPSS and the trial and error methodology were used. The SPSS is a statistical program which estimates the relation of multivariable functions such as, $y=f(x_1,x_2,\ldots,x_n)$. The error functions are root mean square (R^2) and the normalized root mean square error function (NRMSE) expressed as [26]

$$\mathrm{NRMSE}=\sqrt{\frac{\sum(F(x)-f(x))^2}{\sum(f(x)-\bar{f})^2}} \tag{16}$$

where $F(x)$ is the estimated amount, $f(x)$ is the measured data, and $\bar{f}$ is the average of the measured data.

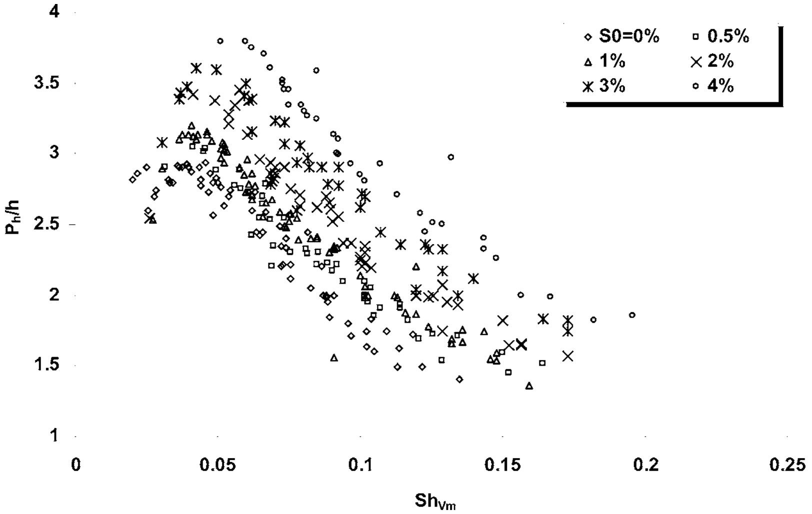

Fig. 10 Dimensionless mean pressure against strouhal number for different pipe inclinations

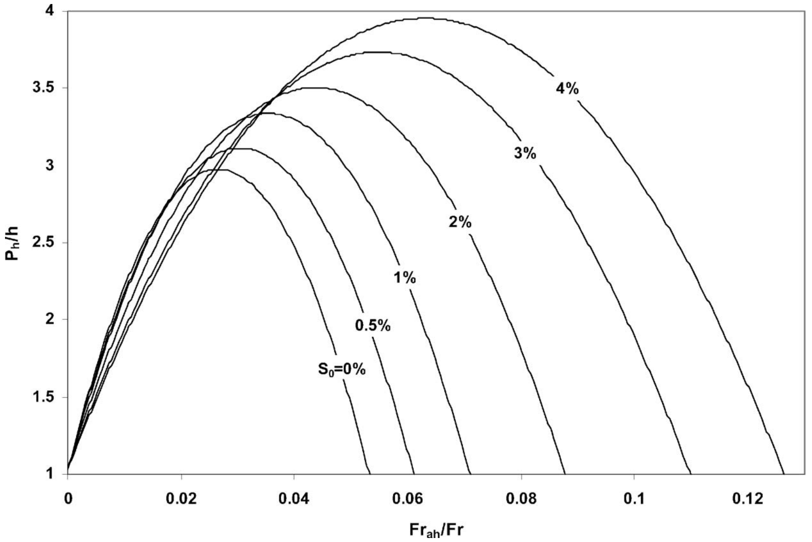

Fig. 11 The effect of dimensionless parameter Fr_{ah}/Fr versus dimensionless mean pressure

The error function NRMSE must be small in order to have the best relation among all parameters. Using the SPSS package, a number of combinations have been tried and the following relations have been obtained

$$\frac{P_h}{h}=\frac{0.19\,\mathrm{Fr}^{0.99}\,K_f^{0.16}wfs^{0.26}}{\mathrm{Sh}^{0.17}\,\alpha^{0.02}\bar{C}^{0.13}} \tag{17}$$

$$\frac{P_h}{h}=0.05\,\mathrm{Fr}^{0.69}+0.15\,\mathrm{Sh}^{-0.29}+0.10K_f^{0.36}+0.11\alpha^{0.53}+0.10\bar{C}^{0.42}+0.03wfs^{0.16}+1.01 \tag{18}$$

$$\frac{P_h}{h}=\frac{0.26\,\mathrm{Fr}^{1.43}\,K_f^{0.81}\alpha^{0.03}}{\mathrm{Sh}^{0.19}\,\bar{C}^{0.2}wfs^{0.26}}+1.2 \tag{19}$$

Figures 21(*a*)–21(*c*) show the comparison between measured and calculated pressure using Eqs. (17)–(19). The majority of the points are within ±10% bound, which shows a very good result for this kind of experimental work with quite a few variables.

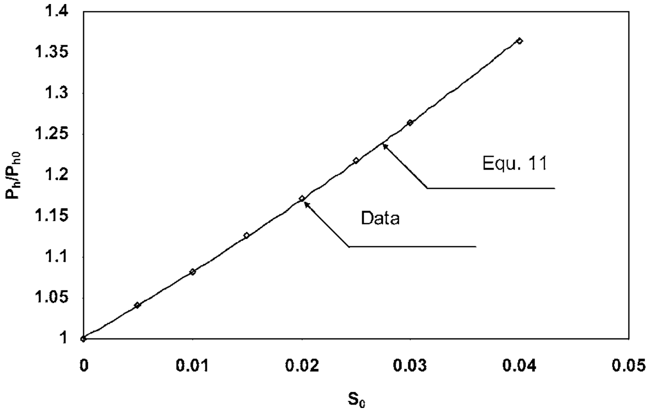

Fig. 12 Relation between pipe inclination and dimensionless mean pressure

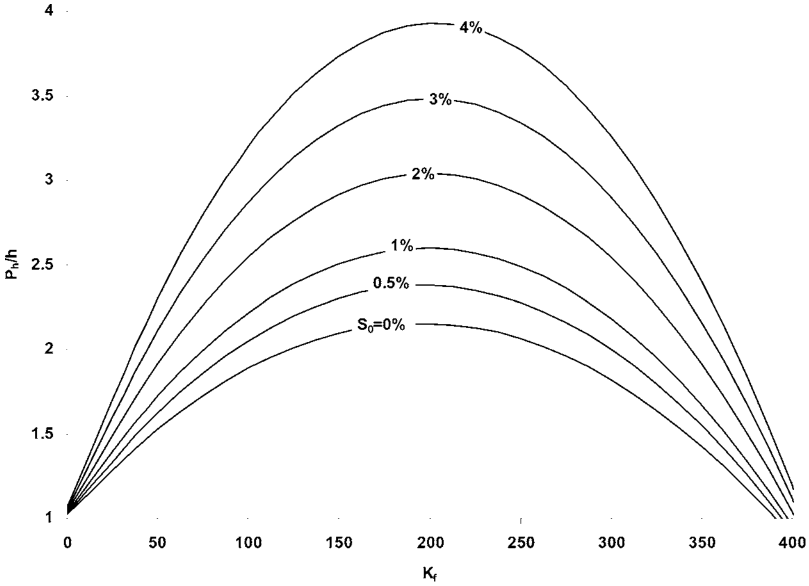

Fig. 13 Dimensionless parameter $K_f = f_{TP}L/D$ versus dimensionless mean pressure for different pipe inclinations

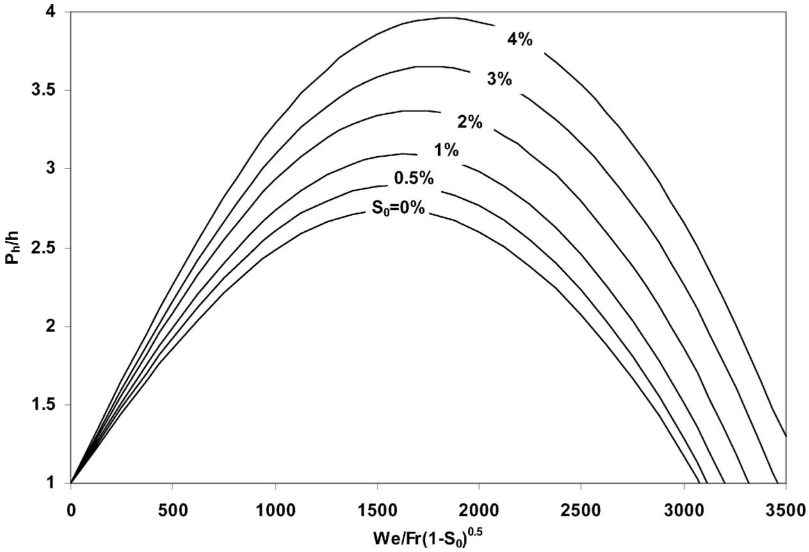

Fig. 14 The relation between P_h/h and dimensionless parameter *wfs*

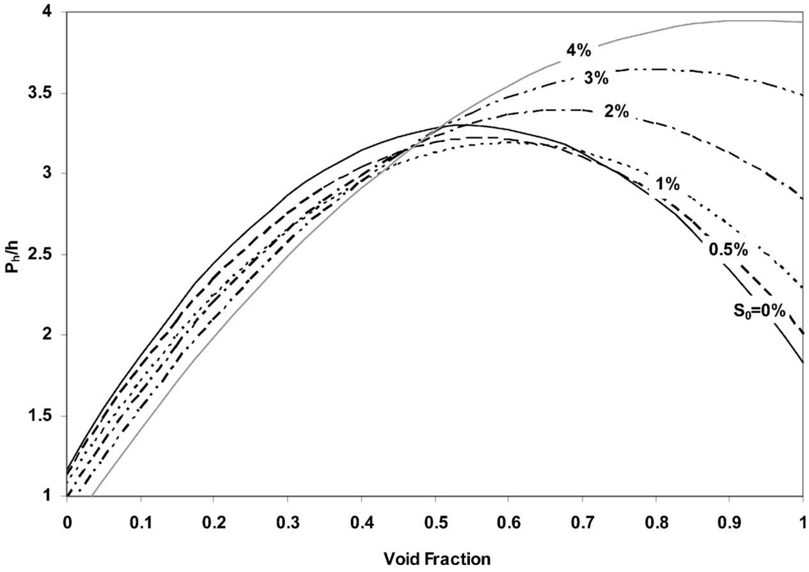

Fig. 15 Influence of void fraction on P_h/h

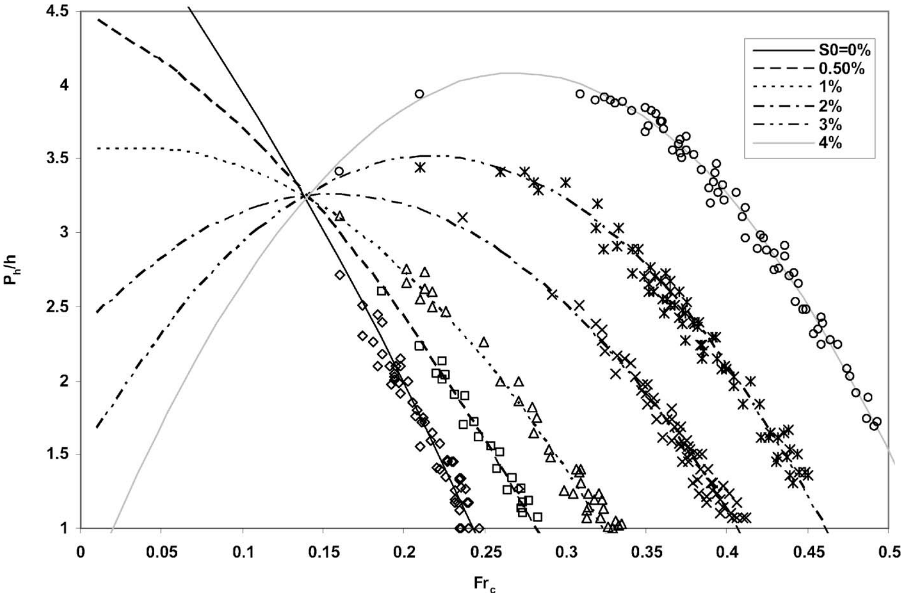

Fig. 16 Variation of dimensionless mean pressure versus Fr_c

Thus, Eq. (19) as the best obtained equation and being a good tool for predicting mean pressure in a water tunnel due to formation of two-phase air-water flow is introduced. Also, this value can be used to obtain maximum and minimum instantaneous pressure using Eq. (6). Each equation has been checked by comparing P_h/h from measured and calculated data. Figure 22 illustrates NRMSE and R^2 for each equation. As it is seen for Eq. (19), lower values of NRMSE and R^2 compared to the other results are obtained.

5 Concluding Remarks

Experimental investigations were carried out to clarify the pressure characteristics of two-phase air-water slug flow in a circular, horizontal, and inclined pipeline. The main parameters affected are shown in Eq. (1) and in the nondimensional form in Eq. (5). While the effects of individual parameters in the equations are shown in Figs. 8–16, the accuracy of present data has been checked with previous available published works (Figs. 18–20). Finally, using the SPSS statistical package, the comprehensive Eq. (19) has been obtained, to show the dimensionless mean pressure, P_h/h, as a function of the most effective parameters. Also, the validity of the suggested equation, using the present results, with a tolerance of ±10% is shown in Fig. 21(*c*). Although Eq. (19) represents the mean pressure variation, but for instantaneous maximum and minimum pressure changes, Fig. 6 and Eqs. (6*a*) and (6*b*) can be used.

Nomenclature

A = the pipe sectional area
A_a = air bubble sectional area
D = pipe inner diameter
$F(x)$ = the estimated amount
G = mass velocity
L = pipe length or characteristic length
L_a = the air bubble length
NRMSE = the error function (normalized root mean square error function)
P = pressure inside the pipe
P_h = mean pressure head

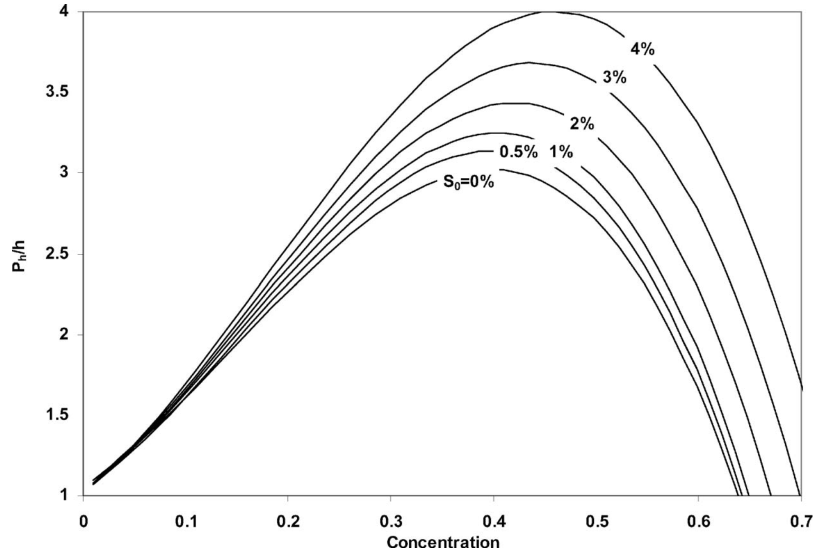

Fig. 17 Variation of P_h/h with concentration

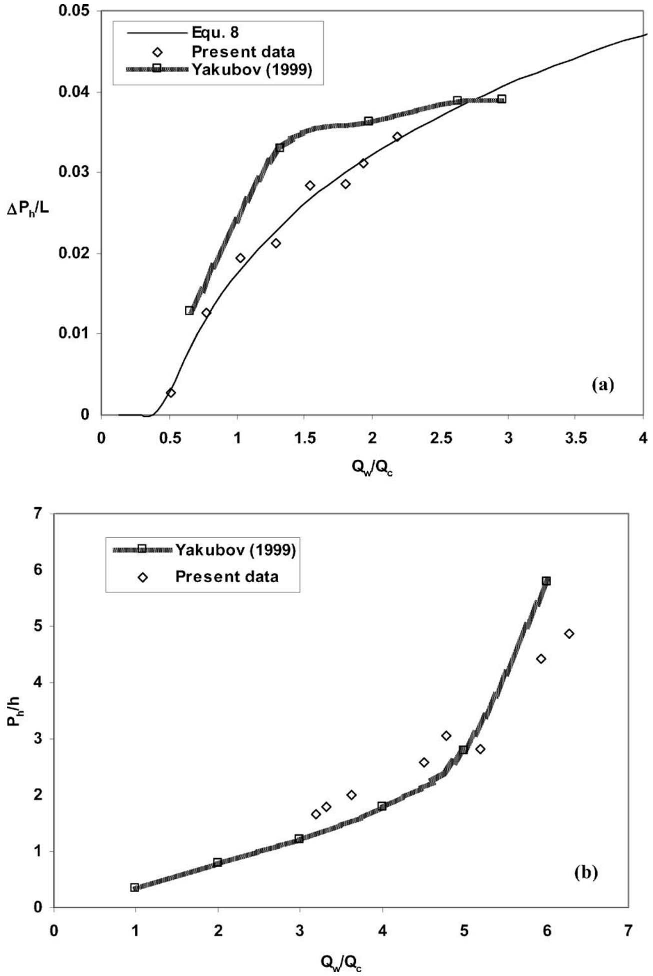

Fig. 18 Comparison of present results with Yakubov for zero slope pipe: (*a*) pressure loss versus water flow rate; (*b*) dimensionless mean pressure versus water flow

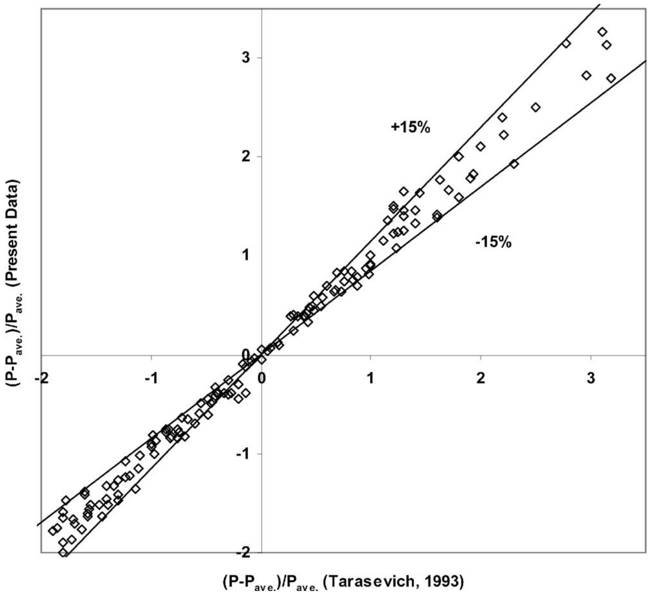

Fig. 20 Comparison of present data with Tarasevich

P_{h0} = mean pressure head in horizontal pipe
Q = discharge
V_m = mixed velocity ($V_m = V_a + V_w$)
V = velocity
a, w = subscripts denote air and water
c = the wave celerity
dP/dx = pressure drop
f = wave frequency
f_{TP} = two-phase friction factor
$f(x)$ = the measured data
$\bar{f}$ = the average of the measured data
g = acceleration due to gravity
h = headwater
x = distance from the pipe entrance
x_m = mass quality
φ = pipe inclination
λ = wavelength
μ = viscosity

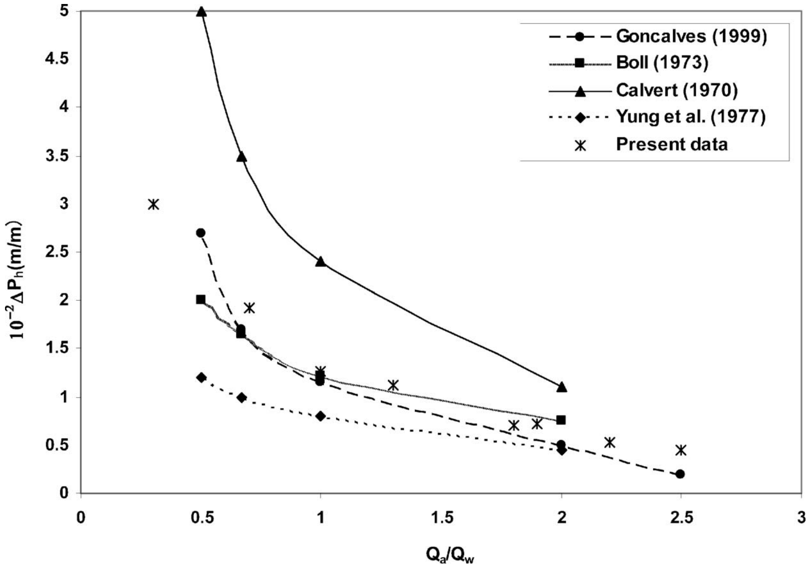

Fig. 19 Comparison of present results with previous works (pressure loss versus air/water rates ratio)

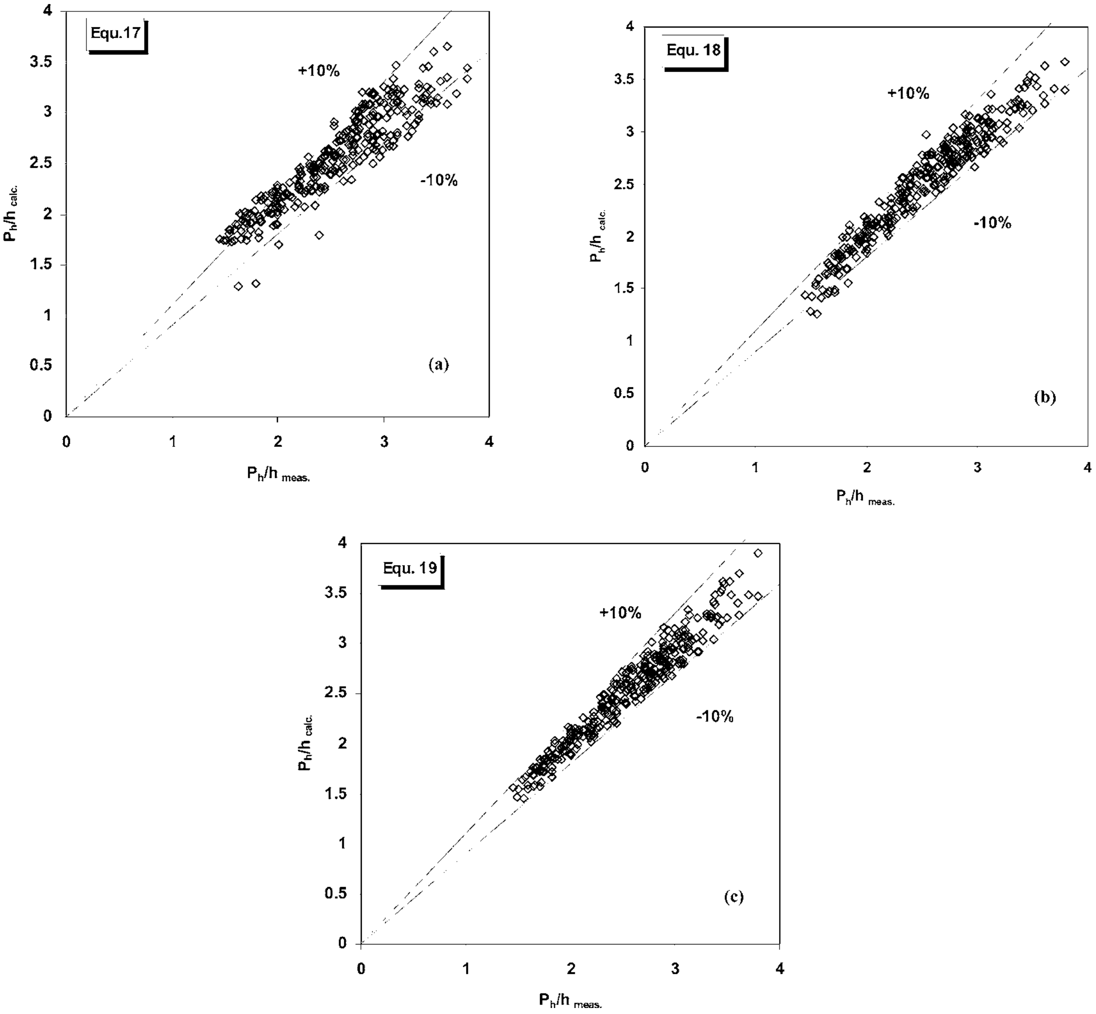

Fig. 21 Observed versus measured data: (*a*) Eq. (17); (*b*) Eq. (18); (*c*) Eq. (19).

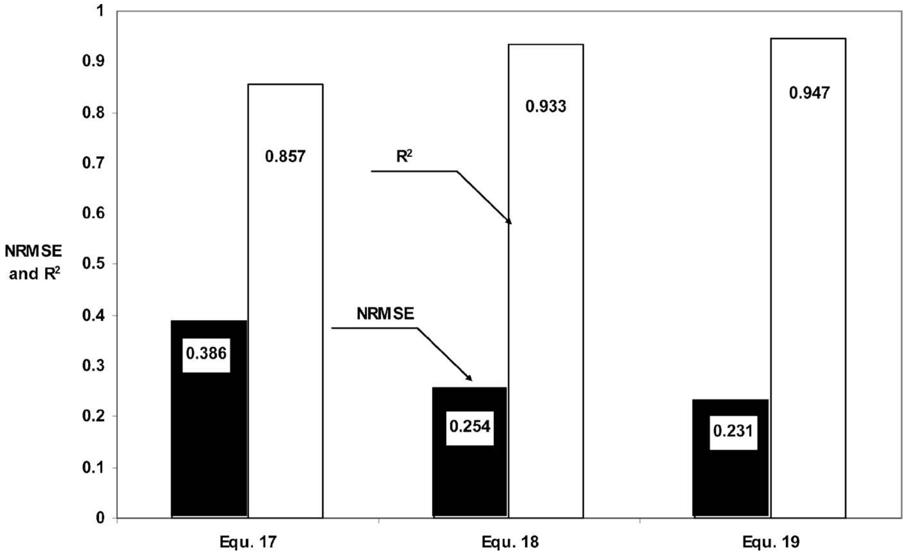

Fig. 22 NRMSE and R^2 for presented relations

μ_m = mixed viscosity
θ = piezometer angle
ρ = density
σ = surface tension
τ_0 = wall shear stress
ξ = functional symbol

Dimensionless parameters

$\bar{C}=\frac{Q_a}{Q_a+Q_w}=\frac{\beta}{1+\beta}$ = air concentration
$Fr=\frac{C}{\sqrt{Lg}}$ or $\frac{Q_a+Q_w}{\sqrt{gD^5}}$ = Froude number
$K_f=f_{\mathrm{TP}}\frac{L}{D}$ = friction coefficient
$\mathrm{Re}=\frac{\bar{\rho}V_mD}{\mu_m}$ = Reynolds number
$\mathrm{Sh}=\frac{Df}{V_m}$ = Strouhal number
$S_0=\sin\varphi$ = pipe slope
$\mathrm{We}=\frac{V_m^2D}{\sigma/\bar{\rho}}$ = Weber number
$\alpha=\frac{L_aA_a}{\lambda A}$ = void fraction
$wfs=\mathrm{We}\Big/\mathrm{Fr}\sqrt{1-S_0}$ = relative dimensionless parameter

Acknowledgment

The authors wish to express their thanks to Professor Barry Azzopardi, professor of Chemical Engineering, University of Nottingham, for his interest and constructive comments on this paper and also are grateful for the support of the Dean of Graduates at Sharif University of Technology.

References

[1] Mattew, P., Peramaki, P. E., Mark, D., and Nelson, P. E., 2000, "The Significance of Two-Phase Flow Regimes in Designing Multi-Phase Extraction Systems," LBG Article, www.lbgweb.com
[2] Lockhart, R. W., and Martinelli, R. C., 1949, "Proposed Correlation of Data for Isothermal Two-Phase Two-Component Flow in Pipes," Chem. Eng. Prog., **45**, pp. 39-48.
[3] Hamam, M. A., and McCorquodale, J. A., 1982, "Transient Conditions in the Transition From Gravity to Surcharged Sewer Flow," Can. J. Civ. Eng., **9**(2), pp. 189–196.
[4] Zhou, F., Hicks, F., and Steffler, P., 1999, "Sewer Rupture Due to Pressure Oscillations in Trapped Air Pockets," Can. J. Civ. Eng., **2**, pp. 491–500.
[5] Azzopardi, B. J., and Baker, G., 2003, "Characteristics of Periodic Structure in Gas/Liquid Two-Phase Flow," Japan Two-Phase Flow Meeting, Guildford.
[6] Zhang, H. Q., Sarica, W. Q. C., and Brill, P. J., 2003, "A Unified Mechanistic Model for Slug Liquid Holdup and Transition Between Slug and Dispersed Bubble Flows," Int. J. Multiphase Flow, **29**, pp. 97–107.
[7] Issa, R. I., and Kempf, M. H. W., 2003, "Simulation of Slug Flow in Horizontal and Nearly Horizontal Pipes With the Two-Fluid Model," Int. J. Multiphase Flow, **29**, pp. 69–95.
[8] Chenoweth, J. W., and Merritt, W. M., 1955, "Turbulent Two-Phase Flow," Petroleum Refiner, **34**(10), pp. 151–155.
[9] Baruna, S., Shamara, Y., and Brosius, M. G., 1990, "Two-Phase Flow Model Aids Flare Network Design," Oil & Gas J., **90**(4), pp. 90–94.
[10] Gudmundsson, J. S., 1994, "Method for Determination of Flow Rate Especially Two-Phase Flow," Norwegian Patent No. 944264.
[11] Erickson, D., and Twaite, D., 1996, "Pipeline Integrity Monitoring System for Leak Detection, Control, Optimization of Wet Gas Pipelines," in *Production Operations and Engineering*, SPE-36607, Brown and Root, eds., Multi-Phase Solutions, Denver.
[12] Silberman, E., 1957, "Sound Velocity and Attenuation in Bubbly Mixtures Measured in Standing Wave Tubes," J. Acoust. Soc. Am., **29**(8), pp. 925–933.
[13] Ruggles, A. E., Lahey, R. T., Drew, D. A., and Scarton, H. A., 1988, "An Investigation of the Propagation of Pressure Perturbations in Bubbly Air-Water Flows," ASME J. Heat Transfer, **110**, pp. 494–499.
[14] Lahey, R. T., 1992, "Wave Propagation Phenomena in Two-Phase Flow," Boiling Heat Transfer, **37**(1), pp. 123–173.
[15] Semenov, N. I., 1964, "Results of Studying the Speed of Sound in Moving Gas-Liquid Systems," Teploenergetika, **11**(6), pp. 46–51.
[16] Martin, C. S., and Padmanabhan, M., 1979, "Pressure Pulse Propagation in Two-Component Slug Flow," J. Fluids Eng., **101**, pp. 44–52.
[17] Matsui, G., Sugihara, M., and Arimoto, S., 1979, "Propagation Characteristics of Pressure Wave Through Gas-Liquid Plug-Train System," Bull. JSME, **22**(173), pp. 1562–1569.
[18] USBR, 1978, Design of small canal structures, Bureau of Reclamation. United States Department of the Interior, Denver, Colorado.
[19] Levy, S., 1999, "*Two-Phase Flow in Complex Systems*," Wiley, New York.
[20] Barenblatt, G. I., 1979, *Similarity, Self-Similarity and Intermediate Asymptotics*, Consultants Bureau, New York.
[21] Zielinski, P. B., and Willemonte, J. R., 1968, "Effect of Viscosity on Vortex-Orifice Flow," J. Hydr. Div., ASCE, **94**(3), pp. 195–205.
[22] Freund, J. E., and Walpole, R. E., 1980, *Mathematical Statistics*, 3rd ed., Prentice-Hall.
[23] Yakubov, B., Tanny, J., Maron, D. M., and Brauner, N., 1999, "Experimental Study on the Characteristics of a Fluidized Bed in Inclined Pipes," Proceedings of the 2nd International Symposium On Two-Phase Flow Modeling and Experimentation, Italy, pp. 1825–1832.
[24] Gonçalves, J. A. S., Fernández, D., and Azzopardi, B. J., 1999, "Experimental Study of Hydrodynamics in Venture Scrubbers With Two Different Liquid Injection Arrangements," Proceedings of the 2nd International Symposium On Two-Phase Flow Modeling and Experimentation, Italy, pp. 701–706.
[25] Tarasevich, V. V., 1993, "The Calculation of the Flows of Two-Phase Mixtures in Pipe Systems," Proceedings of the 1st All-Russia Seminar About Dynamics of Space and Non-Equilibrium Flows of Liquid and Gas, Russia, pp. 111–113.
[26] Gonzalez, J., Rojas, I., Poamares, H., and Orteag, J., 2002, "A New Clustering Techinque for Function Approximation," IEEE Trans. Neural Netw., **13**(1), pp. 132–142.

Young-Do Choi
e-mail: ydchoi@mach.me.ynu.ac.jp

Junichi Kurokawa

Division of Systems Research,
Faculty of Engineering,
Yokohama National University,
79-5 Tokiwadai, Hodogaya-ku,
Yokohama, 240-8501 Japan

Hiroshi Imamura
College Master Hands, Inc.,
1st Floor NT Bldg.,
2-1-31 Midorigaoka, Zama-shi,
Kanagawa, 228-0021 Japan

Suppression of Cavitation in Inducers by J-Grooves

Cavitation is a serious problem in the development of high-speed turbopumps, and an inducer is often used to avoid cavitation in the main impeller. Thus, the inducer often operates under the worst conditions of cavitation. If it could be possible to control and suppress cavitation in the inducer by some new device, it would also be possible to suppress cavitation occurring in all types of pumps. The purpose of our present study is to develop a new, effective method of controlling and suppressing cavitation in an inducer using shallow grooves, called "J-Grooves." J-Grooves are installed on the casing wall near the blade tip to use the high axial pressure gradient that exists between the region just downstream of the inducer leading edge and the region immediately upstream of the inducer. The results show that the proper combination of backward-swept inducer with J-Grooves improves the suction performance of the turbopump remarkably, at both partial flow rates and the design flow rate. The rotating backflow cavitation occurring at low flow rates and the cavitation surge which occurs near the best efficiency point can be almost fully suppressed by installing J-Grooves. [DOI: 10.1115/1.2375126]

Keywords: cavitation, inducer, turbopump, J-Groove, suction performance

1 Introduction

Cavitation occurring in turbomachinery is a problem to users and designers. Therefore, a good amount of research has been conducted to overcome or suppress this phenomenon. Conventional methods of raising the pressure in a minimum pressure region including lowering the pump inlet, reducing inlet pipe loss, or installing an inducer and a booster pump have been proposed. In the case of installing an inducer, many studies (e.g., Lakshminarayana [1] and Japikse [2]) have been performed to improve the suction performance of the pump by optimizing the geometry of the inducer. Because cavitation is a physical phenomenon, it is impossible to completely restrain the outbreak of cavitation, but it is expected that it can be suppressed internally to some extent.

Kurokawa et al. [3–6] have proposed shallow grooves, named "J-Grooves," mounted on a casing wall of turbomachinery in the pressure gradient direction of the main flow as countermeasures to various abnormal flow phenomena such as the rotating stall in parallel-walled vaned and vaneless diffusers, and the rising head curve characteristic with increasing flow rate in mixed and axial flow pumps. From the previous related studies, it has been verified that J-Grooves can suppress various undesirable flow phenomena with rotation by controlling the angular momentum of mainstream. In addition, one more important characteristic of the J-Groove is to increase the pressure in the low pressure region by carrying the high pressure fluid to the low pressure region through the groove. If this characteristic of increasing the pressure at low pressure region can be applied to the control of cavitation, suppression of the cavitation occurring in turbomachinery can be achieved.

Inducers have been used to control cavitation in centrifugal pumps because they contribute to gentle slope of the head drop, and smaller blockage in the passage. However, as the inducer is an impeller operated under the most severe condition of cavitation, various cavitation phenomena including rotating cavitation and cavitation surge occur in the inducer (e.g., Tsujimoto et al. [7]). Moreover, from the report of Imano et al. [8], strong rotating cavitation occurring in the inducer of a liquid hydrogen turbopump has caused engine trouble in the H-II rocket. Kamijo et al. [9] suggested a method to suppress the rotating cavitation but the method was not clearly confirmed to be a general method in a later study by Fujii et al. [10]. For the present problem, it is believed that the J-Groove is an effective method for suppressing rotating cavitation, because the J-Groove controls the angular momentum of main flow.

The purpose of this study is to clarify the effectiveness of cavitation suppression in an inducer by employing J-Grooves. If it could be possible to control the cavitation and to extend the operating range of the inducer, cavitations occurring in various pumps might also be controlled and suppressed by employing J-Grooves because the inducer is operated under the most severe cavitation conditions.

2 Experimental and Computational Method

2.1 Experimental Apparatus and Method. With an experimental apparatus of a sealed circular conduit system including a pressure control tank with a capacity of 2.5 m^3, performance tests and cavitation tests were conducted using a centrifugal pump as shown in Fig. 1. The impeller inlet blade angle varies at each width location of blade inlet such that $\beta_{1,\mathrm{hub}}=21.5$ deg near hub, $\beta_{1,\mathrm{medium}}=15$ deg at a medium width location and $\beta_{1,\mathrm{tip}}=11.5$ deg near the front shroud. The specific speed of the test pump is determined to be $n_s=300$. The cavitation test was conducted after having adjusted dissolved oxygen in the water to lower than 3 ppm by deaeration driving of filtered clean water for 10 h under a lowered internal pressure of the apparatus. The available net positive suction head *NPSH* is controlled by the base pressure in the pressure control tank which is connected to a vacuum pump. The rotational speed n of the test pump is fixed to 2000 min^{-1}. The Reynolds number is 4.2×10^5 characterized by diameter d and tip speed u_t of the inducer. To record the behavior in the cavity around the inducer, the inducer casing was made of transparent acrylic resin. A digital still camera and a stroboscope, synchronized with the inducer rotation, were used to take pictures of the internal flow around the inducer. To measure the static pressure along the inducer wall, 14 pressure taps are installed on the inducer casing wall in the axial direction.

The schematic view and specifications of the inducers are shown in Fig. 2 and Table 1. Three kinds of helical inducers are adopted. The blade number and outer diameter of the inducers are

---

Contributed by the Fluids Engineering Division of ASME for publication in the JOURNAL OF FLUIDS ENGINEERING. Manuscript received September 19, 2005; final manuscript received July 3, 2006. Review conducted by Joseph Katz. Paper presented at The 8th Asian International Conference on Fluid Machinery, 2005.

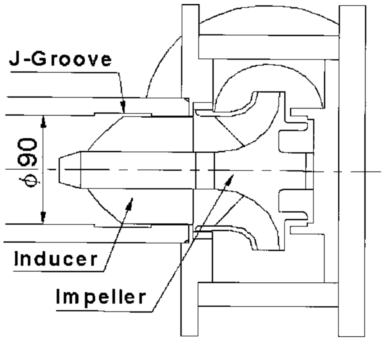

Fig. 1 Schematic view of test pump. (*a*) Flat-plate inducer A ($\beta_1=\beta_2=17.5$ deg); (*b*) cambered inducer B ($\beta_1=13$ deg, $\beta_2=17$ deg); (*c*) flat-plate inducer C ($\beta_1=\beta_2=19.5$ deg).

Table 1 Design parameters of test inducer

Inducer	A	B	C
Inducer diameter	89 mm	89 mm	89 mm
Tip clearance	0.5 mm	0.5 mm	0.5 mm
Blade number	3	3	3
Blade inlet angle at tip	17.5 deg.	13.0 deg.	19.5 deg.
Blade outlet angle at tip	17.5 deg.	17.0 deg.	19.5 deg.
Axial length at tip	85 mm	40 mm	75 mm
Solidity at tip	3.03	1.69	1.62

3 and 89 mm, respectively. Tip clearance between the inducer tip and housing wall is fixed to 0.5 mm. The blade thickness of the three inducers is constant hub to tip and equal to 3 mm. As the blade angle of a helical inducer has a considerable effect on the suction performance (Japikse [2] and Tahara et al. [11]), the inducer blade angle is usually fixed at a very large angle from the axial direction to minimize the occurrence of cavitation on the blade pressure surface. Therefore, a flat-plate helical inducer with a blade angle of 17.5 deg from tangential was adopted as a control (test inducer A). In the case of cambered inducer B, the blade inlet angle from tangential is determined to be 13 deg, but the blade outlet angle is determined to be almost the same as that of test inducer A because a flat-plate helical inducer does not work when the flow achieves the shockless flow rate. Besides, since previous studies by Japikse [2] and Bakir et al. [12] have clarified that the suction performance of an inducer can be improved by applying a backward swept leading edge inducer blade, test inducer B has a backward swept leading edge. For the purpose of improving suction performance even further, test inducer C with a backward swept leading edge is designed to suppress the cavitation occurring on the inducer hub region by adopting CFD results in Sec. 2.2.

The J-Groove, which is installed in the axial direction on the inducer casing wall has a rectangular cross-sectional area. The definition and parameters of different J-Groove configurations are shown in Fig. 3 and Table 2. Four configurations were tested for the experiment. The depth of all J-Grooves is the same, 2 mm. The configuration with 32 grooves, 6 mm width is called J-Groove 1. This is defined as a standard geometry in the present study. J-Groove 2 has half the number of grooves as J-Groove 1 but the width is increased from 6 to 10 mm. J-Groove 3 has the same dimensions as the downstream section of J-Groove 2, but has no groove upstream of the leading edge. J-Groove 4 is the same as J-Groove 2, except that the width is 12 mm. Referring again to Fig. 3, the length of the upstream portion of the J-Groove, L_1, is the length measured from the inducer leading edge. This upstream portion of the J-Groove must be of sufficient length to suppress the swirl flow which occurs at low flow rates [4]. The

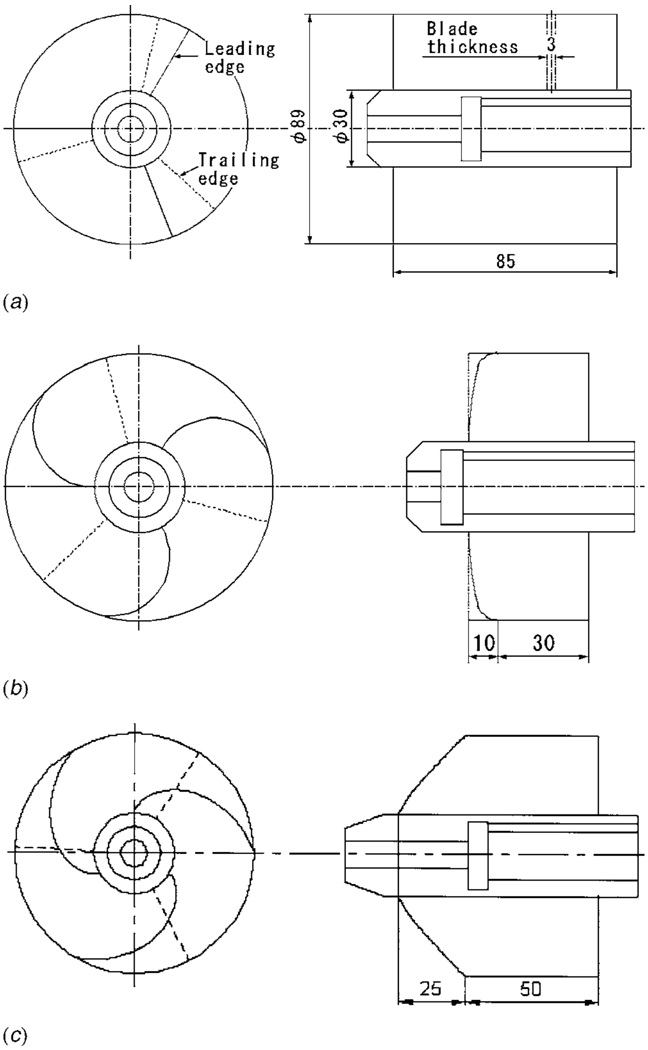

Fig. 2 Test inducers

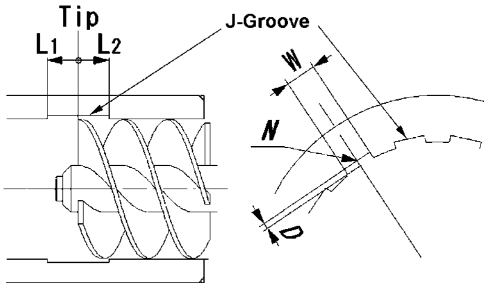

Fig. 3 J-Groove mounted on a casing wall of inducer

Table 2 Parameters of J-Groove

J-Groove	Number N	Width W[mm]	Depth D[mm]	Length $L[mm]$ Upstream L_1	Downstream L_2
1	32	6	2	20	20
2	16	10	2	20	20
3	16	10	2	0	20
4	16	12	2	20	20

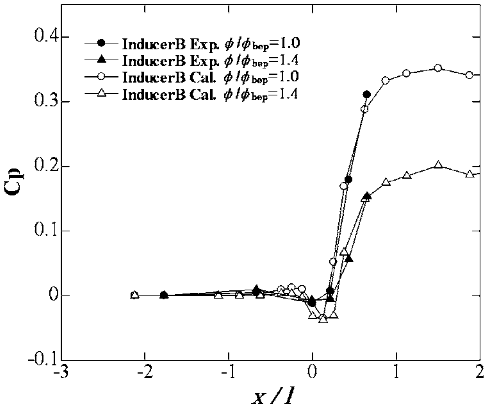

Fig. 4 Comparison of wall pressure distribution without J-Groove for cambered inducer B (ℓ=40 mm). (*a*) r/R=0.40 (near blade hub); (*b*) r/R=0.87 (near blade tip).

downstream portion of the J-Groove likewise must be the correct length in order to suppress cavitation. This length, L_2, is determined using the results of the CFD analysis described in Sec. 2.2.

The uncertainty estimates for each variable in the graphs are based on the method of Abernethy et al. [13]. Measurement uncertainties for pump performance in a noncavitating flow condition are estimated to be $\phi = \pm 1.39\%$, $\psi = \pm 1.0\%$, $\nu = \pm 1.4\%$, and $\eta = \pm 2.23\%$ at the flow rate of best efficiency. For the cavitation test, since the uncertainty on the differential pressure is ±0.5%, the resulting uncertainties of available net positive suction head, suction specific speed, and cavitation number are estimated to be $NPSH = \pm 1.0\%$, $S = \pm 1.15\%$, and $\sigma = \pm 1.0\%$, respectively.

2.2 Determination of J-Groove Effect by CFD Analysis. In order to confirm the effect of J-Grooves on the suppression of cavitation in the best way, the selection of downstream length, L_2, of the J-Groove should be examined. As the pressure gradient in the axial direction of the inducer passage transports fluid from downstream of the inducer leading edge to the upstream area through the J-Grooves, the location of the J-Grooves should be in the region of the maximum pressure gradient. For the case of inducer only operating in the casing, CFD analysis using a commercial code CFX-TASCflow [14], was conducted under the conditions of a single flow passage. The grid number of about 3×10^5 has been used together with the k-ε turbulence model and constant pressure at inlet and averaged outflow at outlet are the used boundary conditions. As shown in Fig. 4, the circumferentially averaged results in inducer B confirms that calculated relative pressure distribution agrees well with the experimental result and the maximum pressure gradient is located in the range of $0 < x/\ell < 0.5$. Therefore, the downstream length of J-Groove is determined to be $x/\ell = 0.5$.

When J-Grooves are installed on the casing wall, suppression of cavitation occurring in the vicinity of a blade tip is expected, but it is difficult to suppress cavitation occurring in the region of an inducer hub. Hence, if the effect of the J-Groove can improve the low pressure in the region of the inducer hub, it would be harder for cavitation to occur in the region, and considerable improvement of the suction performance can be expected. Figure 5 shows the calculated pressure distribution along the blade surface for inducer C at the flow rate of best efficiency (ϕ/ϕ_{bep}=1.0) with and without backward sweep at the leading edge. The pressure distributions near the blade hub (r/R=0.40) and near the blade tip (r/R=0.87) are shown in Figs. 5(*a*) and 5(*b*), respectively. It is clear from the figures that minimum pressure on the blade surface is increased remarkably when applying backward sweep at the leading edge. Without the backward sweep at the leading edge, the region of blade inlet pressure drop is wide in the span direction.

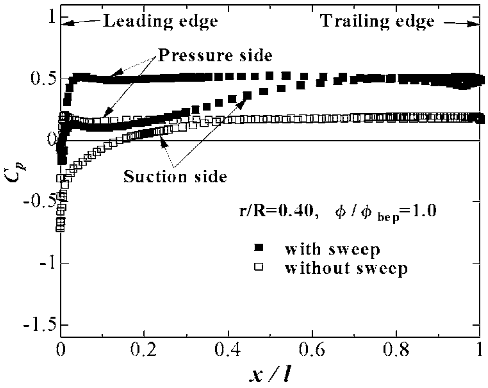

(*a*)

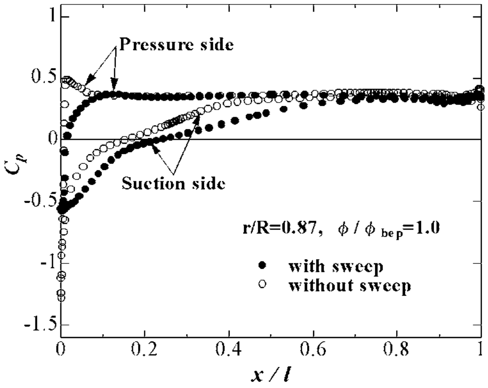

(*b*)

Fig. 5 Calculated pressure distribution along a blade surface for flat-plate inducer C (ϕ/ϕ_{bep}=1.0, $\beta_1=\beta_2$=19.5 deg). (*a*) Effect of inducer; (*b*) effect of J-Groove.

However, with a backward swept leading edge, the pressure drop region is limited to an area near blade tip region. Therefore, the CFD result suggests that suppression of cavitation at the hub region is possible by increasing the pressure at the region using an inducer with backward swept leading edge, and the low pressure near the blade tip region of the inducer can be increased using the J-Grooves. Thus, by referring to the CFD result, a helical inducer with backward swept leading edge and blade angle of 19.5 deg from tangential is designed as inducer C.

3 Results and Discussions

3.1 Pump Performance. Figure 6 presents performance curves of the test pump for noncavitating flow condition. Figure 6(*a*) compares the performance curves for three cases: (1) Main impeller without inducer, (2) main impeller with inducer A, and (3) main impeller with inducer B. Figure 6(*b*) shows performance curves for the cases of the main impeller with inducer A (without J-Groove) and the impeller plus inducer A with J-Grooves 1, 2, and 3.

As shown in Fig. 6(*a*), the best efficiency point of the main pump is located at ϕ_{bep}=0.094 and agrees well with the design flow rate (ϕ_d=0.097). In addition, head increase due to installation of the inducer is only about 5% of the head of the main impeller, and head increase due to the inducer in the flow range near shutoff and high flow rates is small. From the comparison of the performance curves of the inducers A and B, it is clear that inducer B with backward swept leading edge has a little higher head than inducer A over almost the full range of flow rate, but maximum pump efficiency is 61% in the case of the main impeller only, 60% after installation of the inducer A to the main impeller,

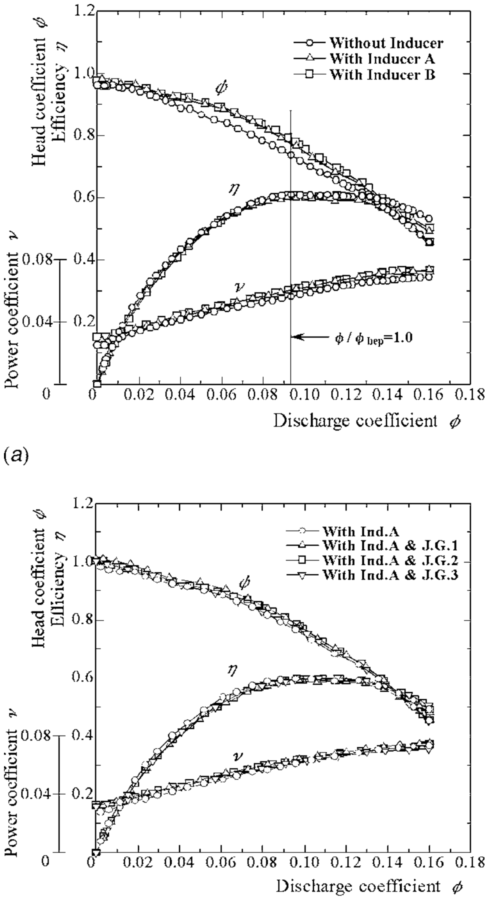

(*a*)

(*b*)

Fig. 6 Comparison of pump performance

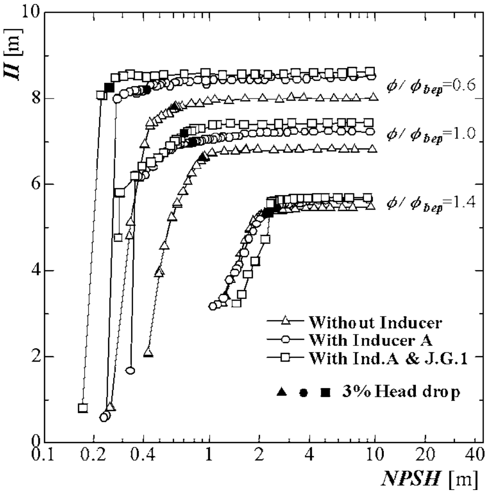

Fig. 7 Improvement of suction performance by inducer and J-Groove

and 61% after installation of the inducer B to the main impeller. Thus the effect of the inducer on the maximum pump efficiency is quite small.

On the other hand, as shown in Fig. 6(*b*), the head coefficient and the power coefficient are increased very little after installation of the J-Groove in the range of low flow rate and at the best efficiency point. It is assumed that the slight change in the performance curves results from the suppression of swirl flow at the inducer inlet as the J-Groove suppresses inlet reverse flow (e.g., Saha et al. [4]) and then, the drop of theoretical head in the inducer gets suppressed. However, pump performance in high flow rate range does not improve even after installation of the J-Groove because there exists no inlet reverse flow in that range.

3.2 Effect of J-Groove on the Suppression of Cavitation. Figure 7 shows comparison of the suction performance of the test pump for the cases of main impeller only, installing inducer A to the main impeller, and installing inducer A to the main impeller with J-Groove 1. Suction performance can be examined using the change of pump head with *NPSH*. *The NPSH* is calculated as follows:

$$NPSH = (p_s - p_v)/\rho g + \nu_s^2/2g \tag{1}$$

Moreover, $NPSH_R$, which is determined at 3% head drop point, is adopted as a reference "breakdown" value.

At the flow rate ratio of ϕ / ϕ_{bep}=0.6 as shown in Fig. 7, in the case of main impeller only, the test pump maintains high head in the range of low *NPSH* and then the head decreases sharply. However, after installation of the inducer in front of the main impeller, test pump maintains high head in the lower *NPSH* range as compared with the case of main impeller only, which indicates improvement of suction performance due to the presence of the inducer. At ϕ / ϕ_{bep}=1.0, for the case of main impeller only, it shows sharp head drop after 3% head drop and for the case of installation of the inducer to the main impeller, head drop shows a gentle gradient even after 3% head drop. At ϕ / ϕ_{bep}=1.4, head starts to drop from high *NPSH* region itself and the effect of inducer on suction performance almost disappears.

In the case of the main impeller with inducer A and J-Groove 1 installed, at ϕ / ϕ_{bep}=0.6, the 3% head drop point shifts more to the range of low *NPSH* than for the main impeller with inducer only. Hence, suction performance improves significantly. At ϕ / ϕ_{bep}=1.0, the aspect of preventing the break fall-off of the test pump does not change very much for the configuration with inducer A with or without the J-Groove. At ϕ / ϕ_{bep}=1.4, the sharp head drop point in the case of the main impeller with inducer A and J-Groove 1 is almost the same as in the case of the main impeller alone.

3.3 Investigation of Optimum Shape of J-Groove. Since Fig. 7 has clarified that J-Groove is effective on suppression of cavitation in the inducer at the flow below ϕ_{bep}, the optimization of the J-Groove shape and its matching with the inducer are examined.

Figure 8 shows suction performance of the test pump with inducer A and three kinds of J-Grooves. By mounting the J-Grooves on the inducer casing, at ϕ / ϕ_{bep}=0.6, the largest shift in 3% head drop point occurs using J-Groove 3, which has the widest groove width. However, at ϕ / ϕ_{bep}=1.4, neither of the J-Grooves show such a desired effect on the suppression of cavitation.

Figure 9 compares suction specific speed *S* for the cases of combination of main impeller, inducers, and J-Grooves over a wide flow range. The suction specific speed *S* is defined as

$$S = n\sqrt{Q}/(NPSH_R)^{3/4} \tag{2}$$

Usually, suction specific speed is defined at the best efficiency point, but, for the comparison of suction performance of the main impeller with inducers and J-Grooves, local $NPSH_R$, determined by *NPSH* at 3% head drop point for each flow rate, has been used for the definition of suction specific speed.

Figure 9(*a*) indicates clearly that the effect of the inducer is remarkable in the flow rate range of $\phi / \phi_{bep} < 1.0$, since the suction specific speed increases appreciably. In addition, inducer B shows comparatively better suction performance over the entire flow rate range. However, at the best efficiency point, installation of any of the 3 inducers does not contribute to the improvement of suction specific speed to an appreciable extent. Rather, inducers A

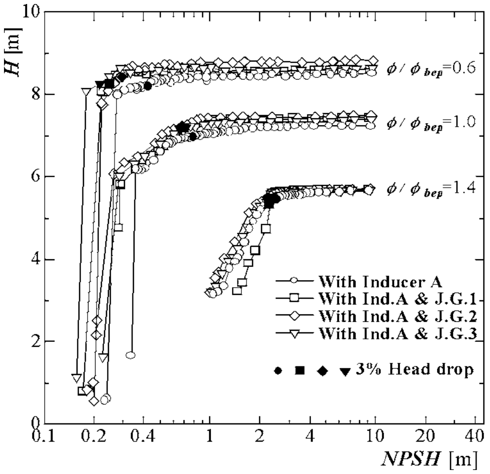

Fig. 8 Effect of J-Groove on the improvement of suction performance. (*a*) Effect of inducer (without J-Groove); (*b*) effect of J-Groove; (*c*) comparison of suction specific speed with inducers and J-Grooves.

and C decrease the suction specific speed in the range of high flow rate as compared with no inducer (main impeller only). The reason for low suction performance may be that the inducer outlet flow has strong swirl even at the best efficiency point (e.g., Takamatsu et al. [15,16]), and the main impeller inlet flow generates cavitation at the blade pressure side, similar to the flow condition of the high flow rate. Therefore, it is conjectured from this result that a flat-plate helical inducer designed with a large blade angle does not contribute to the improvement of suction performance of the main impeller. Although an appreciable improvement of the suction specific speed after installation of the inducer to main impeller is not observed, recall that the main purpose of this study is to confirm the effectiveness of the J-Groove on suppression of cavitation.

Figure 9(*b*) reveals the effect of the J-Grooves on the suction specific speed. In the case of J-Groove 3, which has no upstream length (L_1), the suction specific speed is increased appreciably at low flow rates compared to the impeller with inducer A. The suction specific speed of the impeller with J-Groove 3 at $\phi/\phi_{bep}=0.6$ reaches to $S=3400$. On the other hand, J-Grooves 1 and 2, which have a groove upstream length of $L_1=20$ mm, show comparatively higher effects at high flow rates. This result suggests that the groove length is a very important parameter in the improvement of suction performance.

Figure 9(*c*) compares the suction specific speed of the three inducers with and without J-Groove 1. Along the ordinate, suction specific speed S is normalized by $S_{\text{without ind.}}$. Here, $S_{\text{without ind.}}$ means a suction specific speed for the main impeller only without any inducer or J-Groove. In the flow rate range of $\phi/\phi_{bep}\leqq 1.0$, the combination of J-Groove 1 and inducers B and C each result in considerable improvement in suction specific speed of about 1.6 times $S_{\text{without ind.}}$. In particular, the combination of J-Groove 1 and inducer B shows the greatest improvement of suction specific speed at all flow rates, even nearly 1.25 times of improvement in the high flow rate range of $\phi/\phi_{bep}=1.2$.

The above results suggest that improvement of suction performance is possible even at high flow rate, by adopting the combination of a backward swept inducer and J-Grooves, and further improvement of suction performance can be achieved by optimizing the shape of the J-Groove.

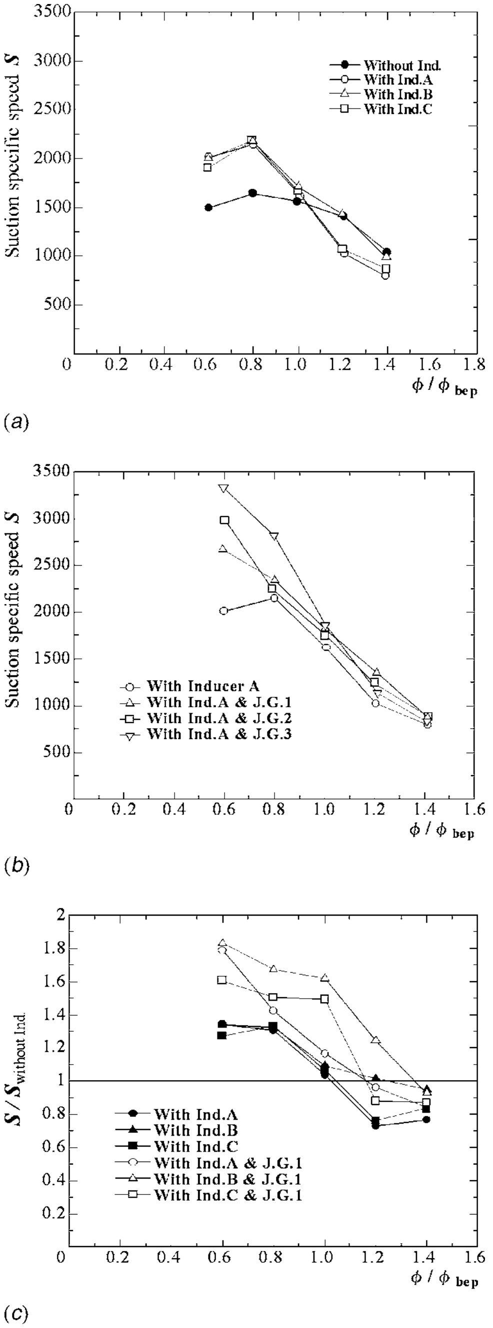

Fig. 9 Improvement of suction specific speed by J-Groove. (*a*) $\phi/\phi_{bep}=0.6$; (*b*) $\phi/\phi_{bep}=1.0$; (*c*) $\phi/\phi_{bep}=1.4$.

3.4 Suppression of Rotating Backflow Cavitation and Cavitation Surge.

In order to investigate the effect of inducer and J-Groove on the suppression of cavitation instabilities, spectral analysis of pressure fluctuation occurring at the inducer inlet ($-x/d=0.94$) is carried out for the main impeller with inducer C, and for the main impeller with inducer C and J-Grooves (Figs. 10 and 11). The normalized frequencies of the cavitation in Figs. 10 and 11 are $f/f_{\text{shaft}}=0.037$ of rotating backflow cavitation and 0.073 of cavitation surge.

For the case of main impeller with inducer C, rotating backflow cavitation occurs in the range of low flow rate ($\phi/\phi_{bep}<1.0$) as shown in Fig. 10(*a*). Here, rotating backflow cavitation means a large cavity cell extending deeply in the axial direction to the upstream of the inducer inlet periodically and rotating in the same direction as the inducer. The rotating backflow cavitation can be suppressed completely by adopting J-Groove 2 as shown in Figs. 11(*a*) and 11(*b*). This can be expected, since the original purpose of the J-Groove was to suppress swirling backflow [3–6]. However, installation of J-Groove 2 causes a cavitation surge just be-

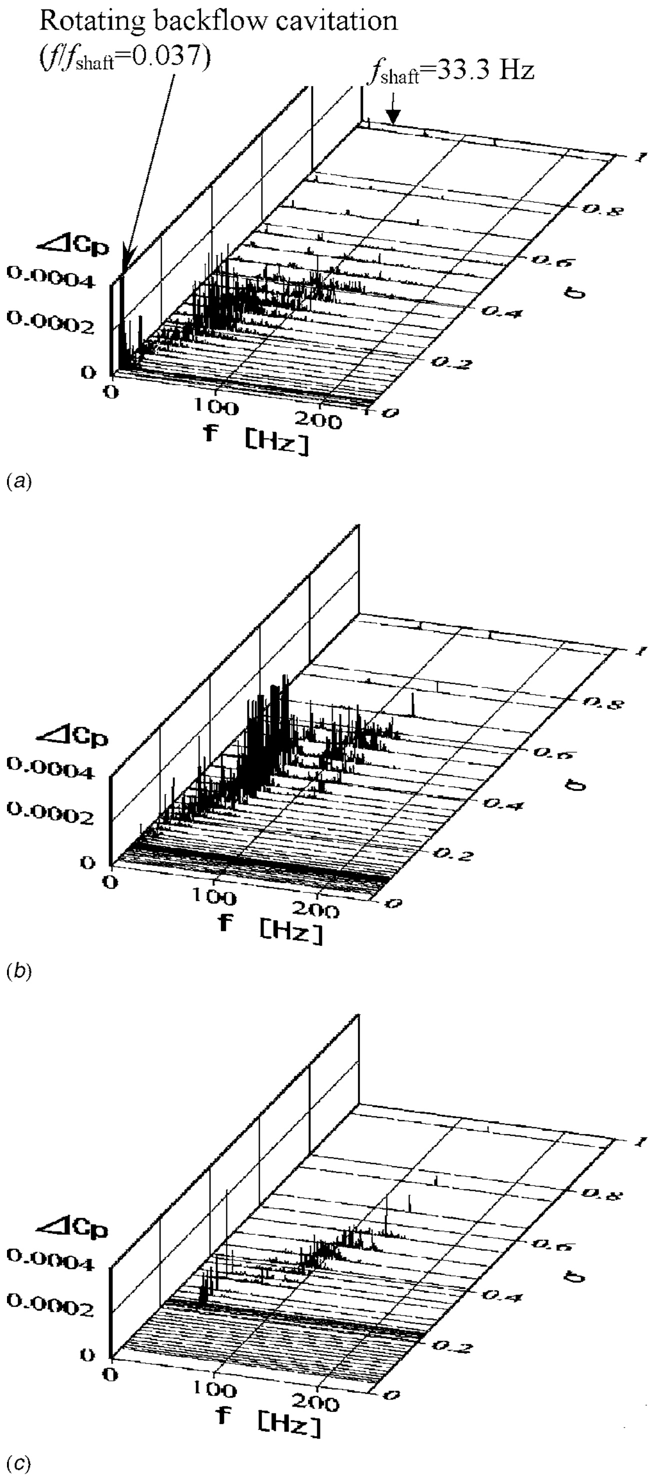

(*a*)

(*b*)

(*c*)

Fig. 10 Spectral analysis with inducer C (f_{shaft}=33.3 Hz). (*a*) ϕ/ϕ_{bep}=0.6 (J-Groove 2); (*b*) ϕ/ϕ_{bep}=1.0 (J-Groove 2); (*c*) ϕ/ϕ_{bep}=1.0 (J-Groove 4).

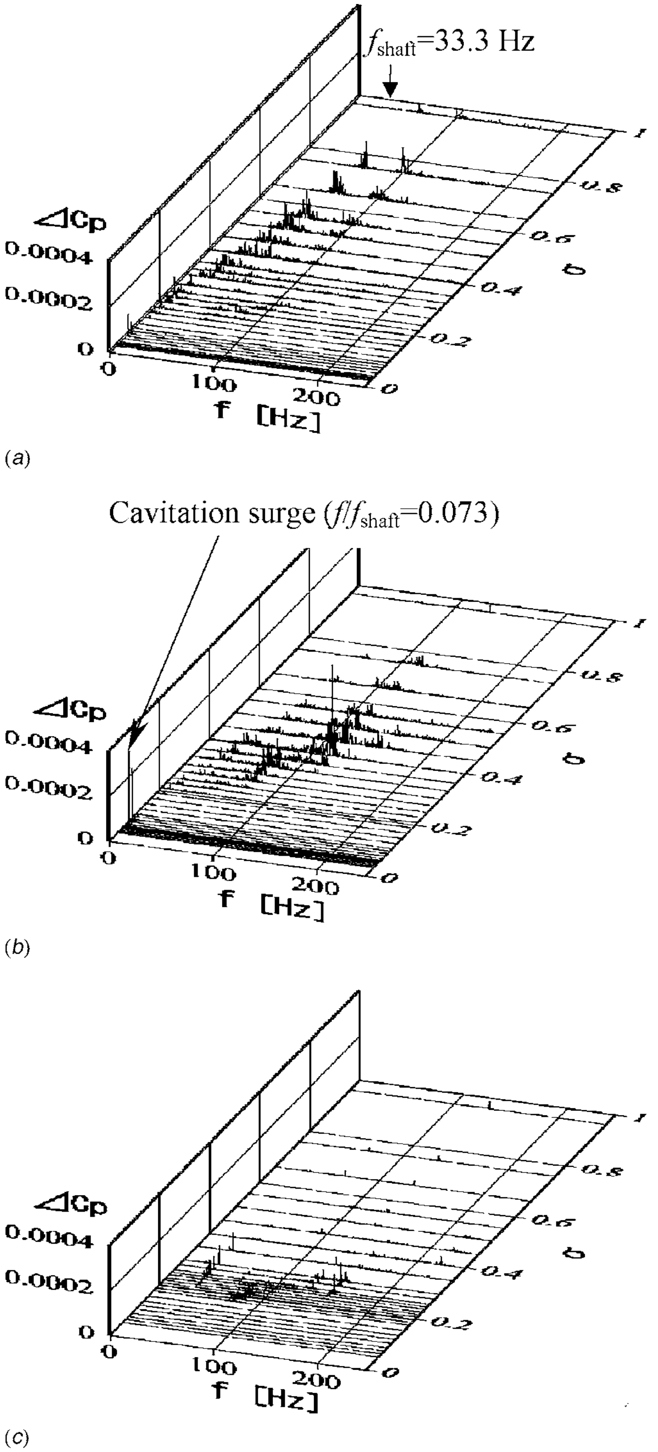

(*a*)

(*b*)

(*c*)

Fig. 11 Spectral analysis with inducer C and J-Grooves (f_{shaft}=33.3 Hz). (*a*) Without J-Groove (ϕ/ϕ_{bep}=0.6); (*b*) with J-Groove 2 (ϕ/ϕ_{bep}=0.6); (*c*) with J-Groove 4 (ϕ/ϕ_{bep}=1.0).

fore the sharp head drop point at the best efficiency point. From the tests conducted with various shapes of J-Groove, it has been found that occurrence of the cavitation surge can be suppressed almost completely as shown in Fig. 11(*c*) with adoption of J-Groove 4, which has a width of 12 mm. Moreover, the J-Groove 4 showed good performance of suppressing cavitation in the range of high flow rates ($\phi/\phi_{bep}>1.0$). Therefore, this fact demonstrates that the J-Groove has two opposite roles, one of which is to cause cavitation surge and the other is to suppress the cavitation surge according to the sensitive geometry of J-Groove.

Figure 12 shows the results of the visualization tests for the occurrence and suppression of the unstable cavitation phenomena. Rotating backflow cavitation (Fig. 12(*a*)), a large cavitation column extending upstream of the inducer inlet, occurs in the case of the impeller with inducer C and no J-Groove at the low flow rate (ϕ/ϕ_{bep}=0.6). However, by installing J-Groove 2 on the inducer

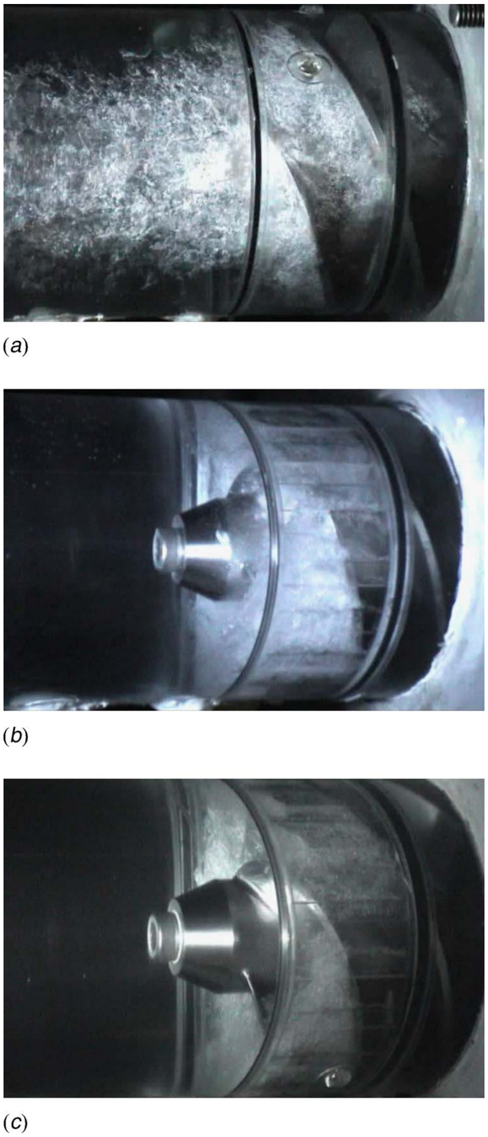

Fig. 12 Suppression of rotating backflow cavitation and cavitation surge (σ=0.05, inducer C)

casing wall (Fig. 12(*b*)), the unstable cavitation phenomena disappears. Moreover, suppression of the cavitation surge at the flow rate of best efficiency ($\phi/\phi_{bep}=1.0$) is possible by substituting J-Groove 4 as shown in Fig. 12(*c*).

4 Conclusions

J-Grooves composed of shallow grooves which are mounted parallel to the pressure gradient on the casing wall of an inducer are employed to suppress cavitating flows in simple, low head inducers. From the results of the present study, the following conclusions have been obtained.

The suction performance of an inducer can be improved remarkably at almost all flow rates by employing J-Groove, particularly when combined with an inducer with a backward swept blade leading edge. The improvement of suction performance by the J-Grooves is considerable particularly in the range of low flow rates. Mismatching of the main impeller to the inducer leads to worsened suction performance at high flow rates but this low suction performance can be improved by installing the J-Groove. Rotating backflow cavitation occurring at low flow rates at the frequency to shaft speed ratio of $f/f_{\text{shaft}}=0.037$ can be almost suppressed by employing J-Grooves. Even though installation of a J-Groove causes cavitation surge ($f/f_{\text{shaft}}=0.073$) just before sharp head drop at the best efficiency point, the cavitation surge can be almost suppressed by optimizing the shape of the J-Groove. The upstream length and the width of J-Groove are important parameters for the improvement of suction performance.

Acknowledgment

The authors wish to express their appreciation to Mr. M. Ito and Mr. M. Kikuchi for their support on the measurements of pump performance and cavitation test.

Nomenclature

A_2 = cross sectional area of impeller outlet
ΔC_p = coefficient of pressure fluctuation ($=\tilde{p}/(0.5\rho u_t^2)$)
C_p = pressure coefficient ($=(p-p_s)/(0.5\rho u_t^2)$)
D = depth of J-Groove [mm]
d = diameter of inducer [mm]
f = frequency of pressure fluctuation [Hz]
f_{shaft} = rotational frequency of inducer [Hz]
H = discharge head [m]
L = length of J-Groove [mm]
l = axial length of inducer blade [mm]
N = number of J-Groove
n = rotational speed [min^{-1}]
$NPSH$ = available net positive suction head [m]
$NPSH_R$ = required net positive suction head [m]
n_s = dimensional specific speed ($=nQ^{1/2}/H^{3/4}$) [min^{-1}, m^3/min, m]
P = pump power [W]
p = pressure [Pa]
p_s = pressure at inducer inlet [Pa]
p_v = vapor pressure [Pa]
$\tilde{p}$ = fluctuating differential pressure of $p-p_s$
Q = flow rate [m^3/s]
R = inducer radius [mm]
r = radial distance from the center of inducer axis [m]
S = dimensional suction specific speed ($=nQ^{1/2}/NPSH_R^{3/4}$) [min^{-1}, m^3/min, m]
u_2 = tip speed of impeller outlet [m/s]
u_t = tip speed of inducer [m/s]
v_s = averaged velocity at inducer inlet
W = width of J-Groove [mm]
x = axial distance from blade tip of inducer inlet to downstream [mm]

Greek Symbols

β = inducer blade angle [deg]
ϕ = discharge coefficient ($=Q/(A_2u_2)$)
η = pump efficiency ($=\rho gQH/P$)
ψ = head coefficient ($=H/(u_2^2/2g)$)
ν = power coefficient ($=P/(\rho A_2u_2^3)$)
ρ = density of working fluid [kg/m^3]
σ = cavitation number ($=(p_s-p_v)/(0.5\rho u_t^2)$)

Subscripts

bep = best efficient point
1 = inlet
2 = outlet

References

[1] Lakshminarayana, B., 1982, "Fluid Dynamics of Inducers - A Review," ASME J. Fluids Eng., **104**, pp. 411–427.
[2] Japikse, D., 2001, "Overview of Industrial and Rocket Turbopump Inducer Design," Proc. CAV2001, Session B7.001

[3] Kurokawa, J., Saha, S. L., Matsui, J., and Kitahora, T., 2000, “Passive Control of Rotating Stall in a Parallel-Wall Vaneless Diffuser by Radial Grooves,” ASME J. Fluids Eng., **122**, pp. 90–96.

[4] Saha, S. L., Kurokawa, J., Matsui, J., and Imamura, H., 2000, “Suppression of Performance Curve Instability of a Mixed Flow Pump by Use of J-Groove,” ASME J. Fluids Eng., **122**, pp. 592–597.

[5] Saha, S. L., Kurokawa, J., Matsui, J., and Imamura, H., 2001, “Passive Control of Rotating Stall in a Parallel-Wall Vaned Diffuser by J-Grooves,” ASME J. Fluids Eng., **123**, pp. 507–515.

[6] Nagahara, T., Manabe, A., Mukai, H., Okamura, T., and Kurokawa, J., 2003, “An Improvement of Performance-Curve Instability in an Axial Flow Pump by Use of J-Grooves,” ASME J. Turbomach., **31**, pp. 614–622.

[7] Tsujimoto, Y., Yoshida, Y., Maekawa, Y., Watanabe, S., and Hashimoto, T., 1997, “Observations of Oscillating Cavitation of an Inducer,” ASME J. Fluids Eng., **119**, pp. 775–781.

[8] Imano, A., and Hashijume, N., 2001, “LE-7 Engine Turbo-pump and a Cause of Failure in H-II Rocket No. 8,” ASME J. Turbomach., **29**, pp. 139–146.

[9] Kamijo, K., and Yoshida, M., 1991, “Experimental Study of LE-7 LOX Pump Inducer,” Trans. Jpn. Soc. Mech. Eng., Ser. B, **57**, pp. 4023–4028.

[10] Fujii, A., Azuma, S., Yoshida, Y., Tsujimoto, Y., Horiguchi, H., and Watanabe, S., 2002, “Higher Order Rotating Cavitation in an Inducer,” Trans. Jpn. Soc. Mech. Eng., Ser. B, **68**, pp. 1466–1473.

[11] Tahara, H., and Manabe, A., 1984, “Influence of Inlet and Outlet Angles of Inducer on Improvement in Suction Performance of Centrifugal Pump,” Trans. Jpn. Soc. Mech. Eng., Ser. B, **50**, pp. 2619–2624.

[12] Bakir, F., Kouidri, S., Noguera, R., and Rey, R., 2003, “Experimental Analysis of an Axial Inducer Influence of the Shape of the Blade Leading Edge on the Performances in Cavitating Regime,” ASME J. Fluids Eng., **125**, pp. 293–301.

[13] Abernethy, R. B., Benedict, R. P. and Dowdell, R. B., 1985, “ASME Measurement Uncertainty,” ASME J. Fluids Eng., **107**, pp. 161–164.

[14] CFX-TASCflow, home page: http://www–waterloo.ansys.com/cfx/

[15] Takamatsu, Y., Furukawa, M., Ishizaka, K., and Nikamoto, H., 1978, “Outlet Flow of a Planar Helical Inducer,” Trans. Jpn. Soc. Mech. Eng., Ser. B, **44**, pp. 950–959.

[16] Takamatsu, Y., Furukawa, M., and Ishizaka, K., 1978, “Suction Performance Improvement of a Centrifugal Pump by Helical Inducer,” Trans. Jpn. Soc. Mech. Eng., Ser. B, **44**, pp. 960–969.

Numerical Analysis of Wall Slip Effects on Flow of Newtonian and Non-Newtonian Fluids in Macro and Micro Contraction Channels

Alfeus Sunarso
e-mail: alfnarso@rheol.mech.eng.osaka-u.ac.jp

Takehiro Yamamoto

Noriyasu Mori

Department of Mechanical Engineering,
Graduate School of Engineering,
Osaka University,
2-1 Yamadaoka, Suita,
Osaka 565-0871,
Japan

We performed numerical simulation to investigate the effects of wall slip on flow behaviors of Newtonian and non-Newtonian fluids in macro and micro contraction channels. The results show that the wall slip introduces different vortex growth for the flow in micro channel as compared to that in macro channel, which are qualitatively in agreement with experimental results. The effects of slip on bulk flow behaviors depend on rheological property of the fluid. For Newtonian fluid, the wall slip always reduces the vortex length, while for non-Newtonian fluid, the strength of the slip determines whether the vortex length is reduced or increased. Analyses on the velocity and stress fields confirm the channel size dependent phenomena, such as the reduction of wall shear stress with the decrease in channel size. With the increase in average shear rate, the Newtonian fluid shows the reduction of wall shear stress that increases in the same trend with slip velocity-wall shear stress function, while for non-Newtonian fluid, the effect of the slip is suppressed by shear thinning effect and, therefore, the reduction of wall shear stress is less sensitive to the change in average shear rate and slip velocity-wall shear stress function. [DOI: 10.1115/1.2375127]

1 Introduction

The flow in micro channel attracts an increasing attention with the advance of micro scale devices, which can be found in many areas such as semiconductor processing and micro electro mechanical system (MEMS). The production processes of such devices deal with the flow of fluid in micro channel. Therefore, the study of flow behaviors of fluid in micro channel should contribute in the improvement of production processes, which in turn improves the quality of micro scale devices.

In the study of fluid flow in micro channel, one should be aware that some factors whose effects can be neglected for the flow in macro channel, significantly affect the flow in micro channel leading to the deviation of flow behavior in micro channel from that in macro channel. The deviation of flow behaviors can be observed even for the flow in simple channel such as flow in rheometry. Chen et al. [1] have reported that the values of viscosity measured using a micro scale slit rheometry are about 30% to 80% lower than that measured using a macro scale capillary rheometry. Vargas and Manero [2] also have reported that the viscosity measured in capillaries decreases as the diameter of capillaries decreases. The dependence of viscosity on the channel size is also observed for a sliding type rheometry as reported by Clasen and McKinley [3]. Furthermore, for the flow in complex channels, it has been reported that the flow of polymer solution in a micro contraction channel shows a different trend in vortex growth as compared to that in a macro channel [4]. Despite the significance of channel-size dependent effects as shown in the experimental results, further investigation is required to clarify the factors governing the different behaviors of flow in macro and micro channels.

In the present work, we performed numerical simulation to investigate the effect of wall slip on the flow in macro and micro contraction channels, which should contribute in the efforts to clarify the mechanism of the different flow behaviors in macro and micro channels. Yasuda et al. [5] have reported that the measurement of velocity field in the upstream region of micro channel showed the different value of velocity near the PDMS (polydimethylsiloxane) wall as compared to that near the glass wall. It was suggested that the velocity difference was caused by the slip between fluid and PDMS wall. There are many other experiments which show the apparent slip behavior, for both Newtonian [6–8] and non-Newtonian [9,10] fluids. This leads us to the hypothesis that wall slip should be the main factor governing the deviation of behaviors of flow in micro channel. In our preliminary work [11], we have performed numerical simulation of the flow of polymeric solution in contraction channels with slip boundary condition, and we have confirmed that the wall slip should be an important factor governing the different vortex growth for the flow in macro and micro channels. Furthermore, we have performed analysis of the effects of different slip velocity-shear stress functions on the behaviors of polymeric flow in macro and micro contraction channels [12]. We have shown that the different slip velocity-shear stress functions affect the bulk flow behaviors in a complex manner, raising the question of how the effects of wall slip should be related to rheological properties of fluid. To clarify the problem, in the present work, we performed further analysis and investigated the effects of wall slip on the flow behaviors of fluids with different rheological properties.

2 Numerical Analysis

2.1 Governing Equations.

To perform the numerical analysis, we have to solve the momentum and continuity equations, a set of constitutive equations and a slip equation. Under the assumption that the fluid is incompressible and isothermal, the momentum and continuity equations are as follows:

$$\rho\left(\frac{\partial \boldsymbol{u}}{\partial t} + \boldsymbol{u}\cdot\nabla\boldsymbol{u}\right) = -\nabla p + \nabla\cdot(\boldsymbol{\tau}_p + 2\eta_s\boldsymbol{D}) \qquad (1)$$

Contributed by the Fluids Engineering Division of ASME for publication in the JOURNAL OF FLUIDS ENGINEERING. Manuscript received September 11, 2005; final manuscript received June 8, 2006. Assoc. Editor: Kenneth Breuer.

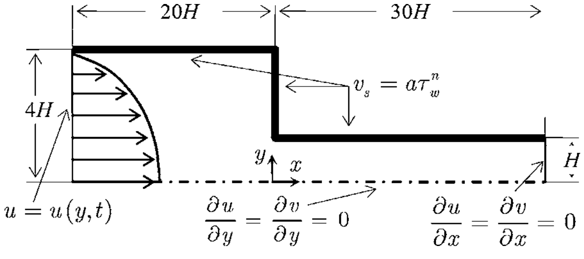

Fig. 1 Channel geometry and boundary conditions

Table 1 Parameter of slip models

Slip Model	a [m/(s·Pa^n)]	n
SM1	1.0×10^{-5}	0.5
SM2	1.5×10^{-5}	1.0
SM3	2.0×10^{-5}	1.5
SM4	1.0×10^{-4}	0.5

Table 2 Range of average shear rates and nondimensional variables

Flow type	$\dot{\gamma}_{\text{avg}}$ [s^{-1}]	Re	Wi
Newtonian, Macro	0.025–50	9×10^{-6}–2×10^{-2}	–
Newtonian, Micro	0.025–50	8×10^{-9}–2×10^{-5}	–
non-Newtonian, Macro	0.025–5	9×10^{-6}–2×10^{-3}	0.1–20
non-Newtonian, Micro	0.025–5	8×10^{-9}–2×10^{-6}	0.1–20

$$\nabla\cdot\boldsymbol{u}=0 \tag{2}$$

where ρ is the fluid density, $\boldsymbol{u}$ is the velocity vector, p is the pressure, $\boldsymbol{\tau}_p$ is the polymeric stress tensor, η_s is the Newtonian viscosity, and $\boldsymbol{D}$ is the rate of deformation tensor.

The polymeric stress tensor $\boldsymbol{\tau}_p$ vanishes for Newtonian fluid, but need to be computed separately for non-Newtonian fluid. To compute $\boldsymbol{\tau}_p$, we used the FENE-P constitutive equation proposed by Bird et al. [13]. This constitutive equation was derived from a simple molecular model (dumbbell) for dilute polymer solution. In this model, the polymeric stress is computed from the dynamics of model molecules in term of the end-to-end vector $\boldsymbol{R}$ of the dumbbell. Here, we follow the formulation used in [14], in which the polymeric stress is expressed in the term of a dimensionless configuration tensor $\boldsymbol{A}=\langle\boldsymbol{RR}\rangle$, where $\langle\,\rangle$ denotes the average value. Based on this formulation, the polymeric stress can be expressed as follows:

$$\boldsymbol{\tau}_p = \eta_p\frac{b+3}{\lambda b}\left(\frac{1}{1-\mathrm{tr}\,\boldsymbol{A}/b}\boldsymbol{A}-\boldsymbol{I}\right) \tag{3}$$

$$\frac{D\boldsymbol{A}}{Dt} = \boldsymbol{\kappa}\cdot\boldsymbol{A}+\boldsymbol{A}\cdot\boldsymbol{\kappa}^T+\frac{1}{\lambda}\left(\boldsymbol{I}-\frac{1}{1-\mathrm{tr}\,\boldsymbol{A}/b}\boldsymbol{A}\right) \tag{4}$$

Here, η_p is the polymeric contribution on viscosity at zero shear rate, $\boldsymbol{\kappa}$ is the velocity gradient tensor ($\kappa_{ij}=\partial u_j/\partial x_i$), λ is a relaxation time, b is the maximum extension parameter, and $\boldsymbol{I}$ is the identity tensor.

To solve Eqs. (3) and (4), the initial value of tensor $\boldsymbol{A}$ should be set such that $\boldsymbol{\tau}_p=\boldsymbol{0}$ at equilibrium. Considering 2D case, from Eq. (3) we have $A_{ij}=0$ for $i\neq j$ and $A_{ij}=1/(1+2/b)$ for $i=j$.

Although the molecular model used in the derivation of the constitutive equation is very simple, this constitutive equation is capable to predict the viscoelastic properties of polymer solutions such as shear thinning property and the presence of positive first normal stress difference in the simple shear flow and strain thickening behavior of viscosity in the purely extensional flow. Furthermore, it has been shown that the constitutive equation is capable to reproduce qualitatively the experimental characteristics of the flow of polymer solution in contraction channels [15].

To account for the wall slip effect, Eqs. (1)–(4) have to be supplemented by a slip equation. Various slip models have been proposed based on various theories, which result in various formulations of slip velocity [16–18]. For gas flow, the slip velocity is usually related to wall shear rate and the Knudsen number [19]. For liquid flow, the slip velocity usually related to wall shear stress [16,17], but more complex models also account for normal stress [18]. Because of the dependence of slip velocity on the properties of fluid and channel surface, the choice of slip model is problem specific.

In the present work, we investigate the effects of wall slip on the behaviors of Newtonian and non-Newtonian fluids in general. Therefore, for the simplicity of computation and analysis, we considered a simple power law slip model in which the slip velocity v_s (m/s) is related to the wall shear stress τ_w (Pa) as follows:

$$v_s = a\tau_w^n \tag{5}$$

where a and n are constant parameters. The slip velocity is directed parallel to the wall with sign opposites to the sign of shear

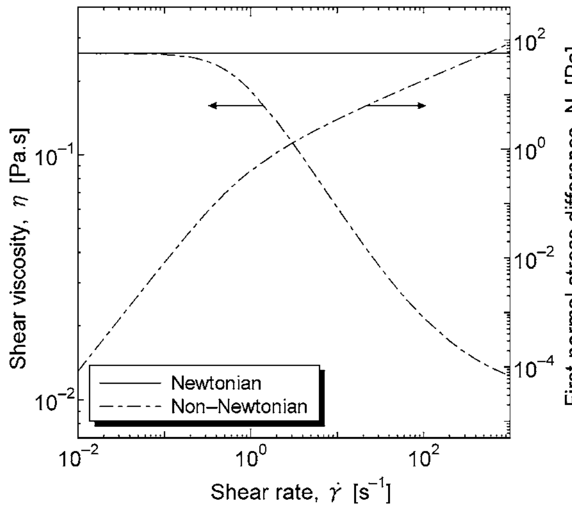

Fig. 2 Shear viscosity η and first normal stress difference N_1

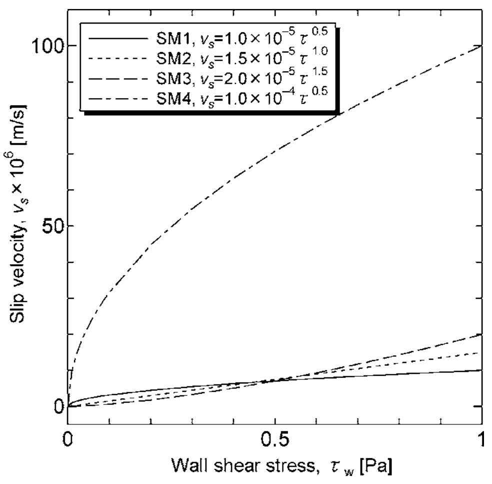

Fig. 3 Slip velocity v_s as a function shear stress τ for various slip models

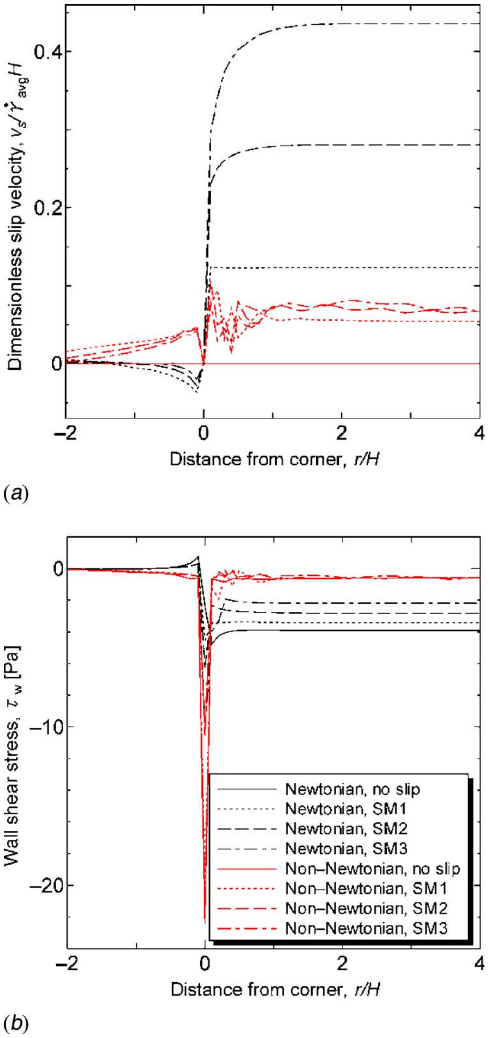

Fig. 4 Values of slip velocity (*a*) and shear stress (*b*) at the wall for the flow in micro channel at $\dot{\gamma}_{\mathrm{avg}}=5\ \mathrm{s}^{-1}$. Distance *r* is measured from the contraction corner ($r=1-y$ for the upstream wall, $r=x$ for the downstream wall).

stress at that point. The wall shear stress is calculated from the stress tensor $\boldsymbol{\tau}=\boldsymbol{\tau}_p+2\eta_s\boldsymbol{D}$ as follows:

$$\tau_w = |\boldsymbol{t}\cdot\boldsymbol{\tau}\cdot\boldsymbol{n}| \tag{6}$$

where $\boldsymbol{t}$ and $\boldsymbol{n}$ represent tangential and normal unit vectors respect to the wall. In the case of the wall is parallel to x or y axis, we obtain $\tau_w=|\tau_{xy}|$.

2.2 Numerical Methods. To solve the governing Eqs. (1)–(5), we adopted the backward tracking Lagrangian particle method [14]. In this method, the solution of velocity and pressure fields is decoupled from the solution of polymeric stress fields. The velocity and pressure fields are computed simultaneously by solving Eqs. (1) and (2) using a stabilized finite element method, in which the discrete elastic stress splitting method [20] is included to improve the stability of computation. The set of constitutive Eqs. (3) and (4) is solved by tracking particles backward in time, and integrating Eq. (4) along the trajectories of particles. Once the configuration tensor has been computed, the extra stress tensor can be computed from Eq. (3). For the approximation spaces, we used biquadratic continuous, bilinear continuous, and bilinear discontinuous representations for the velocity, the pressure, and the polymeric stress, respectively.

To apply the slip boundary condition, the velocity on the wall is computed from the shear stress on the wall at every time step. At high shear rates especially for slip model with $n>1$, it is necessary to use under relaxation technique for the calculation of slip velocity to keep the stability of computation. Therefore, at the time step $i+1$ the slip velocity is computed as follows:

$$v_s^{i+1} = (1-\alpha)v_s^i + \alpha(a\tau_w^n)^{i+1} \tag{7}$$

where α is a relaxation parameter.

2.3 Simulation Conditions. We considered the flow of Newtonian and non-Newtonian fluids in 4 to 1 macro and micro contraction channels. The representative geometry of the channels and the boundary conditions are described in Fig. 1. We set $H=10^{-3}$ m (1 mm) for macro channel and $H=3\times10^{-5}$ m (30 μm) for micro channel.

For the calculation of stress of the Newtonian fluid, we set $\eta_s=0.24$ Pa·s, while for the non-Newtonian fluid, we used the FENE-P model with $\eta_s=0.01$ Pa·s, $\eta_p=0.23$ Pa·s, $\lambda=4$ s, and $b=10$. The predicted rheological properties are shown in Fig. 2. It should be noted that the non-Newtonian fluid shows shear thinning behavior, in which the viscosity decreases as shear rate increases. Furthermore, under simple shear, the first normal stress vanishes for the Newtonian fluid, but exists for the non-Newtonian fluid.

Both no-slip and slip boundary conditions are considered. For the slip boundary condition, the fluid on the wall is allowed to slide along the wall, but not allowed to penetrate the wall. This implies that the direction of slip velocity is strictly tangential to the wall. To fulfill this condition, the slip velocity is computed anywhere at the wall, except at the corners, at which the direction of slip velocity is undefined. If the slip velocity is introduced at the corners, the interpolation in the finite elements surrounding the corners results in the nonvanishing slip velocity component normal to the wall in the region between the corner points and their adjacent points. To avoid this physically unrealistic behavior, the slip velocity at the corners is set to zero.

To consider the effects of different slip velocity-wall shear stress functions, we considered four models with different values of a and n as shown in Table 1. The curves of those models are shown in Fig. 3. In the range of considered average shear rates for non-Newtonian fluid, the slip velocities are in almost the same order for SM1, SM2, and SM3, while for SM4 the value is about ten times higher from that for SM1, SM2, and SM3.

3 Results and Discussion

For the comparison of flow behaviors in macro and micro channels, simulation results are presented in terms of average shear rate $\dot{\gamma}_{\mathrm{avg}}=\bar{V}/H$, because for no slip condition, the behaviors of flow in macro and micro channels under the same average shear rate should be similar. The average shear rate can be related to the Reynolds number Re as follows:

$$\mathrm{Re} = \frac{\rho\bar{V}H}{\eta_0} = \frac{\rho\dot{\gamma}_{\mathrm{avg}}H^2}{\eta_0} \tag{8}$$

where $\bar{V}$ is the average velocity at the exit, and η_0 is the zero shear viscosity ($\eta_0=\eta_s$ for the Newtonian fluid, $\eta_0=\eta_s+\eta_p$ for the non-Newtonian fluid).

For the non-Newtonian fluid, the average shear rate can also be expressed in the term of the Weissenberg number Wi using the following relation:

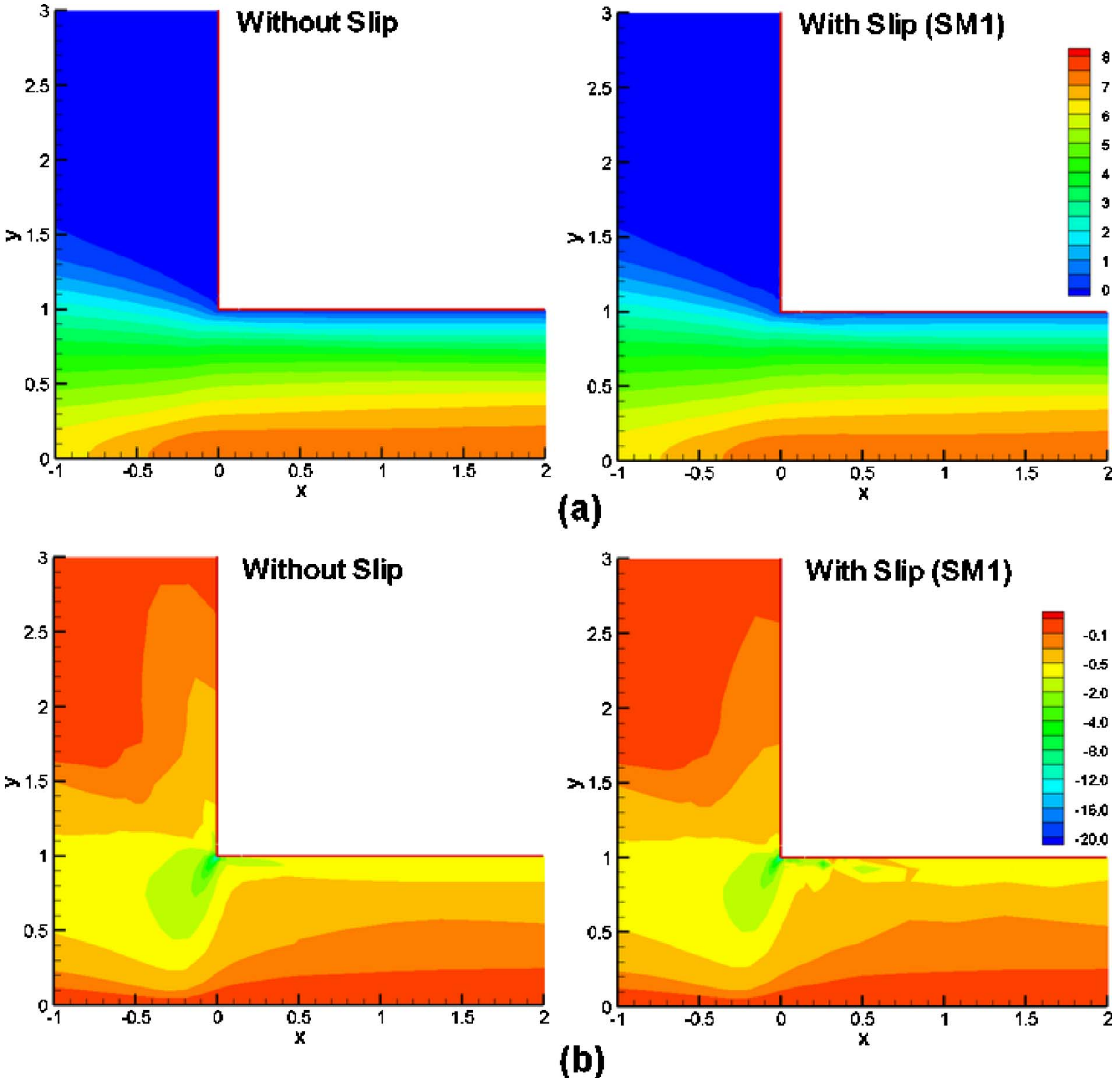

Fig. 5 Contours of variables near the corner for the flow of non-Newtonian fluid in micro channel at $\dot{\gamma}_{avg}=5\ s^{-1}$, (*a*) velocity *u*, (*b*) shear stress τ_{xy}

$$\mathrm{Wi}=\frac{\lambda\bar{V}}{H}=\lambda\dot{\gamma}_{\mathrm{avg}} \tag{9}$$

The considered average shear rates $\dot{\gamma}_{avg}$ and the corresponding values of Re and Wi are shown in Table 2.

3.1 Flow Pattern Near the Re-entrant Corner. Before proceeding with the effects of wall slip on the bulk flow behaviors, we present the behaviors of variables in the vicinity of re-entrant corner. Figure 4 shows the wall values of slip velocity (Fig. 4(*a*)) and shear stress (Fig. 4(*b*)) as the function of distance from the re-entrant corner r for the flow in micro channel at $\dot{\gamma}_{avg}=5\ s^{-1}$. For the upstream wall (vertical wall) we set $r=1-y$ and for the downstream wall (horizontal wall) we set $r=x$. Because the slip velocity at the corner is set to zero, we can observe the steep change in slip velocity in the region near the corner. At the downstream wall, the slip velocity of the Newtonian fluid increases smoothly from zero at the corner to a constant value at $r\approx H$, while for the non-Newtonian fluid, there is fluctuation in slip velocity before reaching a constant value. In the plot of wall shear stress (Fig. 4(*b*)), we can also observe the steep change of wall shear stress near the corner. However, the steep change is more related to the singularity of geometry rather than the singularity of slip boundary condition, because even for the flow without slip the steep change in wall shear stress can also be observed.

Even though there are singularities in geometry and slip boundary condition at the corner, we consider that the effect of these singularities on the bulk flow behaviors is not significance. To show this, we plot in Fig. 5, the contour of velocity u and shear stress τ_{xy} near the re-entrant corner, for the flow of non-Newtonian fluid in micro channel at $\dot{\gamma}_{avg}=5\ s^{-1}$. It can be observed that even there is fluctuation in the slip velocity and wall shear stress, its effect on the bulk flow behavior is not significant, because the fluctuation only introduces nonsmooth patterns in a small region near the downstream wall.

3.2 Effect of Wall Slip on Vortex Growths. The effect of wall slip on the flow patterns is shown in Fig. 6. Vortex length L_v is measured from the contraction part to the critical point at the

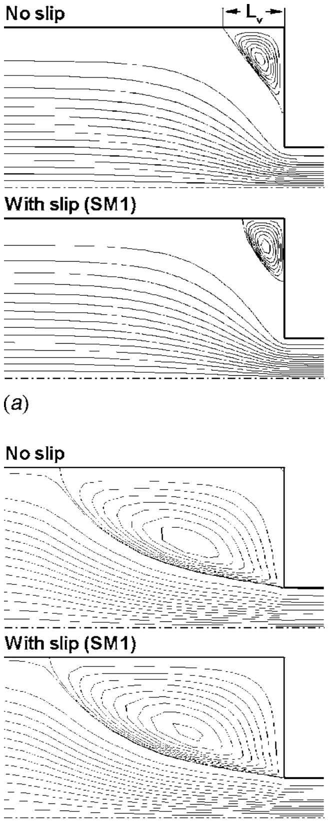

(*a*)

(*b*)

Fig. 6 Stream line patterns of flow in micro channel at $\dot{\gamma}_{avg}$ =5 s^{-1} for Newtonian fluid (*a*) and non-Newtonian fluid (*b*)

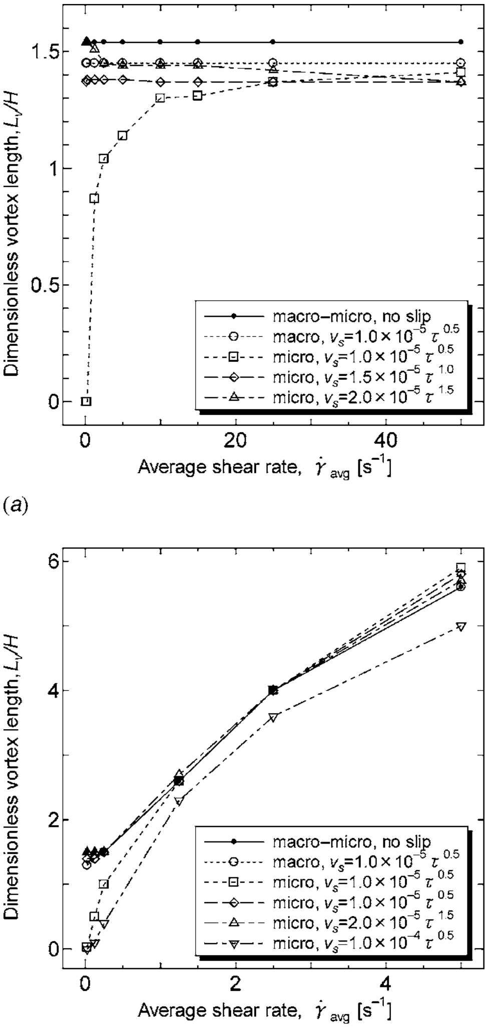

(*a*)

(*b*)

Fig. 7 Effect of wall slip on vortex growth for Newtonian fluid (*a*) and non-Newtonian fluid (*b*)

wall, which divides the forward and backward flow zones. At $\dot{\gamma}_{avg}=5$ s^{-1}, the slip (SM1) reduces the vortex length L_v for Newtonian fluid, while slightly increases the vortex length for non-Newtonian fluid. The modification in vortex length depends on the rheological properties of the fluids, and varies with the change in average shear rate.

Figure 7 shows the dimensionless vortex length L_v/H as a function of the average shear rate $\dot{\gamma}_{avg}$. Because the considered Reynolds numbers are much smaller than unity, the inertia effect on the vortex growth can be neglected. Therefore, for the flow without slip, it can be observed that the vortex growths are similar for the flow in macro and micro channels, even though the Reynolds number for the flow in the macro channel differs from that in the micro channel in the order of 10^3. With the increase in average shear rate, the vortex length is constant for the Newtonian fluid, while increasing for the non-Newtonian fluid.

As noted in our previous work [11,12], the occurrence of wall slip introduces the difference in vortex growth for the flow in macro and micro channels. For the non-Newtonian fluid, the effect of wall slip is not significant for the flow in macro channel, while becomes significant for the flow in the micro channel. As shown in Fig. 7(*b*), the vortex growth for the flow with slip in macro channel is similar to that without slip, except at low average shear rates, where a slight reduction in vortex length can be observed. For the flow in the micro channel at low average shear rates, significant reduction in vortex length can be observed for SM1, while no reduction is observed for SM2 and SM3, except at very low average shear rates for SM2. In contrast, at high average shear rates, the slip slightly increases the vortex length for SM1, SM2, and SM3. Introducing a relatively strong slip, as for SM4, results in reduction of vortex length at both low and high average shear rates.

Referring the experimental results [4], it should be interesting to note that for one type of fluid for which the slip level is considered to be weak, the vortex length for the micro channel is higher than that for the macro channel, while for the other fluids for which the slip level is considered to be strong, the vortex length for the micro channel is lower as compared to that for the macro channel. These results are qualitatively in agreement with our numerical results noted above. From the above results it is reasonable to consider that the slip velocity-shear stress function should play an important role in determining whether the vortex length for the flow in micro channel is lower or higher as compared to that in macro channel.

We considered that the enhancement of vortex length is a typical behavior of the non-Newtonian fluid. For the Newtonian fluids, as shown in Fig. 7(*a*), the occurrence of wall slip always reduces the vortex length, and no vortex enhancement can be observed. Furthermore, even though the reduction depends on the slip models, it can be confirmed that the reduction is more significant for the flow in micro channel as compared to that in macro

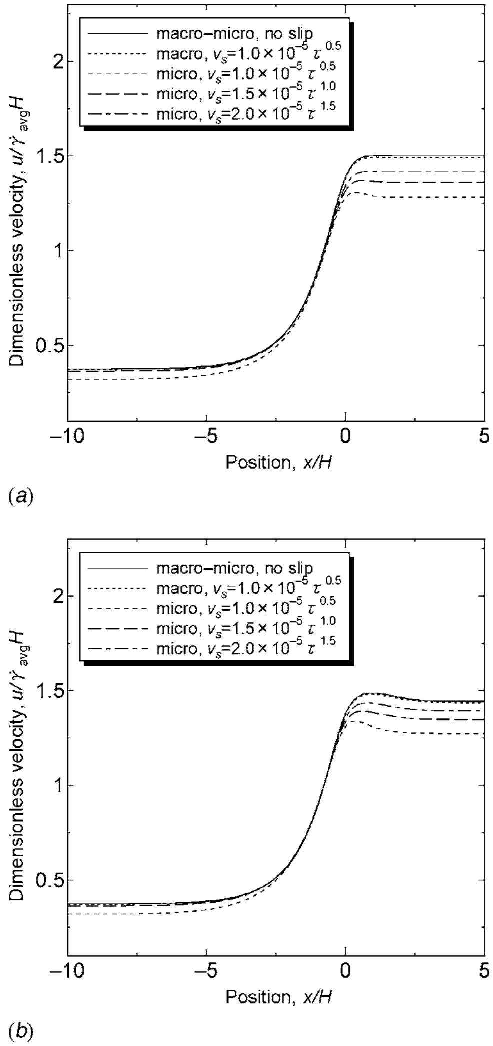

Fig. 8 Profiles of velocity in the flow direction along the centerline at $\dot{\gamma}_{avg}=0.25\ s^{-1}$ for Newtonian fluid (*a*) and non-Newtonian fluid (*b*)

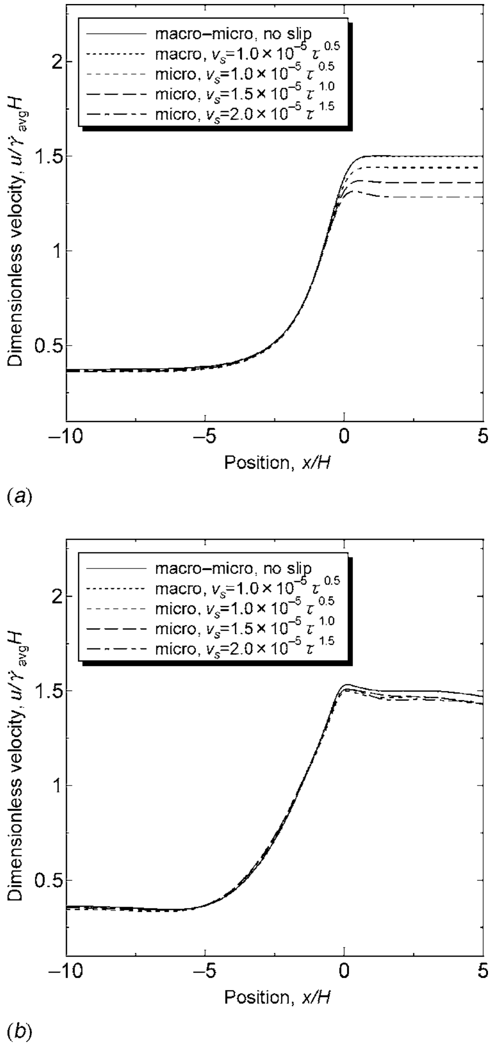

Fig. 9 Profiles of velocity in the flow direction along the centerline at $\dot{\gamma}_{avg}=5\ s^{-1}$ for Newtonian fluid (*a*) and non-Newtonian fluid (*b*)

channel. For the flow in micro channel, with the increase in average shear rate, the reduction in vortex length is nearly constant for SM2, decreasing for SM1, and increasing for SM3.

3.3 Effect of Wall Slip on Velocity Field. The difference in vortex growth should be related to the different effect of wall slip on bulk flow behaviors in macro and micro channels. Figures 8 and 9 show the effect of wall slip on the profiles of velocity in the flow direction u along the centerline ($y=0$). Here, we focused on the effect of slip models with the same level of slip velocity and, therefore, only the results for SM1, SM2, and SM3 are presented.

As shown in Fig. 8, at low average shear rates, the slip shows the similar effect on the velocity at the centerline for both Newtonian and non-Newtonian fluids. For the flow in micro channel, even though all slip models (SM1, SM2, SM3) significantly modify the velocity in the downstream region, significant modification of velocity in the upstream region can be observed only for SM1 but not for SM2 and SM3. It can be considered that modification of velocity in the upstream region should be related to the modification of vortex length. It can be seen that the significant reduction in the upstream velocity for SM1 corresponds to the significant reduction in vortex length.

At high average shear rates as shown in Fig. 9 the effect of wall slip on the velocity in the upstream region becomes less significant as compared to that at low average shear rates. This corresponds to the less significant modification in vortex length at high average shear rates as compared to that at low average shear rates for both Newtonian and non-Newtonian fluids. In the downstream region, the slip reduces the velocity for both Newtonian and non-Newtonian fluids. The reduction of velocity is still significant for the Newtonian fluid, while becomes less significant for the non-Newtonian fluid.

For further investigation of the different slip effects, the profiles of velocity at the cross section of $x=20H$ are presented in Fig. 10. For the Newtonian fluid, significant slip velocity modifies significantly the velocity profile for the flow in the micro channel, while for the non-Newtonian fluid, the slip velocity is less significant and, therefore, the modification in velocity profiles is also less significant.

3.4 Effect of Wall Slip on Stress Field. The suppression of wall slip effect of non-Newtonian fluid at high average shear rates should be related to the shear thinning effect of the fluid. For the shear thinning fluid, the ratio of shear stress to shear rate decreases as the shear rate increases; therefore, even though the

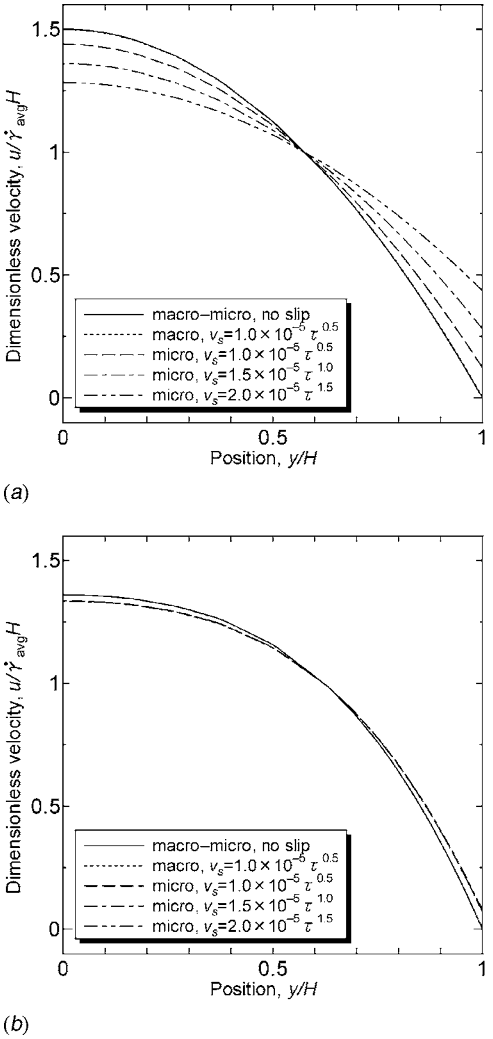

Fig. 10 Profiles of velocity in the flow direction at cross section of $x=20H$ at $\dot{\gamma}_{avg}=5$ s^{-1} for Newtonian fluid (*a*) and non-Newtonian fluid (*b*)

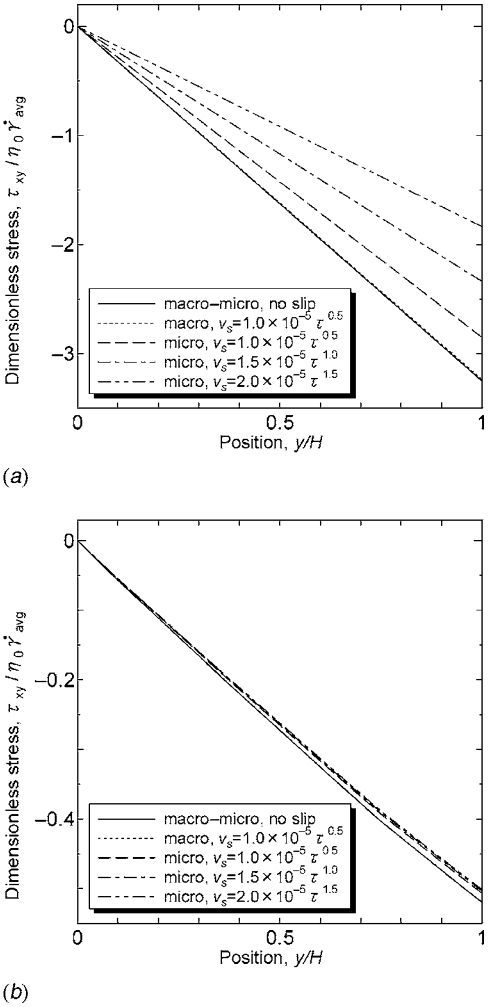

Fig. 11 Profiles of shear stress τ_{xy} at cross section of $x=20H$ at $\dot{\gamma}_{avg}=5$ s^{-1} for Newtonian fluid (*a*) and non-Newtonian fluid (*b*)

absolute value of slip velocity (computed from shear stress) increases with the increase in shear rate, its relative value (normalized respect to average shear rate) decreases with the increases in shear rate. Figure 11 shows the profiles of shear stress at the cross section of $x=20H$ at $\dot{\gamma}_{avg}=5$ s^{-1}. It can be observed that the shear stress for the non-Newtonian fluid (Fig. 11(*b*)) is much lower as compared to that for the Newtonian fluid (Fig. 11(*a*)). Consequently, the computed slip velocity for the non-Newtonian fluid is much lower than that for the Newtonian fluid.

Figure 12 shows the plot of wall shear stress at $x=20H$ as a function of the average shear rate. It can be confirmed that the wall slip reduces significantly the wall shear stress for the flow in the micro channel. For the Newtonian fluid, because the shear stress increases proportionally with the increase in shear rate, the reduction of wall shear increases with power corresponds to the power of slip model. On the other hand, the reduction of wall shear stress is not sensitive to the change in the average shear rate for the non-Newtonian fluid. As noted in our previous work [12], the reduction of wall shear stress increases as the channel size decreases.

The above results support the experimental results reported in [1,2]. Vagras et al. [2] calculated the wall shear stress from the measurement of pressure and flow rate for the flow of polymer solution in capillaries with various diameters. They found that, as diameter of capillary decreases, the wall shear stress decreases in the similar trend as shown in our numerical results (Fig. 12(*b*)). This explains why the viscosity calculated from the measurement data without consideration of wall slip decreases with the decreases in channel size as reported in [1,2].

4 Conclusion

Numerical simulation has been performed to investigate the effect of wall slip on the flow of Newtonian and non-Newtonian fluids in macro and micro contraction channels. It has been shown that the wall slip should play an important role in governing the channel size dependent behaviors as shown in the experimental results. The slip introduces the different trend in vortex growth for the flow in macro and micro channels. For the Newtonian fluid, the slip always reduces the vortex length, while for the non-Newtonian fluid, the strength of slip determines whether the vortex length is decreased or increased. The modification of vortex length is related to the modification of velocity and stress fields in the upstream region. It also has been noted that the slip reduces the wall shear stress, and the reduction increases as the channel size decreases. For the Newtonian fluid, the reduction is proportional to the slip velocity-shear stress function, while for the non-Newtonian fluid, the reduction is suppressed by shear thinning effect and, therefore, is less sensitive to the change in average shear rate.

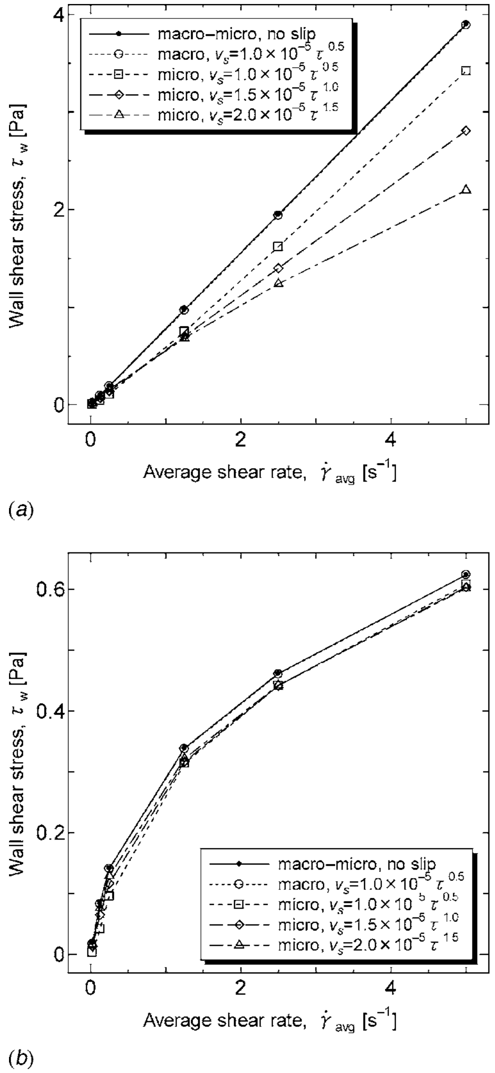

Fig. 12 Wall shear stress τ_w at $x=20H$ as a function of average shear rate $\dot{\gamma}_{avg}$ for Newtonian fluid (*a*) and non-Newtonian fluid (*b*)

References

[1] Chen, S. C., Tsai, R. I., Chien, R. D., and Lin, T. K., 2005, "Preliminary Study of Polymer Melt Rheological Behavior Flowing Through Micro-Channels," Int. Commun. Heat Mass Transfer, **32**, pp. 501–510.

[2] Vargas, L., and Manero, O., 1989, "On the Slip Phenomenon of Polymeric Solutions Through Capillaries," Polym. Eng. Sci., **29**, pp. 1232–1236.

[3] Clasen, C., and McKinley, G. H., 2004, "Gap-Dependent Microrheometry of Complex Liquids," J. Non-Newtonian Fluid Mech., **124**, pp. 1–10.

[4] Yasuda, K., Sugiura, Y., and Mori, N., 2004, "Entry Flow of Polymer Solution Through a Microfluidic Device," *Proc. the XIVth Int. Congress on Rheology*, CD-ROM, NA5.

[5] Yasuda, K., Sugiura, Y., and Mori, N., 2005, "Apparent Slip Flow of Polymer Solutions in a Microchannel With a PDMS Surface," *Advances in Rheology and its Application*, Science Press, Monmouth Junction, NJ, pp. 690–693.

[6] Vinogradova, O. I., 1999, "Slippage of Water Over Hydrophobic Surfaces," Int. J. Min. Process., **56**, pp. 31–60.

[7] Craig, V. S. J., Neto, C., and Williams, D. R. M., 2001, "Shear-Dependent Boundary Slip in an Aqueous Newtonian Liquid," Phys. Rev. Lett., **87**, p. 054504.

[8] Tretheway, D. C., and Meinhart, C. D., 1999, "Apparent Fluid Slip at Hydrophobic Microchannel Walls," Phys. Fluids, **14**, pp. L9–L12.

[9] Muller-Mohnssen, H., Lobl, H. P., and Schauerte, W., 1987, "Direct Determination of Apparent Slip for a Ducted Flow of Polyacrylamide Solutions," J. Rheol., **31**, pp. 690–693.

[10] Barnes, H. A., 1995, "A Review of the Slip (Wall Depletion) of Polymer Solutions, Emulsions and Particle Suspensions in Vicometers: Its Cause, Character, and Cure," J. Non-Newtonian Fluid Mech., **56**, pp. 221–251.

[11] Sunarso, A., Yamamoto, T., and Mori, N., 2005, "Numerical Analysis of Polymeric Flow in Contraction Channels With Slip Boundary Condition," *Proc. 83rd JSME Conf. on Fluid Eng.*, CD-ROM, OS1-107.

[12] Sunarso, A., Yamamoto, T., and Mori, N., 2005, "Numerical Simulation of Polymeric Flow in Contraction Channels: Wall Slip and Channel Size Dependent Effects," *Flow Dynamics*, AIP Conf. Proc. No. 832, AIP, Melville, pp. 341–344.

[13] Bird, R. B., Dotson, P. J., and Johnson, N. L., 1980, "Polymer Solution Rheology Based on a Finitely Extensible Bead-Spring Chain Model," J. Non-Newtonian Fluid Mech., **7**, pp. 213–235.

[14] Wapperom, P., and Keunings, R., 2000, "The Backward-Tracking Lagrangian Particle Method for Transient Viscoelastic Flows," J. Non-Newtonian Fluid Mech., **91**, pp. 273–295.

[15] Prunode, B., and Crochet, M. J., 1996, "Flows of Polymer Solutions Through Contractions Part 1: Flows of Polyacrylamide Solutions Through Planar Contractions," J. Non-Newtonian Fluid Mech., **65**, pp. 269–289.

[16] Brochard, F., and de Gennes, P. G., 1992, "Shear-Dependent Slippage at a Polymer/Solid Interface," Langmuir, **8**, pp. 3033–3037.

[17] Hill, D. A., 1998, "Wall Slip in Polymer Melts: A Pseudo-Chemical Model," J. Rheol., **42**, pp. 581–601.

[18] Joshi, Y. M., Lele, A. K., and Mashelkar, R. A., 2000, "Slipping Fluids: A Unified Transient Network Model," J. Non-Newtonian Fluid Mech., **89**, pp. 303–335.

[19] Yang, J. M., Ho, C. M., Yang, X., and Tai, Y. C., 2001, "Micromachined Particle Filter With Low Power Dissipation," J. Fluids Eng., **123**, pp. 899–908.

[20] Guenette, R., and Fortin, M., 1995, "A New Mixed Finite Element Method for Computing Viscoelastic Flows," J. Non-Newtonian Fluid Mech., **60**, pp. 27–52.

Molecular Dynamics Simulation of Adsorbent Layer Effect on Tangential Momentum Accommodation Coefficient

George W. Finger
Vice President
Mem. ASME
Reynolds, Smith & Hills, Inc.,
RS&H Aerospace & Defense,
2235 N. Courtenay Parkway, Suite C,
Merritt Island, FL 32953

Jayanta S. Kapat
Professor
University of Central Florida,
College of Engineering and Computer Science,
Mechanical, Materials and Aerospace
Engineering,
ENGR I 308,
Orlando, FL 32816

Aniket Bhattacharya
Assistant Professor
Department of Physics,
University of Central Florida,
P.O. Box 162385,
Orlando, FL 32816-2385

The tangential momentum accommodation coefficient (TMAC) is used to improve the accuracy of fluid flow calculations in the slip flow regime where the continuum assumption of zero fluid velocity at the surface is inaccurate because fluid "slip" occurs. Molecular dynamics techniques are used to study impacts of individual gas atoms upon solid surfaces to understand how approach velocity, crystal geometry, interatomic forces, and adsorbed layers affect the scattering of gas atoms, and their tangential momentum. It is a logical step in development of techniques estimating total TMAC values for investigating flows in micro- and nano-channels or orbital spacecraft where slip flow occurs. TMAC can also help analysis in transitional or free molecular flow regimes. The impacts were modeled using Lennard-Jones potentials. Solid surfaces were modeled approximately three atoms wide by three atoms deep by 40 or more atoms long face centered cubic (100) crystals. The gas was modeled as individual free atoms. Gas approach angles were varied from 10 *to* 70 deg *from normal. Gas speed was either specified directly or using a ratio relationship with the Lennard-Jones energy potential (energy ratio). To adequately model the trajectories and maintain conservation of energy, very small time steps (approximately 0.0005 of the natural time unit) were used. For each impact the initial and final tangential momenta were determined and after many atoms, TMAC was calculated. The modeling was validated with available experimental data for He gas atoms at* 1770 m/s *impacting Cu at the given angles. The model agreed within 3% of experimental values and correctly predicted that TMAC changes with angle. Molecular Dynamics results estimate TMAC values from high of 1.2 to low of 0.25, generally estimating higher coefficients at the smaller angles. TMAC values above 1.0 indicate backscattering, which numerous experiments have observed. The ratio of final to initial momentum, when plotted for a gas atom sequence spaced across a lattice cycle typically follows a discontinuous curve, with continuous portions forward and backscattering and discontinuous portions indicating multiple bounces. Increasing the energy ratio above a value of 5 tends to decrease TMAC at all angles. Adsorbed layers atop a surface influence the TMAC in accordance with their energy ratio. Even a single adsorbed layer can have a substantial effect, changing TMAC +/−20%. The results provide encouragement to continue model development and next evaluate gas flows with Maxwell temperature distributions involving numerous impact angles simultaneously.*

[DOI: 10.1115/1.2375128]

Keywords: slip flow, tangential momentum accommodation coefficient, molecular dynamics

1 Introduction

1.1 Explanation of "Slip." Most common or conventional applications of fluid flow past a solid surface uses the so-called no-slip boundary condition, where the fluid velocity at the wall is set equal to the velocity of the solid surface itself, that is, with no slip between the fluid and the solid surface (Eq. (1))

$$u_{\text{gas}}(\text{at } y=0) = u_{\text{wall}} \tag{1}$$

where u is the tangential-to-wall component of velocity and y is the coordinate normal to the surface.

However, the true boundary condition should allow for slip between gas velocity at the wall and the wall itself, the exact extent of which depending on the nature of collisions that gas molecules undergo at the wall [1]. For example, if the gas molecules undergo specular reflection at the solid wall, then the molecules will conserve their tangential momentum and there will be perfect slip between gas and the wall. Even when gas molecules undergo perfectly diffuse reflection at the wall, there will be a slip as given by [2].

$$u_{\text{gas}} - u_{\text{wall}} \equiv (\Delta u)_{\text{slip}} = \lambda\left(\frac{du}{dy}\right)_{\text{wall}} \tag{2}$$

Here, λ is the mean free path for gas molecules. However, for most engineering problems, this more correct boundary condition would not provide any more accurate engineering solution than the more practical boundary condition of Eq. (1), as Eq. (2) can be modified into

---

Contributed by the Fluids Engineering Division of ASME for publication in the Journal of Fluids Engineering. Manuscript received October 27, 2005; final manuscript received June 10, 2006. Review conducted by Joseph Katz.

$$(\Delta u)_{\text{slip}} \approx \lambda \frac{(\Delta u)_{\text{gas}}}{L} \Rightarrow \frac{(\Delta u)_{\text{slip}}}{(\Delta u)_{\text{gas}}} \approx \frac{\lambda}{L} \equiv \text{Kn} \tag{3}$$

Here, $(\Delta u)_{\text{gas}}$ is the change of tangential component of velocity within the gas flow, L is the appropriate length scale of flow in the y direction (which can be boundary layer thickness in external flow or duct radius in internal flow through a circular duct), and Kn is the Knudsen number. As for most continuum flows, Kn is quite small (say, less than 0.001), and the amount slip at the wall is negligible compared to the amount velocity change within the gas itself and hence can be taken to be zero without much loss of accuracy.

1.2 Conditions Where "Slip" Must Be Considered. Situations regularly occur in flow through micro- or nano-channels (where L is not much larger than λ) and in outer space (where the gas is very dilute and λ is quite large in comparison with L), where Kn can no more be considered to be small (that is, less than 0.001), slip at wall must be considered.

Microchannels and nanochannels are used in many microelectromechanical systems (MEMS) and nano-electromechanical systems (NEMS). These channels convey gasses for chemical analysis, actuation, heat transfer, and basic gas delivery. The channels are frequently on the order of 1 μm in width [3] with depths on the order of 500 nm [4]. In these small channels, the surface to volume ratio may be a million times the typical value experienced at macroscale, leading to significant effects from these surface interactions [5]. Slip flow regularly occurs in these MEMS and NEMS devices, which leads to pressure drops and flow rates which are not per the designer's intent and which can reduce device functionality.

Spacecraft on orbit move through a rarefied gas environment. The impact of gas atoms on surfaces of the spacecraft moving through them results in a drag force upon the spacecraft. For smaller satellites, on the order of 1 m in size, in orbits of 150 km the Knudsen number is typically between 30 and 40, indicating a highly rarefied environment [6]. Depending on orbital orientation, the Space Shuttle orbiter at an orbital altitude of 220 km degrades between 1 and 5 km in altitude per day [7]. Slip flow across the surfaces of a spacecraft changes the amount of station keeping propellant required and also changes the reentry characteristics.

1.3 How TMAC is used to Quantify "Slip." The actual amount of slip depends on the nature of reflection that the gas molecules undergo at a solid wall. Maxwell [2] suggested a coefficient to be used to characterize this reflection and to quantify slip. This coefficient represents the portion of incident molecules that undergo perfectly diffuse reflection, This coefficient is now commonly referred to as the TMAC, tangential momentum accommodation coefficient. For a given set of gas atoms impacting a surface, the TMAC is defined for this work as (Eq. (4))

$$\text{TMAC} = \frac{\sum_N m \cdot u_i - \sum_N m \cdot u_f}{\sum_N m \cdot u_i} \tag{4}$$

Here N is the total number of gas atoms in the sample, m is the mass of a gas atom, i is the initial value, and f is the final value before and after the gas atom collides with a solid surface. A TMAC with a value of 1 represents complete tangential momentum transfer to the solid surface. A TMAC value of zero represents perfect reflection with no tangential momentum transfer to the surface.

The TMAC is used to directly calculate the amount of velocity slip occurring at the wall using the following relationship [8]:

$$u_{\text{gas}} - u_{\text{wall}} = \left[\frac{2-\text{TMAC}}{\text{TMAC}} \cdot \lambda \cdot \left(\frac{\delta u}{\delta y}\right)_w\right] + \left[\frac{3}{4} \cdot \frac{\mu}{\rho \cdot T_{\text{gas}}} \cdot \left(\frac{\delta T}{\delta x}\right)_w\right] \tag{5}$$

Table 1 Typical TMAC values

Experimenter	Largest TMAC measured	Smallest TMAC measured	Reference
Bentz	1.11	0.83	[14]
Knetchtel	0.95	0.45	[15]
Lord	0.95	0.35	[16]
Porodnov	1.059	0.803	[17]
Seidl	1.20	0.20	[11]
Thomas	1.075	0.824	[13]
Liu and several others	Approximately 1.0		[18]

The difference between the velocity of the gas at the wall (u_{gas}) and the velocity of the wall itself (u_{wall}) is a function of the TMAC, mean free path (λ), the strain rate at the wall $[(\delta u/\delta y)_w]$, fluid density (ρ), fluid viscosity (μ), temperature of the gas adjacent to the wall (T_{gas}), and temperature change rate at the wall $[(\delta T/\delta x)_w]$. Here x is the tangential coordinate (that is, parallel to the solid wall). Note for a gas and wall with no heat flux at the wall, the equation simplifies to an adiabatic condition that was suggested by Maxwell Eq. (6)

$$u_{\text{gas}} - u_{\text{wall}} = \left[\frac{2-\text{TMAC}}{\text{TMAC}} \cdot \lambda \cdot \left(\frac{\delta u}{\delta y}\right)_w\right] \tag{6}$$

In view of the quantitative definition of TMAC as provided in Eq. (4) and as used in this work, a more generalized version of slip velocity can be presented for the adiabatic case as

$$u_{\text{gas}} - u_{\text{wall}} \equiv (\Delta u)_{\text{slip}} = C(\text{TMAC}) \cdot \lambda \left(\frac{du}{dy}\right)_{\text{wall}} \tag{7}$$

where $C(\text{TMAC})$ is a function of TMAC that decreases with increase in TMAC.

1.4 Typical TMAC Values. Based on the above discussion, one would normally expect the TMAC to fall within the range of 0 to 1. However, there are many experiments [9–13] of flows across surfaces which have resulted in a slightly reversed the flow at the wall surface. This is termed "backscattering." The consequence of this is that the TMAC, as defined above can conceivably have values greater than 1.

Typical values for TMAC are shown in Table 1.

As shown by the range of data in the table, TMAC values have been measured from a high of about 1.2 to a low of about 0.2. These extremes are not typical. A majority of the experimental measurements are in the 1.06 to 0.85 range.

1.5 Common Practice of Assuming a TMAC Value. The many factors which affect the TMAC value are not well understood. Experimental data is specific to a given set of conditions and not readily applied or extrapolated for new situations. Consequently, it has become common practice in calculations and numerical modeling of slip flows to assume a TMAC value. The most common TMAC assumption is a value of 1, although values as low as 0.5 have been noted.

1.6 Complicating Factor of Adsorbed Layers on the Surface. The surface which is exposed to the moving gas may not be the intended base material. Atoms or molecules may have adhered to the surface by van der Waals forces in what is termed physical adsorption. The adsorbed materials may be in multiple layers. Gad-el-Hak [8] has suggested investigating adsorbed layers to determine their surface effects. This is one of the factors potentially affecting TMAC and a prime subject of this work.

2 Scope of Work/Problem Definition

According to Barber and Emerson [19] experiments indicate the TMAC is substantially a function of the following:

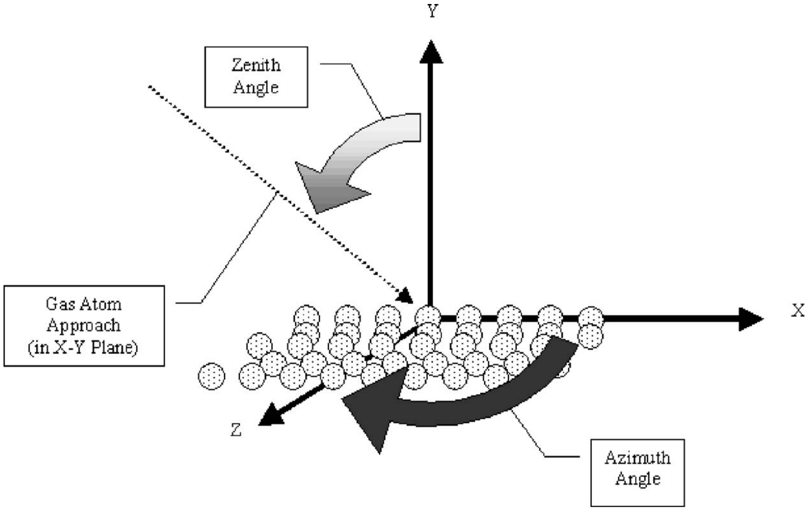

Fig. 1 Azimuth and zenith angles

- Molecular weight of the gas
- Energy of the incoming molecules
- Wall material
- Condition (roughness) of the surface
- Temperature of the surface

The challenge is to develop a deterministic molecular dynamics (MD) model which utilizes these influencing factors to give useful TMAC results, but is simple to use and can be validated. This work uses a free molecular regime deterministic MD simulation model to estimate the TMAC of rare gas to solid surface interactions, for a given set of conditions. It takes into account all of the above factors, except the temperature of the surface. (It is specified for this initial work that no heat transfer takes place across the boundary.) The initial MD model looks at many individual single gas atoms impacting a surface with uniform energy and a constant angle of approach. From this a TMAC for a certain gas, solid, energy, and angle can be calculated and compared for validation.

The work builds on the efforts of others who performed TMAC experiments to gather data at a variety of impact angles [11,20,18,15] and who developed earlier TMAC related MD models of gas to surface interactions [21–26].

2.1 Ultimate Goal of Using MD to Estimate Overall TMAC Using Maxwellian Distribution. An ultimate goal of this TMAC research is to develop the methodology to calculate the TMAC for a given set of gas, solid, and energy conditions. This current MD model represents a logical first step in that process. The calculation of TMAC with a specified angle and velocity is a subset of the problem of calculating the composite TMAC over all the angles and velocities which would result from a Maxwellian gas temperature distribution superimposed upon a velocity flow field. The validation of this MD model for a specified angle and velocity will then allow further model evolution involving Maxwell velocity distributions, larger sample sizes, and calculation of the complete TMAC for a given set of flow conditions.

2.2 Simplifying Assumptions. Several assumptions were made to make the scope of this initial work more manageable: The solid atoms are assumed to be immobile. This assures the collision is adiabatic and conserves energy. However, this also neglects the internal vibrations of the solid. The time of a typical collision modeled is about one order of magnitude greater than the period of the applicable Debye frequency and most other lattice vibration frequencies. The typical collision involves tens of solid atoms within the Lennard-Jones cut-off radius. Therefore during a collision it is likely that the many involved solid atoms would complete several vibration cycles each. Neglecting the motions of individual solid atoms is not expected to introduce more than a first order error in the simulation. This assumption is similar to other MD simulations which have set the mass of the solid atom to be 10^{10} times the mass of the impacting atom, which also results in fixed solid atoms [27]. It is also similar to the "adiabatic approximation" used in lattice dynamics analyses [28].

A single gas atom is involved in each gas-to-solid interaction. The gas is specified to be sufficiently rare that during the gas to solid interaction, no other gas atoms influence the interaction. Free molecular regime results correlate closely with slip flow regime results [29]. The model begins and ends with the gas atom on the order of 0.1λ (one tenth of a mean free path) from the surface of the solid. Therefore, the gas is sufficiently rare that during the entire gas-to-solid interaction, no other gas molecules are likely to influence the interaction.

The azimuth angle is specified to convey the gas atom on the centerline of one of the unit cell faces (Fig. 1). Only the zenith angle (measured from the solid surface normal) is allowed to vary. The out of plane forces cancel out. This is then a limited three-dimensional (3D) simulation is of what is substantially a 2D event. This results in fewer solid atoms in the MD simulation and faster run times for this initial work.

The simulation does not model making or breaking of atomic bonds. It is a collision type model to aid in the understanding of TMAC.

2.3 Topics Investigated. The following topics were investigated:

- Angle of approach: The zenith angle (measured from the solid surface normal) was varied to determine for a given gas, solid, and energy combination how the TMAC would be affected. This angle was varied from 10 to 70 deg.
- Energy ratio: The energy ratio (ER) of a gas-to-solid impact is defined as the ratio of the gas atom's kinetic energy to the Lennard-Jones energy coefficient (ε) (Eq. (8)):

$$\mathrm{ER} = \frac{\frac{1}{2} \cdot m \cdot V^2}{\varepsilon} \tag{8}$$

The ER provides a way to simultaneously consider m (mass of the gas atom), V (velocity of the gas atom), and ε. The Lennard-Jones value of ε represents magnitude of the attractive "well depth" energy of the interaction. In the case of unlike atoms, the Lennard-Jones ε is calculated as the geometric mean of the ε for the two individual atoms. If the

Table 2 Lennard-Jones coefficients

Atom	σ (m)	ε (as used) (J)	ε (as given) (ε/k_B)	Data sources
Carbon	3.35×10^{-10}	7.2×10^{-22}	51.2 K	Tildesley and Madden [36]
Copper	2.3×10^{-10}	9.3×10^{-20}	3.5 eV	Hess and Kroger [30]
Hydrogen	2.81×10^{-10}	1.2×10^{-22}	8.6 K	Murad and Gubbins [37]
Helium	2.28×10^{-10}	1.4×10^{-22}	10.2 K	Maitlandet al. [38]
Oxygen	2.95×10^{-10}	8.6×10^{-22}	61.6 K	English and Venables [39]

Lennard-Jones ε is much greater than an atom's kinetic energy, the gas atom path is dominated by these attractive surface forces. It would likely experience multiple "bounces" before leaving the cut-off radius (Rc), or could conceivably be captured by the surface, thereby "wetting" it or being adsorbed by it. If the Lennard-Jones ε is much less than an atom's kinetic energy, the gas atom path is dominated by the inertial momentum of the atom, moving quickly past the attractive potential zone into the strongly repulsive zone, then being ejected in a similar manner, with few "bounces."

- Adsorbed layer(s): Uniform adsorbed layers of different ER were varied from 1, 2 and 3 layers deep atop a solid surface.

3 Methodology/Numerical Method

3.1 Molecular Dynamics Method. The molecular dynamics method uses Newton's laws of motion in combination with numerical integration techniques to determine the accelerations, velocities, and positions of each of the involved gas atoms at each time step. The forces are determined using the Lennard Jones potential, summed over all of the atoms involved in the collision. The force is the gradient of this potential and given in Eq. (9).

$$f_{ij}=\left(\frac{48\cdot\varepsilon}{\sigma^2}\right)\cdot\left[\left(\frac{\sigma}{r_{ij}}\right)^{14}-\frac{1}{2}\cdot\left(\frac{\sigma}{r_{ij}}\right)^{8}\right]\cdot r_{ij} \qquad (9)$$

The sum of the forces is equal to the mass times the acceleration. The sum of the forces is known. The gas atom's mass is known. The calculated acceleration may be integrated over small time steps to yield velocities and positions with respect to time. In this case, the "leapfrog" integration method used was second order accurate in time.

A samples size of 500 gas atoms were positioned as equally spaced over two lattice spacing distances and evaluated individually. This resulted in two "cycles" of data. For all gas atoms, the ratio of tangential momenta (final time step/initial time step) on an individual and moving average basis was calculated. A moving average amount was set equal to the number of gas atoms spread across one lattice distance. This allowed a check to see if the moving average and total averages had stabilized or if more atoms in the sample were needed.

3.2 Specific Values Used. L-J coefficients: Lennard-Jones coefficients for the involved materials interacting with like atoms were taken from published literature and shown in Table 2.

Cut-off radius: The "cut-off radius" (Rc) is the nondimensionalized distance beyond which Lennard-Jones potentials and forces are neglected. In MD texts, it is recommended to set Rc equal to 2.5, where the interaction energy is 0.016 of the well depth [32]. In MD simulations by Banavar and others involving fluid and solid interactions an Rc equal to 2.5 is also commonly used [27]. For many MD simulations we are dealing with gas atoms spread out over a large volume. Few atoms are typically involved close to the cut-off radius at any given time step. Neglecting the occasional atom at a distance has a small effect. However in simulations involving an interaction with a solid, there are numerous time steps in succession with many solid atoms lying just outside of this arbitrary cut-off radius. Their cumulative effect on the trajectory of the gas atom is significant. For this work, we are interested in these interactions at the solid surface, which may have dense solid atoms and additional layers of contaminants. As described below an Rc of 3.5 was used to enhance convergence.

Time step: The "natural time unit" of this simulation is (10)

$$\tau=\left(\frac{m\cdot\sigma^2}{\varepsilon}\right)^{1/2} \qquad (10)$$

Here τ is the natural time unit, σ is the Lennard-Jones gas length scale, m is the mass of the gas atom, and ε is the geometric mean of the Lennard-Jones energies for the gas and surface atoms. The natural time unit for the helium-copper interaction is 1.3×10^{-12} s. Surface contaminants would change it slightly. The time step used in the MD simulation is a fraction of the natural time unit of the interaction. In MD texts, it is considered over the range of 0.001τ to 0.005τ [32]. In MD simulations by Banavar and others a time step of 0.005τ is also commonly used [27,33]. As described below in the convergence discussion, a time step of 0.0005 τ was typically used for this MD model to minimize error and maximize energy conservation.

Starting height: It is important for the gas atom to start its travel toward the solid surface from a distance greater than the cut-off radius. Likewise, the MD simulation proceeds until the gas atom has again moved outside the cut-off radius from all the solid atoms. In this manner the complete interaction is evaluated. Therefore, the starting height above the solid for the simulation was set greater than the cut-off radius, typically to 1 nm.

3.3 Convergence and Accuracy of the Numerical Solution. For each of the 500 gas molecules impacting the solid in a simulation run, the initial and final kinetic energy was compared and verified to be conserved. For the time step selected, the simulation conserves energy for each of the gas molecules to third order or greater accuracy, even after thousands of time steps.

Convergence of the TMAC estimate and conservation of energy was tested as a function of time step. The simulation quickly converges for appropriate time steps, as shown in Table 3:

Based on this analysis, the typical time step used was 0.0005τ. This value is several orders of magnitude within the convergence range and does not introduce significant error.

The effect of varying the cut-off radius Rc was evaluated. The TMAC was evaluated at a fixed angle of approach for Rc varying from 1.5 to 4.5. Error was evaluated for each of the runs in com-

Table 3 Typical MD simulation convergence

Time step	Percent variation from base TMAC estimate (error)	Conservation of energy, worst gas atom (%)
0.10 τ	Does not converge	-
0.05 τ	0.3714	10
0.025 τ	0.0103	92
0.010 τ	0.0005	99.8
0.001 τ	0.0000	99.996
0.0001 τ	0.0000	99.99985
0.00001 τ	Base TMAC value	99.99999

Table 4 MD Cut-off radius convergence

Cut-off radius (Rc)	Percent variation from base TMAC estimate (error)	Number of solid atoms in collision
1.5	23.68	7
2.5	1.24	26
3.5	0.21	42
4.5	Base TMAC estimate	90

parison to the value determined with the Rc of 4.5 (Table 4). Larger Rc reduced the error, but greatly increased the number of solid atoms to be evaluated in the model. A Rc of 3.5 was selected as a good compromise, introducing an error of less than 1% while keeping the number of solid atoms manageable.

Occasionally a gas atom will undertake a long series of bounces with the solid. Rather than calculate through 20 or more bounces, an attempt was made to terminate after certain number of bounces (or a certain number of time steps) when a "cut-off" limit was reached. The future path of the gas molecule was then assumed to be completely randomized. The MD calculation was terminated for that atom. The gas atom was assigned the average tangential velocity of a random atom leaving the surface (zero) and a normal velocity equal to that required to maintain conservation of energy. In order to understand the effect of this process better, a sample set of MD simulations were run under conditions which resulted in a large number of multiple collisions. A series of 500 gas atoms were impacted upon a solid surface at a fixed angle of approach. The bounce and time step limits were changed over the multiple runs in order to evaluate the effect. It is interesting to note that even after five or six successive impacts, some measurable effect on tangential momentum remains, and the arbitrary termination of the tangential momentum can introduce significant error. Therefore, for the MD simulations conducted, the time step cutoff and bounce cutoff were set high enough to assure that less than 1% of the gas atoms were terminated in this manner.

In summary, the numerical techniques used maintain conservation of energy for each gas atom order and converge upon a solution. We know error is introduced by the use of the cut-off radius (about 1%), use of time step and bounce MD cutoffs (about 1%). The simplifying assumptions stated, the model limitations stated and the Lennard-Jones potential model used are anticipated to introduce error of the first order, which we do not attempt to further quantify at this time.

4 Validation

4.1 Selection of Seidl data. Of the TMAC data surveyed, data by Seidel and Steinheil [11] was selected for validating this model because it provides not just a single TMAC value, but separate TMAC values for each of seven impact angles on a prepared, cleaned, and characterized surface with a known impact velocity. The data set chosen for validation represents a copper crystal surface, face 100, with multiple adsorbed layers being impacted by Helium atoms at 1770 m/s.

4.2 Analysis of Seidl Data. Seidl evaluated the accuracy and repeatability of his experimental process. The accuracy was greater at the larger angles of approach than at the smaller angles. Using the plus and minus limits he suggests, the actual TMAC values are bounded as follows (Table 5).

Seidl states that the material was electrolytically polished. Material which has been electrolytically polished does not present an "ideal crystal surface." The actual condition of the surface was not reported further, but can be deduced from the typical performance of electropolishing, which reduces surface roughness readings by about 50% and smoothes or eliminates discernable features [34]. In this case, the copper with 5 μm grinding grooves was stated to be electropolished. The resulting copper surface would be expected to be in the 2.5 μm roughness category with a smooth, featureless surface. Seidl goes on to describe a contaminant layer as follows, "the surfaces are completely covered by adsorbent layers, which are,…, made up mainly of hydrocarbons and water." The stated contaminants (hydrocarbons and water) therefore exist in more than one layer mixed in with the irregular surface of a copper 100 crystal.

Table 5 Seidl experimental data

Angle	Seidl variability	Seidl lower TMAC value	Seidl lower TMAC value
10	0.100	0.86	1.06
20	0.080	0.81	0.97
30	0.065	0.77	0.90
40	0.050	0.73	0.83
50	0.040	0.71	0.79
60	0.030	0.69	0.75
70	0.020	0.66	0.70

4.3 Modeling of Seidl Experimental Conditions. For the validation MD model, the previously stated Lennard-Jones coefficients for Cu and He were used, along with the specified velocity, approach angles, and other values previously identified. Based on the adsorbed layer material description, a weighted mix of hydrogen, oxygen, carbon, and copper atoms was developed. The exact geometry, material ratios, or pattern at nanoscale are not known. This presented a substantial number of possible combinations. It was decided to model the adsorbed layer as a set of ideal atoms with common Lennard-Jones coefficients matching the composite value of the layer. The assumed mix was in the following ratio: one carbon atom, one oxygen atom, two hydrogen atoms, and two copper atoms. This resulted in an $\varepsilon_{\text{composite}}$ of 3.13×10^{-20} J, weighted on number of atoms and a $\sigma_{\text{composite}}$ of 2.308×10^{-10} m weighted on the number of atoms and their individual ε. The adsorbed layer atoms were located on the same crystal lattice as the base material. Fourteen MD simulation runs of 500 gas atoms at each of seven approach angles were run for adsorbed layers two atoms deep and three atoms deep.

4.4 Validation Comparison Results. The MD simulation correctly predicted that the TMAC changes with the angle of impact. The MD simulation correctly estimated the direction of the slope regarding changes of the TMAC with the angle of impact. The magnitude of difference between the MD simulation data average and the Seidl data average is just a few percent (less than 3%). It is generally more accurate as the angle of approach is increased. Overall, for two series of simulation runs, the MD model produced 13 of 14 data points within the experimental data range. A comparison plot is included as Fig. 2.

5 Results and Discussion

5.1 Energy Ratio Results Review. As described in a previous paper [35] energy ratio has a substantial affect on TMAC. Figure 3 illustrates the effect of ER on TMAC. In general, increasing energy ratio above a value of 5 reduces TMAC at all angles. Reducing ER tends to decrease the proportion of single bounce impacts, which leads to the more random multiple bounce impacts and a generally a larger TMAC. This is illustrated by way of the sequenced plot of the final to initial tangential momentum ratio for each of the 500 gas atoms in an MD run, as will be described later.

For a He atom impacting a bare Cu surface under the conditions given, the resulting ER is about 2.9.

5.2 Results of Adsorbed Layer(s) With Large ER Difference. The Lennard-Jones value used for ε for Cu was 9.3×10^{-20} J. In order to understand the effect of adsorbed layers with a large ER difference, the Lennard-Jones ε of the upper one or two layers was decreased substantially. The ε of the adsorbed layer atoms (interacting with like atoms) was reduced to 3.4

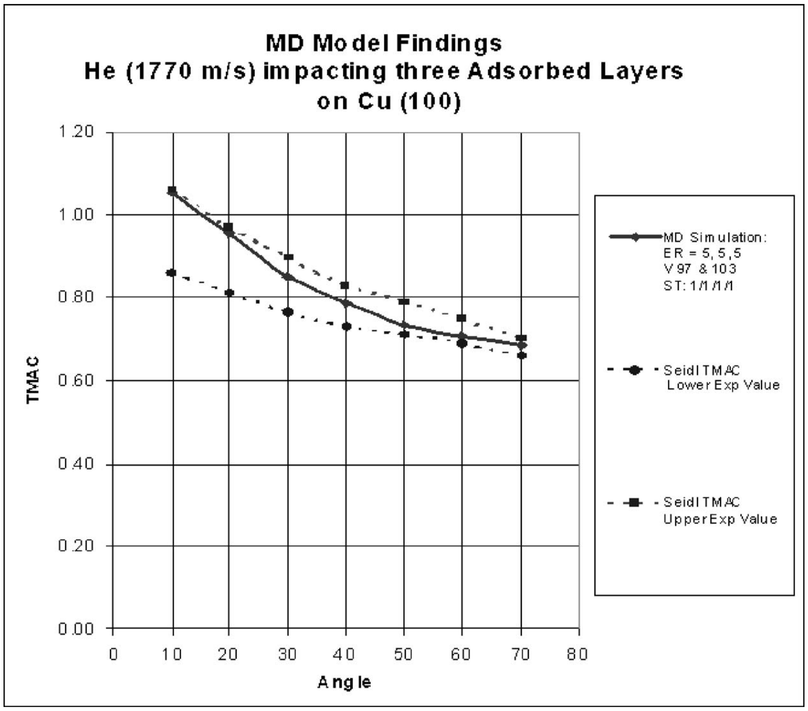

Fig. 2 MD model results baseline validation

$\times 10^{-22}$ J, as may result from an adsorbed mix of H, C, and O, with a composite ER of 48. Figure 4 illustrates the modeled effect of adding one or two such layers of an adsorbent atop a Copper like fcc 100 crystal plane. The adsorbent atoms are located in the same fcc arrangement as the base material. The result is that the gas atom impacting the surface now sees a combination of solid atoms which have a varying ER within the solid. As it approaches it is exposed to atoms with high ER. At the closest point of the impact it is exposed to atoms with both large and small ER. The result is a markedly different TMAC result.

As shown in Fig. 3 a uniform adsorbed layer two atoms deep would reduce the TMAC significantly at all angles of approach. The resulting surface acts similar to that with a uniform large ER of 70 as shown in Fig. 2.

With a single adsorbed layer a more interesting result occurs. At large zenith angles the TMAC is reduced as expected. However, at small zenith angles, the TMAC is increased to the point of back-scattering.

5.3 Results of Adsorbed Layer(s) With Small ER Difference. A similar analysis was performed using an adsorbed layer with an ER just slightly more than the Cu base material. Figure 5 illustrates the effect of adding one, two, or three layers of an adsorbent atop a Copper like fcc 100 crystal plane. The adsorbent atoms are located in the same fcc arrangement as the base material. In this case however, the energy ratio resulting from the adsorbent material was 4.9 or 5.0 versus an ER for the base material of 2.9. An ER difference such as this could occur with a base material with nonplanar surface with Cu and H, O, and C like atoms all present in every layer. It could also occur if the Cu surface was plated with a metal alloy resulting in this ER.

Note that the first adsorbed layer still has a substantial effect on TMAC. The top adsorbent layer in close proximity to the impact-

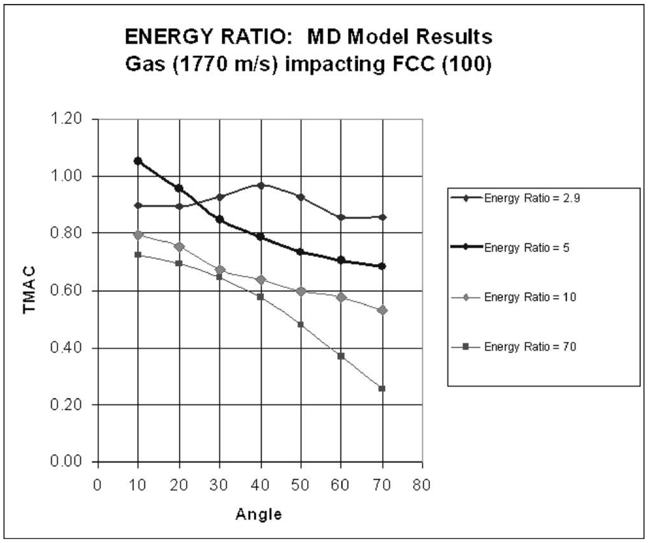

Fig. 3 Energy ratio model results

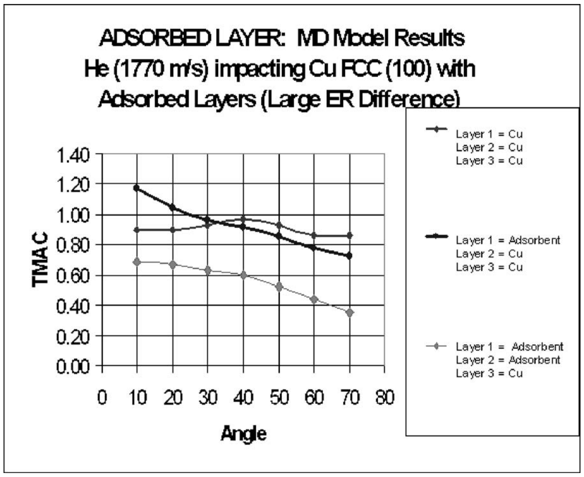

Fig. 4 Adsorbed layers-data summary for large ER difference

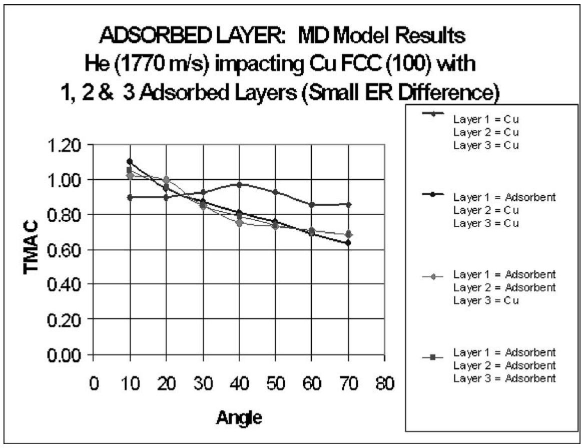

Fig. 5 Adsorbed layers-data summary for small ER difference

ing gas atom and even the small ER change can have a substantial effect. However, the second and third adsorbent layers do not seem to have a significant impact.

5.4 Trajectory Analysis. Figure 6 shows the trajectories (path plots) of ten typical gas atoms. Each plot shows the same ten gas atoms as they impact the surface at slightly different locations. The top plot has a bare Cu surface with an ER of 2.9 for all three solid atomic layers. Under these conditions, most of these impacts are of the multiple bounce type, with a result of a TMAC of about 0.9. In the middle plot, the upper layer of solid atoms has the ER of 48, with the two lower layers maintaining the ER of 2.9. This resulted in fewer gas atoms experiencing multiple bounces and a much different TMAC value, about 1.2. In the lower plot, the upper two layers of solid atoms have an ER of 48, with the lower layer maintaining the ER of 2.9. This resulted in none of the gas atoms experiencing multiple bounces and a much reduced TMAC value, about 0.7.

It is evident an important effect of the addition of high ER adsorbed layers is to change the type of impacts from multiple "bounce" to a single "bounce."

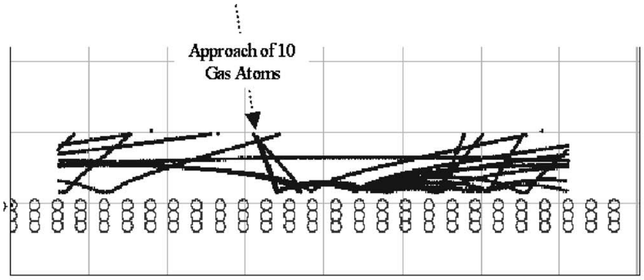

No Adsorbed Layers, Angle = 10 Degrees

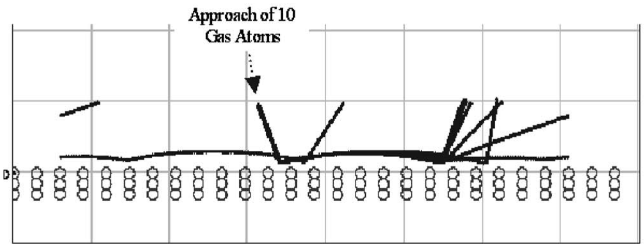

1 Adsorbed Layer, Angle = 10 Degrees

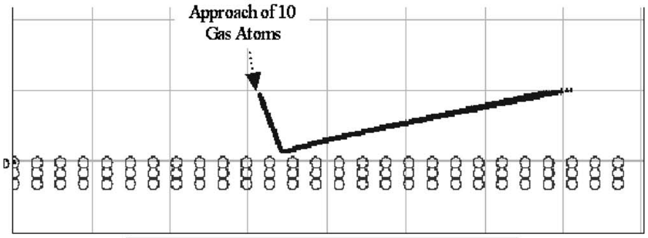

2 Adsorbed Layers, Angle = 10 Degrees

Fig. 6 Adsorbed layers-gas atom path plots

5.5 Momentum Ratio Curve Analysis and Possible Backscattering Explanation. Figure 7 is a plot of the ratio of initial tangential momentum to final tangential momentum for each of the 500 gas atoms from the three 10 deg MD runs. If the ratio is positive, it indicates forward scattering. If negative, backscattering. Recall the 500 gas atoms are each spaced to start at slightly different positions, so as to spread the sample over two lattice cycles. As the starting position of the gas atoms progress across the lattice this plot follows a piecewise continuous curve. The continuous portions occur when the gas atom experiences a simple, single bounce type impact. This single bounce type impact may be either forward scattering or backscattering. The cycle of the plot follows the impact geometry, repeating for the two lattice cycles. The discontinuous portions occur when there are multiple bounces during a single gas atom collision event. These tend to truncate both the forward and backscattering peaks off the curve.

The upper plot shows the result with an ER of 2.9 for all three solid atomic layers. Note that both the forward scattering and the backscattering portions of the curve have been truncated by the discontinuous portions. This tends to reduce both forward scattering and backscattering, resulting in the TMAC of 0.9.

In the middle plot the upper layer of solid atoms has the ER of 48, with the two lower layers maintaining the ER of 2.9. In this single adsorbent layer case, the high ER top layer has restored some of the curve's continuity, but more at the backscattering portion of the curve than the forward scattering portion. Many of the potentially forward scattering gas atoms are still experiencing multiple bounces, with mixed TMAC ratio results. The backscattering portions of this curve are nearly continuous. This has substantially raised the TMAC to 1.2, a net backscattering situation.

In the lower plot, the upper two layers of solid atoms have the ER of 48, with the lower layer maintaining the ER of 2.9. For this case (two adsorbent layers), the complete continuity of the curve has been restored. The curve is continuous in both the forward scattering and the backscattering regions. Since there is more forward scattering than backscattering, the result is to lower the TMAC to about 0.7.

6 Conclusions

Adsorbed layer(s) on the surface of a material can change the TMAC significantly, and must be accounted for to accurately calculate flows in many micro- and nano-channels. An adsorbent layer one atom deep can have a substantial effect, even if its ER is not much different from the base material. For large ER differences, additional layers can have further substantial effect.

Examination of a plot of final to initial tangential momentum ratios for a sequence of atoms typically shows a piecewise continuous progression, with portions forward scattering and portions backscattering. The curve follows the lattice position cycle of the approaching gas atoms and therefore this conclusion is dependent on the assumption that the uppermost layer of the surface (adsorbed layer) presented a perfect crystal structure. Net backscattering has been noted to occur when the forward scattering portion of the cycle became more discontinuous than the backscattering portion, and seems to be affected by ER.

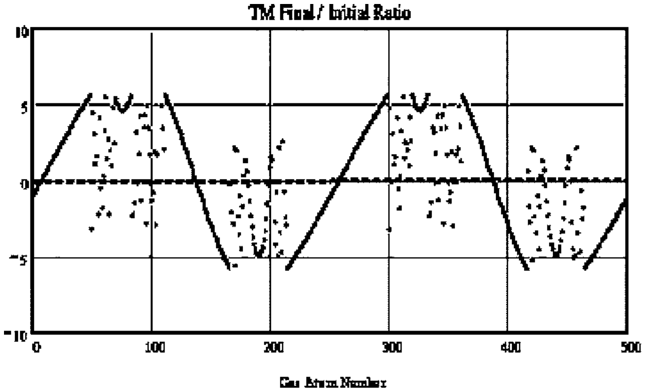

No Adsorbed Layers, Angle = 10 Degrees

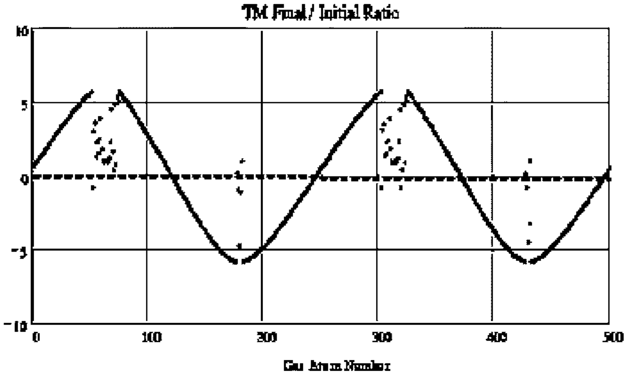

1 Adsorbed Layer, Angle = 10 Degrees

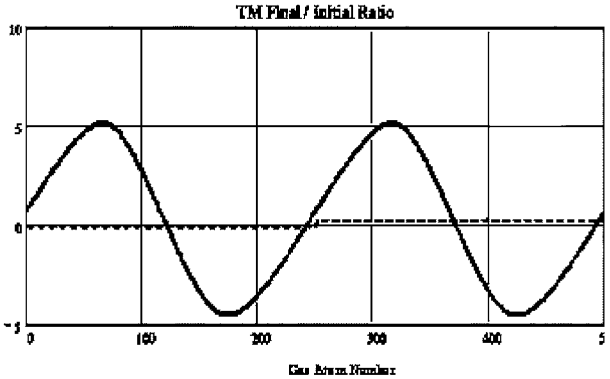

2 Adsorbed Layers, Angle = 10 Degrees

Fig. 7 Adsorbed layers-ratio plots

6.1 Topics for Future Study. This initial work has verified the basic concept that a MD model can provide useful insight into understanding and estimating TMAC. However, further work is necessary to expand the usefulness of the model. Next we plan to expand the model to include 3D geometry functionality across all azimuth angles and to include gas atom populations with a Maxwellian temperature distribution. This will allow further validation with a greater range of materials and existing data. Further work with this enhanced model will then examine additional crystal plane types, atomic, and nanoscale surface irregularities and will revisit this adsorbed layer analysis, but using individual adsorbed atoms and their distinct Lennard-Jones coefficients instead of common composite coefficient values for all atoms in the adsorbed layer.

Acknowledgment

The authors thank Dr. S. Balachandar, Associate Editor, Journal of Fluids Engineering and the referees of this paper for providing insightful and helpful comments to clarify and improve the work. G. W. Finger thanks Reynolds, Smith and Hills, Inc. for providing research funding, computer time and other technical resources for accomplishing this work.

Nomenclature

ε = Lennard-Jones characteristic energy
λ = mean free path
ϕ = Lennard-Jones energy potential
σ = Lennard-Jones characteristic length
τ = natural time step
E = energy of gas atom
ER = energy ratio
i = gas atom number
j = solid atom number
f = Lennard-Jones force
L-J = Lennard Jones
m = meter
m_i = mass of gas atom i
N = total number of gas atoms
MD = molecular dynamics
MEMS = Microelectromechanical systems
NEMS = Nanoelectromechanical systems
r_{ij} = distance between atoms i and j
Rc = cut-off radius
TMAC = tangential momentum accommodation coefficient
U = velocity of continuum flow field
V_i = velocity of gas atom

References

[1] White, F., 1991, *Viscous Fluid Flow*, McGraw Hill, pp. 47–49.
[2] Maxwell, J. C., 1879, "On Stresses in Rarified Gases Arising from Inequalities of Temperature," Philos. Trans. R. Soc. London, **170**, pp. 231–256.
[3] Arkilic, E. B., Breuer, K. S., and Schmidt, M. A., 1994, "Gaseous Flow in Micro channels. Application of Micro fabrication to Fluid Mechanics," ASME FED, **197**, pp. 57–66.
[4] Pfahler, J., Harley, J., Bau, H., and Zemel, J., 1991, "Gas and Liquid Flow in Small Channels," *Winter Annual Meeting*, ASME, pp. 49–60, ASME, Atlanta, GA.
[5] Barber, R. W., Emerson, D. R., and Gu, X., 2004, "Rarefied Gas Dynamics in Micro-devices," http://www.cse.clrc.ac.uk/ceg/rgd.shtml, Council for the Central Laboratory of the Research Councils (CCLRC).
[6] Herrero, F. A., 1985, "The Lateral Surface Drag Coefficient of Cylindrical Spacecraft in a Rarefied Finite Temperature Atmosphere," AIAA J., **23**, pp. 862–867.
[7] Griffin, M. D., and French, J. R., 1991, *Space Vehicle Design* (Education Series), AIAA, Washington, DC.
[8] Gad-el-Hak, M., 1999, "The Fluid Mechanics of Microdevices - The Freeman Scholar Lecture," ASME J. Fluids Eng., **121**, pp. 5–33.
[9] Berman, A. S., and Maegley, W. J., 1972, "Internal Rarefied Gas Flows with Backscattering," Phys. Fluids, **15**, pp. 772–779.
[10] Davis, D. H., Levenson, L. L., and Milleron, N., 1964, "Effect of 'Rougher-than-Rough' Surfaces on Molecular Flow through Short Ducts," J. Appl. Phys., **35**, pp. 529–532.
[11] Seidl, M., and Steinheil, E., 1974, "Measurement of Momentum Accommodation Coefficients on Surfaces Characterized by Auger Spectroscopy," *SIMS and LEED. Rarefied Gas Dynamics, Eighth International Symposium*, Stanford University, New York, NY, 9, E 9.1–E 9.12.
[12] Maegley, W. J., and Berman, A. S., 1972, "Transition from Free - Molecule to Continuum Flow in an Annulus," Phys. Fluids, **15**, pp. 780–785.
[13] Thomas, L. B., and Lord, R. G., 1972, "Comparative Measurements of Tangential Momentum and Thermal Accommodations on Polished and Roughened Steel Spheres," *Rarefied Gas Dynamics, Eighth International Symposium*, Stanford University, New York, NY, pp. 405–412.
[14] Bentz, J. A., Tompson, R. V., and Loyalka, S. K., 1997, "The Spinning Rotor Gauge: Measurements of Viscosity, Velocity Slip Coefficients, and Tangential Momentum Accommodation Coefficients for N-2 and CH4," Vacuum, **48**, pp.

817–824.

[15] Knechtel, E., and Pitts, W., 1969, "Experimental Momentum Accommodation on Metal Surfaces of Ions Near and Above Earth Satellite Speeds," Rarefied Gas Dyn., **5**, pp. 1257–1266.

[16] Lord, R. G., 1976, "Tangential Momentum Accommodation Coefficients of rare Gases on Polycrystalline Metal Surfaces. Rarefied Gas Dynamics," *Eighth International Symposium*, Stanford University, New York, NY, 10, pp. 531–538.

[17] Porodnov, B. T., Suetin, P. E., Borisov, S. F., and Akinshin, V. D., 1973, "Experimental Investigation of Rarefied Gas Flows in Different Channels," J. Fluid Mech., **64**, pp. 417–437.

[18] Liu, S. M., Sharma, P. K., and Knuth, E. L., 1979, "Satellite Drag Coefficients Calculated from Measured Distributions of Reflected Helium Atoms," AIAA J., **17**, pp. 1314–1319.

[19] Barber, R. W., and Emerson, D. R., 2002, "Numerical Simulation of Low Reynolds Number Slip Flow Past a Confined Sphere," *23rd International Symposium on Rarefied Gas Dynamics*, Whistler, Canada, Daresbury Laboratory, Daresbury, Warrington, England.

[20] Saltsburg, H., and Smith, J. N., 1966, "Molecular Beam Scattering from the (111) Plane of Silver," J. Chem. Phys., **45**, pp. 2175–2183.

[21] Oman, R., Bogan, A., Weiser, C., and Chou, H., 1964, "Interactions of Gas Molecules with an Ideal Crystal Surface," AIAA J., **2**, pp. 1722–1730.

[22] Oman, R., 1967, "Numerical Calculations of Gas-Surface Interactions," AIAA J., **5**, pp. 1280–1287.

[23] Knechtel, E., and Pitts, W., 1973, "Normal and Tangential Momentum Accommodation for Earth Satellite Conditions," Astronaut. Acta, **18**, pp. 171–184.

[24] Koplik, J., Banavar, J., and Willemsen, J., 1988, "Molecular Dynamics of Poiseuille Flow and Moving Contact Lines," Phys. Rev. Lett., **60**, pp. 1282–1285.

[25] Koplik, J., and Banavar, J., 1998, "No-Slip Condition for a Mixture of Two Liquids," Phys. Rev. Lett., **80**, pp. 5125–5128.

[26] Cieplak, M., Koplik, J., and Banavar, J., 1999, "Applications of Statistical Mechanics in Subcontinuum Fluid Dynamics," Physica A, **274**, pp. 281–293.

[27] Koplik, J., Banavar, J., and Willemsen, J., 1989, "Molecular Dynamics of Fluid Flow at Solid Surfaces," Phys. Fluids A, **1**, pp. 781–794.

[28] Srivastava, G., 1990, *The Physics of Phonons*, IOP Publishing Ltd., Bristol, England.

[29] Eckert, E. R., and Drake, R. M., 1987, *Analysis of Heat and Mass Transfer*, Hemisphere Publishing Co., New York, NY.

[30] Hess, S., and Kroger, M., 2002, "Elastic and Plastic Behavior of Solid Models," Technische Mechanik Band, **22**, pp. 79–88.

[31] Allen, M. P., and Tildesley, D. J., 1989, *Computer Simulation of Liquids*, J. W. Arrowsmith, Ltd., Bristol, England.

[32] Rapaport, D. C., 2004, *The Art of Molecular Dynamics Simulation*, Cambridge University Press, Cambridge, UK.

[33] Tomassone, M., Couzis, A., Maldarelli, Banavar, J., and Koplik, J., 2001, "Molecular Dynamics Simulation of Gaseous-Liquid Phase Transitions of Soluble and Insoluble Surfactants at a Fluid Surface," J. Chem. Phys., **115**, pp. 8634–8642.

[34] Delstar, 2005, "Electropolishing, Passivating and Mechanical Polishing," www.delstar.com/polishing.htm, Delstar Metal Finishing, Inc.

[35] Finger, G., Kapat, J., and Bhattacharya, A., 2006, "Analysis of Tangential Momentum Accommodation Coefficient Using Molecular Dynamics Simulation," *44th AIAA Aerospace Sciences Meeting and Exhibit*, (AIAA, ed.), AIAA, Reno, NV.

[36] Tildesley, D. J., and Madden, P. A., 1981, "An Effective Pair Potential for Liquid Carbon Disulphide," Mol. Phys., **42**, pp. 1137–1156.

[37] Murad, S., 1978, "LINEAR and NONLINEAR. Quantum Chemistry Program Exchange," QCPE, **12**, pp. 357.

[38] Maitland, G. C., Rigby, M., Smith, E. B., and Wakeham, W. A., 1981, *Intermolecular Forces: Their Origin and Determination*, Clarendon Press, Oxford.

[39] English, C. A., and Venables, J. A., 1974, "The Structure of Diatomic Molecular Solids," Proc. R. Soc. London, **A340**, pp. 57–80.

Direct Numerical Simulation of Turbulent Flow Around a Rotating Circular Cylinder

Jong-Yeon Hwang

Kyung-Soo Yang
e-mail: ksyang@inha.ac.kr

Department of Mechanical Engineering,
Inha University,
Incheon, 402-020,
Korea

Klaus Bremhorst
Division of Mechanical Engineering,
The University of Queensland,
Brisbane Qld 4072,
Australia

Turbulent flow around a rotating circular cylinder has numerous applications including wall shear stress and mass-transfer measurement related to the corrosion studies. It is also of interest in the context of flow over convex surfaces where standard turbulence models perform poorly. The main purpose of this paper is to elucidate the basic turbulence mechanism around a rotating cylinder at low Reynolds numbers to provide a better understanding of flow fundamentals. Direct numerical simulation (DNS) has been performed in a reference frame rotating at constant angular velocity with the cylinder. The governing equations are discretized by using a finite-volume method. As for fully developed channel, pipe, and boundary layer flows, a laminar sublayer, buffer layer, and logarithmic outer region were observed. The level of mean velocity is lower in the buffer and outer regions but the logarithmic region still has a slope equal to the inverse of the von Karman constant. Instantaneous flow visualization revealed that the turbulence length scale typically decreases as the Reynolds number increases. Wavelet analysis provided some insight into the dependence of structural characteristics on wave number. The budget of the turbulent kinetic energy was computed and found to be similar to that in plane channel flow as well as in pipe and zero pressure gradient boundary layer flows. Coriolis effects show as an equivalent production for the azimuthal and radial velocity fluctuations leading to their ratio being lowered relative to similar nonrotating boundary layer flows. [DOI: 10.1115/1.2375133]

Keywords: rotating circular cylinder, turbulence, direct numerical simulation

1 Introduction

Turbulent flow around a rotating circular cylinder has a variety of applications including wall shear stress and mass-transfer measurement related to the corrosion studies [1–5] but is also of interest in the context of flow over convex surfaces where standard turbulence models perform poorly [6]. The present interest is in flow-affected corrosion where high Schmidt numbers, typically greater than 1000, are involved. It is generally accepted that in this case the diffusion layer, where the bulk of the resistance to mass transfer exists, lies within the laminar sublayer characterized by a velocity profile which varies linearly with the distance from the wall [7,8]. The geometrical configuration of the flow is rather simple; it has two homogeneous directions just like plane channel flow. Furthermore, the curvature introduced by the cylinder surface may significantly affect the turbulence structure in the vicinity of the cylinder [9]. Consequently, there is a lack of detail of the flow field over the geometry on which corrosion is to be predicted. This provides the motivation to understand turbulence structure and flow mechanisms associated with this flow. However, little work has been done on this topic mainly due to the inherent difficulty of instantaneous flow measurement in the thin wall layer of a rotating cylinder surface. It is also a region of the flow which is not readily accessible with turbulence models thus leaving DNS as the only viable means of investigation.

With the advancement of computer technology, numerical investigations of the mechanism of turbulence began to attract researchers' attention. Early numerical studies concentrated on modeling Reynolds stress terms created in the ensemble-averaged Navier-Stokes (NS) equations. However, significant amounts of data were required to determine reliable model coefficients.

With the recent development of high-performance computers and efficient numerical algorithms, direct numerical simulation (DNS) can solve the NS equation directly without modeling the Reynolds stresses. For initial studies using DNS, a computational investigation of turbulent channel flow was carried out about 20 years ago [10–12]. Especially, turbulence statistics that were obtained by Kim et al. [11] enabled many researchers to understand turbulence more clearly. Mansour et al. [12] computed the budgets for the Reynolds stresses and for the dissipation rate of the turbulence kinetic energy by using the DNS data of turbulent channel flow. Spalart [13] performed DNS for the turbulent boundary layer on a flat plate with zero pressure gradient, and Chung et al. [14] carried out DNS of turbulent concentric annular pipe flow. Turbulent flow over a backward-facing step was studied by Le et al. also using DNS [15]. Closely related works are those [16,17] for flow in the confined space between a rotating inner cylinder and a stationary outer one but these lead to turbulent Taylor-Couette flow for which a well defined vortex pair exists within the space.

In the present study, DNS of turbulent flow around a rotating circular cylinder was performed. This flow configuration can be fundamentally important as an effective model for studying turbulence as well as turbulence models although the latter aspect is not being pursued in the present study. Recently, turbulent flow around a rotating cylinder with two backward-facing steps mounted axisymmetrically with respect to the axis of rotation was investigated using DNS by Yang et al. [18,19], who obtained results that were in good agreement with their experimental result. However, to the best of our knowledge, there have been no in-depth studies of the mechanism and structure of turbulence around smooth rotating surfaces. In the present study, turbulence structure and turbulence kinetic energy budgets are investigated by using highly resolved DNS for three Reynolds numbers, $\mathrm{Re}_R^*=161$, 348, and 623, based on the cylinder radius R and friction velocity (u^*).

Contributed by the Fluids Engineering Division of ASME for publication in the JOURNAL OF FLUIDS ENGINEERING. Manuscript received June 16, 2005; final manuscript received June 13, 2006. Assoc. Editor: Ugo Piomelli.

The main purpose is to elucidate the basic turbulence mechanism around a rotating cylinder to provide a better understanding of flow fundamentals.

2 Formulation and Numerical Methods

The governing incompressible continuity and momentum equations are

$$\nabla \cdot \boldsymbol{u} = 0, \tag{1}$$

$$\frac{\partial \boldsymbol{u}}{\partial t} + (\boldsymbol{u} \cdot \nabla)\boldsymbol{u} = -\frac{1}{\rho}\nabla P + \nu \nabla^2 \boldsymbol{u} - 2\boldsymbol{\Omega} \times \boldsymbol{u} \tag{2}$$

where $\boldsymbol{u}$, ρ, and ν denote velocity, density, and kinematic viscosity of the fluid, respectively. The last term in Eq. (2) represents the Coriolis force in the reference frame rotating at constant angular velocity ($\boldsymbol{\Omega}$) with the cylinder. Since the centrifugal force is conservative, it is included in the pressure term, and does not affect the velocity field [20]. Thus, P in Eq. (2) includes not only pressure but also the centrifugal potential.

The governing equations are discretized by using a finite-volume method for a generalized coordinate system. Spatial discretization is second-order accurate. A hybrid scheme is used for time advancement; nonlinear terms are explicitly advanced by a third-order Runge-Kutta scheme, and the other terms are implicitly advanced by the Crank-Nicolson scheme. A fractional step method [21] is employed to decouple the continuity and momentum equations. The resulting Poisson equation is solved by a multigrid method. Details of the numerical algorithm used in the code follow Rosenfeld et al. [21].

3 Choice of Parameters and Boundary Conditions

The cylinder radius is 0.01 m, and the outer boundary of the computational domain is located 0.07 m from the axis of rotation, Fig. 1(*a*). The spanwise size (W) of the domain is 0.024 m at rpm=200 and 500, and 0.012 m at rpm=1,000. The spanwise length is large enough to contain the longest wavelength of turbulence in the spanwise direction. A body-fitted O-type grid system is employed, and the number of computational cells determined by a grid-refinement study is $128 \times 96 \times 256$ in the azimuthal (S), radial (r or y), and spanwise (z) directions, respectively, Fig. 1(*b*). The minimum grid sizes in S and r directions are $\Delta S^+_{\min}=17.8$ and $\Delta r^+_{\min}=0.09$, respectively, for rpm=500; the grid size in z direction is $\Delta z^+=3.3$ ($\Delta z^+=2.9$ for rpm=1000). They are quite small compared with those of turbulent channel flow [11], and were verified for adequacy by grid refinement. One-dimensional energy spectra were computed and found to drop by at least three decades at the high wave numbers. The periodic boundary condition is employed in the homogeneous spanwise direction. The outer boundary condition needs special attention. To minimize computational costs, a proper boundary condition is employed as suggested by Yang et al. [18]. That is

$$\frac{\partial u}{\partial r} = \Omega, \quad v = 0, \quad \frac{\partial w}{\partial r} = 0 \tag{3}$$

where u, v, and w represent the azimuthal, normal, and spanwise velocity components, respectively. This outer boundary condition enables use of a reasonably small computational domain in the radial direction. The use of this boundary condition contrasts with the shear outer boundary used by Bilson and Bremhorst [16,17] which leads to vortical flows in the enclosed space. The advantage of the present outer boundary condition is that no shear effects are generated at that boundary.

Table 1 shows the computed mean flow parameters, where U_i and u^* denote the rotating speed of the cylinder measured at the cylinder surface and the friction velocity, respectively. Re_R is the Reynolds number based on the cylinder radius R and U_i while Re_R^* is based on R and u^*. As the transitional Re_R^* is 100, the flows at all three Reynolds numbers are expected to be fully turbulent [22].

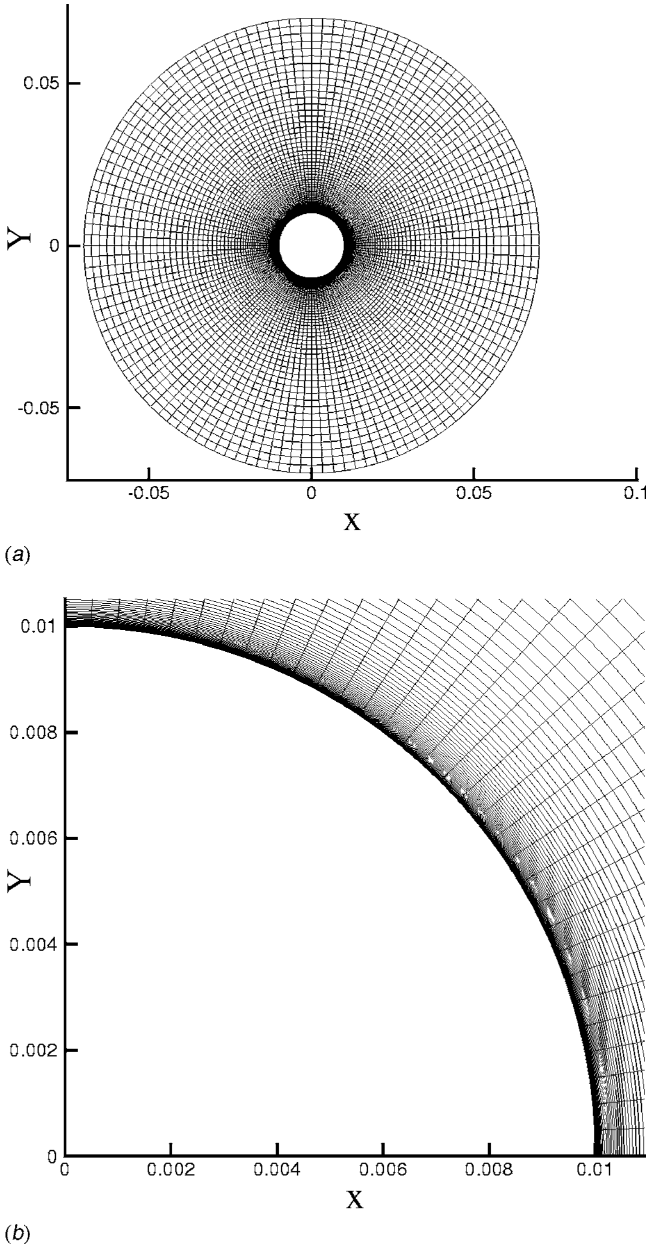

Fig. 1 Computational domain and grid system; (*a*) total view, (*b*) magnified view

Table 1 Mean flow parameters with respect to the rotating reference frame

Case	rpm	U_i	u^*	U_i/u^*	Re_R	Re_R^*	Ro
1	200	0.21	0.019	11.1	1810	161	0.5
2	500	0.52	0.040	13.0	4480	348	0.5
3	1000	1.05	0.072	14.6	9050	623	0.5

4 Results and Discussion

4.1 Averaged Flow Field. After the flow reached statistically steady state, instantaneous flow fields were collected for statistical evaluation. Approximately 30,000 sample data were collected in

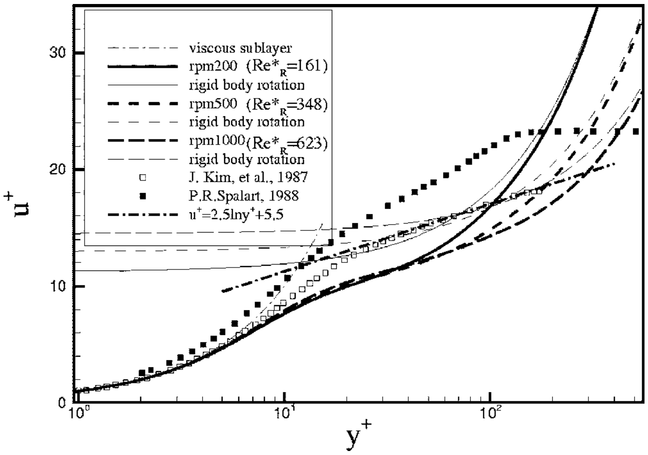

Fig. 2 Mean velocity profiles in the wall region

the homogenous streamwise and spanwise directions and 50 sample data in the time direction. Accordingly, more than 1.5 million data samples were collected.

Figure 2 shows the averaged velocity profiles in the wall region in wall units for the three cases of Reynolds number. A viscous sublayer exists at $0<y^+<5$ where viscosity is important and the turbulent stresses are smaller than those in other regions. Moreover, the three rotational speeds show no Reynolds number dependence. Present results are quite similar to those of the turbulent channel flow [11], turbulent pipe flow [23], and turbulent boundary-layer flow over a flat plate [13]. This similarity is due to the fact that these flows are dominated by viscosity and not the outer flow. The buffer layer corresponds to the range, $5<y^+<20$ where good agreement of velocity profiles is noticed for the three different rpm with only a small difference for the lower Reynolds number. However, the magnitude of the normalized streamwise mean velocity is smaller than that of the turbulent channel or boundary layer flow. The fully turbulent region is in $20<y^+<400$, where the turbulent stresses and fluxes are more important than in the region of the viscous sublayer. As y^+ increases beyond $y^+=400$, the velocity profile asymptotically approaches the motion of rigid body rotation, corresponding to each rotating speed. In the region $20<y^+<70$ as seen in the rotating reference frame, a logarithmic region is noted for the two higher Reynolds numbers with a slope approximately equal to the inverse of the von Karman constant as found in the flat plate, channel, and pipe flows. The difference in level of the log law given by the constant 5.5 for these flows is merely a reflection of the effective origin of the logarithmic region. In the present case, the smaller extent of the buffer layer relative to that found in these other flows and as seen in Fig. 2, leads to a lower level for the logarithmic line.

Root mean square (rms, denoted by $\langle\rangle$) velocity fluctuations normalized by friction velocity in the vicinity of the cylinder surface are displayed in Fig. 3 for rpm=500 compared with those of the turbulent channel [11] and boundary layer flow [13]. The trends are similar. However, the magnitude of streamwise rms velocity fluctuations is smaller than that of the turbulent channel or boundary layer flow near the cylinder surface leading to a smaller ratio of $\overline{u'^2}/\overline{v'^2}$. As for channel and pipe flows, the value of $\langle u'\rangle$ is greater than those of other components while $\langle v'\rangle$ is negligibly small near the wall with the slope in the radial direction of $\langle v'\rangle$ being zero at the wall.

Figures 4(*a*) and 4(*b*) present two-point correlations for rpm =500 of the three fluctuating velocity components in the streamwise direction and spanwise direction, respectively, at $y^+=10.5$. In Fig. 4(*a*), the correlation value falls off to zero within 450 wall units, corresponding to 75 deg in the circumferential direction which means that the largest eddies occupy less than one quadrant of the flow domain. Figure 4(*b*) shows that the correlation values in the spanwise direction fall off to zero within $z^+=100$, approximately corresponding to 11% of the spanwise computational do-

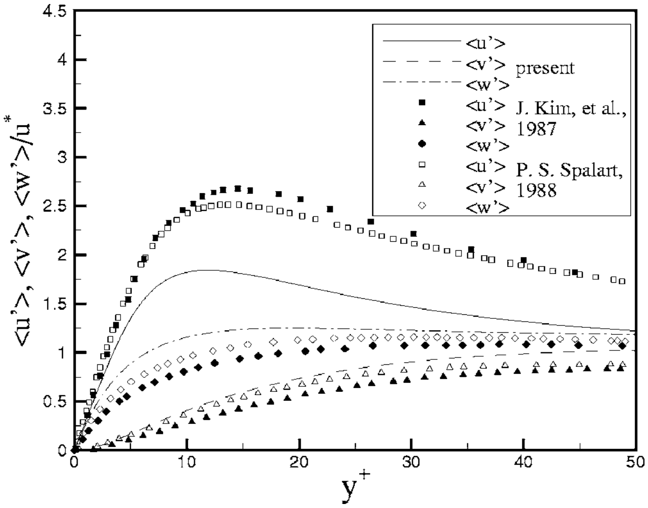

Fig. 3 Rms velocity fluctuations normalized by friction velocity in the wall region at rpm=500

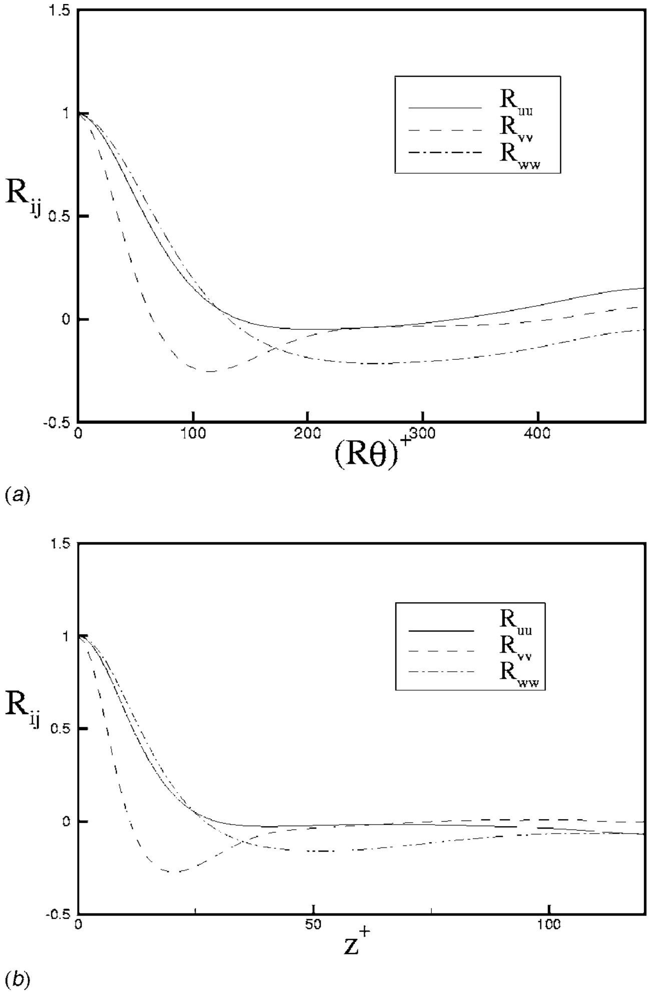

(*a*)

(*b*)

Fig. 4 Two point correlation coefficients at rpm=500; (*a*) azimuthal separations, (*b*) spanwise separations

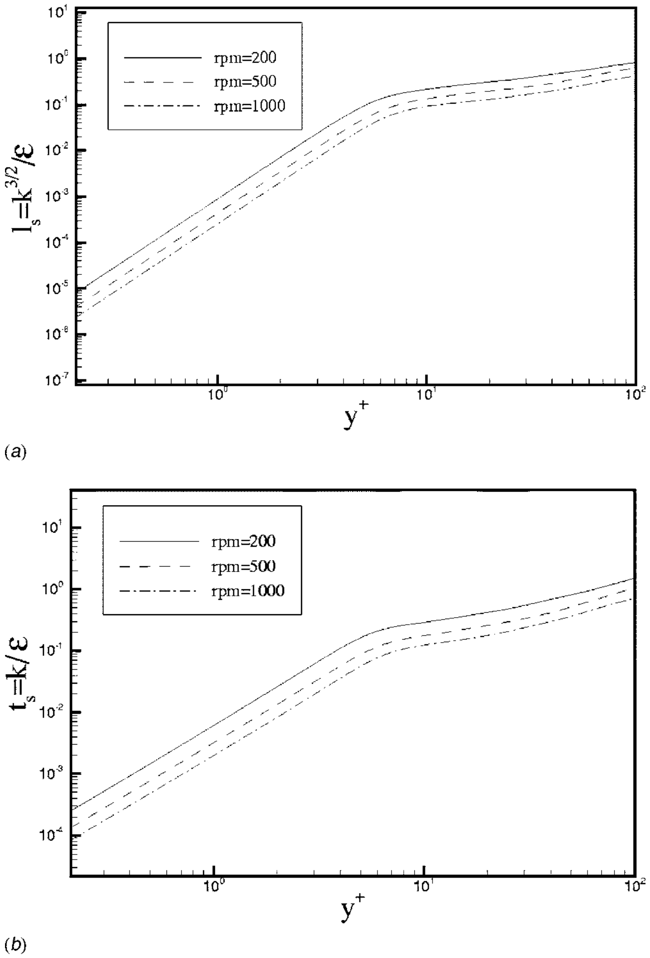

Fig. 5 Turbulence length and time scales in the wall region at three cases of rpm; (*a*) turbulence length scale, (*b*) turbulence time scale

main. This confirms that the spanwise computational domain is sufficiently large to contain the largest eddies. The spanwise wavelength of the streamwise velocity fluctuation (u') is about two times longer than that of the radial velocity fluctuation (v') as can be identified from the spanwise correlation coefficients (R_{uu}, R_{vv}) in Fig. 4(*b*).

Figures 5(*a*) and 5(*b*) show turbulence length scale (l_s) and turbulence time scale (t_s) in the wall region for three different rpm, respectively. These are defined by using the turbulent kinetic energy (k) and dissipation rate (ε) as follows:

$$l_s = k^{3/2}/\varepsilon, \quad t_s = k/\varepsilon \tag{4}$$

where k and ε are defined as

$$k = \tfrac{1}{2}(\overline{u_i' u_i'}), \quad \varepsilon = \tfrac{1}{2}\varepsilon_{ii} \tag{5}$$

where $\varepsilon_{ii}=2\nu\overline{(\partial u_i'/\partial x_k)(\partial u_i'/\partial x_k)}$ and repeated indices follow the summation convention.

These length and time scales decrease in a consistent manner with increasing rpm. As y^+ approaches the cylinder surface, both l_s and t_s gradually decrease, and then their slopes suddenly change in the buffer layer at the edge of the viscous sublayer for all three cases. It is conjectured that this trend is mainly due to the sudden change of the rms velocity fluctuations in that region, Fig. 3, and is probably associated with the sweeps and ejections usually found in the turbulent wall layer up to $y^+=15$ [24].

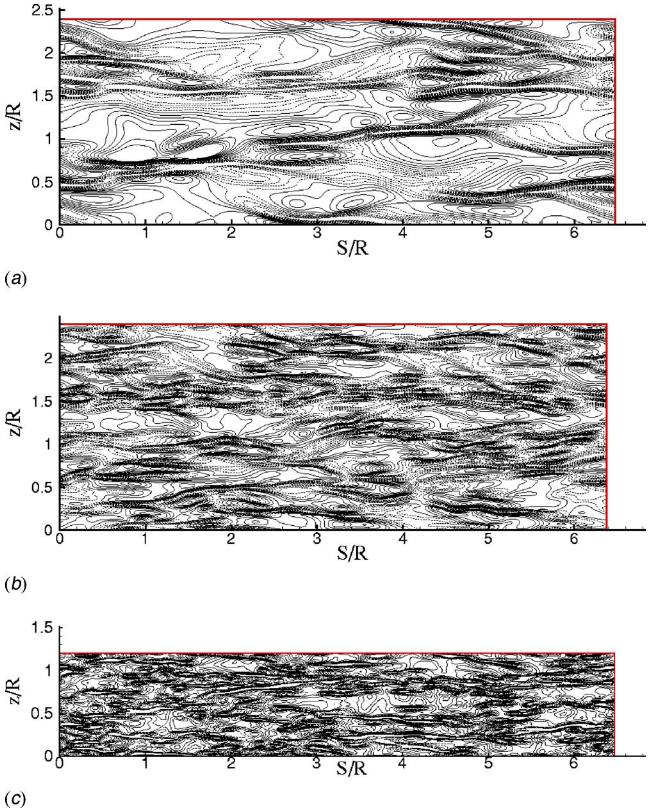

Fig. 6 Instantaneous contours of streamwise velocity fluctuation at various rpm; solid and dotted lines denote positive and negative values, respectively, and increment is 0.4; (*a*) rpm =200, (*b*) rpm=500, and (*c*) rpm=1000

4.2 Instantaneous Flow Field. Figure 6 shows instantaneous contours of the streamwise velocity fluctuation on the *S*-*z* surface at $y^+=10$ for various rpm. As the rpm increases, the length scales in the circumferential and spanwise directions decrease, and streaks are clearly noticed in the streamwise direction. Particularly, in Fig. 6(*b*) at rpm=500, the length scales in the circumferential and spanwise directions are about 300–350 and 100 based on the wall unit, respectively; these length scales are approximately consistent with those inferred from the two-point correlations indicated in Fig. 4. The contours of flow away from the wall $(v'>0)$ and towards it $(v'<0)$ are consistent with the streaky structure associated with the ejections and sweeps observed in other turbulent wall layers [24].

Severe intermittency, three-dimensionality, and a wide range of turbulent length scales of flow structures limit spectrum analysis using Fourier transform theories. Therefore, in the present study, spectrum analysis using wavelet transform is carried out to elucidate the spatial characteristics of single turbulence events such as sweeps, ejections, and individual vortices or vortical structures more clearly [25–28].

Wavelet transform is a recently developed mathematical technique, allowing one to transform a field into both space and time scale on a more localized basis. This gives a more direct indication of the extent of structures and also of their frequency content. In its generalized form, the wavelet transform of the real-valued signal function $f(x)$ with respect to the complex valued wavelet $\Psi(T)$ is defined by Eq. (6).

$$Wf(a,b) = \frac{1}{\sqrt{|a|}}\int_{-\infty}^{\infty} f(x)\Psi^*(T)dx \tag{6}$$

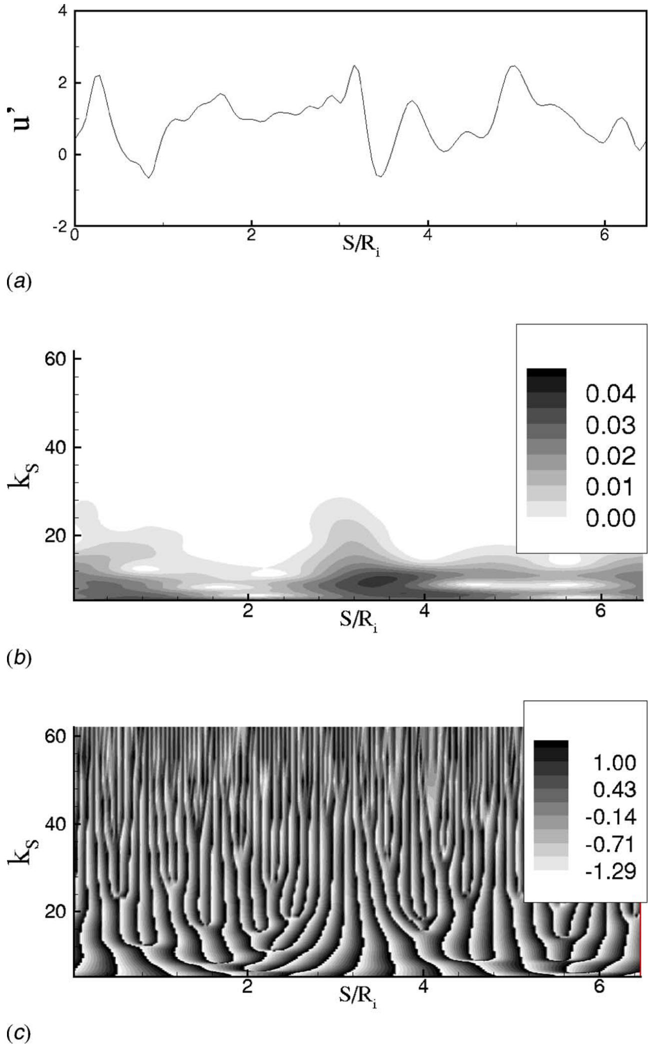

Fig. 7 Wavelet transform of *u′* in the azimuthal direction at y^+=10 for rpm=500; (*a*) signal along *s*, (*b*) contours of modulus, and (*c*) contours of phase

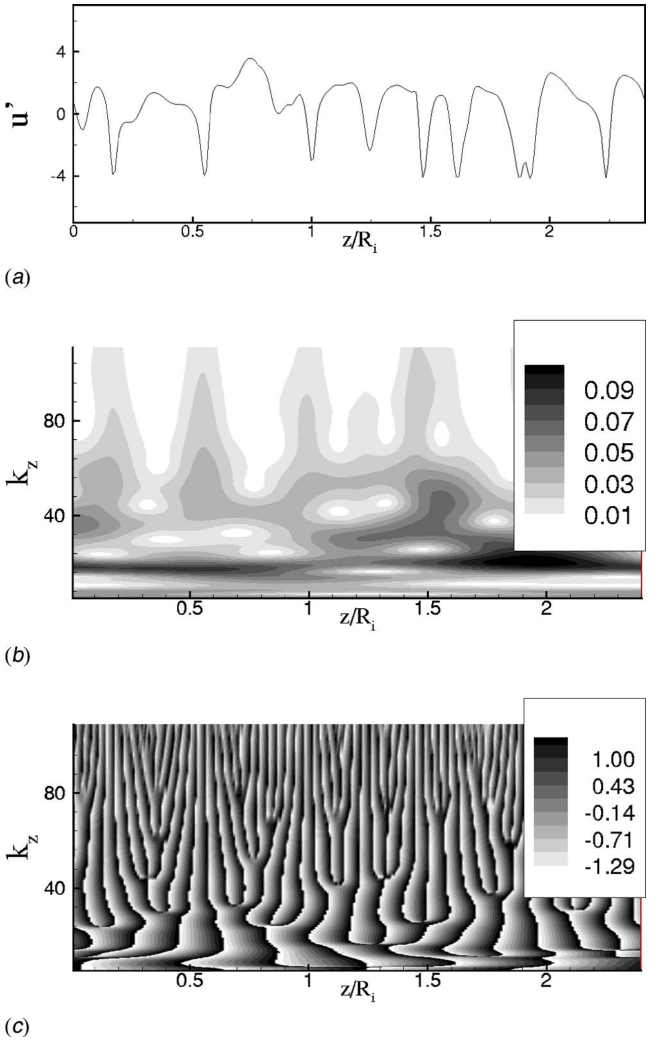

Fig. 8 Wavelet transform of *u′* in the spanwise direction at y^+=10 for rpm=500; (*a*) signal along *z*, (*b*) contours of modulus, and (*c*) contours of phase

$$T=(x-b)/a \tag{7}$$

where $Wf(a,b)$ is the coefficient of wavelet, a is a scale dilation parameter, b is a translation parameter, and Ψ^* is the complex conjugate of the wavelet function. Accordingly, wavelet coefficient $Wf(a,b)$ can be interpreted as the relative contribution of the scale a to the signal at the location b; the wave number at a local position corresponds to the inverse value of scale a. The most commonly used wavelet is the Morlet wavelet $\Psi(T)$ defined as [29]

$$\Psi(T)=\exp(\hat{k}Ti)\exp(-T^2/2) \tag{8}$$

where $\hat{k}$ (=6 for the present study) denotes a plane wave of the wave vector modulated by a Gaussian envelope of unit width. From the complex-valued wavelet coefficients, one can obtain the modulus Wf_M, meaning the energy density, defined as

$$Wf_M=\sqrt{(Wf_R)^2+(Wf_I)^2} \tag{9}$$

where Wf_R and Wf_I are the real and imaginary parts of Wf, respectively. Therefore, Wf_M in a specified direction represents the envelope line of maximum Wf_R [26].

Figures 7(*a*) and 7(*b*) represent the time signal function at y^+ =10 along the direction S and contours of Wf_M, respectively. The dominant wave number is approximately 10 as identified by the larger values of Wf_M. Figure 7(*c*) shows the contours of phase (Wf_P) of Wf_R and Wf_I, defined as

$$Wf_P=\tan^{-1}\left(\frac{Wf_I}{Wf_R}\right). \tag{10}$$

By examining the contours of Wf_p, a wide range of length scales of u' in space can be identified. A cone of influence [28], associated with the major event in the u' signal, Fig. 7, can be seen at S/R_i=3.3–3.4, and is also reflected in the larger values of the modulus contours at the same S/R_i. The alignment in phase of the small scales with the large scale event (large k_S) is readily seen. A similar pattern is seen at S/R_i=0.2.

Wavelet transform of u' in the spanwise direction at y^+=10 for rpm=500 is shown in Fig. 8. The dominant waves with wave numbers of 7–10 appear more evenly in the spanwise direction compared to that in the azimuthal direction (Fig. 7). However, waves associated with sharp negative peaks seen in Fig. 8(*a*) lead to high wave numbers of well above 40 which occur intermittently in the spanwise direction. Computationally, this means that a significant number of grid points are required in the spanwise direction to capture these flow events. Actually, the grid-refinement study showed that flow properties are quantitatively sensitive to the resolution in the spanwise direction. The u' signal trace of Fig. 8(*a*) shows major events of closer spacing than that of Fig. 7(*a*). These events are also reflected in the modulus and phase of the wavelet transform and are indicative of the streaky structure [11] seen in Fig. 6.

4.3 Turbulent Kinetic Energy Budget. In turbulence modeling, the various terms in the Reynolds-stress transport equations (RSE) must be modeled. Durbin and Pettersson Rief [30] modified the ε-equation by introducing dependency on rotational effects. Such modeling is unnecessary with DNS as these terms can be computed explicitly. In the present study, the basic mean flow (U), which has only the circumferential mean velocity component, is homogeneous in the axial and circumferential directions. Therefore, the budgets of the Reynolds stresses and the turbulent kinetic energy can be given as follows:

$$\overline{u'^2}-\text{budget}$$

$$0=\underbrace{-2\left[\overline{u'v'}\frac{dU}{dr}+\frac{\overline{u'v'}}{r}U\right]}_{P_{11}}\underbrace{-\left[\frac{1}{r}\frac{\partial r\overline{u'u'v'}}{\partial r}+\frac{2\overline{u'u'v'}}{r}\right]}_{T_{11}}$$

$$\underbrace{+\nu\left[\frac{1}{r}\frac{\partial}{\partial r}\left(r\frac{\partial\overline{u'u'}}{\partial r}\right)+\frac{2}{r^2}(\overline{v'^2}-\overline{u'^2})\right]}_{D_{11}}$$

$$\underbrace{-\frac{2}{\rho r}\overline{u'\frac{\partial p'}{\partial\theta}}}_{\Pi_{11}}+\underbrace{4\Omega\overline{u'v'}}_{C_{11}}\underbrace{-2\nu\left[\overline{\left(\frac{\partial u'}{\partial\theta}+v'\right)^2}\frac{1}{r^2}+\overline{\left(\frac{\partial u'}{\partial r}\right)^2}+\overline{\left(\frac{\partial u'}{\partial z}\right)^2}\right]}_{\varepsilon_{11}} \tag{11}$$

$$\overline{v'^2}-\text{budget}$$

$$0=\underbrace{4\frac{\overline{u'v'}}{r}U}_{P_{22}}\underbrace{-\left[\frac{1}{r}\frac{\partial r\overline{v'v'v'}}{\partial r}-\frac{2\overline{u'u'v'}}{r}\right]}_{T_{22}}$$

$$\underbrace{+\nu\left[\frac{1}{r}\frac{\partial}{\partial r}\left(r\frac{\partial\overline{v'v'}}{\partial r}\right)+\frac{2}{r^2}(\overline{u'^2}-\overline{v'^2})\right]}_{D_{22}}$$

$$\underbrace{-\frac{2}{\rho}\overline{v'\frac{\partial p'}{\partial r}}}_{\Pi_{22}}\underbrace{-4\Omega\overline{u'v'}}_{C_{22}}\underbrace{-2\nu\left[\overline{\left(\frac{\partial v'}{\partial\theta}-u'\right)^2}\frac{1}{r^2}+\overline{\left(\frac{\partial v'}{\partial r}\right)^2}+\overline{\left(\frac{\partial v'}{\partial z}\right)^2}\right]}_{\varepsilon_{22}} \tag{12}$$

$$\overline{w'^2}-\text{budget}$$

$$0=\underbrace{-\frac{1}{r}\frac{\partial r\overline{w'w'v'}}{\partial r}}_{T_{33}}\underbrace{+\nu\frac{1}{r}\frac{\partial}{\partial r}\left(r\frac{\partial\overline{w'w'}}{\partial r}\right)}_{D_{33}}\underbrace{-\frac{2}{\rho}\overline{w'\frac{\partial p'}{\partial z}}}_{\Pi_{33}}$$

$$\underbrace{-2\nu\left[\overline{\left(\frac{\partial w'}{\partial\theta}\right)^2}\frac{1}{r^2}+\overline{\left(\frac{\partial w'}{\partial r}\right)^2}+\overline{\left(\frac{\partial w'}{\partial z}\right)^2}\right]}_{\varepsilon_{33}} \tag{13}$$

$$k-\text{budget}$$

$$0=\underbrace{-\left[\overline{u'v'}\frac{dU}{dr}-\frac{\overline{u'v'}}{r}U\right]}_{P_k}\underbrace{-\frac{1}{r}\frac{\partial r\overline{v'k'}}{\partial r}}_{T_k}\underbrace{+\nu\frac{1}{r}\frac{d}{dr}\left(r\frac{d\overline{k'}}{dr}\right)}_{D_k}$$

$$\underbrace{-\frac{1}{\rho}\left[\overline{\frac{u'}{r}\frac{\partial p'}{\partial\theta}}+\overline{v'\frac{\partial p'}{\partial r}}+\overline{w'\frac{\partial p'}{\partial z}}\right]}_{\Pi_k}-\varepsilon \tag{14}$$

where the terms in the right-hand sides of (11)–(14) denote the production rate (P), turbulent transport rate (T), viscous diffusion rate (D), velocity pressure-gradient term (Π), Coriolis term (C), dissipation rate term (ε), and k' denotes the instantaneous turbulent kinetic energy. These transport equations are nondimensionalized with u^{*4}/ν. The velocity pressure-gradient term is presented consistent with the approach described by Mansour et al. [12]. The turbulent kinetic energy budget, Eq. (14), is simply half the sum of the normal stress components of Eqs. (11)–(13). It is noteworthy that the Coriolis component does not appear in the $\overline{w'^2}$ budget as it can only occur when a radial movement of fluid is involved. Consequently, the term is equal and opposite in Eqs. (11) and (12) to denote a simple interchange of energies. The effect is similar to production with C_{11} in Eq. (11) reducing production of the azimuthal velocity fluctuation while in Eq. (12) C_{22} increases production of the radial velocity fluctuation.

Figures 9(*a*)–9(*c*) show the turbulent kinetic energy budget for the three different rotational speeds and Fig. 9(*d*) gives the ratio of production to dissipation rate for the three cases. Comparison with DNS and experimental data of Mansour et al. [12], Spalart [13], and Laufer [23] shows that the trends of different components contributing to the transport of k are similar. Production peaks in the region $y^+=10-15$. In each of these cases viscous diffusion has a maximum loss between $y^+=5-10$ and rises to a maximum gain at the wall. Below $y^+\sim 8$ dissipation rate in all cases rises rapidly to a maximum at the wall and is balanced by viscous diffusion.

Turbulent transport of k is significant only in the region $y^+=5-15$ where it changes from a loss to a gain as the wall is approached. In all cases, the pressure related terms are negligible. In the region $y^+>30$, only production and dissipation rate remain significant and are in equilibrium as seen from Fig. 9(*d*). At the smallest Reynolds number (rpm) a small excess of dissipation rate over production is noted. This can be attributed to the fact that the flow is only just above transition to turbulent flow. The maximum of production relative to dissipation rate, Fig. 9(*d*), near $y^+=8-10$ is consistent with boundary layer, channel, and pipe flows. The data of Figs. 9(*a*)–9(*c*), although normalized on the shear velocity, indicate a Reynolds number dependence of magnitude of peaks and wall values for production and dissipation rate but location of the peaks is independent of Reynolds number.

In the present case Coriolis effects are present. Figure 10 shows the Coriolis terms in the Reynolds stress budgets of the fluctuating circumferential and radial velocity components for various values of rpm. The magnitude of C_{11} equals that of C_{22}, and their signs are opposite, as identified in Eqs. (11) and (12). As rpm increases, the magnitudes of C_{11} and C_{22} decrease but this is only due to the normalization used. The Coriolis terms were argued to affect production of $\overline{u'^2}$ and $\overline{v'^2}$ and this is the likely reason for the ratio of $\overline{u'^2}/\overline{v'^2}$ being just above unity at larger y^+ whereas values for other nonrotating boundary layers are typically twice this value and higher [13,23,24]. Coriolis terms are seen to be negligible in the laminar sublayer.

5 Conclusion

In the present study which is of particular relevance in the study of near wall effects such as met in flow affected corrosion, DNS of low Reynolds number turbulent flows around a rotating circular

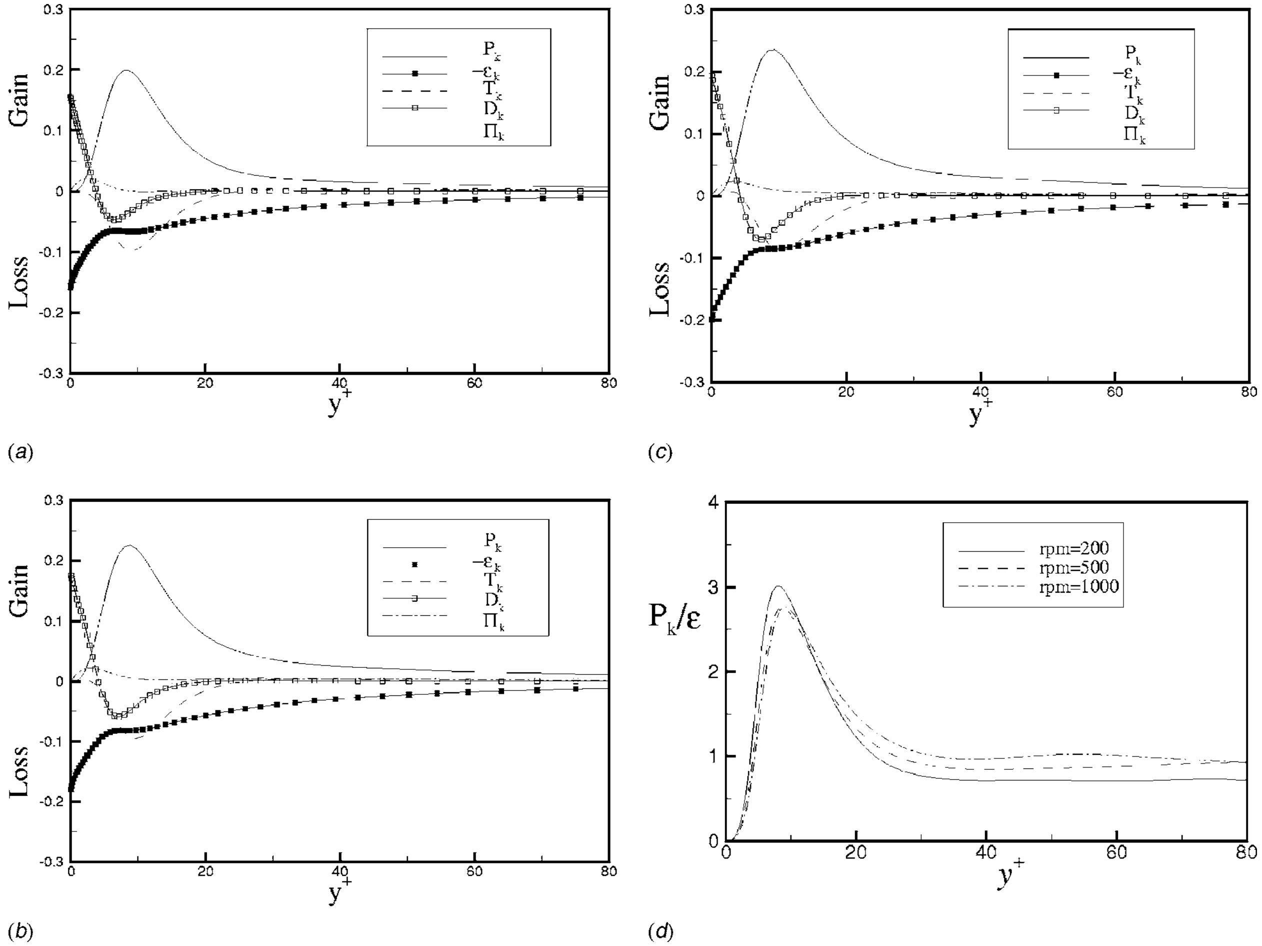

(*a*) (*c*)

(*b*) (*d*)

Fig. 9 Turbulent kinetic energy budget in the wall region; (*a*) rpm=200, (*b*) rpm=500, (*c*) rpm=1000, and (*d*) ratio of production of *k* relative to its dissipation rate

cylinder was performed. Turbulent structures in the flow are qualitatively similar to those of turbulent channel, pipe, and zero pressure gradient boundary layer flows, as confirmed by turbulence statistics but the streamwise turbulence level is lower and the ratio of streamwise to wall normal velocity fluctuation levels is also lower. Logarithmic layer with a slope of the inverse of the von Karman constant is found to exist with respect to the rotating reference frame.

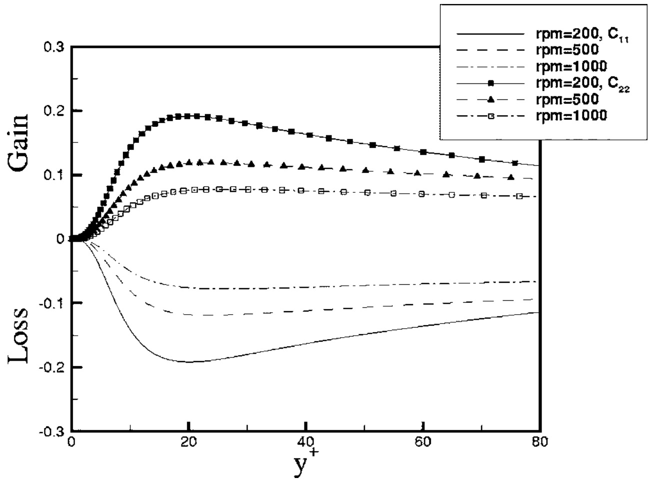

Fig. 10 Coriolis terms in the Reynolds stress budgets in the wall region

Wavelet transform was performed to examine the spatial and wave number characteristics of the turbulent coherent structures. The dominant waves with wave numbers of 7–10 appear more evenly in the spanwise direction than in the azimuthal (streamwise) direction. Moreover, high-wave number waves occur intermittently in the spanwise direction but not in the azimuthal direction thus showing that a wide range of turbulent length scales exists in the spanwise direction. Flow visualization plots indicate streaky structures similar to those found in the other wall flows with similar streamwise to lateral length ratios and are suggestive of the typical ejection and sweep dominated near wall flows. The spacing of these structures decreases as the rotational speed of the cylinder increases.

The terms in the transport equations for the Reynolds stresses and turbulent kinetic energy were computed by using DNS data produced in the present study. As Reynolds number (rpm) increases, so do the production and dissipation rates in the turbulent kinetic energy budget even though these are normalized with the shear velocity. While levels of the various turbulent kinetic energy budget terms differ from pipe, duct, and boundary layer flows, their ratios are similar, including the ratio of production to dissipation which tends to unity in the outer flow.

Coriolis effects are shown to be equivalent to additional production which leads to an effective reduction in the azimuthal velocity fluctuation relative to the radial one. Consequently, the ratio of the two is lower than for channel, pipe, and zero pressure gradient boundary layer flows. The normalized magnitudes of Coriolis terms in the Reynolds stress budgets decrease as rpm increases. They are significant in the bulk of the flow but become negligible in the laminar sublayer.

Acknowledgment

This work was supported by Inha University Research Grant.

Nomenclature

P = pressure (Pa)
R = cylinder radius (m)
Re_R = Reynolds number based on cylinder radius and the surface velocity of the cylinder ($=R^2\Omega/\nu$)
Re^* = Reynolds number based on friction velocity and cylinder radius ($=u^*R/\nu$)
Ro = Rossby number based on cylinder diameter and the surface velocity of the cylinder ($=U_i/2R\Omega=0.5$)
r = radial coordinate (m)
S = streamwise coordinate (m)
t = time (s)
U_i = surface velocity of the cylinder ($=R\Omega$), (m/s)
u = streamwise (circumferential) velocity (m/s)
u^* = friction velocity ($=\sqrt{\tau_w/\rho}$), (m/s)
u_i = velocity component (m/s)
v = radial velocity (m/s)
W = spanwise length of computational domain (m)
w = spanwise velocity (m/s)
y^+ = normalized distance from the wall ($=yu^*/\nu$)
y = distance from the wall (m)
z = spanwise coordinate (m)

Greek Letters

ν = kinematic viscosity (m^2/s)
ρ = density (kg/m^3)
Ω = angular velocity (s^{-1})

Superscripts

$-$ = time and spatial averaged quantity
$\prime$ = fluctuating value

Other Symbols

$\langle\rangle$ = rms averaged quantity

References

[1] Silverman, D. C., 1988, "Rotating Cylinder Electrode - Geometry Relationships for Prediction of Velocity-Sensitive Corrosion," Corrosion (Houston), **44**(1), pp. 42–49.
[2] Bienkowski, J., 1998, "A Rotating Cylinder Electrode With Surface Roughness," Honors thesis, Department of Mechanical Engineering, University of Queensland, Brisbane, Australia.
[3] Nesic, S., and Postlethwaite, J., 1990, "Relationship Between the Structure of Disturbed Flow and Erosion-Corrosion," Corrosion (Houston), **46**(11), pp. 874–880.
[4] Gabe, D. R., 1974, "The Rotating Cylinder Electrode," J. Appl. Electrochem., **4**(2), pp. 91–108.
[5] Gabe, D. R., and Walsh, F. C., 1983, "The Rotating Cylinder Electrode: A Review of Development," J. Appl. Electrochem., **13**(1), pp. 3–21.
[6] Pettersson, B. A., Andersson, H. I., and Hjelm-Larsen, 1996, "Analysis of Near-Wall Second Moment Closures Applied to Flows Affected by Streamline Curvature," *Engineering Turbulence Modelling and Experiments 3*, W. Rodi and G. Bergeles, eds., Elsevier, New York.
[7] Levich, V. G., 1962, *Physicochemical Hydrodynamics*, Prentice-Hall, Inc., New Jersey, p. 59.
[8] Hanratty, T., and Campbell, J., 1996, "Measurements of Wall Shear Stress," *Fluid Mechanics Measurements*, R. Goldstein, ed., Taylor and Francis, Washington, D.C., pp. 575–648.
[9] Hebrard, J., Metais, O., and Salinas-Vasquez, M., 2004, "Large-Eddy Simulation of Turbulent Duct Flow: Heating and Curvature Effects," Int. J. Heat Fluid Flow, **25**(4), pp. 569–580.
[10] Moin, P., and Kim, J., 1982, "Numerical Investigation of Turbulent Channel Flow," J. Fluid Mech., **118**, pp. 341–377.
[11] Kim, J., Moin, P., and Moser, R., 1987, "Turbulence Statistics in Fully Developed Channel Flow at Low Reynolds Number," J. Fluid Mech., **177**, pp. 133–166.
[12] Mansour, N. N., Kim, J., and Moin, P., 1988, "Reynolds-Stress and Dissipation-Rate Budgets in a Turbulent Channel Flow," J. Fluid Mech., **194**, pp. 15–44.
[13] Spalart, P. R., 1988, "Direct Simulation of a Turbulent Boundary Layer up to $R_\theta=1410$," J. Fluid Mech., **187**, pp. 61–98.
[14] Chung, S. Y., Rhee, G. H., and Sung, H. J., 2002, "Direct Numerical Simulation of Turbulent Concentric Annular Pipe Flow, Part 1: Flow Field," Int. J. Heat Fluid Flow, **23**, pp. 426–440.
[15] Le, H., Moin, P., and Kim, J., 1997, "Direct Numerical Simulation of Turbulent Flow Over a Backward-Facing Step," J. Fluid Mech., **330**, pp. 349–374.
[16] Bilson, M., and Bremhorst, K., 2003, "Comparison of Turbulent Scalar Transport in a Pipe and a Rotating Cylinder," 3rd International Conference on CFD in the Minerals and Process Industries, CSIRO, Melbourne, CSIRO Australia.
[17] Bilson, M., and Bremhorst, K., 2004, "DNS Study of the Instantaneous and Mean Flow on Scalar Transport in Turbulent Taylor-Couette Flow," 11th International Symposium on Flow Visualization, University of Notre Dame, Indiana, USA, Optimage Ltd, Edinburgh, UK.
[18] Yang, K.-S., Hwang, J.-Y., Bremhorst, K., and Nesic, S., 2003, "Numerical Investigation of Turbulent Flow Around a Rotating Stepped Cylinder for Corrosion Study," Can. J. Chem. Eng., **81**(1), pp. 26–36.
[19] Yang, K.-S., Hwang, J.-Y., Bremhorst, K., and Nesic, S., 2002, "Turbulent Flow Around a Rotating Stepped Cylinder," Phys. Fluids, **14**(4), pp. 1544–1547.
[20] Lezius, D. K., and Johnston, J. P., 1976, "Roll-Cell Instabilities in Rotating Laminar and Turbulent Channel Flow at Low Reynolds Number," J. Fluid Mech., **177**, pp. 153–175.
[21] Rosenfeld, M., Kwak, D., and Vinkur, M., 1994, "A Fractional Step Solution Method for the Unsteady Incompressible Navier-Stokes Equations in Generalized Coordinate Systems," J. Comput. Phys., **94**, pp. 102–137.
[22] Nesic, S., Bienkowski, J., Bremhorst, K., and Yang, K.-S., 2000, "Testing for Erosion-Corrosion Under Disturbed Flow Conditions Using a Rotating Cylinder With a Stepped Surface," Corrosion (Houston), **56**(10), pp. 1005–1014.
[23] Laufer, J., 1954, "The Structure of Turbulence in Fully Developed Pipe Flow," NACA TN1174.
[24] Hinze, J. O., 1975, *Turbulence*, 2nd Ed., McGraw-Hill, New York.
[25] Farge, M., 1992, "Wavelet Transforms and Their Applications to Turbulence," Annu. Rev. Fluid Mech., **24**, pp. 395–457.
[26] Jang, C. M., Furukawa, M., and Inoue, M., 2003, "Frequency Characteristics of Fluctuating Pressure on Rotor Blade in a Propeller Fan," JSME Int. J., Ser. A, **46**(1), pp. 163–172.
[27] McClusky, H. L., Holloway, M. V., Beasley, D. E., and Ochterbeck, J. M., 2002, "Continuous Wavelet Transforms of Instantaneous Wall Pressure in Slug and Churn Upward Gas-Liquid Flow," J. Fluids Eng., **124**, pp. 625–633.
[28] Lau, K.-M., and Weng, H., 1995, "Climate Signal Detection Using Wavelet Transform: How to Make a Time Series Sing," Bull. Am. Meteorol. Soc., **76**(12), pp. 2391–2395.
[29] Morlet, J., Arens, G., Fourgeau, I., and Giard, D., 1982, "Wave Propagation and Sampling Theory," Geophysics, **47**, pp. 203–236.
[30] Durbin, P. A., and Pettersson Reif, B. A., 2001, *Statistical Theory and Modeling for Turbulent Flows*, Wiley, Chichester, West Sussex, UK.

Ryo Morita
Fumio Inada
CRIEPI

Michitsugu Mori
Kenichi Tezuka
TEPCO

Yoshinobu Tsujimoto
Osaka Univ.

CFD Simulations and Experiments of Flow Fluctuations Around a Steam Control Valve

Under certain opening conditions (partial opening) of a steam control valve, the piping system in a power plant occasionally experiences large vibrations. To understand the valve instability that is responsible for such vibrations, detailed experiments and CFD calculations were performed. As a result of these investigations, it was found that under the middle-opening (partial opening) condition, a complex three-dimensional (3D) flow structure (valve-attached flow) sets up in the valve region leading to a high pressure region on a part of the valve body. As this region rotates circumferentially, it causes a cyclic asymmetric side load on the valve body, which is considered to be the cause of the vibrations. [DOI: 10.1115/1.2375123]

Keywords: control valve, middle-opening, CFD, supersonic flow, valve-attached flow

1 Introduction

In some cases, a steam control valve (Fig. 1) in a power plant causes large vibrations in the piping system that can be attributed to fluctuations generated in the valve under the partial-valve-opening (middle-opening) condition. For the maintenance and the management of the plant, the valve system needs to be improved to prevent the onset of hydrodynamic instabilities. However, in the case of the steam control valve, it is difficult to understand the flow characteristics in detail experimentally because the flow around the valve has a complex 3D structure and becomes supersonic ($M > 1$). For these reasons, the details of the flow around the valve are not fully understood and CFD simulations are required to understand the underlying complex flow structure associated with the valve.

In the past, Jibiki et al. [1] and Araki et al. [2] have conducted experimental studies of the steam control valve. They analyzed the characteristics of certain shapes of the steam control valve and found the region responsible for the pressure fluctuations. However, they were unable to pinpoint the exact reasons for the fluctuations. Utilizing experiments, Ziada et al. [3] modified the control valve geometry to reduce the stress of the piping caused by the noise generated at the valve below the piping fatigue limit. They first changed the valve stem from a single-stage pressure drop system to multiple stages and achieved noise reduction at the downstream piping. However, this transformation from a single-stage to multiple stages increased valve vibrations. Then, they changed the valve structure back to the single-stage type, added 12 slits, and finally achieved the reduction of the downstream noise and valve vibrations. Hans et al. [4] conducted many model experiments with various geometries to verify the scaling rules relating to the valve noise. They found from these tests that the normalized acoustic power depends on the pressure ratio and valve design only, but is independent of valve size, fluid, and absolute value of pressure. Many other studies of control valves [5–7] have been conducted, but most of them focus on the control of the noise caused by turbulence and shock waves; moreover, there is no report that details the 3D flow structure around the valve under the partial-opening condition.

In this study, we focus on the details of the flow fluctuations around the steam control valve under the partial-opening condition, and conduct air experiments and CFD calculations to understand the cause of the fluctuations.

2 Experimental Apparatus

The schematics of the experimental apparatus are shown in Fig. 2. Compressed air is supplied from a compressor (1) to the test section (4) through a turbine flowmeter (2). The air from the test section is discharged through a downstream pipe (5) and a silencer (6).

The test section is composed of a valve and a valve seat with radii of 30 and 21 mm, respectively, and pressure taps for measuring wall pressure time history. Figure 3 shows the valve and valve seat geometries together with the location of the pressure taps. Each pressure measurement point has four pressure holes in the circumferential direction. The holes are installed 30 deg. from the center of the valve (A_1-A_4) and on the valve seat (B_1-B_4). We used Teac CCQ-093 pressure transducers that have been flush-mounted and the measurements were carried out with a 20×10^{-6} s sampling rate for unsteady pressure measurements.

It is possible to adjust the valve smoothly using a pulse motor and the support structure of the valve is sufficiently rigid to avoid

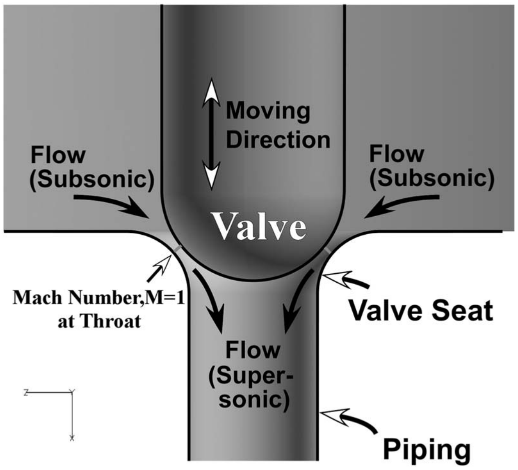

Fig. 1 Schematic of steam control valve

Contributed by the Fluids Engineering Division of ASME for publication in the JOURNAL OF FLUIDS ENGINEERING. Manuscript received July 26, 2005; final manuscript received June 11, 2006. Assoc. Editor: Georges L. Chahine. Paper presented at the 2004 ASME Heat Transfer/Fluids Engineering Summer Conference (HT-FED2004), July 11–15, 2004, Charlotte, North Carolina, USA.

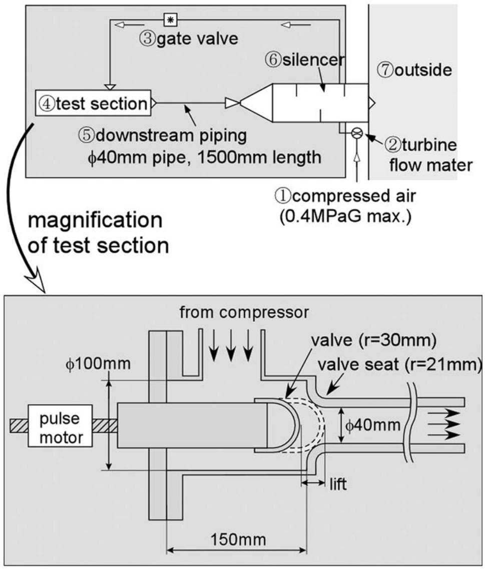

Fig. 2 Outline of experimental apparatus

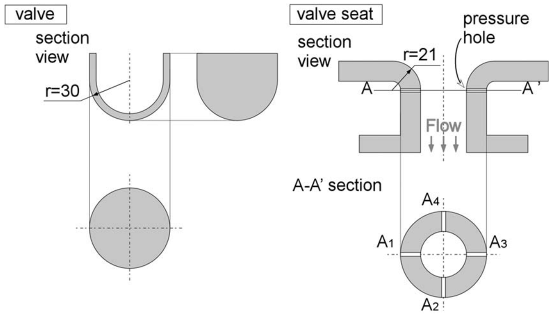

Fig. 3 Details of a valve and a valve seat, and points of pressure measurement

the flow-induced vibration of the valve. We determined the peak frequencies by the hammering test to be 372, 812, and 2130 Hz.

We define "lift" as the axial displacement of the valve body from a fully closed position and "opening ratio (OR)" as the ratio of lift to the seat diameter, where the seat diameter is the radius of the contact circle between the valve and the valve seat. The experimental conditions are listed in Table 1.

Table 1 Experimental condition

Fluid	Air
Inlet pressure	0.5 MPa
Exit pressure	About 0.1 MPa (Atmospheric pressure)
Valve shape	Hemisphere (radius 30 mm)
Valve seat shape	Curved surface (radius 21 mm)
Downstream pipe	$\phi 40$, about 1.5 m length
Lift	0.2 mm–2.0 mm
Seat diameter	49.3 mm
Opening ratio	0.00406–0.0406
Pressure measurements	Valve 4 points in circumferential dir. from the center to the position of 30 deg. (A_1–A_4) Valve seat 4 points in circumferential dir. at the curved surface ends (B_1–B_4)

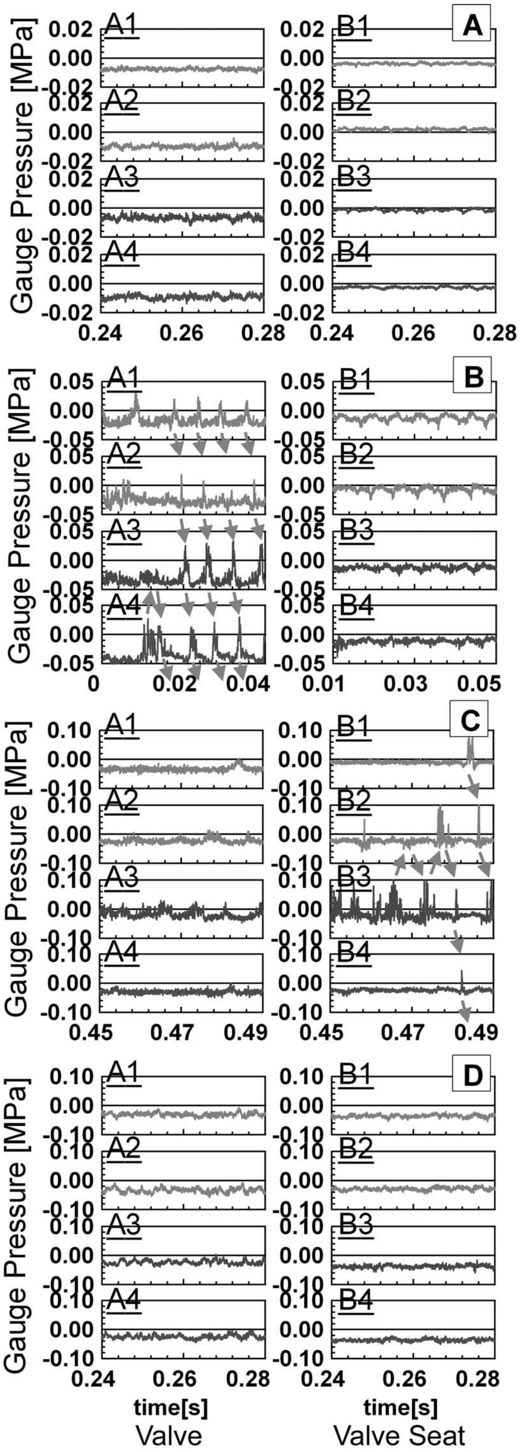

Fig. 4 Time history of wall pressure on valve (A_1-A_4) and valve seat (B_1-B_4) (inlet pressure: 0.5 MPa, arrows show the propagating direction)

3 Experimental Results

The time histories of wall pressure (A_1-A_4 or B_1-B_4) under the inlet pressure $p_{\text{inlet}}=0.5$ MPa and 0.2, 0.8, 1.6, and 2.0 mm lift (OR: 0.00406, 0.0162, 0.0325, 0.0406) are shown in Fig. 4. When

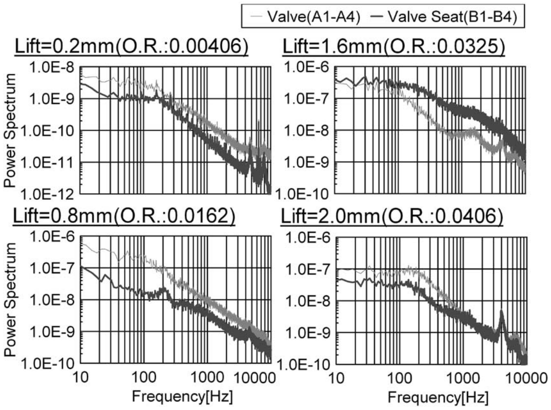

Fig. 5 FFT analysis of pressure history (inlet pressure: 0.5 MPa)

the lift is 0.2 mm (OR: 0.00406, small opening), there are no large pressure fluctuations and the flow has a symmetrical pattern.

When the lifts are 0.8 and 1.6 mm (OR: 0.0162, 0.0325, middle-opening), pressure spikes can be observed, which propagate in the circumferential direction, as indicated by arrows in Fig. 4. At the 0.8 mm lift, the fluctuations can be seen at the valve (A_1-A_4) and the amplitude is approximately 0.05 MPa. Moreover, the propagation direction suddenly changes to the opposite direction (e.g.,∼0.004 and 0.012 s). At the 1.6 mm lift, the fluctuations can be seen at the valve seat (B_1-B_4) and the amplitude is ∼0.1 MPa (larger than that under the 0.8 mm condition). A change in propagation direction is also observed in this case (at approx. 0.46 and 0.48 s) and happens randomly. This means that the propagation direction of the pressure fluctuations is a random (or quasi-periodic) phenomenon. We call these pressure fluctuations, "rotating pressure fluctuations."

We observe the rotating pressure fluctuations in the lift range of 0.5–1.6 mm (OR: 0.00406–0.0325). When the lift increases, the amplitude of the fluctuations increases. However, when the lift becomes 2.0 mm (OR: 0.0406, large opening), this fluctuation suddenly disappears and the flow becomes calm again.

Figure 5 shows the FFT results of the wall pressure (A_1-A_4, B_1-B_4) at 0.2, 0.8, 1.6, and 2.0 mm lifts (OR: 0.00406, 0.0162, 0.0325, 0.0406). The average values of A_1-A_4 (or B_1-B_4) are plotted here. In these figures, we can see a small peak at 4000–5000 Hz (O marked in the figures). As the speed of sound is approximately 340 m/s, this peak frequency corresponds to the first radial mode of acoustic resonance in the pipe. However, no peak corresponding to the rotating pressure fluctuations can be observed in any of the results. The reason for this is that, this is a random (or quasi-periodic) phenomenon as pointed out previously, so that FFT analysis does not show any peak associated with this phenomenon.

In the case of the region where the rotating pressure fluctuations occur, Fig. 6 shows the pressure time histories in which the direction of the rotating pressure fluctuations is maintained in the same direction, and Table 2 summarizes the characteristics of the rotating pressure fluctuations. (The propagation frequency is evaluated from Fig. 6 because it is impossible to evaluate them from FFT.)

The frequency of the fluctuations is 150 Hz at the 0.7 mm lift (OR: 0.0142), and it decreases when the lift increases. At the 1.6 mm lift (OR: 0.0325), the frequency becomes 75 Hz, half the value of that at the 0.7 mm lift. We can also see that when the lift increases, the region of the fluctuations moves from around the valve (A_1-A_4) to around the valve seat (B_1-B_4). Because the pressure measurement position on the valve (A_1-A_4) is closer to the piping center than that on the valve seat (B_1-B_4) and the frequency is lower when the lift is larger, it is supposed that the rotating pressure fluctuations move from the piping center to the wall. Moreover, the amplitude of the fluctuations increases when lift increases.

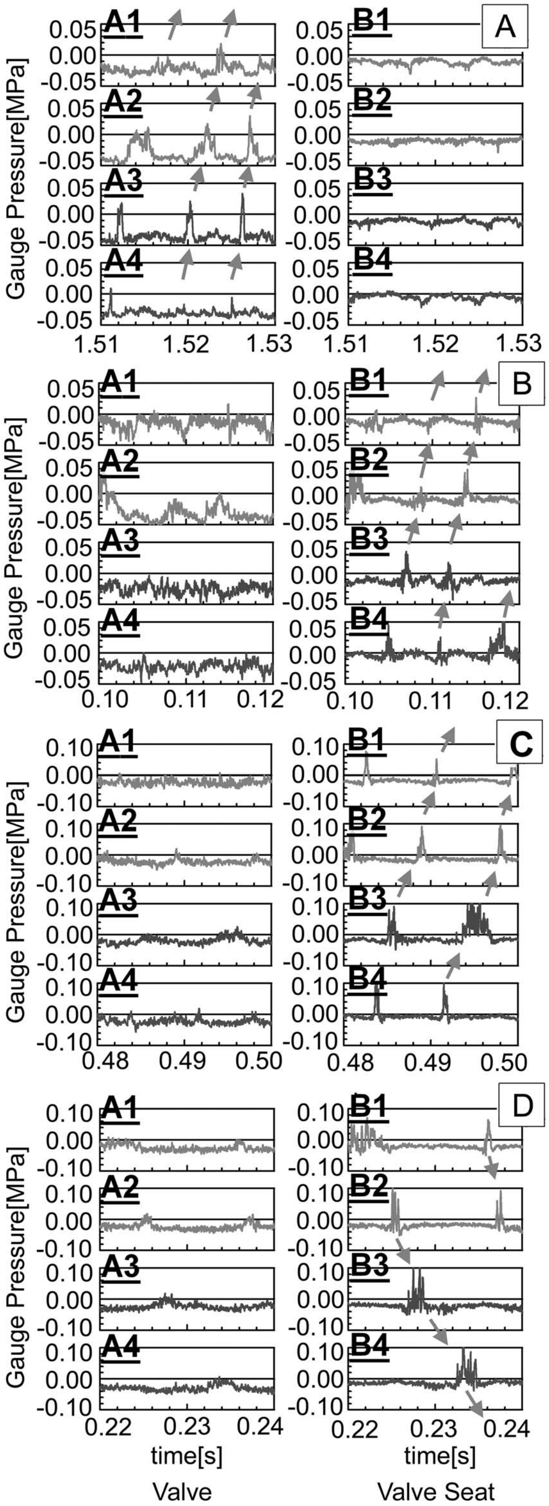

Fig. 6 Comparison of pressure rotation pattern (inlet pressure: 0.5 MPa)

4 CFD Code

Our 3D unsteady compressible flow CFD code, "MATIS-C (Multi-Dimensional Accurate Time Integration Simulation) Code" solves the 3D compressible NS equations and is discretized by the

Table 2 Characteristics of pressure fluctuation

Lift (open. ratio)	Pressure fluctuation		Rotation freq.[a]	Amp. (avg.) (MPa)
	Valve (A_1–A_4)	Valve seat (B_1–B_4)		
0.7 mm (0.0142)	*O*		150 Hz	0.03
0.9 mm (0.0183)		*O*	130 Hz	0.04
1.2 mm (0.0243)		*O*	110 Hz	0.06
1.6 mm (0.0325)		*O*	75 Hz	0.075

[a] Rough estimate.

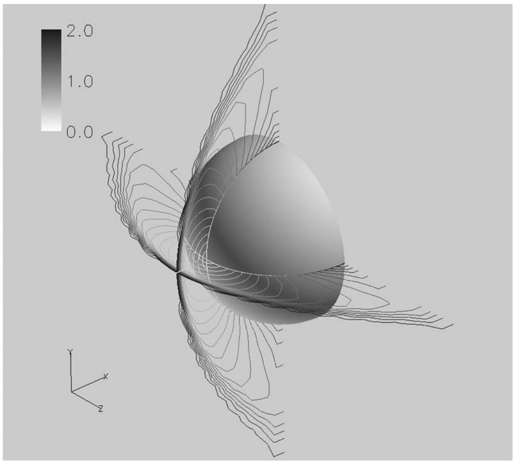

Fig. 7 Mach contour around a sphere (Mach number=2.0)

finite difference method. We utilize the second-order Harten-Yee's TVD scheme [8] for the convective term and the second-order central difference scheme for the viscous term. To calculate unsteady phenomena accurately, we used the second-order backward difference operator with the Newton iterative procedure and LU-SGS algorithm [9] for matrix inversion. Turbulent calculations such as those for the flow in the steam valve are carried out utilizing LES methodology with modified Smagorinsky model (Takakura et al. [10]), and van Driest wall damping function. Table 3 shows the details of the MATIS-C code.

For the validation of MATIS-C, we performed some benchmark tests. First, to check the spatial accuracy, the detached shock position on a sphere in supersonic flow was calculated and compared with the experimental data. Figure 7 shows the Mach number contour in some sections, and Fig. 8 shows the normalized shock position against the inlet Mach number. We can see the 3D shape of the detached shock, and the positions of the shock agree well with the experimental results.

Next, to check temporal accuracy, the von Karman vortex around a circular cylinder under the subsonic flow condition was calculated and compared with the experimental data. Figure 9 shows the Strouhal number of the lift coefficient versus the Reynolds number. The CFD results agree well with the experimental results quantitatively.

After benchmark tests, CFD calculations of flow in the valve were conducted. Figure 10 shows a bird's-eye view of a computational mesh. The shapes of the valve and the valve seat, and the downstream length are the same as the experiments. The total mesh number is approximately 500,000 points, 66 points are arranged in the circumferential direction and seven points are overset to prevent error accumulation by the boundary condition in the circumferential direction. The normalized wall distance y^+ between the wall and the first mesh is approximately three.

The calculations were performed with the following conditions:

(i) Since the operating fluid is air the ideal gas approximation was used;
(ii) total pressure and total temperature are fixed at 0.5 MPa and 300 K, respectively, at the inlet;
(iii) velocity at the inlet is calculated by extrapolating the Riemann invariant;
(iv) a static pressure of 0.1 MPa is fixed at the exit. All other variables at the exit are extrapolated;
(v) nonslip ($u=v=w=0$) and adiabatic conditions are specified at all wall boundaries.

Table 3 A feature of MATIS-C[a] code

	3D-FDM Based LES
Fluid	Compressible flow (Mach number, $M>0.3$)
Government equations	Mass conservation eq. Momentum conservation eq. Energy conservation eq. for 3-D compressible flow
Discretization	Convective term Harten-Yee's upwind TVD (2nd order) (Ref. [8]) Viscous term Central difference (2nd order)
Time marching	2nd order backward diff. with Newton iteration (2nd order) Implicit method: LU-SGS (Ref. [9])
Turbulence model	Modified Smagorinsky model (Ref. [10]) with van Driest type function

[a] Multi-dimensional accurately time integration simulation for compressible fluids.

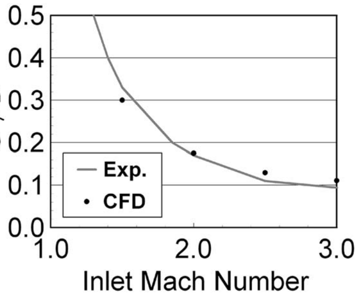

Fig. 8 Detached shock position versus inlet Mach number

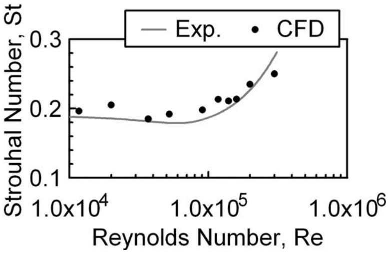

Fig. 9 Strouhal number of Karman vortex versus Reynolds number

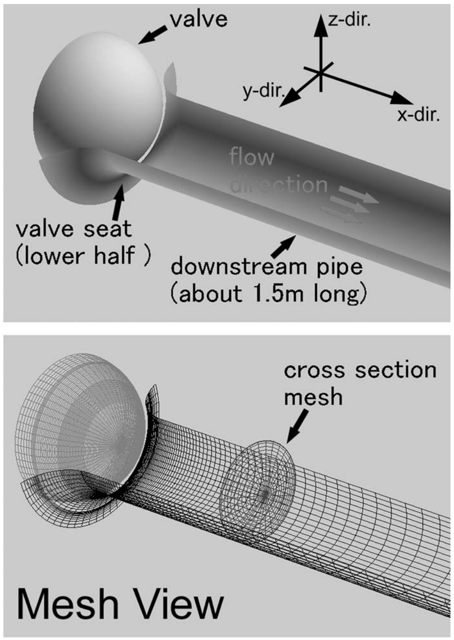

Fig. 10 Bird's view of computational mesh

Calculation was conducted at lifts of 0.2, 0.5, 0.8, 1.0, 1.2, 1.6, and 2.0 mm (OR: 0.00406, 0.0101, 0.0162, 0.0203, 0.0243, 0.0325, 0.0406).

5 CFD Results

Figure 11 shows the time histories of the wall pressure (A_1-A_4, B_1-B_4 correspond to the positions of the pressure holes in Fig. 3) at 0.2, 1.6, and 2.0 mm lifts (OR: 0.00406, 0.0325, 0.0406) and Fig. 12 shows the comparison of the rms. pressure amplitude. As seen in Fig. 11, under the small- (0.2 mm) or large- (2.0 mm) opening condition, the pressure fluctuations are noticeably absent in both CFD results and the experiments, and the absolute values of the pressure from CFD results agree well with experiments.

When the lift is 1.6 mm, the rotating pressure fluctuations can be seen in CFD results similar to those observed in the experiment. The frequency and amplitude also agree well with experiments. The CFD calculations show that the propagation direction changes quite suddenly to the opposite direction.

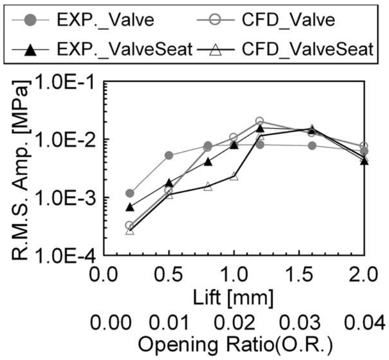

Fig. 12 RMS amplitude of pressure fluctuations

From Fig. 12, though differences between CFD and experiment under the small-opening condition caused by the mesh quality can be seen, CFD results agree with the experimental results in terms of amplitude except for the small opening condition and it is found that the amplitude increases when lift increases in the 0.4–1.6 mm lift range.

We found that CFD results can also reproduce the rotating pressure fluctuations, and the results agree with those of the experiment quantitatively. Furthermore, visualization of the CFD solutions also provided us with a detailed structure of the flow: Figure 13 shows the static pressure distribution and velocity vector in the flow sections (Figs. 13(*a*) and 13(*b*)) and *A*-*A*′ section (Fig. 13(*c*)). The red region denotes that the pressure in this region is higher than that in other regions. The bold arrow drawn in the figure shows the direction of the flow.

When the lifts are 0.2 and 2.0 mm, the flow downstream of the valve is axisymmetric and there is no large fluctuation or asymmetry in the pressure distribution. On the other hand, when the lift is 1.6 mm, the flow becomes asymmetric and part of the flow (the flow from left to right in Fig. 13(*b*)) attaches to the valve (called "the valve-attached flow") and collides with the flow from the opposite side. The resultant high-pressure region as well as the associated vortex structure are shown in Fig. 13(*c*). This valve-

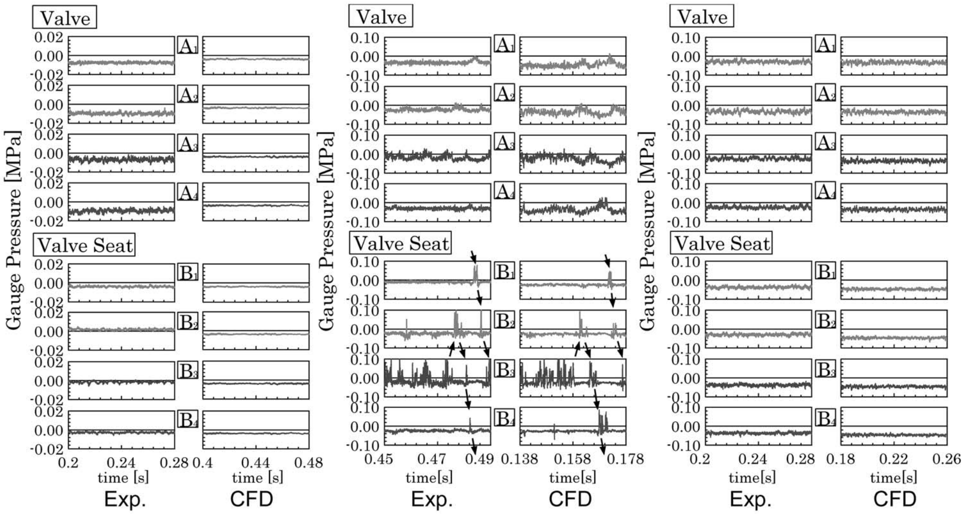

(a) Lift:0.2 mm(O.R.:0.00406) (b) Lift:1.6 mm(O.R.:0.0325) (c) Lift = 2 .0mm(O.R.:0.0406)

Fig. 11 Comparison between exp. and CFD (inlet pressure: 0.5 MPa)

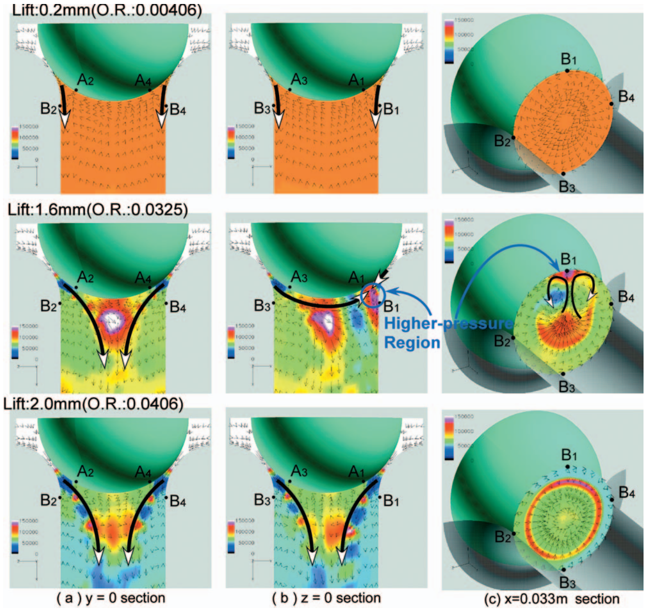

Fig. 13 Static pressure distribution and velocity vector (CFD)

attached flow is observed only at the lift range of 0.5–1.6 mm, which agrees well with the region in which the rotating pressure fluctuations are observed in the experiment.

Figure 14 shows the time histories of the pressure distribution and the velocity vector in the A-A' section at the 1.6 mm lift. The bold arrows drawn in the figures indicate the flow pattern. The time corresponds to the time in Fig. 12(b)-CFD.

At 1.65 s, when the high-pressure region caused by the valve-attached flow occurs at B_3 (shown in Fig. 12(b)-CFD), a pressure spike can be seen at B_3 (shown in Fig. 14(a)). In addition, when the high-pressure region propagates in the circumferential direction, the pressure fluctuations rotate in the same direction. This alludes to the fact that the rotating pressure fluctuations are caused by the valve-attached flow.

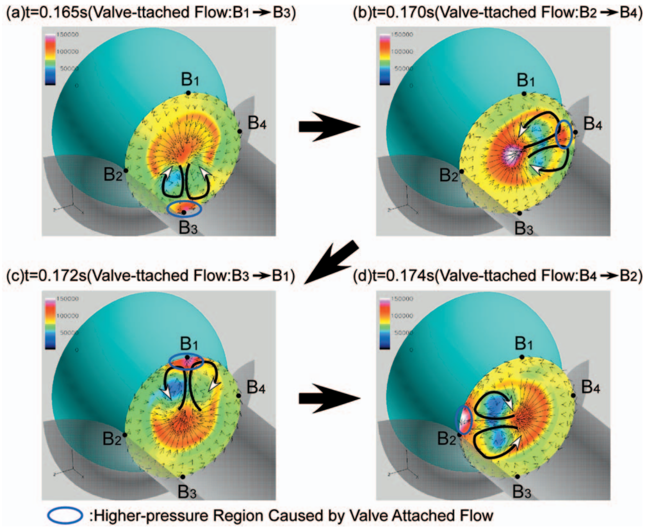

Fig. 14 Time history of pressure distribution and velocity vector (CFD, Lift: 1.6 mm (OR: 0.0325), x=0.033 m section)

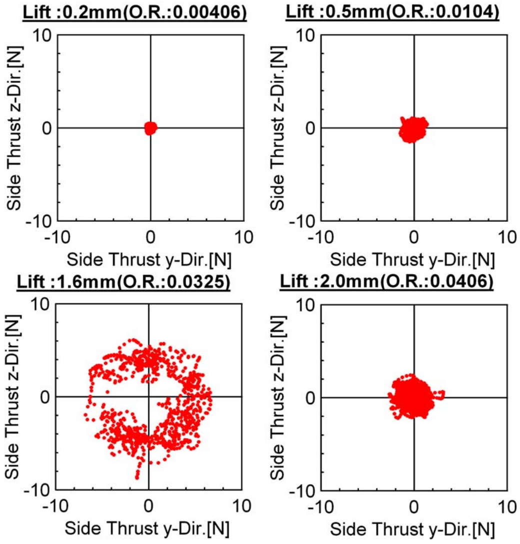

Fig. 15 Lissajous figure of side load (CFD)

Lissajous' figures of the side thrust to the valve (y-z direction) are shown in Fig. 15. At the 0.5 and 1.6 mm lifts, when the rotating pressure fluctuations occur, the side thrust on the valve also rotates, and if the amplitude of the fluctuations increases, the side thrust also increases (compare 0.5 and 1.6 mm lift data). This means the rotating pressure fluctuations (caused by the valve-attached flow) cause the rotating side thrust, and the amplitude of the side thrust becomes larger when the fluctuation becomes larger. This is thought to be one of the causes of the vibrations that occur on the valve and the piping system under the middle-opening condition.

6 Conclusion

Using experiments and CFD calculations, flow instabilities around a steam control valve under the middle-opening condition were investigated. We can draw the following conclusions.

Pressure fluctuations propagating in circumferential direction, which named "rotating pressure fluctuations," are observed only under the middle-opening condition.

The amplitude of the rotating pressure fluctuations increases and propagation frequency decreases as lift increases, within the lift range in which the fluctuation is observed.

The CFD code "MATIS-C" can reproduce unsteady phenomena that are observed experimentally, and the unsteady region, amplitude and frequency agree well with those of the experiment.

The rotating pressure fluctuations are caused by an asymmetrical flow attached to the valve body (called "the valve-attached flow").

The large side thrust experienced by the valve correlates with the presence of the rotating pressure fluctuations and is the leading cause of vibrations to the valve and the piping system under the middle-opening condition.

References

[1] Jibiki, H., et al., 2000, "Flow Vibration of Steam Control Valves (in Japanese)," Turbo Machinery, **28**(4), pp. 33–37.

[2] Araki, T., et al., 1981, "Flow-Induced Vibration of Steam Control Valves (in Japanese)," Toshiba Review, **36**(7), pp. 648–656.

[3] Ziada, S., et al., 2001, "Acoustic Fatigue of a Steam Dump Piping Exited by Valve Noise," ASME J. Pressure Vessel Technol., **123**, pp. 461–468.

[4] Hans, R., et al., 1997, "Verification of Scaling Rules for Control Valve Noise by Means of Model Tests," ASME FSI, Aeroelast., FIV, Noise, **2**, pp. 455–462.

[5] Baumann, H. D., 1984, "Coefficients and Factors Relating to the Aerodynamic Sound Level Generated by Throttling Valves," Noise Control Eng. J., **22**, p. 6–1.

[6] Baumann, H. D., 1991, “Determination of Peak Internal Sound Frequency Generated by Throttling Valves for the Calculation of Pipe Transmission Losses,” Noise Control Eng. J., **36**, pp. 75–83.
[7] Reethof, G., et al., 1986, “A Theoretically Based Valve Noise Prediction Method for Compressible Fluids,” ASME J. Vib., Acoust., Stress, Reliab. Des., **108**, pp. 329–338.
[8] Yee, H., 1987, “Upwind and Symmetric Shock-Capturing Schemes,” NASA TM 89464.
[9] Yoon, S., and Jameson, A., 1988, “Lower-Upper Symmetric-Gauss-Seidel Method for the Euler and Navier-Stokes Equations,” AIAA J., **26**(9), pp. 1025–1026.
[10] Takakura, Y., Ogawa, S., et al., 1989, “Turbulence Models for 3D Transonic Viscous Flows,” *Proc. AIAA 9th Comp. Fluid Dynamics Conf.*, 89-1952-CP, pp. 240–248.

Thermal and Flow Fields Modeling of Fast Spark Discharges in Air

O. Ekici

O. A. Ezekoye

M. J. Hall

R. D. Matthews

Department of Mechanical Engineering,
The University of Texas at Austin,
Austin, TX 78712

In this study, a two-dimensional axisymmetric computational model of spark discharge in air is presented to provide a better understanding of the dynamics of the process. Better understanding of the modeling issues in spark discharge processes is an important issue for the automotive spark plug community. In this work we investigate the evolution of the shock front, temperature, pressure, density, geometry, and flow history of a plasma kernel using various assumptions that are typically used in spark discharge simulations. A continuum, inviscid, heat conducting, single fluid description of the flow is considered with radiative losses. Assuming local thermal equilibrium, the energy input due to resistive heating is determined using a specified current profile and temperature-dependent gas electrical conductivity in the gap. The spark discharge model focuses on the early time flow physics, the relative importance of conduction and radiation losses, the influence of thermodynamic model choice and ambient pressure effects.

[DOI: 10.1115/1.2375130]

Introduction

In this paper, we present a two-dimensional axisymmetric computational model of ultra fast (90 ns) spark discharge in air. The goal of the study was to evaluate and test various assumptions that are typically used in plasma and blast wave dynamics during the spark discharge process. Better understanding of the dynamics of spark type discharges is important for a number of applications. As an example, improved fuel economy under the constraint of stricter emissions standards is an important objective of current internal combustion engine designs. One strategy to achieve this objective is the use of fuel-lean combustion. In general, however, increasing the air/fuel ratio leads to an increase in cycle-to-cycle variation resulting in partial burns and misfire cycles. Satisfactory ignition and combustion can only be achieved by an extended ignition limit and a shorter initial burn time under these conditions. Improving the overall ignition process thus extends the lean ignition limit in spark ignition engines [1,2]. Many factors affect the ignition process. Examples include equivalence ratio, spark discharge energy input, rate of energy input, spark gap parameters, heat losses to the electrodes, the specific combustion reactions in the early stages of discharge, and flow field characteristics. Various assumptions are made in the literature regarding the relative importance of these factors. Improvements in the understanding of spark discharges will facilitate improvements in spark ignited engine operation.

While there is a rich history of studies of flame kernel ignition, there is much less work on early time spark plasma physics [2–6]. One might consider that early time for a spark system refers to time before combustion kinetics are significant contributors to the rate of energy deposition in the spark discharge. During this early period ($t < 20\ \mu$s), the particular characteristics of the energy deposition process affect the plasma expansion and the development of thermal regions capable of initiating the combustion chemistry. There remain questions on the optimal methods for electrical energy addition. Maly and Vogel [3] present a summary of essential properties of three spark discharge modes: Breakdown, arc, and glow and suggest that to ensure high ignition probabilities, the total energy should be transferred to the mixture as quickly as possible during the breakdown phase. However, there is a lack of consensus regarding their conclusion, and continued research seeks to clarify the relative energy transfer budgets during spark ignition. Another important issue in spark discharge studies is the durability of the spark plug. A recent study by Soldera et al. [5] investigated the phases of the discharge and electrode erosion patterns using a high-speed camera and oscilloscope. Soldera et al. indicate that significant material erosion can occur in the arc phase which often follows breakdown. The highest power densities occur within approximately 10 μs after breakdown. The study by Soldera et al. highlights how ignition system parameters influence spark plug durability.

Several levels of modeling have been used to gain better understanding of the processes that influence flame kernel development. Global thermodynamic models (zero-dimensional) have been formulated by Herweg and Maly [7]; Shen et al. [8]; Lim et al. [2]; and Anbarasu et al. [9]. These models are by construction incapable of resolving the early time dynamics. In fact, they often rely on specification of some early time plasma profile to begin the flame kernel evolution. Exceptions exist such as Lim et al. [2] where they model the spark kernel development in two different time domains. Taylor-Sedov's point explosion theory [10] is used for the early blast wave phase, and the solution for this process is then used as the initial condition for the zero-dimensional thermal evolution model. Similarly, Anbarasu et al. [9] obtain the initial plasma kernel size after the breakdown process by solving for the blast wave generated during breakdown. There has been little exploration of how the one-dimensional approximation in the Taylor-Sedov solution compares to more complex physical modeling, for example, in the prediction of temperature.

Computational fluid dynamics (CFD) simulations of spark physics provide opportunities to simulate times approaching the time for breakdown. Sher and co-workers investigated spark discharge and flame kernel processes in a series of studies [1,11–14]. In their early work they derived an energy balance that algebraically predicts the plasma kernel radius and temperature after breakdown, while in their most recent study they used values suggested by Maly and Vogel [3]. In the study of Kravchik et al. [1], several issues were examined with respect to the flame kernel growth. The existence of the shock wave was noted as well as the importance of increased discharge energy on the rate at which the kernel grows. While significant understanding came out of these studies, there are issues that were not addressed. For example, it is

---

Contributed by the Fluids Engineering Division of ASME for publication in the JOURNAL OF FLUIDS ENGINEERING. Manuscript received February 8, 2006; final manuscript received June 10, 2006. Assoc. Editor: Subrata Roy.

unclear if and how the current profile, as might be measured for an actual spark circuit, was used in determining the energy deposition. Also, the numerical code appears to be a low numerical order technique. It is useful to know if higher order techniques predict different physics. Other studies in the literature have also used CFD techniques to investigate spark processes. Akram investigated the spark discharge physics in air using one-dimensional and two-dimensional models [15–17]. In a recent study [17], Akram presented a two-dimensional model simulating spark discharge in air to show the influence of electrode geometry and gas dynamic effects on the formation of the high temperature kernel. In our study, we examine the thermodynamic model used by Akram and compare it against two other models. A study by Thiele et al. [18] presented a numerical simulation of spark ignition including detailed chemistry and ionization. Their model investigated times from the blast wave formation through to the early stages of flame development in methane/air mixtures. In another study [19], Thiele et al. primarily focus on geometry effects as they might affect flow physics.

Given that many physical mechanisms may impact the discharge and ignition process, it is a formidable challenge to model the event. In the present paper, we present a spark discharge model focusing on the details of the flow physics, the relative importance of heat loss to the electrodes by conduction and radiation losses, the influence of thermodynamic model choice, and ambient pressure effects. We use one of the few experimental data sets available in the literature (Borghese et al.) to validate and test the models and approximations. The Borghese et al. [20] data provide density measurements in a plasma driven by an ultra-fast spark (<90 ns duration) circuit at various times. Although this data set is for times much shorter than typical spark plugs, it serves as validation for some of the models that we test. We also compare a one-dimensional solution for the temperature profile with more detailed two-dimensional axisymmetric simulations. To the authors' knowledge, no previous studies have systematically documented the influence of the choice of thermodynamic model on the evolution of the temperature profile, pressure distribution, etc.

Spark Discharge Modeling

The conditions under which the theoretical models used in this study to simulate the spark discharge process are valid are discussed below. The arc discharge has axial symmetry in cylindrical coordinates. The flow field is assumed laminar because the effect of turbulence is often considered to be negligible during the early stages of the discharge process [4,20,21]. Body forces are neglected. We assume that the magnetic field induced by the electrical current during discharge is also negligible. Generally, the low current densities observed in spark discharges allow us to neglect self-induced magnetic forces compared to the pressure effects (the induced electrical "pressure" represents 1% of the thermodynamic pressure when the current magnitudes are on the order of 10^3 A) [22]. Also, the very short duration of the discharge in this study makes the self-induced magnetic field effects negligible. In spark discharge processes local thermal equilibrium (LTE) is reached after the formation of a conducting channel, i.e., breakdown. The duration of breakdown is on the order of 10 ns, and that period cannot be simulated by the present model because the gas during the breakdown period is not in equilibrium. Breakdown physics is incorporated into the model by initial conditions. A continuum, single fluid description of the flow is considered where we assume that all the constituents of the plasma behave the same. An inviscid, heat conducting fluid description is used. In low temperature problems it is general practice that ignoring viscosity requires ignoring conductivity, but under the relatively high temperature conditions considered here free electrons play an important role in the thermal conductivity while they have a negligible effect in the momentum transport because of their low mass [17]. The electrodes are considered as infinite heat sinks where their surface temperature is taken as 300 K. The plasma is considered to be optically thin [1]; therefore, it is transparent to its own radiation. The gas (dry air) is assumed to be initially at rest and the pressure is initially spatially uniform.

Governing Equations

In accordance with the assumptions stated above under the modeling section, the following governing equations are used in cylindrical coordinates:

Mass conservation:

$$\frac{\partial \rho}{\partial t} + \nabla \cdot (\rho \boldsymbol{V}) = 0 \tag{1}$$

Momentum conversation:

$$\frac{\partial \rho \boldsymbol{V}}{\partial t} + \nabla \cdot (\rho \boldsymbol{V}\boldsymbol{V}) = -\nabla P \tag{2}$$

Energy conservation:

$$\frac{\partial E}{\partial t} + \nabla \cdot (E\boldsymbol{V}) = -\nabla \cdot (\boldsymbol{V}P) + \nabla \cdot \boldsymbol{q} + \dot{q}'''_{\mathrm{el}} + \dot{q}'''_{\mathrm{rad}} \tag{3}$$

The total energy per unit volume in Eq. (3) is defined as

$$E = \rho\left[e + \tfrac{1}{2}(\boldsymbol{V}\boldsymbol{V})\right] \tag{4}$$

Constitutive Relations. To close the system of equations we need constitutive relations, namely thermal and caloric equations of state. In the present study, the air is considered to be a single substance and species are not treated separately. The real gas contributions to the flow physics such as dissociation, ionization, vibrational, and rotational energies are incorporated through specified thermodynamic models and the resultant equation of state. We use three different thermodynamic models to investigate the effects of each on the simulation results and also on the computational time requirement.

Thermodynamic Model 1 (TDM-1). The first model employs the constant specific heat ratio, γ, approach which is widely used in high speed gas dynamics problems. This method replaces the real gas air by a surrogate ideal gas with the average molecular weight of dry air and constant specific heat ratio. The thermal equation of state with gas constant associated with air is

$$p = \rho R T \tag{5}$$

The model utilizes a relation between the pressure and volume specific energy in which γ is a parameter

$$e = \frac{P}{\gamma - 1} \tag{6}$$

In this study, an effective value of 1.16 is chosen for γ which is consistent with the average value of γ over the temperature range of interest. The specific heat ratio, γ, is calculated using thermodynamic data/models which typically give the internal energy as a function of temperature. Please refer to Fig. 1 for the γ variation with temperature (at four pressures) for an equilibrium air plasma using two different thermodynamic models. For one model (i.e., Capitelli et al. [23]) only atmospheric pressure γ data are presented. For the other (Akram [17]), which has an explicit pressure dependence, we present four pressures. Further discussion of Fig. 1 is provided under the pressure effects section in the results and discussion.

Thermodynamic Model 2 (TDM-2). The second model, which was originally suggested by Plooster [24], found applications with some modifications in various papers including the spark discharge simulations of Akram [17]. In this method, a simplified equation of state for a surrogate diatomic gas "air$_2$" was devised to obtain an estimate of the effects of real air [24]. The weighted averages of the molecular weight, rotational moment of inertia,

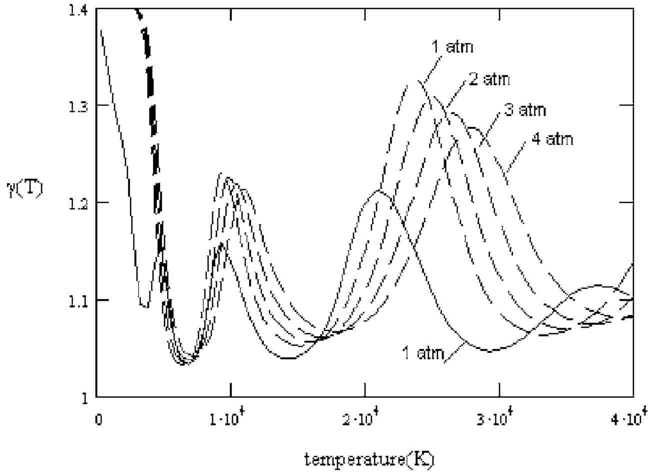

Fig. 1 Specific heat ratio for air under LTE (solid curve with TDM-3, dashed curves with TDM-2)

energies of dissociation, first and second ionization, and the statistical weights of the ground states of the molecular, atomic, and ionic O_2 and N_2 are used to represent air_2. The contribution of vibrational degrees of freedom to the internal energy is included in Akram [17] while it was neglected in the original formulation. Although this method approximates the thermodynamic properties of real air quite well at temperatures above 10,000 K, there is more error in the approximation in the temperature range of 3000–9000 K because of the very different dissociation energies of O_2 and N_2 and the neglected contribution of NO. The thermal and caloric equations of state are determined by means of a Saha equation under the assumption that dissociation and ionization occur consecutively. This approximation works well unless the pressures are very high. Based upon the summarized assumptions [17,24], the constitutive thermodynamic relations are

Thermal equation of state

$$p = \rho RT[1 + A_0 + 2(A_1 + A_2)] \tag{7}$$

Caloric equation of state

$$\varepsilon = RT\left[\tfrac{1}{2}(5 + A_0) + 3(A_1 + A_2)\right] + A_0 I_0 + A_1 I_1 + A_2 I_2 \tag{8}$$

where

$$A_0 = 2[1 + (1 + 2B_0)^{1/2}]^{-1}$$

$$B_0 = C_0 \rho T^{-1/2}\left[1 - \exp\left(-\frac{\theta_v}{T}\right)\right]^{-1} \exp\left(\frac{I_0}{RT}\right)$$

$$A_1 = 2[1 + (1 + 2B_1)^{1/2}]^{-1}$$

$$B_1 = C_1 \rho T^{-3/2} \exp\left(\frac{I_1}{2RT}\right)$$

$$A_2 = 2[1 + 2B_2 + (1 + 6B_2 + B_2^2)^{1/2}]^{-1}$$

$$B_2 = C_2 \rho T^{-3/2} \exp\left(\frac{I_2}{2RT}\right)$$

In these expressions, the A_i are the levels of dissociation and ionization, θ_v is the vibrational temperature, I_i are the specific energies of the dissociation or ionization reactions, and C_i are the constants that depend on the statistical weights. The respective values of the parameters used here are given in Table 1.

Thermodynamic Model 3 (TDM-3). In the third model, thermodynamic properties presented by Capitelli et al. [23] are used. In that study, they report analytical expressions for thermodynamic and transport properties in the temperature range of 50–100,000 K with an error less than 5% compared to calculated data. The plasma composition and the thermodynamic properties have been obtained from the internal partition functions tabulated by Giordano et al. [25]. Species considered are: N_2, N_2^+, N, N^+, N^{2+}, N^{3+}, N^{4+}, O_2, O_2^+, O_{2-}, O, O^-, O^+, O^{2+}, O^{3+}, O^{4+}, NO, NO^+, and e^- at atmospheric pressure with the assumption that the plasma is in local thermodynamic equilibrium. Only the thermodynamic properties that are presented by Capitelli et al. [23] are incorporated in the present study because our aim is to investigate the influence of those specified thermodynamic properties on the simulated flow physics while the same transport properties are used for all three models. One would expect that the atmospheric pressure thermodynamic properties would yield errors at very early times because of the high pressures during that period; we will assess the effect of these pressure property-related errors in the course of the simulations. A temperature dependent gas constant is used in the equation of state and an energy-temperature ($\epsilon - T$) curve using the properties presented by Capitelli [23] is employed as the caloric equation of state.

Table 1 Physical properties of air_2

Gas constant, R (J/kgK)	$2.88 * 10^2$
Specific dissociation energy, I_0 (J/kg)	$2.930577 * 10^7$
Specific first ionization energy, I_1 (J/kg)	$9.591766 * 10^7$
Specific second ionization energy, I_2 (J/kg)	$2.062056 * 10^8$
Constant in Saha equation for dissociation, C_0 ($m^3K^{3/2}/kg$)	$4.817588 * 10^{-4}$
Constant in Saha equation for first ionization, C_1 ($m^3K^{3/2}/kg$)	$1.101416 * 10^4$
Constant in Saha equation for second ionization, C_2 ($m^3K^{3/2}/kg$)	$1.033965 * 10^4$
Vibrational temperature, θ_v (K)	3150

Electrical Heat Source. Electrical power input (per unit volume) to the gas due to resistive heating is given by

$$\dot{q}_{\mathrm{el}}''' = \boldsymbol{j} \cdot \boldsymbol{E} \tag{9}$$

where $\boldsymbol{j}$ is the current density and $\boldsymbol{E}$ is the electric field. A generalized Ohm's law for an electrically neutral plasma can be written as

$$\boldsymbol{j} = \sigma(\boldsymbol{E} + \boldsymbol{u}_e \times \boldsymbol{B}) \tag{10}$$

With the assumption of a negligibly small magnetic field, and unidirectional flow of the current in the z-direction within the cylindrically symmetric current channel, the Joule heating term is written as

$$\dot{q}_{\mathrm{el}}''' = \frac{j_z^2}{\sigma} \tag{11}$$

where σ is the electrical conductivity of the plasma. The electrical conductivity has a strong temperature dependence. Using total current, i, the source term can be distributed over the plasma channel [1,18,19] by

$$\dot{q}_{el}''' = \sigma \frac{i^2}{\left(\int_0^{r_{el}} 2\pi r \sigma(r,z) dr\right)^2} \tag{12}$$

Therefore, the electrical power input into the plasma through Joule heating can be calculated and distributed using the specified current input.

Transport Properties. In this study, transport properties, namely the thermal and electrical conductivities for high temperature dry air, are based on the data presented in Boulos et al. [22]. It is worth noting that those tables are evaluated under the thermal

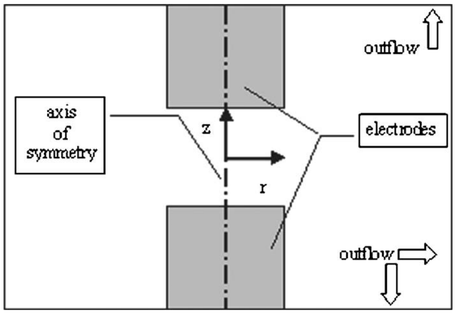

Fig. 2 Computational domain and electrode geometry

and chemical equilibrium conditions of atmospheric pressure. The errors associated with changes in pressure are assumed to be small because the dependence of transport properties on pressure is very small compared to the dependence on temperature. As an example, several order of magnitude changes occur in the transport properties over the temperature range of interest while for an order of magnitude pressure range, the transport properties do not change even within an order of magnitude [26]. In addition, the overpressure within the spark gap, which is also the high temperature zone and where the most deviations should be expected, decreases in value to less than 500 kPa in the first two hundred or so nanoseconds.

Radiative Heat Transfer. Radiative loss is one of the most important problems in energy transport of thermal plasma modeling. The strict treatment of radiation is a very computationally expensive and involved problem which is generally handled as a separate problem by itself. In this study tabulated values of the net emission coefficient as a function of temperature are used. This is actually one of the simplest and most widely used methods for evaluating radiation losses in thermal plasmas. This method assumes transparent radiation from the finite volume without absorption. We adopted the net emission coefficient for dry air at atmospheric pressure calculated by Naghizade-Kashani et al. [27] into our simulation.

Numerical Solution and Computational Domain

The flux corrected transport (FCT) algorithm developed by Boris et al. [28,29] is used with some problem-specific modifications to advance all dependent variables in time. FCT is a high-order, explicit, finite difference code that includes a group of subroutines for solving nonlinear, time-dependent continuity equations. This monotone, conservative, positivity-preserving algorithm can accurately compute steep gradients, allowing grid scale numerical resolution. The algorithm itself can treat one-dimensional, Cartesian, cylindrical, or spherical and generalized nozzle coordinates. Multidimensional problems are solved by time-splitting in the different coordinate directions.

Figure 2 shows the schematic of the cylindrical electrodes and the axisymmetric computational domain. The gap between the electrodes is taken equal to 2 mm, where the electrodes have 1 mm diameter. The flow is considered to be symmetric with respect to the r and z axes, which allows performing the solution for one quadrant of the domain of interest. The solution domain ranges from 0 to 8 mm in r and −6.50 to 6.50 mm in the z directions. The model employs 270 by 160 nonuniformly distributed cell volumes with the minimum mesh size of $10\ \mu\text{m} \times 20\ \mu\text{m}$. The minimum time-step used in the solution is 0.25 ns.

The calculation procedure for a single time-step can be summarized as follows:

(i) Given the initial conditions, thermodynamic and transport properties are calculated for each cell as a function temperature;
(ii) the governing equations are integrated in a specifed direction for a half time-step to find first order accurate approximations to the dependent conserved variables. More details are provided in Boris et al. [28]
(iii) the total energy is used to calculate the temperature and pressure according to the thermodynamic model used (this requires iterative solution for TDM-2 and TDM-3 because of the nonlinear temperature dependence of internal energy);
(iv) thermodynamic and transport properties are calculated using updated cell temperatures;
(v) the governing equations are integrated to the full time-step to find dependent variables that are second order accurate in time. More details in are provided in Boris et al. [28];
(vi) new temperature and pressure values are calculated at the end of the time-step using total energy and the prescribed thermodynamic model;
(vii) Procedures (ii)–(vi) are repeated to integrate the governing equations in the other direction to complete the full time-step for two-dimensional computational domains.

Initial and Boundary Conditions

Arc initiation within the spark gap is achieved with the breakdown of the gas between the electrodes. As already mentioned in the modeling discussion, the formation of the conducting channel cannot be simulated with a single substance equilibrium model and is beyond the scope of this work. Therefore, our simulation starts just after breakdown of the air between the electrodes using the conditions at the end of breakdown as initial conditions. High-temperatures, high pressures, and ambient density are specified for the current-carrying plasma channel at the initial time [1,3,17]. The initial plasma radius is taken as 0.1 mm and the plasma temperature is set to 10,000 K; these values are in the range given by Akram [17]. It is worth noting that simulation results are relatively insensitive to changes in the initial radius between 0.05 and 0.15 mm and in the initial temperature between 7500 and 15,000 K. The corresponding pressure is calculated using the thermal equation of state.

Electrodes are treated as walls with slip conditions. The symmetry axis is $r=0$, and outflow boundary conditions are used for the other boundaries of the computational domain. Since the electrode bodies are not part of the computational domain, and governing equations are solved only for the gas part, surface temperatures have to be assigned to calculate the heat transfer between the gas and the solid boundaries. As mentioned in the modeling section, isothermal surfaces are given the temperature of 300 K. It is assumed that the temperature rise of the electrodes is negligible compared to the existing temperature differences between the plasma and electrodes surfaces during the early stages of the discharge [1].

Results and Discussion

We used the experimentally measured current profile of Borghese et al. as an input to our model [20]. In their study, a very fast spark discharge was used to experimentally investigate the development of the high temperature kernel in atmospheric pressure nitrogen. The same current profile was used in the computational study by Akram [17]. Using this current profile allows us to compare our predictions against both experimental and numerical results.

Effect of Thermodynamic Models. The current profile and calculated energies for different thermodynamic models (TDM) are given in Fig. 3. Energy deposited to the gas during the discharge is calculated from Eq. (12). Prediction of energy deposition by the three TDMs are in good agreement with the experimental energy deposition value of 14 mJ reported by Borghese et al. [20] and with the predicted energy deposition value of 12 mJ reported by Akram [17]. In Fig. 4, the blast wave radius predictions of our

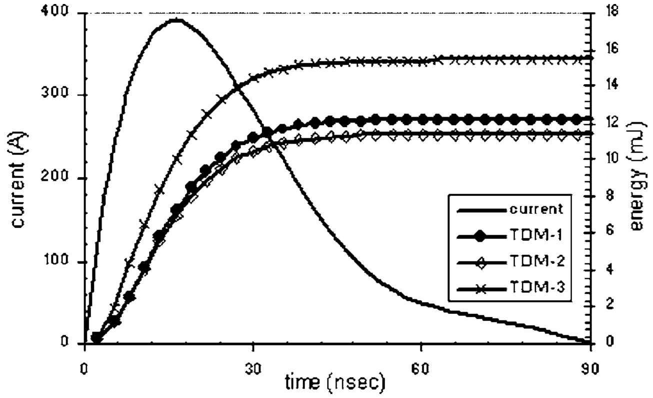

Fig. 3 Current and cumulative energy deposition as a function of time

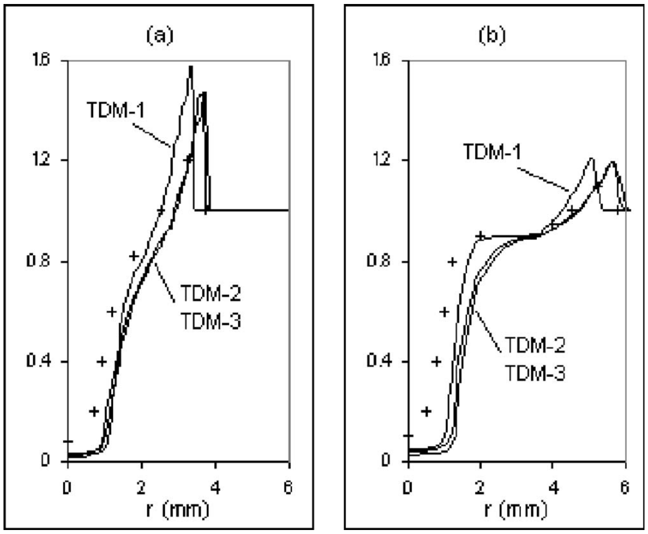

Fig. 5 Scaled mass density profiles in the $z=0$ plane at 5 μs (*a*), and at 10 μs (*b*); "+" experiment [20]

simulation are compared to experimental results [20] for the first 15 μs of the flow. The agreement with the experimental data and among the different thermodynamic models' predictions is quite satisfactory. The largest deviation from the experimental data is for TDM-3 which can be a result of the relatively higher energy deposition observed for this case as presented in Fig. 3.

The scaled mass density profiles (normalized by the density at atmospheric pressure and temperature) in the $z=0$ plane at 5 and 10 μs are given in Figs. 5(*a*) and 5(*b*), respectively. It is observed that they match well with computational [17] and experimental [20] results presented in the references. As can be seen in Fig. 5, TDM-2 and TDM-3 predictions are almost identical while TDM-1 predicts a slightly stronger shock with a slightly smaller radius. Temperature distributions as a function of radius for different models in the equilateral ($z=0$) plane at 10 μs are given in Fig. 6. Relatively higher temperatures are predicted with TDM-3 compared to TDM-2 and TDM-1. The differences between the predicted temperatures can be explained by differences in the average specific heat capacity associated with each thermodynamic model. Note that the time shown in Fig. 6 (10 μs) is a "long" time after the energy deposition time (90 ns) has ended. The temperature profiles are in the cooling stages of the discharge process. When we examine the temperature profiles during the energy deposition (early) times, we find that TDM-3 has the lowest temperatures consistent with the fact that it has relatively higher mean specific heat capacity. During the cooling process, the rate of decrease of the temperature for TDM-3 is slower than for the other models because of its higher "thermal capacitance." A simple model for energy deposition was formulated to test these claims and the model showed similar trends as the computational results. In the simple model we assumed energy deposition with constant heat capacity. We find that the predicted temperatures at "long" times are higher for the higher specific heat capacity model although at shorter times (i.e., during energy deposition) the higher heat capacity model shows lower temperatures.

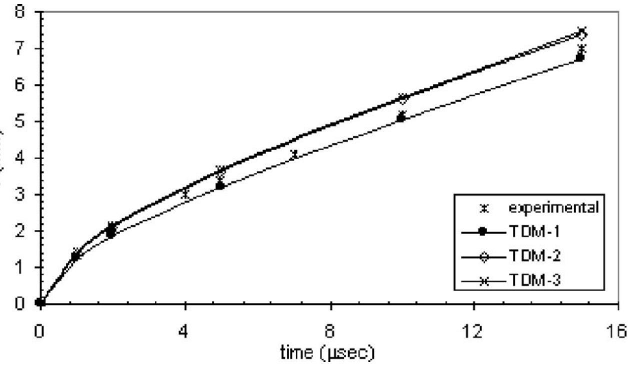

Fig. 4 Shock wave radius as a function of time

There are significant differences in run times for the three different thermodynamic models, as can be seen in Table 2. Table 2 shows the computational costs for the base case simulation run to a time of 40 μs. The simulations were performed on workstations with 1.8 GHz Pentium Xeon processors and 1 GB of RAM that were running SuSE Linux. The increased computational costs of the TDM-2 and TDM-3 models relative to TDM-1 are because of the need to iteratively find temperature from the integrated total energy at each time step. In addition, TDM-2 has increased computational costs relative to TDM-3 because of the cost of computing the exponential functions in the model.

Multidimensional Flow and Heat Loss Effects. To gain better insight into the physics, we present two more cases in Fig. 6 using

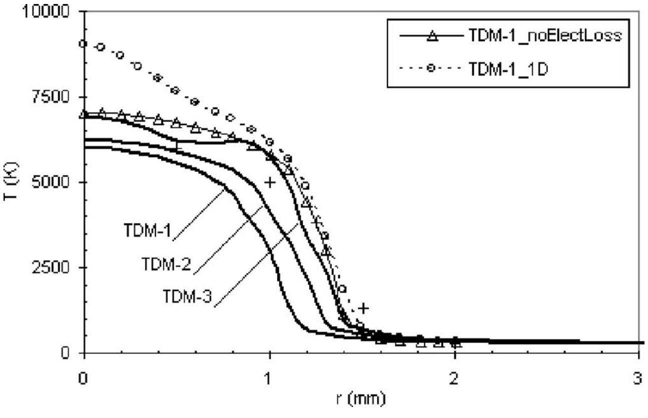

Fig. 6 Temperature as a function of radial coordinate at 10 μs for the $z=0$ plane; "+" model predictions of Akram [17]

Table 2 Comparison of computational time requirements

Thermodynamic model	Computational time
TDM-1	~3 h
TDM-2	~33 h
TDM-3	~11 h

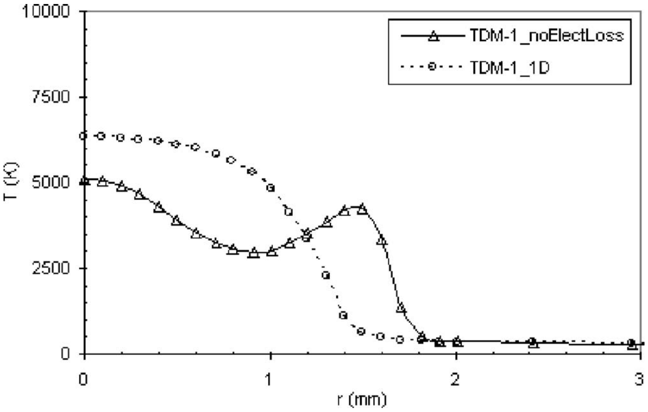

Fig. 7 Temperature as a function of radial coordinate at 20 μs for the $z=0$ plane

TDM-1. The first one is a one-dimensional (1D) model which physically has no electrode or gap effects; the second one is an axisymmetric model with adiabatic electrodes. The influence of heat losses to the electrodes can be seen by comparing TDM-1 and TDM-1 with no electrode losses. The comparison of the 1D versus adiabatic electrode case shows the influence of flow effects on the temperature distribution. We see that electrode losses decrease the temperature (approximately 20%) in the high temperature zones. We see that the more accurate flow/dimensionality model predicts lower temperatures within the spark gap, but does not change the high temperature (>2000 K) kernel radius for the equilateral plane at 10 μs. The temperature distributions at 20 μs in Fig. 7 give additional information about flow effects; a "dip" occurs in the temperature profile for the two-dimensional simulations on the symmetry axis. We will show in later figures that this cooling dip is a result of cooler external fluid flowing into the symmetry axis. These two-dimensional effects cannot be predicted using the one dimensional model. Two-dimensional contour plots give us more insight into the mixing effects generated as a result of the two-dimensional flow in the computational domain.

The temperature and pressure contours are shown in Figs. 8 and 9, respectively, at 2.0 μs. TDM-1 results are presented unless otherwise specified. It is seen that the blast wave grows much faster than the plasma kernel. The pressure in the blast wave is a maximum in the $z=0$ plane and decreases toward the electrodes. The

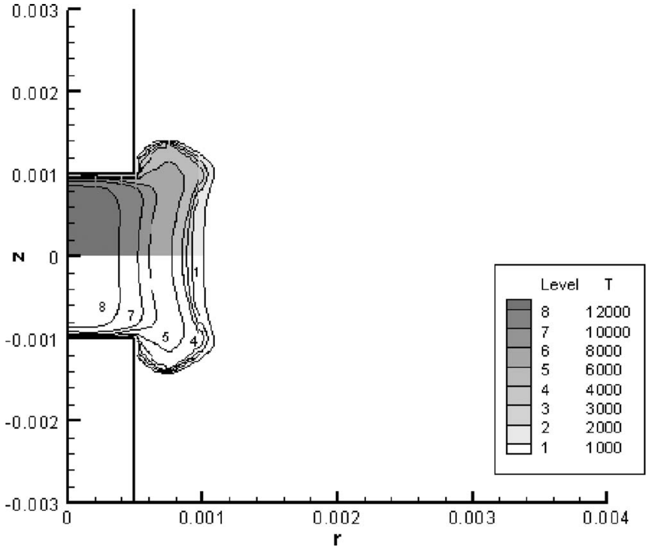

Fig. 9 Temperature distribution at 2.0 μs

shape of the plasma kernel is a result of the interaction of the kernel with the colder and higher density gas at the exit of the gap. This colder gas prevents further growth of the kernel in the radial direction. These results are similar to those of Akram [17] and Thiele et al. [18,19].

Pressure and temperature contours at 5 μs in the computational domain are provided in Figs. 10 and 11. The blast wave is still growing although its strength is weakening, as can be seen from the pressure values. It is also important to note that pressure values within the gap are lower than atmospheric pressure as a result of the sudden and strong expansion. This low-pressure region induces a strong backflow of the cold gas toward the spark gap. The growth of the plasma kernel is almost stopped at this point, and the maximum temperatures within the gap start to decrease rapidly because of the conductive and convective processes.

The velocity vector field in the computational domain at 5.0 μs is given in Fig. 12. It is seen that vortices start to form near the corners of the electrodes. We believe that the vortices observed in these simulations are mainly produced by the slipstream as discussed in Sun and Takayama [30]. A velocity jump through the slipstream causes a roll up of the slipstream and forms a large

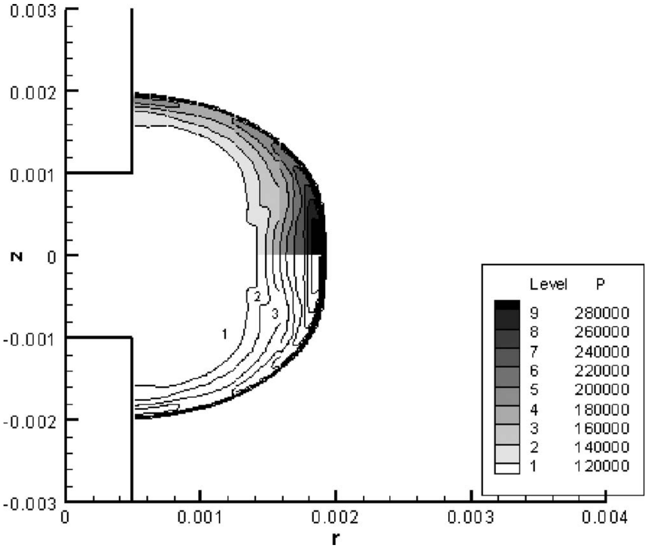

Fig. 8 Pressure distribution at 2.0 μs

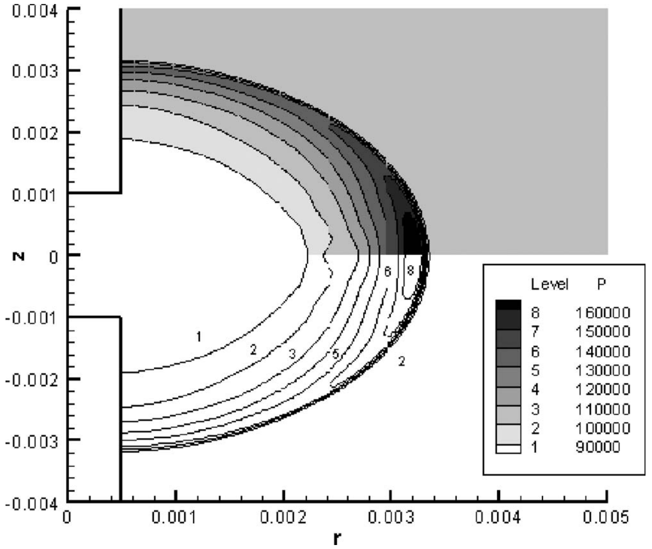

Fig. 10 Pressure distribution at 5.0 μs

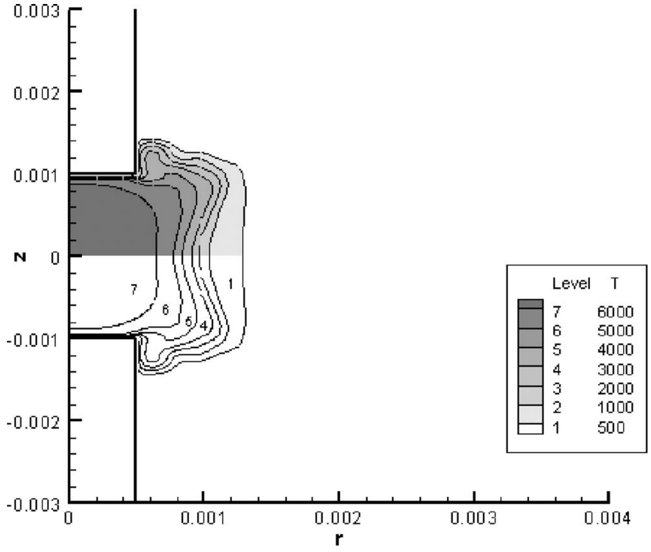

Fig. 11 Temperature distribution at 5.0 μs

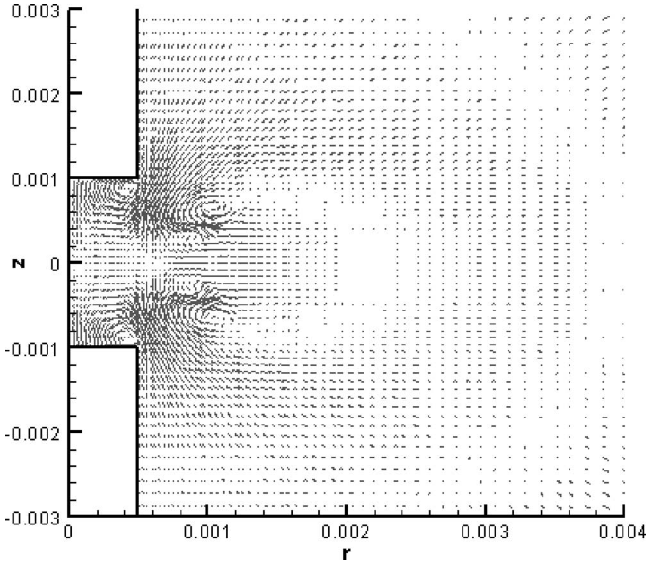

Fig. 13 Velocity vector field at 10.0 μs

portion of the main vortex. Sun and Takayama note that baroclinic/compressibility effects also contribute to the main vortex formation but are much less important when compared to vortex formation by the slipstream for problems with sharp corners and large wall angles. Also, fresh gas flows inward along the $z=0$ plane as well as towards the gap near the corners. Effects of this cold gas movement toward the spark gap and in the recirculation corners on the electrodes will be clearly observed in the temperature contours at later times. The velocity vector field and temperature contour plots are given in Figs. 13 and 14, respectively. It is seen that the plasma kernel cannot grow in a spherical shape because of the strong cold gas inflow near the corners of the electrodes. Two distinct vortex pairs can be seen in Fig. 13, one of which is within the spark gap near the corner, and the other is outside the gap close to the $z=0$ plane; very similar observations can be found in the results presented by Akram [17].

At later times, the cold gas flow near the electrodes pinches-off high temperature lobes outside of the spark gap. The cold gas flow into the spark gap mixes with the initial high temperature gases in the gap and is the basis for the differences in temperature profiles presented in Fig. 7 between the 1D and axisymmetric models. Figure 15 shows the formation of high temperature pockets in the computational domain. It appears that the flow field causes this formation for all of the different thermodynamic models used in this study. From the chemical kinetics point of view, a relevant temperature contour range is assumed to be from 1000 to 2200 K. All three results are in good qualitative agreement, although contours for TDM-2 and TDM-3 are closer to each other than the ones of TDM-1. The neck of the high temperature pocket for TDM-1 is thinner than for the other two models, and it has noticeably higher temperatures within the spark gap.

Energy losses by radiation and conduction to the electrodes are shown as functions of time in Fig. 16 for different thermodynamic models. Most of the radiation loss happens in the first 2 μs for all three cases since the temperatures are relatively higher in the computational domain. Radiation loss for TDM-1 is significantly larger than the radiation losses for TDM-2 and TDM-3 which are closer to each other. This high radiation loss for TDM-1, which is a result of relatively high temperatures observed, can be attributed to the lower thermal capacitance associated with that thermody-

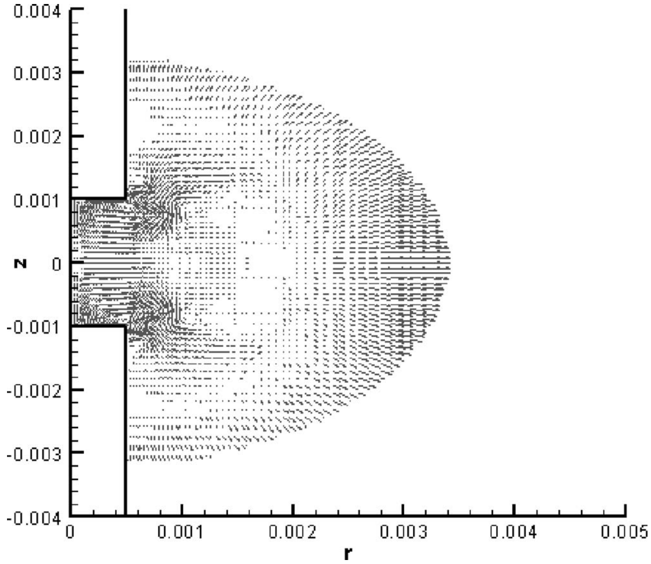

Fig. 12 Velocity vector field at 5.0 μs

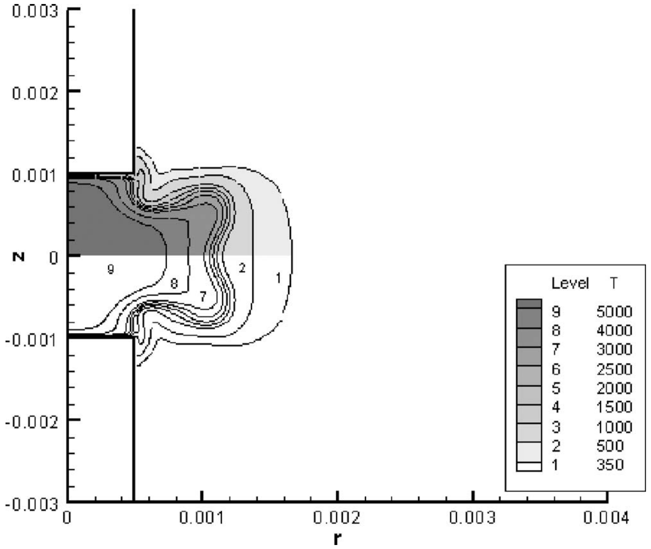

Fig. 14 Temperature distribution at 10.0 μs

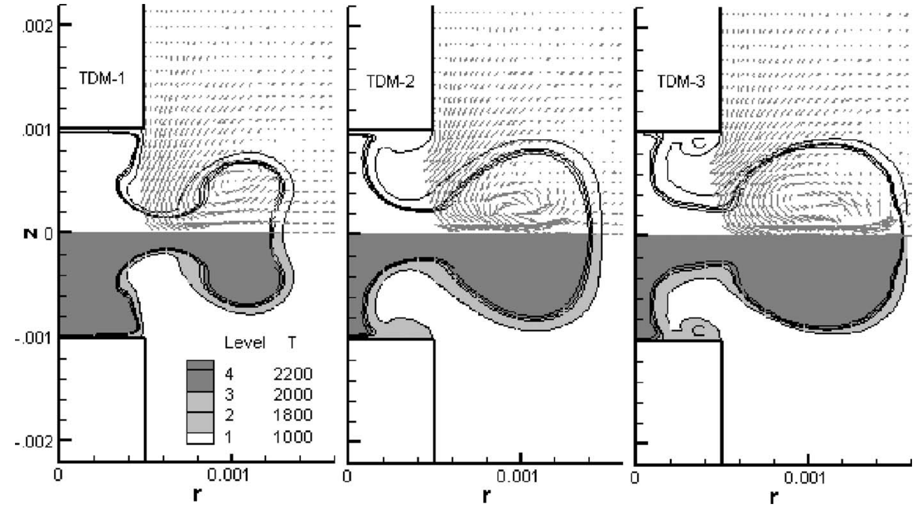

Fig. 15 Temperature contours for the assumed ignition range at 15.0 μs, for TDM-1, TDM-2, and TDM-3

namic model compared to the others. For all the models, the conductive losses are about one order of magnitude larger than the radiative losses. Considering the total energy deposited for all three cases (~14 mJ), approximately one-third of this energy is lost to the electrodes showing the importance of conduction losses. It is interesting to see that the conduction loss for TDM-3 is approximately 20% larger than the other two TDMs. Detailed analysis of the results shows that the differences in conduction losses are mainly due to the radial-component of the conduction on the sidewalls, although this component is only one quarter of the total loss from conduction. Vortex formation near the corner of the electrodes enhances diffusional mixing of the hot gas leaving the spark gap with the cold exterior gas. Similar flow patterns are observed for all three cases while the effects on the mixed temperatures are different. The differences in the final mixed temperature are associated with the effective heat capacity of the particular gas. Since each thermodynamic model has a different thermal capacitance, it is not surprising that there are different mixed temperatures. As it was discussed earlier, the larger effective heat capacity of TDM-3 results in higher gas temperatures associated with it after vortex mixing. Rate of decrease of the temperature is slower for the TDM-3 than for the other models because of its relatively higher thermal capacitance. The vortex formation and resulting complex flow pattern also contribute to the energy transfer between the hot gas and the radial electrode surface. Therefore, TDM-3 shows relatively higher temperatures in the vicinity of the electrodes by sustaining its high temperatures compared to the other models, which manifests itself as higher conduction losses in the radial direction.

Pressure Effects. In this section, simulation results are presented to investigate the effects of ambient pressure on the flow physics and the global spark discharge process. We use the same current profile as was previously used in earlier sections of this paper. In general, the current profile will be different for any given circuit driving current through a spark plug at different pressures. However, our assumption can be realized by assuming that circuit parameters are changed to provide more energy at higher pressures to match the current profiles. Presented results show trends and help us gain more insight into the spark discharge physics. There are two important points that must be mentioned before presenting the simulation results. The first one is that we used the

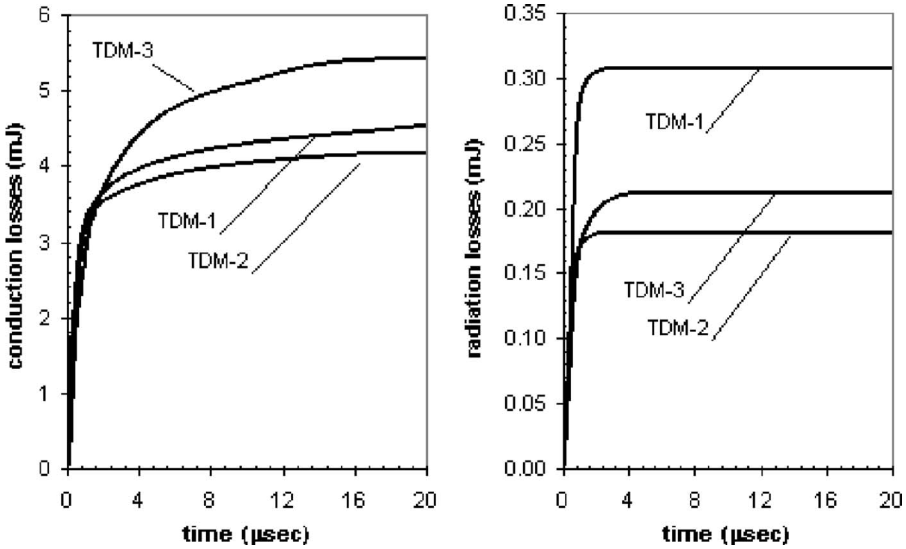

Fig. 16 Conduction to the electrodes and radiated energy as a function of time

same transport properties that we used for the base cases (1 atmosphere ambient pressure). As we previously mentioned, these properties were developed for one atmosphere conditions. As a result there are increased errors in transport properties associated with higher than atmospheric pressure simulations. Also as has been discussed in earlier sections, although it is much smaller when compared to the temperature effects; pressure changes will cause changes in equilibrium compositions which will influence transport properties of the mixture. The second point is that we used the effective γ thermodynamic model (TDM-1) for these simulations. This is a reasonable approach because we found that the average specific heat ratio variation with pressure is less than the variation between two different thermodynamic models (cf. Fig. 1). The integrated average specific heat ratio in the temperature range of 300 to 30,000 K is 1.113 for TDM-3 and 1.165 for TDM-2 at 1 atm; it is 1.167, 1.167, and 1.163 at 2, 4, and 8 atm, respectively, for TDM-2.

The calculated energy deposition is presented in Fig. 17 as a function of time at different pressures. It is seen that energy input to the gas increases with increasing ambient pressure. In Fig. 18, the total energy deposition as a function of ambient pressure is presented in a log-log plot. The power law governing deposited energy with pressure is 1.4. Blast wave and plasma kernel radii are given as a function of time in Fig. 19. We define the plasma kernel as the region where the temperature is above 2000 K. The percentage decrease of the blast wave radius with increasing pressure, relative to 1 atm is shown in Fig. 20. Similarly, the percentage decrease of the plasma kernel radius with increasing, pressure relative to 1 atm. is shown in Fig. 21. It is interesting to note that a pressure increase of a factor 8 results in blast wave and kernel radii decreases of no more than 30% at any given time. In general, the pressure effect on the blast wave radius is relative small compared to the pressure effect on the plasma kernel radius.

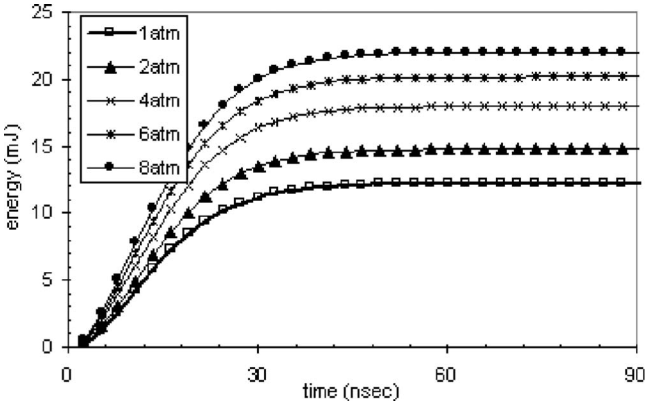

Fig. 17 Energy deposition as a function of time at different pressures

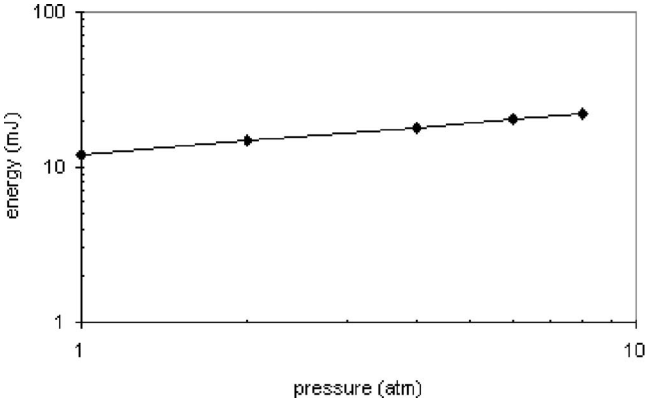

Fig. 18 Total deposited energy as a function of pressure

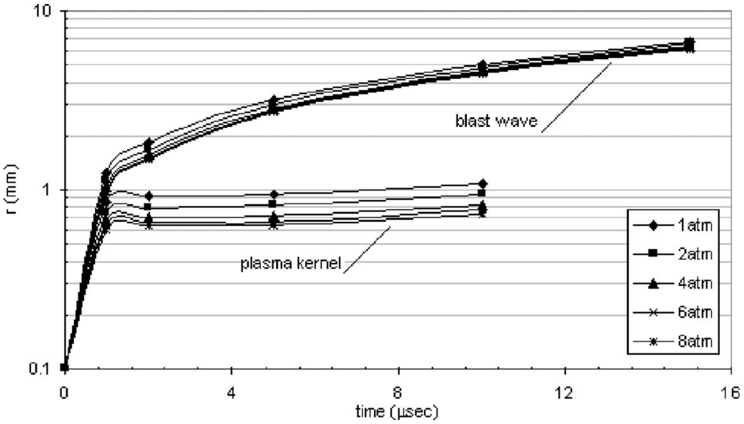

Fig. 19 Blast wave and plasma kernel radii as a function of time

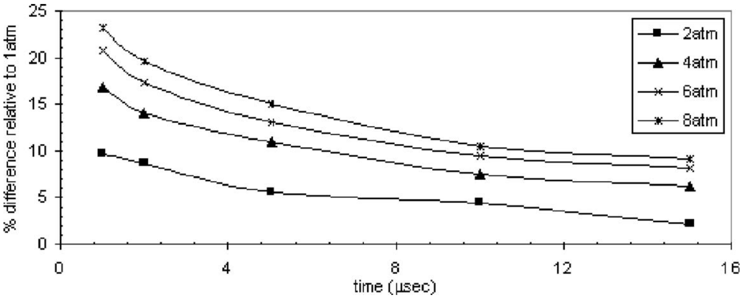

Fig. 20 Percentage decrease in blast wave radius relative to 1 atm values

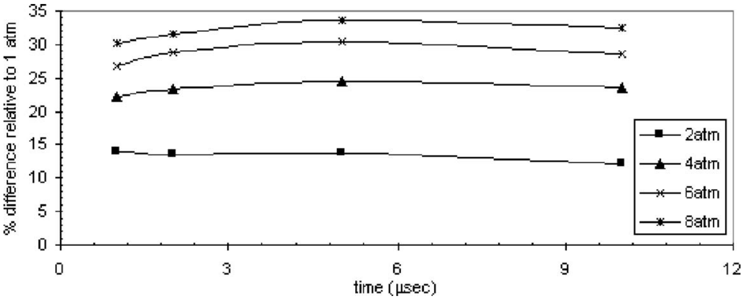

Fig. 21 Percentage decrease in plasma kernel radius relative to 1 atm values

Conclusions

As previously noted, operating requirements in spark-ignited, internal-combustion engines will require more sophisticated ignition systems. Simulation will be an integral part of the design of advanced spark ignitors. This study presents a theoretical model to simulate spark discharge in air. We hope that the findings of the research will aid other spark researchers in their choices of submodels, and also in their understanding of the flow coupling processes to transport and mixing in the near spark gap area.

We investigated the influences of different thermodynamic models available in literature on the simulation results and on the computational cost. Predicted total discharge energies by the three thermodynamic models are very similar to each other and also compared very well to the experimentally measured energy of Borghese [20]. The three thermodynamic models also do quite well in predicting the blast wave radius and the scaled mass density. For very similar results, computational costs are very different for the three thermodynamic models.

We compared one-dimensional and two-dimensional (axisymmetric) models to understand flow physics better. It is found that the one-dimensional model predicts the evolution of high temperature regions reasonably well until the recirculating flows, observed in two-dimensional model, begin. These recirculating flows begin at approximately 10 μs and are associated with the relatively lower pressures found in the spark gap after the initial expansion has occurred. Centerline temperatures are higher for the one-dimensional simulations compared to the two-dimensional simulations due to the influx of cold gas into the spark gap that mix with centerline fluid for the two-dimensional simulation case. We also found that conduction losses to the electrodes which cannot be predicted by one-dimensional models are much larger than the radiation losses.

For all three thermodynamic models, the conductive losses are about one order of magnitude larger than the radiative losses. Most of the radiation loss happens in the first 2 μs for all three thermodynamic models. Considering the total energy deposited for all three cases ($\sim$14 mJ), approximately one-third of this energy is lost to the electrodes showing the importance of conduction losses. It is interesting to see that the conduction loss for TDM-3 is approximately 20% larger than for the other two TDMs.

Finally, we investigated the effects of initial operating pressure on the results. We found that both the blast wave and plasma kernel radii decrease with increasing pressure while the decrease in plasma kernel radius relative to the 1 atm values is slightly greater than that the decrease in the blast wave radius. On the other hand, it is found that the deposited energy is a weakly increasing function of the pressure.

Nomenclature

A_i = levels of dissociation and ionization
$\boldsymbol{B}$ = magnetic induction field
C_i = constants that depend on the statistical weights of the particles
E = total energy per unit volume
$\boldsymbol{E}$ = electric field
e = volume specific energy
I_i = specific energies of the dissociation or ionization
i = total electrical current
$\boldsymbol{j}$ = current density (per unit area)
P = pressure
$\boldsymbol{q}$ = source term for conduction heat transfer
$\boldsymbol{q}_{\text{el}}$ = source term for electrical energy deposition
$\boldsymbol{q}_{\text{rad}}$ = source term for radiation heat transfer
R = gas constant
r = radial coordinate
T = temperature
t = time
$\boldsymbol{u}_e$ = velocity of a charged particle
$\boldsymbol{V}$ = velocity field components
z = axial coordinate
γ = specific heat ratio
ε = mass specific energy
θ_{ϖ} = vibrational temperature
ρ = density
σ = electrical conductivity

References

[1] Kravchik, T., Sher, E., and Heywood, J. B., 1995, "From Spark Ignition to Flame Initiation," Combust. Sci. Technol., **108**, pp. 1–30.
[2] Lim, M. T., Anderson, R. W., and Arpaci, V. S., 1987, "Prediction of Spark Kernel Development in Constant Volume Combustion," Combust. Flame, **69**, pp. 303–316.
[3] Maly, R., and Vogel, M., 1978, "Initiation and Propagation of Flame Fronts in Lean CH_4-air Mixtures by the Three Modes of the Ignition Spark," *17th Symposium (International) on Combustion*, pp. 821–831.
[4] Bradley, D., and Lung, F. K.-K., 1987, "Spark Ignition and the Early Stages of Turbulent Propagation," Combust. Flame, **69**, pp. 71–93.
[5] Soldera, F. A., Mucklich, F. T., Hrastnik, K., and Kaiser, T., 2004, "Description of the Discharge Process in Spark Plugs and its Correlation With the Electrode Erosion Patterns," IEEE Trans. Veh. Technol., **53**, pp. 1257–1265.
[6] Reinmann, R., 1998, "Theoretical and Experimental Studies of the Formation of Ionized Gases in Spark Ignition Engines," *Lund Reports on Combustion Physics, LRCP-37*, Lund Institute of Technology, Lund, Sweden.
[7] Herweg, R., and Maly, R. R., 1992, "A Fundamental Model for Flame Kernel Formation in S.I. Engines," SAE Paper No. 922243.
[8] Shen, H., Hinze, P. C., and Heywood, J. B., 1994, "A Model for Flame Initiation and Early Development in SI Engine and its Application to Cycle to Cycle Variations," SAE Paper No. 942049.
[9] Anbarasu, M., Abata, D. L., and Moilanen, P. C., 1994, "Modeling of Early Pressure Rise and Flame Growth in a Spark Ignition Engine," SAE Paper No. 941930.
[10] Sedov, L. I., 1959, *Similarity and Dimensional Methods in Mechanics* (translated by M. Friedman), Academic Press, New York.
[11] Sher, E., and Refael, S., 1982, "Numerical Analysis of Early Phase Development of Spark-Ignited Flames in CH_4-air Mixture," *19th Symposium (International) on Combustion*, pp. 251–257.
[12] Rafael, S., and Sher, E., 1985, "A Theoretical Study of Ignition of a Reactive Medium by Means of Electrical Discharge," Combust. Flame, **59**, pp. 17–30.

[13] Sher, E., and Keck, J. C., 1986, “Spark Ignition of Combustible Gas Mixtures,” Combust. Flame, **66**, pp. 17–25.

[14] Sher, E., Ben-Ya’ish, J., and Kravchik, T., 1992, “On the Birth of Spark Channels,” Combust. Flame, **89**, pp. 186–194.

[15] Akram, M., and Lundgren, E., 1996, “The Evolution of Spark Discharges in Gases: I. Macroscopic Models,” J. Phys. D, **29**, pp. 2129–2136.

[16] Akram, M., 1996, “The Evolution of Spark Discharges in Gases: II. Numerical Solution of One-Dimensional Models,” J. Phys. D, **29**, pp. 2137–2147.

[17] Akram, M., 1996, “Two-Dimensional Model for Spark Discharge Simulation in Air,” AIAA J., **34**, pp. 1835–1845.

[18] Thiele, M., Selle, S., Riedel, U., Warnatz, J., Schießl, R., and Maas, U., 2002, “A Detailed Two-Dimensional Study of Spark Ignition Including Ionization,” SAE Paper No. 2002-01-1110.

[19] Thiele, M., Warnatz, J., and Maas, U., 2000, “Geometrical Study of Spark Ignition in Two Dimensions,” Combust. Theory Modell., **4**, pp. 413–434.

[20] Borghese, A., D’Alessio, A., Diana, M., and Venitozzi, C., 1988, “Development of Hot Nitrogen Kernel, Produced by a Very Fast Spark Discharge,” *22nd Symposium (International) on Combustion*, pp. 1651–1659.

[21] Akindelle, O. O., Bradley, D., Mak, P. W., and McMahon, M., 1982, “Spark Ignition of Turbulent Gases,” Combust. Flame, **47**, pp. 129–155.

[22] Boulos, M. I., Fauchais, P., and Pfender, E., 1994, *Thermal Plasmas*, Plenum Press, New York, Vol. 1.

[23] Capitelli, M., Colona, G., Gorse, C., and D’Angola, A., 2000, “Transport Properties of High Temperature Air in Local Thermodynamic Equilibrium,” Eur. Phys. J. D, **11**, pp. 279–289.

[24] Plooster, M. N., 1970, “Shock Waves From Line Sources. Numerical Solutions and Experimental Measurements,” Phys. Fluids, **13**, pp. 2665–2675.

[25] Giordano, D., Capitelli, M., Colona, G., and Gorse, C., 1994, ESA STR-237.

[26] Selle, S., and Riedel, U., 2000, “Transport Coefficients of Reacting Air at High Temperatures,” AIAA 2000-0211, 38th Aerospace Sciences Meeting and Exhibit, January 10–13, Reno, NV.

[27] Nagizadeh-Kashani, Y., Cressault, Y., and Gleizes, A., 2002, “Net Emission Coefficient of Air Thermal Plasmas,” J. Phys. D, **35**, pp. 2925–2934.

[28] Boris, J. P., Landsberg, A. M., Oran, E. S., and Gardner, J. H., 1993, “LCPFCT- Flux-Corrected Transport Algorithm for Solving Generalized Continuity Equations,” Report No. NRL/MR/6410-93-7192, Naval Research Laboratory, Washington, DC.

[29] Boris, J. P., and Book, D. L., 1997, “I. Shasta, a Fluid Transport Algorithm That Works,” J. Comput. Phys., **135**, pp. 172–186.

[30] Sun, M., and Takayama, K., 2003, “Vorticity Production in Shock Diffraction,” J. Fluid Mech., **478**, pp. 237–256.

Robert F. Kunz

Howard J. Gibeling

Applied Research Laboratory,
Pennsylvania State University,
University Park, PA 16803

Martin R. Maxey
Brown University,
Providence, RI 02912

Gretar Tryggvason
Worchester Polytechnic Institute,
Worchester, MA 01609

Arnold A. Fontaine

Howard L. Petrie

Applied Research Laboratory,
Pennsylvania State University,
University Park, PA 16803

Steven L. Ceccio
University of Michigan,
Ann Arbor, MI 48109

Validation of Two-Fluid Eulerian CFD Modeling for Microbubble Drag Reduction Across a Wide Range of Reynolds Numbers

An Eulerian two-fluid computational fluid dynamics model has been developed for flows with microbubble drag reduction (MBDR). This paper focuses on recent validation studies for MBDR flows across a spectrum of Reynolds numbers. Direct numerical simulations and two sets of experimental flat plate boundary layer measurements are studied. In this paper, the interfacial dynamics and other models used are first presented, followed by detailed comparisons with the validation cases. Emphasis is placed on the modeling strategies required to capture measured volume fraction, bubble size, and bubble velocity distributions, as well as skin friction drag reduction. [DOI: 10.1115/1.2375124]

Introduction

When gas flow is injected into liquid boundary layers, significant drag reduction can be achieved. Beyond a certain critical injection flow rate the entire surface becomes enveloped in a layer of gas, but for injection rates well below this regime, the boundary layer flow is characterized as laden with a size spectrum of microbubbles with local gas volume fractions that can exceed 0.5. The physics associated with these microbubble laden boundary layer flows, and attendant drag reduction, have been studied for decades (McCormick and Bhattacharyya [1], Bogdevich and Evseev [2], Legner [3], Marie [4], Merkle and Deutsch [5], Kato et al. [6], Meng and Uhlman [7], for example), but remain only partially understood, and remain a source of ongoing experimental and analytical/computational modeling.

The drag reduction that can be achieved is known to be dependent on gas injection flow rates, gas type, Reynolds number, Froude number, streamwise pressure gradient, surface roughness, bubble size, details of the injection scheme, and the presence of surfactants, each of which have been studied experimentally in the literature. The inherent difficulties in obtaining measurements on complex configurations at high Reynolds numbers across such a wide range of parameters, motivates the development of a modeling capability that accommodates microbubble drag reduction (MBDR) physics.

Direct numerical simulation of bubbly flows can provide insight into the physics of bubbly boundary layer flows, and help guide closure for multiphase Reynolds averaged (or otherwise averaged) Navier-Stokes methods. However, direct numerical simulation of high concentration bubbly boundary layers over practical geometries will not be computationally feasible for decades due to the very high Reynolds numbers ($>10^9$ for surface ships), high bubble volume fractions (>0.5), and inherent three dimensionality and complexity of realistic injector and hull form geometries. On the other hand, two-fluid computational fluid dynamics (CFD) models that invoke averaging and attendant closure of the instantaneous physics are attractive for MBDR flows because: (1) simulations can be performed for realistic configurations within processor hours-to-weeks on modern parallel computers; (2) first order physical mechanisms *known* to be important in MBDR (bubble dynamics, mixture density, buoyancy, and turbulence effects) can be incorporated; and (3) all of the physical mechanisms currently *conjectured* to be important in MBDR (and discussed below) can be modeled within a two-fluid prescription. Accordingly, two-fluid CFD is the level of modeling employed in the present work.

Though much controversy still exists (including among the coauthors of this paper) regarding the physical mechanisms of MBDR, several mechanisms have been put forward as playing a role in the observed drag reduction including: (1) transport effects associated with mixture density, and thereby Reynolds stress, being diminished in the turbulent boundary layer (TBL) (e.g., Legner [3]); (2) turbulence energy extraction associated with breakup (Meng and Uhlman [7]); (3) diminished turbulence production associated with dilatation caused by local gradients of bubble concentration in the vicinity of the quasistreamwise vortical structures (Ferrante and Elghobasi [8,9]); and (4) bubble deformation and associated disruption of production related vortical structures (Tryggvason and Lu [10]). Each of these mechanisms are plausibly significant at the very high Reynolds numbers and gas volume

---

Contributed by the Fluids Engineering Division of ASME for publication in the JOURNAL OF FLUIDS ENGINEERING. Manuscript received August 11, 2005; final manuscript received May 27, 2006. Assoc. Editor: Timothy J. O'Hern. Paper presented at the 2nd International Symposium on Seawater Drag Reduction.

fractions of interest in maritime application of MBDR, but the difficulties associated with experimental measurements and direct numerical simulations (DNS) simulations at high Reynolds numbers and gas volume fractions, make it difficult to assess the relative importance of these potential contributors.

The authors have been evolving the CFD code used in this paper for MBDR applications for several years (Kunz et al. [11]). This experience has led us to the belief that bubble transport, interfacial dynamics, and mass transfer (coalescence and breakup), and the resulting distribution of lower mixture density near the wall, remains a major contributor to MBDR. This belief is based on our observations, included herein, that modeling the bubble kinematics and dynamics such that local bubble gas fraction, bubble velocities, and bubble sizes are well predicted across and along a TBL, leads to good predictions of drag reduction. Whether simply "getting the mixture density right" represents the most important element of MBDR at high Reynolds numbers remains unknown. Therefore, the ability of a CFD model to predict local bubble transport physics, with good accuracy, is necessary, but perhaps not sufficient, for predicting MBDR accurately at naval application scales.

The bubble dynamics and mass transfer (coalescence and breakup) physics present in MBDR flows are challenging to model. The very high gas fractions that arise violate the disperse-flow assumptions that are invoked in most open literature interfacial dynamics models for bubbly flows. High local gas fraction also contributes to the paucity of experimental validation data that is available for these flows, especially distributions of flow parameters normal to the wall, so validation of models that are proposed is difficult.

Nevertheless models must accommodate: (1) the interface dynamics of drag, virtual mass, lift, and dispersion, leading to bubble distributions that are characterized by gas volume fraction profiles that are peaked at wall distances less than 0.3δ; (2) breakup and coalescence physics, competing to establish an evolving bubble size distribution, where most bubbles lie in the $100-500\ \mu$m range; and (3) injected gas, subject to very high liquid shear that leads to rapid breakup of the jet of gas emanating from the injector, which at high gas injection rates form sheet-like or tendril-like structures, extending well into, and significantly perturbing the boundary layer.

The need to develop models for the high gas fraction, high Reynolds number flow regimes observed in MBDR requires validation data across a wide range of Reynolds numbers. At low Reynolds numbers, DNS can be performed to obtain very detailed local validation data, new or improved understanding of the underlying physical mechanisms at play, and model guidance for ensemble or otherwise averaged macroscale CFD models. Research of this type has been carried out by the third and fourth authors of this paper under the same U.S. Defense Advanced Research Projects Agency (DARPA) program that sponsored the engineering code development pursued by the first and second authors. Some of this DNS work is used in the validation studies summarized in this paper, and manuscripts dedicated to this topic appear in Dong et al. [12], Tryggvason and Lu [10].

As part of this coordinated DARPA sponsored MBDR program, a very high Reynolds flat plate measurement program has been carried out by the seventh author of this paper and his colleagues (Sanders et al. [13]). This program has provided near prototypical Reynolds number validation data that is employed in validation studies summarized below. Lastly, a moderate Reynolds number flat plate MDBR experimental program has been carried out under the same sponsorship to provide wall normal distributions of gas fraction and bubble velocity for the third class of validation studies summarized below. This work, carried out by the fifth and sixth authors of this paper and their colleagues is described in Fontaine et al. [14].

As stated above, the results of three classes of applications are presented across a wide range of Reynolds numbers. First, a temporally evolving channel flow with microbubble injection is simulated at Reynolds numbers ranging from $200 \leqslant \mathrm{Re}^* \ (\equiv u^* h/\nu) \leqslant 800$. These Eulerian two-fluid simulations are compared to direct simulations based on the force coupling method (FCM) developed by the third author of this paper.

Recently obtained flat plate measurements, taken in the 12 in. water tunnel at the Pennsylvania State University Applied Research Laboratory, represent the second class of MBDR flows used for validation. These measurements include bubble volume fraction profiles, bubble velocity profiles, shear stress measurements, and photographically obtained/processed bubble size and deformation distributions for three gas injection flow rates at Reynolds numbers from $3.1\times 10^6 \leqslant \mathrm{Re}_x \leqslant 9.4\times 10^6$.

The final set of validation studies focus on a very high Reynolds number flat plate (HIPLATE) measurements performed in the large cavitation channel (LCC) operated by the U.S. Navy in Memphis, TN. These measurements include bubble velocities, bubble size distributions, and shear stress measurements for a range of gas injection flow rates at Reynolds numbers up to $\mathrm{Re}_x = 2.1\times 10^8$.

The authors' preliminary work in this area (Kunz et al. [11]) employed almost exclusively "standard" (i.e., open literature) models for interfacial dynamics, and did not model coalescence and breakup at all. The availability of the present DNS data, and two sets of flat plate data for evolution of the modeling was critical in the validation process. Indeed, each of these data sets elucidated major errors in the local conditions predictions returned by the code, that gave rise to further modeling efforts. The resulting evolution of the model set that arose from these efforts is summarized in detail below and is principally related to: turbulence dispersion; large gas-volume fraction; and large relative velocity impact on drag, virtual mass, and near wall models; and mass transfer.

The paper is organized as follows: First the governing differential system, closure models, and numerics are presented. Each of the three validation studies are then presented. A summary discussion is provided that characterizes the authors' view of the status and remaining challenges of this work.

Theoretical Formulation

Governing Equations. The single-pressure ensemble averaged continuity and momentum equations are cast in conservation law form as

$$\frac{\partial}{\partial x_j}(\alpha^k \rho^k u_j^k) = \sum_{k\neq l}(\Gamma^{lk} - \Gamma^{kl})$$

$$\frac{\partial}{\partial x_j}(\alpha^k \rho^k u_i^k u_j^k) = -\alpha^k \frac{\partial p}{\partial x_i} + \frac{\partial}{\partial x_j}\left[\alpha^k u_t^k\left(\frac{\partial u_i^k}{\partial x_j} + \frac{\partial u_j^k}{\partial x_i}\right)\right] + \rho^k \alpha^k g_i + M_i^{kl} + \sum_{k\neq l}(D^{kl}[u_i^l - u_i^k] + \Gamma^{lk} u_i^l - \Gamma^{kl} u_i^k) \qquad (1)$$

where each field's density ρ^k, is here taken as constant. Superscripts k and l designate donor and receptor fields for mass transfer (Γ^{kl}), and drag (D^{kl}) and nondrag (M_i^{kl}) interfacial forces.

Physical Models. The authors apply the generalized n-field formulation in Eq. (1) to MBDR flows in two ways. The more fundamental approach involves solving a single continuous liquid field and a number of bubble fields, "binned" by size. In this approach each bubble field exchanges momentum with the continuous field through drag and nondrag interfacial forces which depend in magnitude on the local interfacial area density of that field $A_{\mathrm{int}} = 6\alpha^{\mathrm{gas}}/D_b$ (for spherical bubbles). This approach was used in our earlier work (Kunz et al. [11]), where up to 11 bubble fields were solved.

Interfacial Area Density Transport. An alternative is to solve a single gas field continuity and momentum equation, and employ an interfacial area density transport (IADT) equation to determine a local mean characteristic diameter for the bubbles. This approach significantly reduces the model's CPU requirements compared to solving an $(N+1)$-field system (N bubble fields). The numerical complexity associated with interfield transfer terms is also reduced considerably.

Since coalescence and breakup can be fully accommodated in the context of IADT (details presented below), the physical appropriateness of employing IADT rests on whether the bubble dynamics can be sufficiently captured using a single local mean gas-liquid interfacial area, with an assumed/modeled distribution of bubble size about that mean. This is demonstrated to be the case for MBDR flow below.

Following Hibiki et al. [15], the IADT equation with source terms for breakup and coalescence can be written

$$\frac{\partial A_{\text{int}}}{\partial t} + \nabla \cdot (A_{\text{int}}\vec{V}^{\text{gas}}) = \Phi_B + \Phi_C \qquad (2)$$

where Φ_B and Φ_C are source terms for breakup and coalescence, respectively. The source terms are rates of change of interfacial area concentration

$$\Phi_B \equiv \frac{1}{3\psi}\left(\frac{\alpha^{\text{gas}}}{A_{\text{int}}}\right)^2 \varphi_B; \quad \Phi_C \equiv \frac{-1}{3\psi}\left(\frac{\alpha^{\text{gas}}}{A_{\text{int}}}\right)^2 \varphi_C \qquad (3)$$

where ϕ_B and ϕ_C are the rates of change of bubble number density $(1/(\mathrm{m}^3\mathrm{s}))$ due to breakup and coalescence, respectively. The factor ψ depends on the bubble shape, here taken as spherical, so $\psi = 1/(36\pi)$. The particular models used for breakup and coalescence for MBDR are presented below.

Figure 1 illustrates that the dynamics of MBDR can be sufficiently captured using a single local mean gas-liquid interfacial area, with an assumed/modeled distribution of bubble size about that mean. Three HIPLATE MBDR cases are considered, corresponding to three gas injection rates. First, each case was run with three bubble fields using an approximation to the experimentally measured bubble size distribution. Then each case was run using a single gas field and interfacial area density as described above. For these comparisons no coalescence or breakup was incorporated so as to isolate the effect of the different interfacial dynamics modeling approaches. Details of the HIPLATE simulations are provided below, but Fig. 1 serves to illustrate that incorporating interfacial area density has only a small impact on accuracy of DR and bubble velocity predictions for MBDR.

Bubble Dynamics. A corrected Stokes drag law is employed

$$D^{kl} = \frac{1}{8}\rho^{\text{liq}} C_D |u_i^l - u_i^k| A_{\text{int}}, \quad A_{\text{int}} = \frac{6\alpha^{\text{gas}}}{D_b} \qquad (4a)$$

$$C_D = \frac{24}{\mathrm{Re}_B} f_D(\mathrm{Re}_B) \qquad (4b)$$

where the local bubble Reynolds number is $\mathrm{Re}_B \equiv \rho^{\text{liq}} |\bar{V}^{\text{rel}}| D_b / \mu_m$. For water without impurities, the drag-law correction (Loth [16], for example) is

$$f_D = 1 + (3/6)\mathrm{Re}_B \quad \text{for } \mathrm{Re}_B < 0.1$$

$$f_D = 1 + 0.0565\,\mathrm{Re}_B^{0.525} \quad \text{for } 0.1 \leqslant \mathrm{Re}_B \leqslant 500 \qquad (4c)$$

For contaminated (tap) water, the drag-law correction for solid spheres (Loth et al. [16], for example) is used.

$$f_D = 1 + (3/16)\mathrm{Re}_B \quad \text{for } \mathrm{Re}_B < 1$$

$$f_D = 1 + 0.1935\,\mathrm{Re}_B^{0.6305} \quad \text{for } 1 \leqslant \mathrm{Re}_B \leqslant 285$$

$$f_D = 1 + 0.015\,\mathrm{Re}_B + 0.2283\,\mathrm{Re}_B^{0.427} \quad \text{for } 285 < \mathrm{Re}_B \leqslant 2000 \qquad (4d)$$

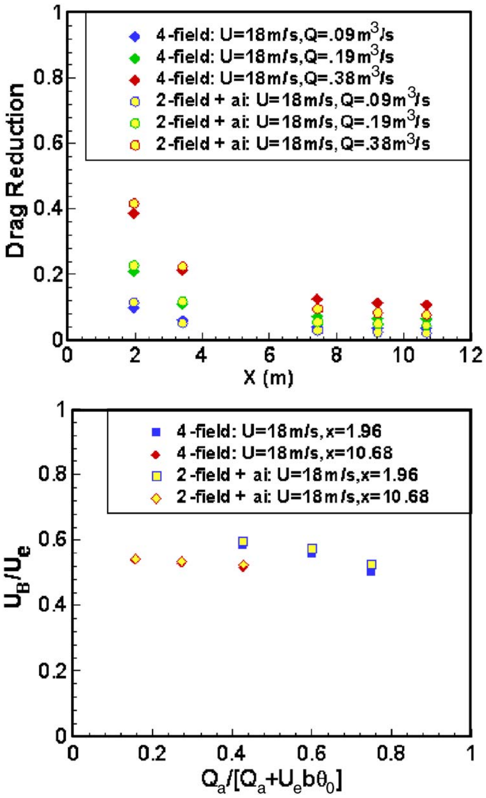

Fig. 1 Comparison of two-field and four-field simulations for $U_\infty = 18$ m/s HIPLATE cases. (top) Drag reduction vs. x. (bottom) Normalized bubble velocity vs. normalized flow rate.

In addition to water purity, locally high gas volume fraction and bubble deformation can influence the drag, so corrections to the spherical bubble, disperse flow model in Eq. 4 may be appropriate. For uniformly disperse flows, an increased drag coefficient is appropriate (Richardson-Zaki [17], for example), and for flows where gas structures are streamlined (bubble columns, sheets) a reduced drag coefficient is appropriate. The authors believe that this latter effect is important in the near injector region of MBDR flows, where application of the standard disperse flow model gives rise to too much local drag, thereby inhibiting the penetration of the injected gas into the boundary layer. This observation became clear in the course of the HIPLATE validation studies, where a significant defect in measured bubble velocity could not be obtained unless a "cluster" drag model was incorporated. Specifically, we have adapted a model proposed by Johansen and Boysan [18] to an Eulerian framework:

$$C_D = C_{D0}(1. - 1.54[\mathrm{MIN}(.5157, \alpha^{\text{gas}})]^{2/3}) \qquad (5)$$

where C_{D0} is the original drag coefficient in Eq. (4b), α^{gas} is the total gas volume fraction and the MIN function is provided to ensure that the corrected drag coefficient does not drop to below 1% of the uncorrected value. The importance of incorporating such a cluster drag form is demonstrated below.

Virtual mass is modeled following Lahey and Drew [19]

$$\vec{M}_{VM}^{\text{liq-gas}} = \alpha^{\text{gas}}\rho^{\text{liq}} C_{VM}\left[\frac{D\vec{V}^{\text{gas}}}{Dt} - \frac{D\vec{V}^{\text{liq}}}{Dt}\right] \qquad (6)$$

By incorporating virtual mass, bubble response times are increased (by several orders of magnitude in the $D_b \cong 100-500\ \mu\mathrm{m}$ range of relevance to MBDR), so the rapid acceleration of injected bubbles toward the freestream velocity is slowed. This in turn reduces the relative velocity at the first HIPLATE measurement station providing significantly improved comparison with the measurements as illustrated below.

Bubble lift is significant in MBDR flows. Near the injector, large relative velocities and liquid shear is present. Also, the authors believe that lift is a major contributor to loss of MBDR persistence. Specifically, the relative velocity gives rise to a lift force away from the wall, which at the scales of interest, gradually starves the near wall boundary layer of bubbles resulting in recovery of the boundary layer toward single phase skin friction values. The model employed in the present work also follow Lahey and Drew [19]

$$\vec{M}^{\text{liq-gas}}_{\text{LIFT}} = \alpha^{\text{gas}}\rho^{\text{liq}}C_L\vec{V}^{\text{rel}} \times \nabla \times \vec{V}^{\text{liq}} \tag{7}$$

Illustration of the topological and DR effects of lift are provided below.

An empirical turbulent near-wall bubble lift force has been implemented based on the formulation of Kawamura and Yoshiba [20]. This force can be thought of as a repulsive force due to wall collisions. The form of the wall-lift force used is

$$F_{\text{WL}} = C_{\text{WL}}(\pi D_B^3/6)\rho^{\text{liq}}(k/D_B)F_{\text{damp}}$$

$$F_{\text{damp}} = 0.5[1 - \tanh(y_{\text{wall}}/D_B - 1.5)] \tag{8}$$

where F_{damp} decays the force to zero away from the wall and the model constant used here $C_{\text{WL}}=0.012/\sqrt{1+\text{St}_k}$ is significantly smaller than that proposed by Kawamura and Yoshiba. The Stokes number is defined as $\text{St}_k=D_B^2\rho^{\text{liq}}\varepsilon/(18k\mu_m)$.

Two models for dispersion based on homogeneous turbulence have been implemented. Lopez de Bertodano [21] presented a dispersion model assuming homogeneous, isotropic turbulence. This model form, with a Stokes number correction from Moraga et al. [22] is

$$\vec{M}^{\text{liq-gas}}_{\text{TD}-L} = -\rho^{\text{liq}}kC^L_{\text{TD}}C_\mu^{1/4}\frac{1}{\text{St}_r(1+\text{St}_r)}\frac{\nabla\alpha^{\text{gas}}}{\alpha^{\text{gas}}} \tag{9a}$$

with the Stokes number defined as $\text{St}_r \equiv \tau_r/\tau_c$. The bubble response time τ_r and the turbulent time scale of the continuous phase τ_c (based on the characteristic length of turbulent eddies and the relative velocity of the bubble) are given by

$$\tau_r = \frac{4}{3}\frac{D_b}{C_D|\vec{V}_{\text{rel}}|}, \quad \tau_c = C_\mu^{3/4}\frac{k}{\varepsilon} \tag{9b}$$

The homogeneous turbulent dispersion model due to Carrica et al. [23] is

$$\vec{M}^{\text{liq-gas}}_{\text{TD}-C} = -\rho^{\text{liq}}\frac{\nu_T^{\text{liq}}}{S_{\text{CT}}}C^C_{\text{TD}}\frac{3}{4}\frac{C_D}{D_B}|\vec{V}_{\text{rel}}|\frac{\nabla\alpha^{\text{gas}}}{\alpha^{\text{gas}}} \tag{10}$$

where the turbulent Schmidt number $S_{\text{CT}}=1$.

At the high gas volume fractions that occur in MBDR applications, dispersion is enhanced by collisions among bubbles. A new dispersion model is presented here, based on the collision frequency from the Prince-Blanch [24] coalescence model. This dispersion mechanism is used in addition to one of the homogeneous turbulence dispersion models discussed above. A summary of the new model is given here.

The collision-induced dispersion model is implemented in the framework of the Carrica et al. [23] gradient-diffusion force model. The general expression for the dispersive force per unit volume may be written as

$$\vec{M}^{\text{liq-gas}}_{\text{TD-coll}} = -\rho\frac{\nu_T^{\text{liq}}}{S_{\text{CT}}}C^{\text{coll}}_{\text{TD}}\frac{\nabla\alpha^{\text{gas}}}{\alpha^{\text{gas}}} \tag{11}$$

We assume the dispersion model coefficient is an unknown function of the "dispersive collision rate," which excludes bubbles that coalesce. To properly formulate the coefficient relationship, the collision rate must be normalized. For that purpose we choose a turbulent bubble characteristic time defined as

$$\tau_{\text{BC}} = k^{3/2}/(|\vec{V}^{\text{rel}}|\varepsilon) \tag{12}$$

where k is the turbulent kinetic energy. Note that this bubble response time is different than that normally used to define the Stokes number above.

It is assumed that the bubbles that do not coalesce rebound and thus contribute to the turbulent dispersion process. Thus a normalized dispersive collision rate $\overline{\theta}^{\text{TD}}$ for two bubbles with an equivalent volume v_{eq} is written as

$$\overline{\theta}^{\text{TD}} = \theta^T_C V_{\text{eq}}(1-\lambda_{\text{eff}})\tau_{\text{BC}}$$

$$V_{\text{eq}} = 2(\pi D_B^3/6) \tag{13}$$

where θ^T_C and λ_{eff} are the turbulent collision rate and collision coalescence efficiency defined in Eq. (15).

At present, the turbulent collision-dispersion coefficient $C^{\text{coll}}_{\text{TD}}$ is chosen to be proportional to the square root of the dispersive collision rate (normalized by a representative time scale τ_{BC})

$$C^{\text{coll}}_{\text{TD}} = \frac{\hat{C}^{\text{coll}}_{\text{TD}}}{\tau_{\text{BC}}}[\overline{\theta}^{\text{TD}}]^{1/2} \tag{14}$$

Note that the square-root form in Eq. (14) is consistent in functional form with the collision pressure concept (Batchelor [25]).

In the present work, the force constants in the interfacial dynamics models, Eqs. (2)–(14), are taken as

$$C_L = 0.03, \quad C_{\text{VM}} = 0.5, \quad C^C_{\text{TD}} = 10, \quad C^L_{\text{TD}} = 0.5, \quad \hat{C}^{\text{coll}}_{\text{TD}} = 200$$

Breakup and Coalescence. For coalescence we use the Prince and Blanch [24] rate kernel and for breakup we use the Martinez-Bazan et al. [26] rate kernel. Assuming that the mass transfer rates may be evaluated using the mean bubble diameter D_B the bubble collision rate is written

$$\varphi_C = \theta^T_C\lambda_{\text{eff}}, \quad \theta^T_C = n_B^2\left(\frac{\pi}{2}\right)\varepsilon^{1/3}D_B^{7/3}$$

$$\lambda_{\text{eff}} = \exp(-t_B/\tau_B) \tag{15}$$

where n_B is the bubble number density, ε is the turbulence energy dissipation rate, λ_{eff} is the collision efficiency (i.e., the probability that a collision results in coalescence), t_B is the time required for two bubbles of diameter D_B to coalesce, and τ_B is the contact time for the two bubbles. In the interfacial area density formulation, the bubble number density is given by: $n_B=A_{\text{int}}/(\pi D_B^2)$.

The time required for two bubbles to coalesce is given by

$$t_B = \left(\frac{(0.5D_B)^3\rho^{\text{liq}}}{16\sigma}\right)^{1/2}\ln\left(\frac{h_o}{h_f}\right) \tag{16}$$

where h_0 is an initial film thickness between two bubbles as they just come into contact, and h_f is a final critical film thickness where rupture occurs and the bubbles coalesce. For air-water systems, the film thickness values quoted by Prince and Blanch (from other sources) are $h_0=10^{-4}$ m and $h_f=10^{-8}$ m. Finally, an estimate of the contact time for bubbles in turbulent flow was made by Levich [27] from dimensional analysis. A modification due to the relative velocity between the bubbles is noted by Carrica et al. [23] resulting in the following expression:

$$\tau_B = \frac{D_{\text{ch}}}{|\vec{V}^{\text{rel}}_B| + 2(0.5D_{\text{ch}}\varepsilon)^{1/3}} \tag{17}$$

where D_{ch} is a characteristic length related to the bubble sizes and $|\vec{V}^{\text{ref}}_B|$ is the mean relative velocity between the colliding bubbles. The characteristic length D_{ch} in Eq. (17) may be taken as an adjustable parameter in this model. In the absence of better information, D_{ch} will be taken as $D_{\text{ch}}=D_B$, following Chesters and Hofman [28].

The breakup frequency of Martinez-Bazan et al. [26] is given by

$$\theta_B^T = \frac{K_g}{D_B}\sqrt{\beta_M(\varepsilon D_B)^{2/3} - 12\sigma/(\rho D_B)} \tag{18}$$

where the model constants are $\beta_M=8.2$ and $K_g=0.25$. The maximum stable bubble size that can exist without breaking is given by

$$D_{\text{ST}} = \left(\frac{12\sigma}{\beta_M \rho}\right)^{3/5} \varepsilon^{-2/5} \tag{19}$$

An approximate formulation including bubble breakup and coalescence within the interfacial area framework was proposed by Lehr and Mewes [29]. Lehr and Mewes solved the population balance equation "to describe the evolution of bubble sizes in two-phase flow." To reduce the numerical complexity due to a large number of equations and strong coupling, they formulated an equation for average bubble volume (equivalent to the interfacial area transport equation) using an approximate analytical approach. A summary of the Lehr-Mewes approach follows. Source terms in the population balance equation involve breakup and coalescence kernel functions that are a function of the bubble volume v. By assuming that an arithmetically averaged bubble volume $(\bar{v})$ may be used in the kernel functions, a simplified solution for the bubble number-density distribution function $f(v)$, result

$$f(v) = \frac{\alpha_g}{\bar{v}^2}\exp\left(-\frac{v}{\bar{v}}\right) \tag{20}$$

$$n_B = \int_0^\infty f(v')dv' = \frac{\alpha_g}{\bar{v}} \tag{21}$$

Lehr and Mewes obtained a transport equation for average bubble volume with simplified source terms due to breakup and coalescence (equivalent to the source terms Φ_B and Φ_C and in Eq. (2)). The bubble number-density pan distribution function (PDF) implies a bubble size distribution consistent with the above noted assumptions. We use this PDF to evaluate bubble number densities for discrete "bins." The bins are defined as follows:

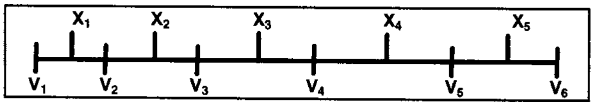

Here x_i is the representative bubble bin volume (e.g., average or midpoint volume) of bin "i" and v_{i-1} and v_i are the lower and upper bin volumes of bin "i," respectively. The number density PDF of bubbles in bin "i" is then

$$N_{B(i)} = \frac{\alpha_g}{\bar{v}}\left(e^{-v_{i-1}/\bar{v}} - e^{-v_i/\bar{v}}\right) \tag{22}$$

This result approaches the number density PDF for a sufficiently large number of bins and a sufficiently large maximum bin volume. Also the first bin is assumed to contain all bubbles from zero bin volume to the uppermost volume of this bin (i.e., $v_1=0$). Further to prevent errors due to an insufficiently "large" maximum volume, the distribution must normalized such that $\Sigma_{\text{all bins}} N_{B(i)} = 1$.

Turbulence model. The authors' work in the MBDR area has involved applying low and high Reynolds numbers from two-equation turbulence models (Kunz et al. [11]) and a low Reynolds number four-equation $v2f$ model (Durbin [30]). Our experience has been that, for MBDR flows, the particular choice of turbulence model is of secondary importance compared to bubble dynamics and mass transfer models in returning accurate gas fraction distributions (which as discussed above is, at the least, a necessary condition for accurate prediction of MDBR). For all of the results presented in this paper a high Reynolds number k-ε model is applied for the liquid field

$$\frac{\partial}{\partial x_j}(\alpha\rho u_j k) = \frac{\partial}{\partial x_j}\left[\alpha\left(\mu + \frac{\mu_t}{\sigma_k}\right)\frac{\partial k}{\partial x_j}\right] + P - \alpha\rho\varepsilon + S_k$$

$$\frac{\partial}{\partial x_j}(\alpha\rho u_j \varepsilon) = \frac{\partial}{\partial x_j}\left[\alpha\left(\mu + \frac{\mu_t}{\sigma_\varepsilon}\right)\frac{\partial \varepsilon}{\partial x_j}\right] + C_1\frac{\varepsilon}{k}P - C_2\frac{\varepsilon}{k}\alpha\rho\varepsilon + S_\varepsilon \tag{23}$$

In Eq. (23), all field indicator superscripts are eliminated as only the liquid field is solved. S_k and S_ε are available source/sink terms to: extract turbulence energy associated with breakup (Meng and Uhlman [7], Kunz et al. [11]), and reduce production due to MBDR mechanisms proposed by various authors (Ferrante and Elghobashi [8,9], Tryggvason and Lu [10]). These source terms are set to zero in the present work as they play only a secondary role in the prediction of gas fraction distribution and the DR distributions predicted by the code.

Numerics/Code. The code used in the present work is three dimensional, unstructured, parallel, and supports an arbitrary number of constituents. The algorithm follows segregated pressure based methodology. A colocated variable arrangement is used and a lagged coefficient linearization is applied. One of several diagonal dominance preserving, face-based finite volume spatial discretization schemes is selected for the momentum, volume fraction, interfacial area density, and turbulence transport equations. Mixture volume continuity is introduced through a pressure correction equation, based on the SIMPLE-C algorithm (Van Doormal and Raithby [31]). At each iteration, the discrete momentum equations are solved approximately, followed by a more exact solution of the pressure correction equation. Turbulence scalar, volume fraction, and interfacial area density equations are then solved in succession.

Several algorithmic elements critical to the accuracy and robustness of two-fluid simulations with significant interfield transfer are incorporated. These include: (1) interfield coupling of drag and mass transfer terms within the preconditioning, linear solver, and artificial dissipation elements of the scheme; (2) appropriate discretization of lift and dispersion forces to prevent odd-even decoupling in the solution; and (3) formulation of virtual mass as a convection operator.

Standard inflow, symmetry, wall, and outflow boundary conditions are employed. For scintered metal plate injection, porous wall boundary conditions are used, where an area permeability λ is specified. Shear force on porous boundary faces is apportioned as $F=\tau_w A_f(1-\lambda)$, where A_f is the face area and $A_f\lambda$ is the area available for injection flux.

Further details on the code and numerics are available in Kunz and Venkateswaran [32] and Kunz et al. [33].

FCM Studies. Due to the large number of models and coefficients involved, and the strong coupling among physical effects, it is desirable to examine the models in a systematic manner and isolate models where possible. In general this is not feasible using experimental data. Therefore, we utilize numerical simulations using DNS/FCM (force-coupling method, e.g., Lomholt and Maxey [34]). Several fully developed channel flow simulations with bubbles have been performed using the DNS/FCM procedure (Dong et al. [12]) for the purpose of "calibration" of the dispersion models used in the Reynolds-Averaged Navier-Stokes (RANS) two-fluid CFD framework.

The DNS/FCM cases start from a baseline DNS of a channel flow without bubbles at a certain Reynolds number (Re^*), the statistically stationary state representing a fully developed channel flow. The bubbles are introduced at $t=0$ throughout the domain in specific transverse planes, and allowed to evolve in time using

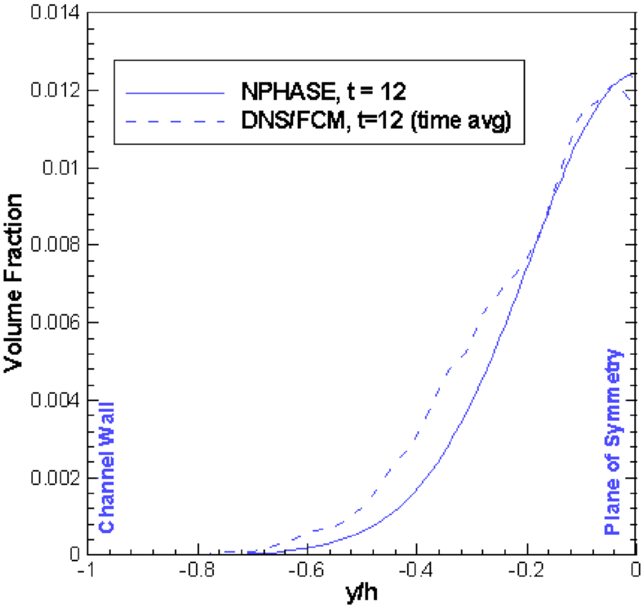

Fig. 2 Low volume fraction comparison between RANS and FCM

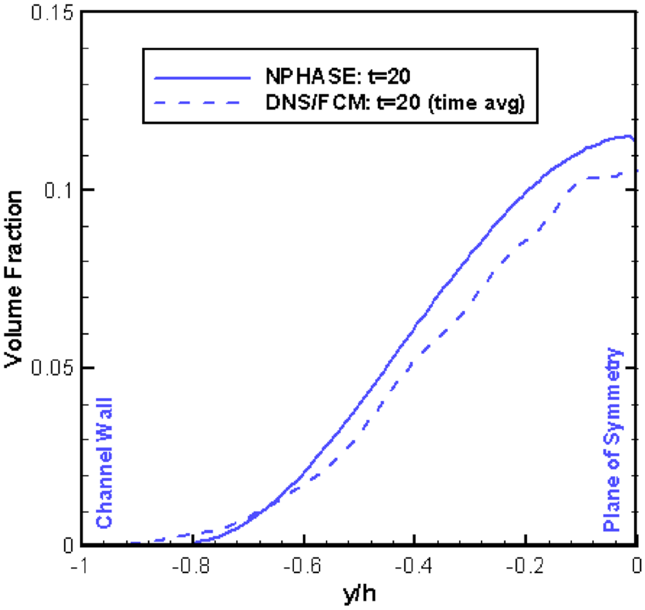

Fig. 3 High volume fraction comparison between RANS and FCM

FCM. An "equivalent" RANS case simulates a fully developed channel flow with bubbles introduced at the upstream boundary. A comparison may be made between averaged DNS profiles at time, t_{DNS}, and RANS profiles at downstream distance $x_{\mathrm{RANS}} = t_{\mathrm{DNS}} U_{\mathrm{avg}}$, where U_{avg} is the average (bulk) velocity in the channel. Since the average flow speed is used to convert distance to time, the comparison is not exact. Further, there was no coupling of the bubble dynamics to the baseline DNS for the results shown here.

For the cases reported here $\mathrm{Re}^* \approx 377$, $U_{\mathrm{avg}} = 2/3$ and two initial bubble volume fractions were used. The channel half-height is $h = 1$ for both cases. The first case seeds the bubbles very near the channel center plane ($y=0$) with a low average volume fraction ($\alpha_{\mathrm{avg}} \approx 0.0036$) and a bubble diameter $D/h = 0.06$. The second case seeds the bubbles over a region from $-0.2 < y/h < 0.2$ with a high initial peak volume fraction $\alpha_{\max} \approx 0.21$, and a bubble diameter $D/h = 0.1$. These cases were chosen to minimize wall collisions and allow us to concentrate on evaluation of the dispersion models.

The latter case demonstrates the importance of collision-induced bubble dispersion compared to conventional homogeneous-turbulence dispersion, as the predictions without collision induced dispersion are poor. The Lopez de Bertodano [21] homogeneous model and the collision-induced model were used for the results shown. For bubble drag we used a clean water (no impurities) drag correction, Eq. (4*c*).

Figure 2 shows the volume fraction profiles for FCM and RANS cases with a low average volume fraction. The FCM result is a short-time average corresponding to $t_{\mathrm{DNS}} = 12$. The profiles are not expected to match exactly for the reasons noted above, as well as possible uncertainties in two-fluid model coefficients compared to the implied FCM equivalent effects (drag, lift, etc.). Figure 3 shows the volume fraction profiles for FCM and RANS with a high initial volume fraction. The FCM result is a short-time average corresponding to $t_{\mathrm{DNS}} = 20$.

The RANS results shown here required a collision-induced dispersion model coefficient of 1000, compared to 200 for equivalent HIPLATE cases. There may be unknown scaling relations between these low Reynolds number RANS cases with relatively large bubbles and the very high Reynolds number HIPLATE cases. This behavior will be explored further in the future as FCM simulations are performed at higher Reynolds number and with smaller bubbles.

Though not shown here, agreement between the baseline DNS mean flow results and the RANS predictions for velocity and turbulence kinetic energy were very good. The good agreement shown here provides confidence in the functional form of the dispersion models employed in the multifluid RANS code.

Twelve-inch Water Tunnel Studies. As part of the present study, near-wall volume fraction profile data has been acquired along with estimates of bubble velocity, bubble sizes, and drag reduction. This data was taken in the ARL Penn State University 12-in. diameter tunnel with a rectangular test section designed especially for MBDR studies (details in Fontaine et al. [25]). The data shown here was acquired in May 2004 using an early version of the confocal probe instrumentation discussed by Fontaine et al. [25]. Volume fraction data beyond a peak value of about 0.35 is not shown since reliable data could not be obtained due to bubble cloud interference and poor signal-to-noise ratio.

The test setup is described in detail in Fontaine et al. [25]. In summary, the rectangular test section begins at $X=0$; the injector axial length is 9.5 mm, centered at $X=339$ mm; mini-balance 1 (MB1) is centered at $X=409.5$ mm; mini-balance 2 (MB2) is centered at $X=523.8$ mm; mini-balance 3 (MB3) is centered at $X=638.1$ mm; and the axial length of each balance is 38 mm.

The comparisons were made for three tunnel speeds and three gas injection rates, though only a subset is shown here. The upstream computational boundary location was set to match the virtual origin inferred from measured velocity profile data (used to compute the boundary layer displacement thickness; $(\delta^*)^{5/4}$ is then extrapolated to zero). The injected bubble sizes were based on an approximation to the measured bubble size distribution at the first measurement station (mini-balance 1—MB1). Four bubble fields were selected with diameters chosen to represent the data adequately. The bubble size bins used were $D_B = 110$, 200, 340, and 500 μm. Bubble breakup and coalescence were not considered in the results presented here.

Volume fraction comparisons are shown at measurement stations 2 (MB2) and 3 (MB3) in Figs. 4–7. Reliable volume fraction data was not obtained at MB1 in most cases. Figure 4 shows the volume fraction profile for the conditions $U = 13.7$ m/s (tunnel

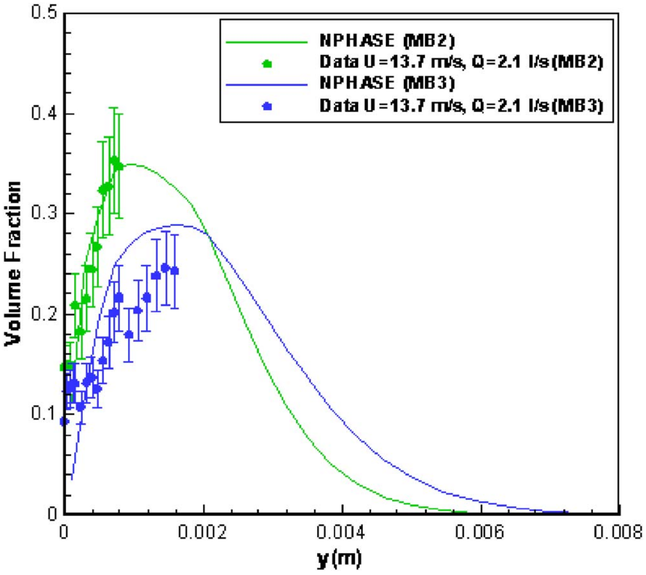

Fig. 4 Void fraction profiles for 12-in. tunnel comparison for *U*=13.7 m/s, *Q*=2.1 l/s

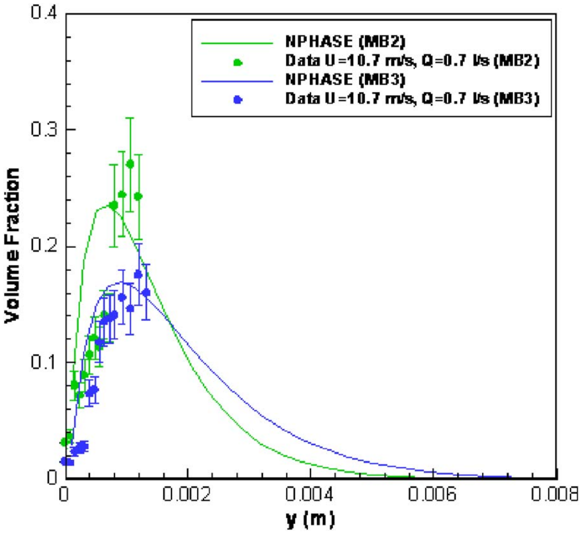

Fig. 6 Void fraction profiles for 12-in. tunnel comparison at *U*=10.7 m/s, *Q*=0.7 l/s

speed) and injection volume flow rate $Q=0.0021\ \mathrm{m}^3/\mathrm{s}$ (2.1 l/s). Figure 5 shows the volume fraction profiles at MB2 for total gas and individual bubble sizes for the same conditions. Figures 6 and 7 show the profiles for a speed of $U=10.7$ m/s, and flow rate $Q=0.7=2.1$ l/s, respectively. Generally the agreement between experiment and predictions is quite good, though near-injector modeling uncertainties remain.

In Fig. 8 the measured bubble velocities are compared with the predictions for $U=13.7$ m/s and $Q=0.7$ l/s. The symbols indicate bubble velocity and the solid line is the predicted liquid-phase velocity, which was not measured. The differences between prediction and measurement may be due to modeled bubble drag and virtual mass effects and/or uncertainty in establishing the wall-normal location in the experiment.

The predicted and measured drag reduction (DR) values at MB2 are shown in Fig. 9 for all flow conditions. Reasonable agreement is evident, except at the highest flow rate and lowest tunnel speed. In contrast to the HIPLATE drag reduction shown below, the DR at MB1 (not shown) was either accurately predicted or overpredicted. In these small-scale tests the first measurement location is closer to the injector in wall units than that in HIPLATE. Thus injection region physics are even more important. Further there is a rapid variation in wall shear force versus axial distance between the injector and the first measurement location, which implies that the correct time scales must be accurately captured to obtain accurate predictions. The latter depends on the "correct" balance among a large number of physical mechanisms (hence, models), and validation of these models becomes critically dependent on detailed validation data and/or simulations (such as DNS/FCM).

HIPLATE Studies. The final set of validation results focus on high Reynolds number flat plate (HIPLATE) measurements carried out by the seventh author of this paper and his colleagues in

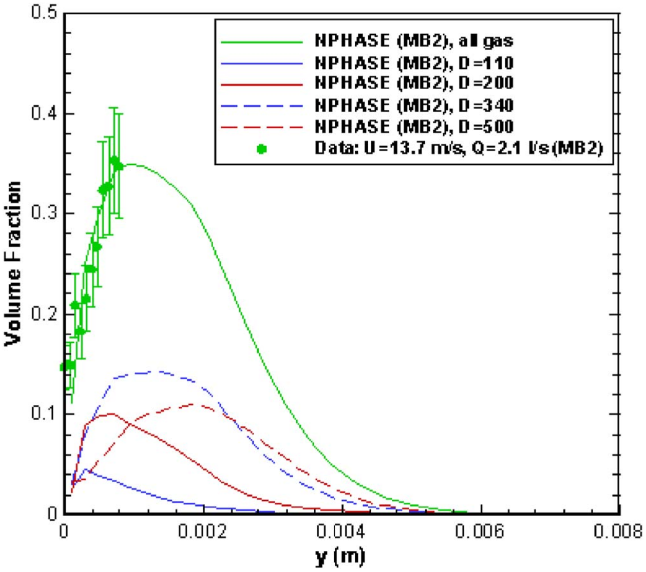

Fig. 5 Void fraction profiles at MB2 for 12-in. tunnel comparison for *U*=13.7 m/s, *Q*=2.1 l/s. Profiles for four bubble fields and total gas are shown.

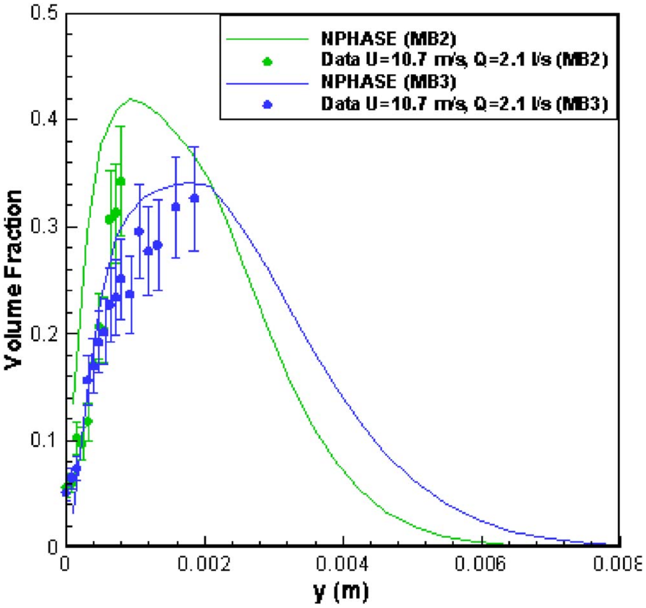

Fig. 7 Void fraction profiles for 12-in. tunnel comparison at *U*=10.7 m/s, *Q*=2.1 l/s

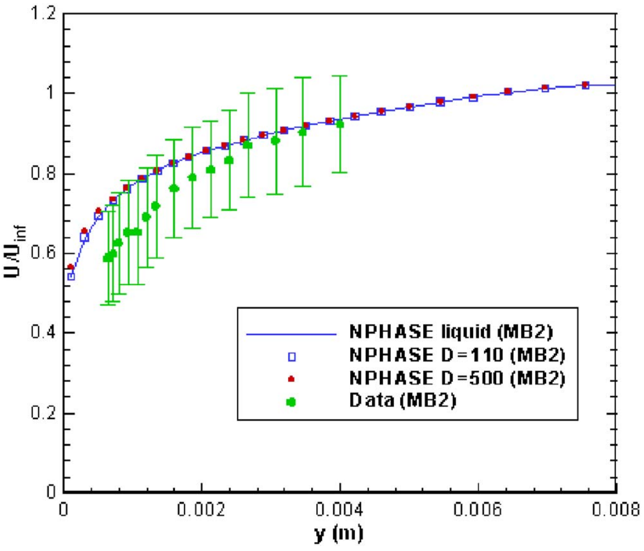

Fig. 8 Bubble velocities for $U=13.7$ m/s, $Q=0.7$ l/s at MB2

the large cavitation channel (LCC) operated by the U.S. Navy in Memphis, TN (Sanders et al. [13]). These measurements include point bubble velocities, bubble size distributions, and shear stress measurements for a range of gas injection flow rates at flat plate Reynolds numbers up to $\mathrm{Re}_x=2.1\times 10^8$.

Figure 10 shows a diagram of the test geometry. The HIPLATE is 12.9-m long and spans the LCC test section (3.05 m). Most of the experimental data was taken at three freestream velocities (6, 12, and 18 m/s) and four gas injection rates (0.000, 0.094, 0.189, and 0.378 m^3/s [0, 200 400, and 800 scfm]) through the most upstream injector, located $x=1.32$ m from the boundary layer tripped leading edge. The plate was mounted “upside down” (gas injected downward) which gave rise to Froude number effects discussed below.

Tunnel blockage for these experiments was minimal ($\delta^*/W < 0.01$), and all measurements were taken in the middle third span, thereby justifying the two-dimensional CFD model shown with a symmetry boundary condition imposed at the upper boundary. Compressed air was injected through the 2.65 m span injector, which was designed to deliver evenly distributed air flow through a 3.2 mm sintered stainless steel slab having 40 μm pores.

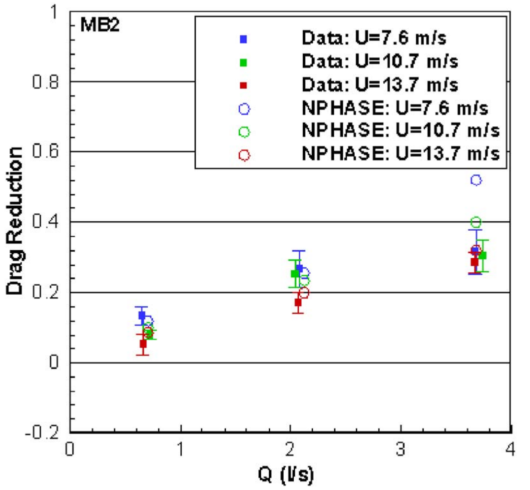

Fig. 9 Drag reduction at MB2

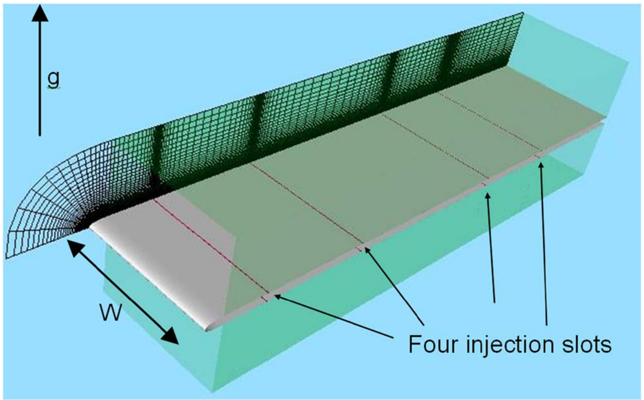

Fig. 10 Diagram of HIPLATE

Two sets of results are presented for HIPLATE. Since bubble diameter distributions were obtained photographically at $x=1.96$ m (0.64 m downstream of injection) and $x=10.68$ m, the first set of results uses the measured bubble distribution at $x=1.96$ as boundary conditions for the injected gas flow. Breakup is not modeled, but coalescence is. This first exercise allowed us to explore the performance of the bubble dynamics models separately without the complications of modeling the breakup of the injected gas structures.

Figure 11 shows predicted DR versus x for the 18-m/s tunnel velocity cases. Skin friction reduction is well predicted, lying within experimental uncertainty, except at the highest injection rate, at the axial location nearest the injector. Of particular importance, is that persistence (or lack thereof) is fairly well predicted, a modeling challenge that is closely tied to the evolving equilibrium of lift, dispersion, drag, and buoyancy. Figure 12 shows a view of the predicted gas volume fraction distribution for the $U_\infty=18$ m/s, $Q=0.378$ m^3/s case. The view is scaled by a factor of 200 in the y direction. Of particular interest is the near evacuation of bubbles from the near-wall region well downstream. This

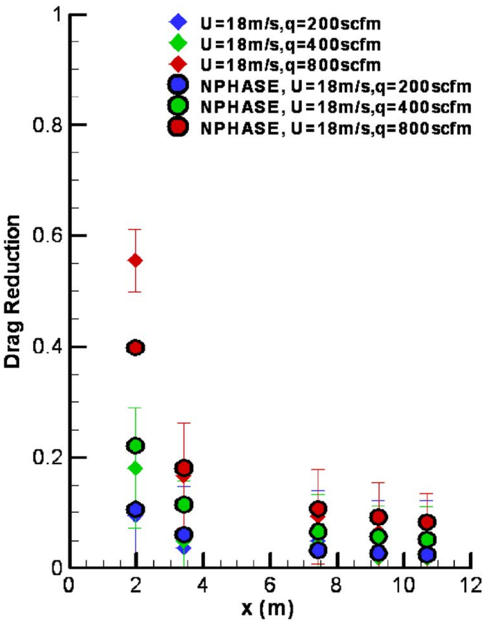

Fig. 11 Comparison of predicted and measured DR vs. x for $U_\infty=18$ m/s HIPLATE

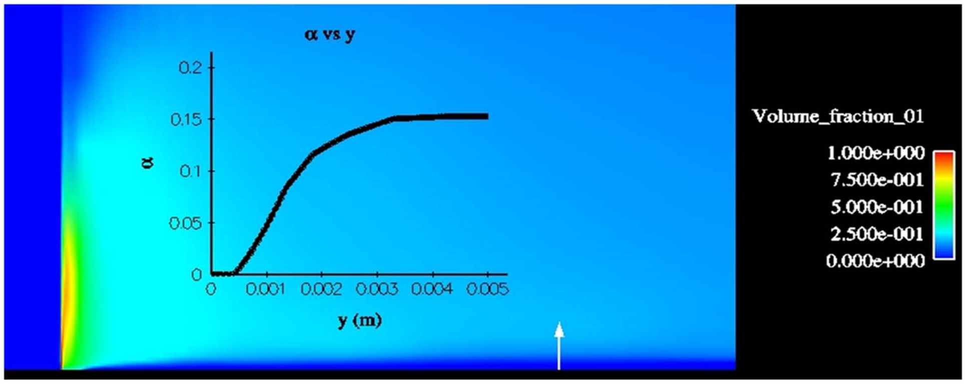

Fig. 12 Predicted gas volume fractions. Contour plot+profile at $x=10.68$ m for $U_\infty=18$ m/s, $Q=0.378$ m^3/s HIPLATE case (y coordinate scaled by 200).

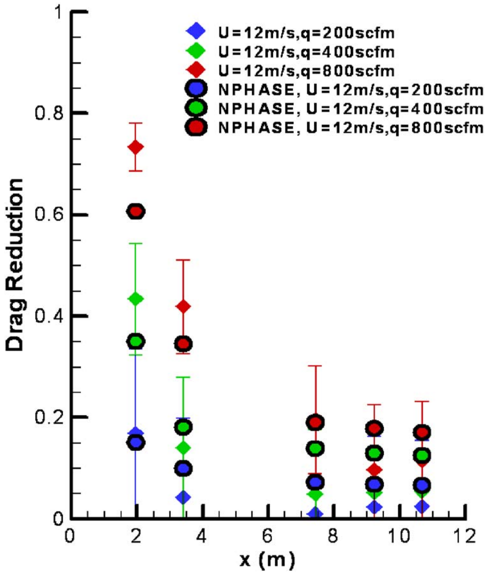

Fig. 13 Comparison of predicted and measured DR vs. x for $U_\infty=12$ m/s HIPLATE

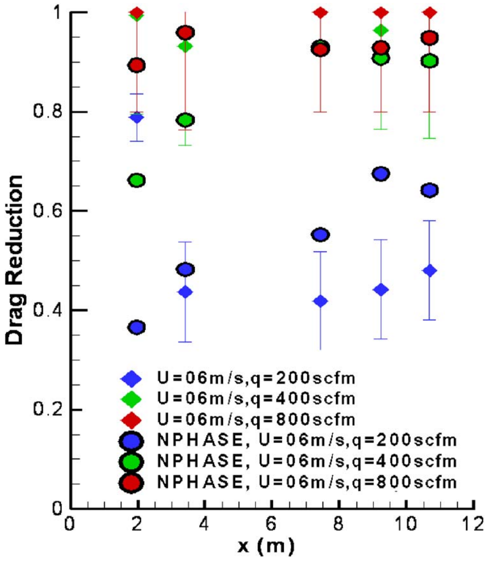

Fig. 14 Comparison of predicted and measured DR vs. x for $U_\infty=6$ m/s HIPLATE cases

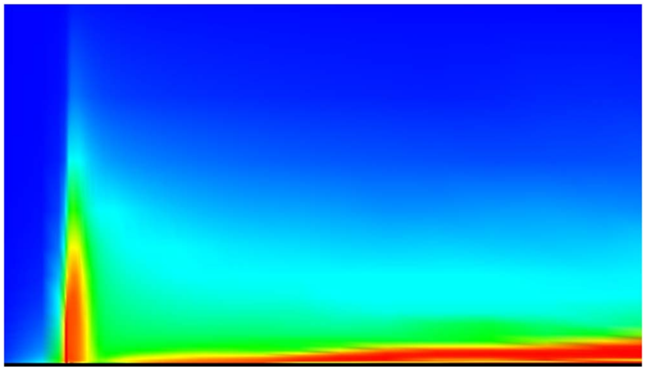

Fig. 15 Predicted gas volume fraction contour plot for $U_\infty=6$ m/s, $Q=0.378$ m^3/s HIPLATE case (y coordinate scaled by 50)

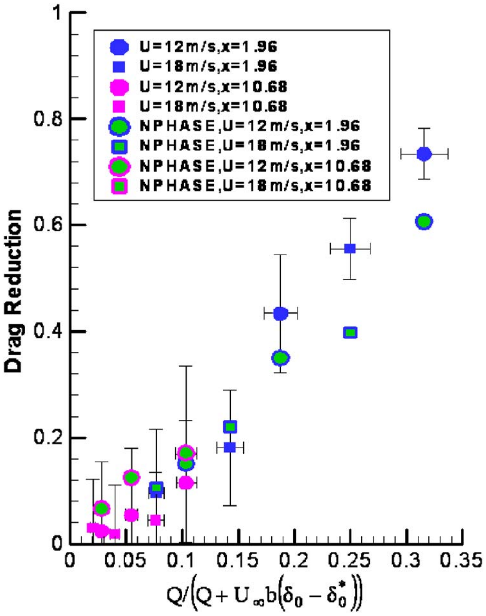

Fig. 16 Comparison of predicted and measured DR vs. volumetric fraction of gas flow rate at upstream and downstream shear stress measurement stations for $U_\infty=12$ and 18 m/s HIPLATE cases

"nearly gas-free" layer, on the order of 1-mm thick, was observed experimentally by the HIPLATE team and is clearly attendant to the loss of persistence observed experimentally and computationally.

Figure 13 shows predicted DR versus x for the $U_\infty=12$ m/s HIPLATE runs. The results are almost as good as at 18 m/s, again with the largest discrepancies arising near the injector plate. At this lower tunnel freestream velocity, a trend is observed of underprediction of DR near the injector and overprediction of DR downstream. We have observed that increasing the lift force modestly improves downstream persistence predictions for $U_\infty=18$ and 12 m/s, but that doing so gives rise to worse underprediction of DR near the injectors. The model constants used therefore represent a compromise that we hope to overcome through improved injector region modeling as discussed below.

Figure 14 shows predicted DR versus x for the $U_\infty=6$ m/s HIPLATE runs. By virtue of the "plate-up" of the HIPLATE configuration, the HIPLATE experimental team observed that these lower Froude number cases exhibited the formation of a continuous gas film at the higher two gas injection rates, and an intermittent bubbly flow-gas film flow at $Q=0.094$ m^3/s. Accordingly this experimentally observed flow regime transition gave rise to very high drag reduction (DR=1 along much of the plate for $Q=0.189$, and 0.378 m^3/s) as illustrated in the figure. Despite the fact that the dynamics models used are expressly valid only for disperse bubbly flows, the CFD analysis qualitatively returns the experimentally observed topology and DR, as shown in Figs. 14 and 15. We view this as largely fortuitous, though it gives us some indication that the magnitudes of the dynamics models scale in a physically reasonable manner compared to buoyancy.

Figure 16 shows a comparison of predicted and measured DR versus volumetric fraction of gas flow rate $Q/(Q+Q_{\text{water}})$, at the most upstream and furthest downstream shear stress measurement stations for $U_\infty=12$ and 18 m/s. Q_{water} is the volume flux of water in the boundary layer when gas is not injected, and is estimated from $Q_{\text{water}}=U_\infty b(\delta_0-\delta_0^*)$ where b is the span of the injector and δ_0,δ_0^* are the boundary layer 99% and displacement thicknesses, respectively, without air injection.

Using rapid shutter speed photography, the HIPLATE experimental team obtained bubble velocity estimates for the bubbles closest to the wall, at the most upstream and furthest downstream measurement stations. These measurements and predictions are compared for $U_\infty=12$ and 18 m/s cases in Fig. 17. There bubble velocity is plotted against volumetric fraction of gas flow rate, defined using $Q_{\text{water}}=U_\infty b(\theta_0)$, where θ_0 is the local single phase momentum thickness. (The conventional but alternative gas flux scalings used in Figs. 16 and 17 were chosen for consistency with the published presentation of experimental results).

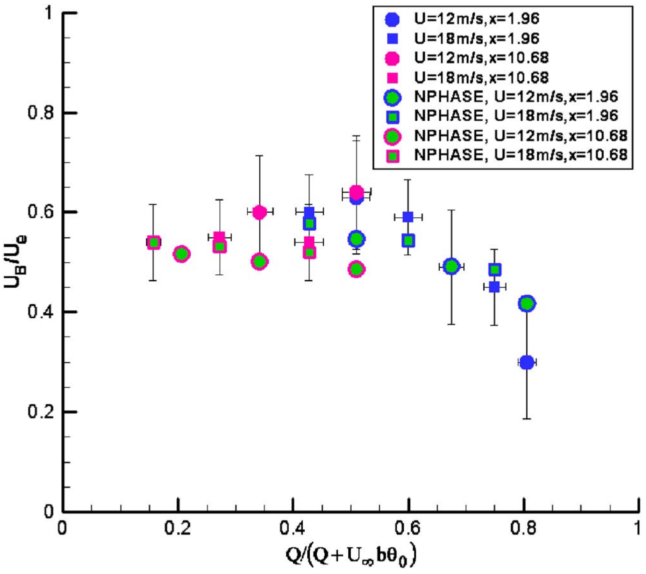

Fig. 17 Comparison of predicted and measured bubble velocity vs. volumetric fraction of gas flow rate at upstream and downstream measurement stations for $U_\infty=12$ and 18 m/s HIPLATE cases

The CFD model does well in matching these velocities. Downstream, this correspondence mainly reflects the model's ability to predict the boundary layer liquid velocity at a given standoff distance, since relative velocities are very small there ($<1\% U_\infty$). However, just downstream of the injector, lower bubble velocities are observed, especially at higher $Q/U_\infty A_{\text{inj}}$. Though the details of the physics between injection and the upstream velocity measurement location are not directly observed, these lower measured bubble velocities indicate that: (1) the bubble relative velocity remains significant there (say on the order of $0.1^* U_\infty$), and (2) the boundary layer is perturbed by the gas injection and the liquid momentum defect has not yet recovered. Neither of these effects can be suitably modeled unless drag is small and virtual mass effects are accounted for. Specifically, the reduced interfacial area and drag associated with the gas structures near injection give rise to a deeper penetration of the gas jet into the boundary layer with an attendant increased perturbation of the boundary layer. This reduced drag effect is modeled using the cluster drag law in Eq. (5). Also, virtual mass increases the bubble response time by orders of magnitude, thereby returning a non-negligible relative velocity at $x=1.96$ m.

Figure 18 shows the predicted bubble velocities obtained with virtual mass and cluster drag models turned off. The velocities are seen to be significantly over-predicted for reasons discussed above.

Figure 19 illustrates the mean bubble diameter and implicit bubble distributions corresponding to the computations shown above. These are not to be viewed as predictive, since the measured bubble size distributions were used as boundary conditions and breakup was not modeled. They are presented to show that experimentally observed bubble sizes were accommodated in the foregoing result and for comparison to the fully implemented mass transfer results show below.

We next proceeded to a more complete model set including the

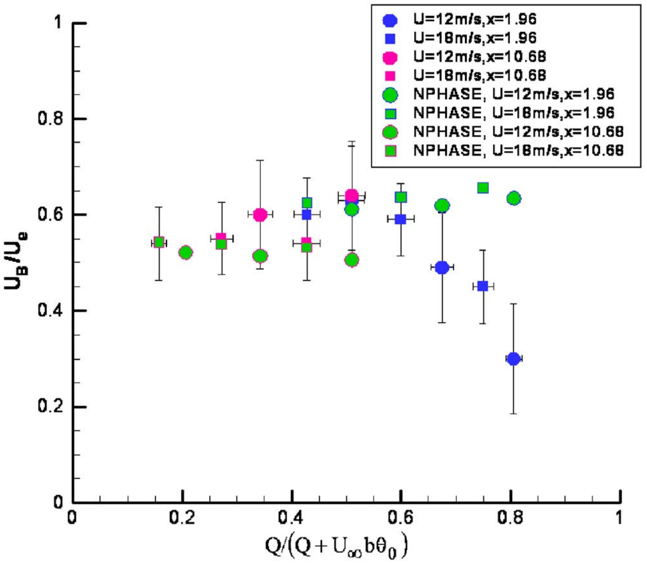

Fig. 18 Comparison of predicted and measured bubble velocity vs. volumetric fraction of gas flow rate at upstream and downstream measurement stations for $U_\infty=12$ and 18 m/s HIPLATE cases. Virtual mass and cluster drag set to zero.

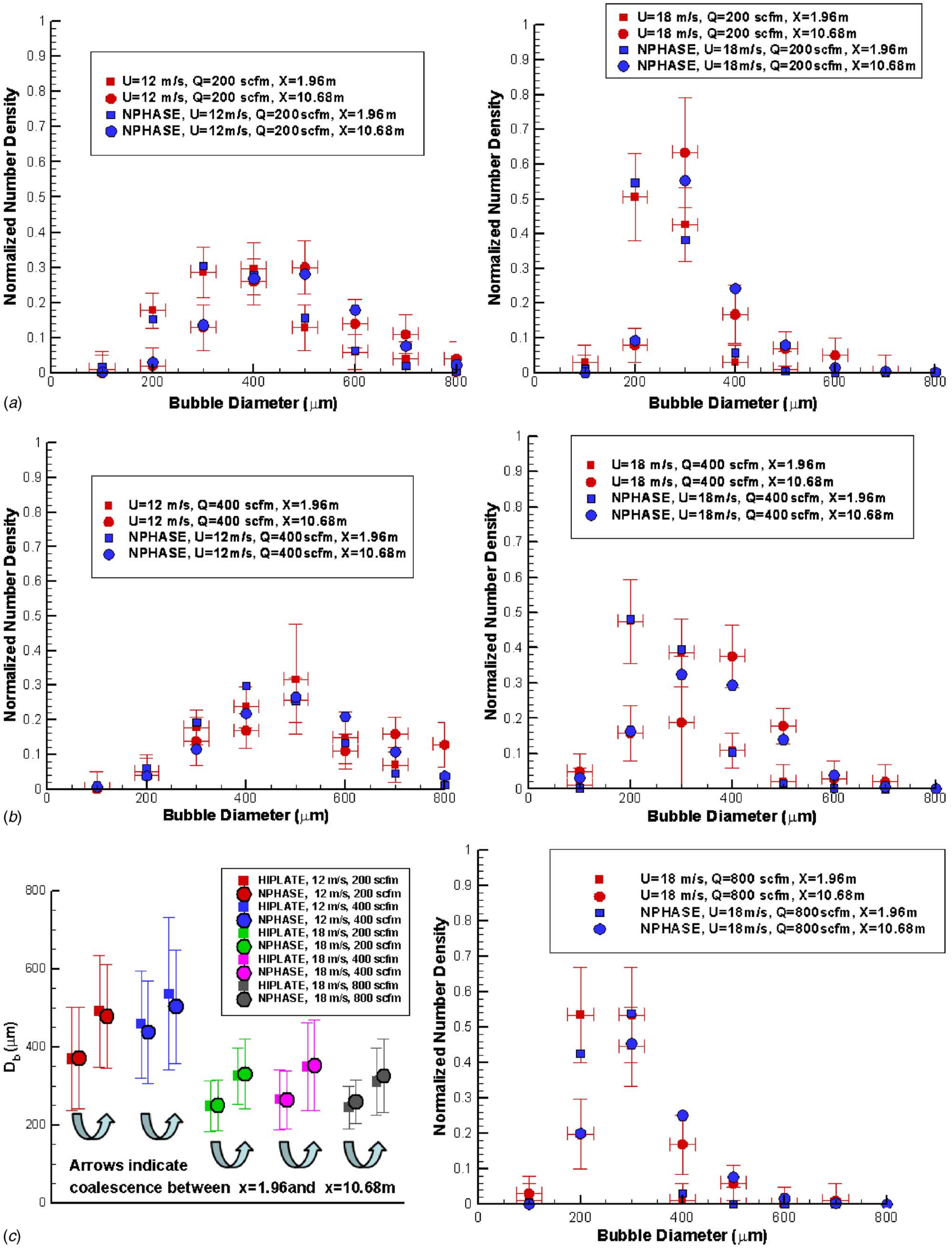

Fig. 19 Comparison of computed and measured bubble size distributions and mean diameters for the five HIPLATE cases where these measurements were taken

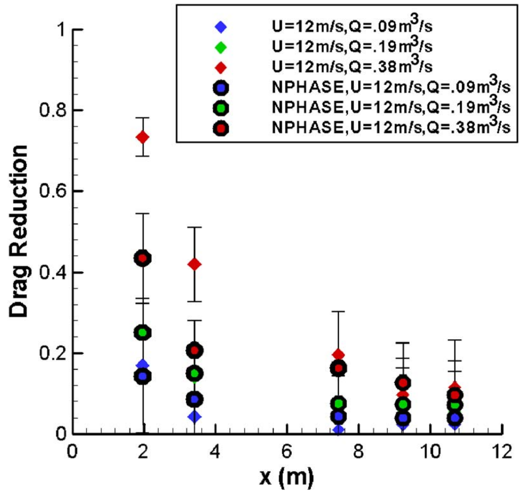

Fig. 20 Comparison of predicted (with breakup and coalescence) and measured DR vs. *x* for U_∞=12 m/s HIPLATE

breakup and coalescence models described in Eqs. (15)–(19) along with the bubble size distribution function in Eq. (22). Results for this "full-up" simulation include drag reduction (DR) versus x for U_∞=12 and 18 m/s (Figs. 20 and 21), the bubble number density distribution versus bubble diameter, and the mean bubble diameter and standard deviation (Fig. 22). Bubble velocity is omitted since the results are nearly identical to those shown in Fig. 17. In performing these simulations it became evident that additional physical modeling is required to properly treat the "gas sheet" breakup process in the near-injection region. This is an ongoing effort, so here we used a plausible injected mean bubble diameter (for each case) assuming that the gas sheet emanates as discrete bubbles. Thus a balance between breakup, coalescence, and all the dynamics mechanisms is predicted.

Figures 20 and 21 show a somewhat lower DR than the previous simulations at the first two measurement stations, x=1.96 and 3.41 m, for U_∞=12 m/s, and lower at x=1.96 m for U_∞=18 m/s. DR is predicted well at the other measurement locations.

Figure 22 shows bubble size results for the same five cases shown in Fig. 19. The agreement is good for U_∞=12 m/s and fair for U_∞=18 m/s. It is evident that the mean diameter differences are larger for U_∞=18 m/s than for U_∞=12 m/s. Also, U_∞=18 m/s results exhibit too much breakup between x=1.96 and 10.68 m.

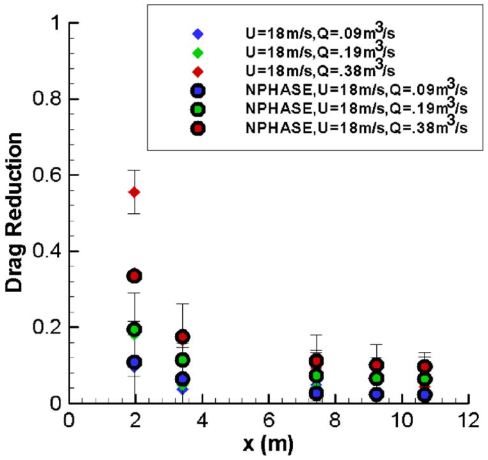

Fig. 21 Comparison of predicted (with breakup and coalescence) and measured DR vs. *x* for U_∞=18 m/s HIPLATE

Both the DR and bubble size results indicate the need for improved modeling in the injection region—primarily gas sheet transport and breakup in a multifluid RANS framework. Further, the impact of using the mean bubble diameter in the breakup and coalescence rates must be quantified with more rigorous treatment of those terms. Exploration and improvement of these modelling shortcomings is underway.

Conclusions

This paper has summarized the validation status of a CFD tool development program for MBDR predictions. An Eulerian two-fluid model has been presented with specifics regarding physical models for interfacial dynamics, breakup, and coalescence. Validation studies for three cases demonstrate that the salient physics associated with obtaining correct bubble distributions and DR in MBDR are being modeled with good accuracy.

Acknowledgment

This work was supported by the U.S. Defense Advanced Research Projects Agency, Advanced Technology Office, Friction Drag Reduction Program, with Dr. Lisa Porter as technical monitor.

Nomenclature

A, A_{int} = area, interfacial area density
C_1, C_2, C_μ = turbulence model constants
C_D,C_L,C_{VM},C_{TD} = force coefficients
D_B,$\bar{D}$, D_{ch} = bubble diameters, length scale
D^{kl} = drag kernel
DR = drag reduction ($=1-C_f/C_{f0}$)
f = n_B distribution function
f_D = drag law correction function
g_i = gravity vector
h = channel half-height
h_0, h_f = initial, final film thickness
k = turbulent kinetic energy
M^{kl} = nondrag force
N_B, n_B = bubble number densities
P = turbulence energy production
p = static pressure
Q = gas volumetric flow rate
Re_B = bubble Reynolds number
St_k,St_r,St_T = Stokes, Schmidt numbers
t_b = time scale
U_∞ = freestream velocity
u_i = Cartesian velocity component
$\vec{V}$ = velocity vector
v = bubble volume
x_i = Cartesian coordinate
α = volume fraction
δ, δ^* = boundary layer thicknesses
ε = turbulence dissipation rate
ϕ = general transport scalar
Φ_B, Φ_C, ϕ_B, ϕ_C = coalescence, breakup kernels
$\bar{\theta}^{\text{TD}}$ = dispersive collision rate
θ_C^T, θ_B^T = turbulent collision, breakup rates
λ_{eff} = collision coalescence efficiency
Γ^{kl} = mass transfer rate
μ_m = molecular viscosity
μ_T = turbulent viscosity
ν_T = turbulent kinematic viscosity
ρ = density
ψ = bubble shape function
σ = surface tension
σ_k, σ_ε = turbulent Prandtl numbers

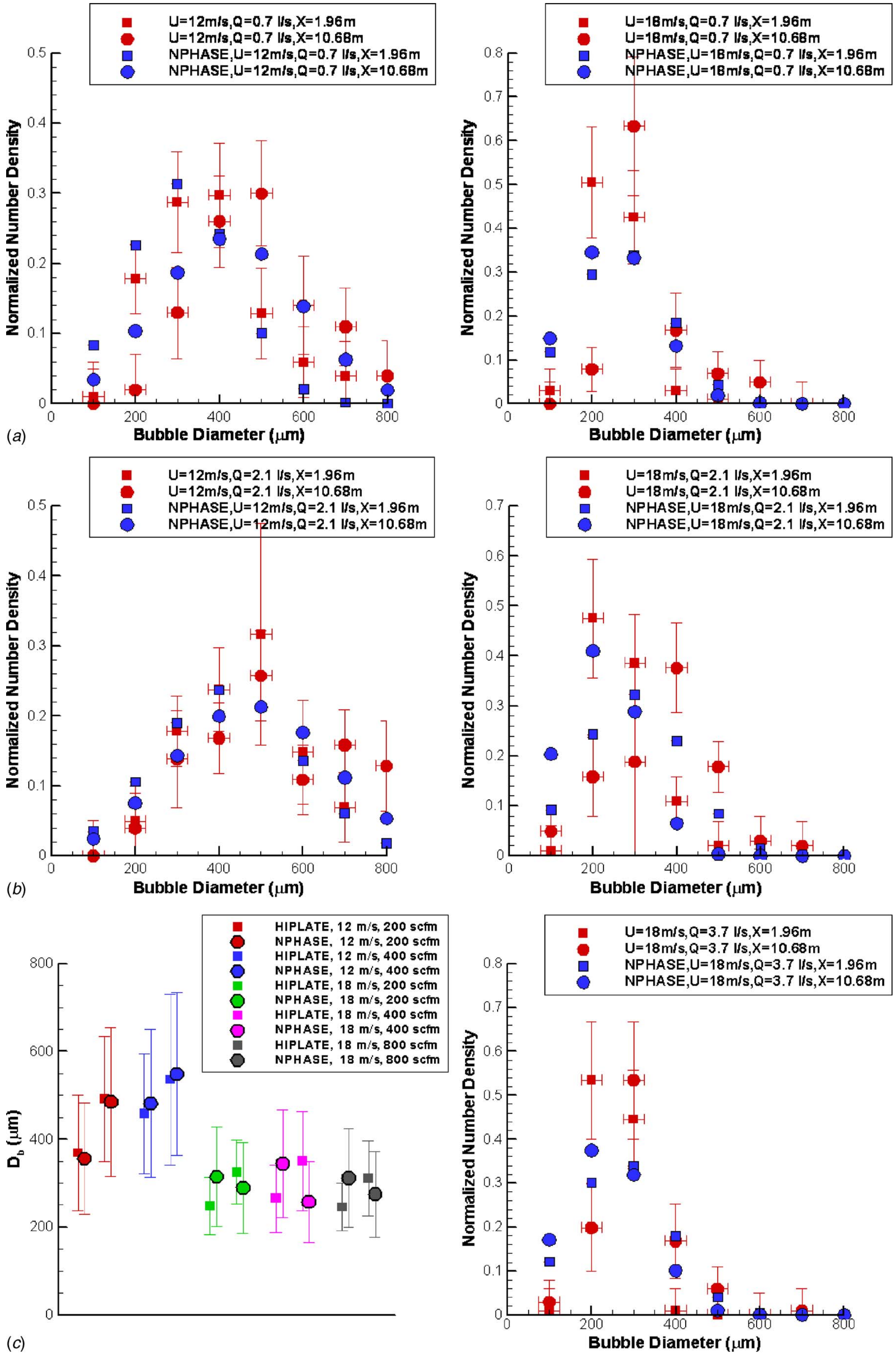

Fig. 22 Comparison of predicted (with breakup and coalescence) and measured bubble size distributions and mean diameters for the five HIPLATE cases where these measurements were taken

$\tau_r, \tau_c, \tau_{\mathrm{BC}}, \tau_B$ = time scales

References

[1] McCormick, M. E., and Bhattacharyya, R., 1973, "Drag Reduction on a Submersible Hull by Electrolysis," Nav. Eng. J., **85**, pp. 11–16.

[2] Bogdevich, V. G., and Evseev, A. R., 1976, "Effect of Gas Saturation on Wall Turbulence," *Investigation of Boundary Layer Control*, S. S. Kutateladze and G. S. Migirenko, eds., Thermophysics Institute Publishing, Novosibirsk, Siberia (in Russian).

[3] Legner, H. H., 1984, "A Simple Model for Gas Bubble Drag Reduction," Phys. Fluids, **27**(12), pp. 2788–2790.

[4] Marie, J. L., 1987, "A Simple Analytical Formulation for Microbubble Drag Reduction," PCH, PhysicoChem. Hydrodyn., **8**(2), pp. 213–220.

[5] Merkle, C. L., and Deutsch, S., 1992, "Microbubble Drag Reduction in Liquid Turbulent Boundary Layers," Appl. Mech. Rev., **45**(3), Part 1, pp. 103–127.

[6] Kato, H., Miura, K., Yamaguchi, H., and Miyanaga, M., 1998, "Experimental Study on Microbubble Ejection Method for Frictional Drag Reduction," J. Mar. Sci. Technol., **3:3**, pp. 122–129.

[7] Meng, J. C. S., and Uhlman, J. S., 1998, "Microbubble Formation and Splitting in a Turbulent Boundary Layer for Turbulence Reduction," *Proceedings of the International Symposium on Seawater Drag Reduction*, Newport, RI, July, US Office of Naval Research, Arlington, VA, pp. 341–355.

[8] Ferrante, A., and Elghobashi, S., 2004, "On the Physical Mechanisms of Drag Reduction in a Spatially Developing Turbulent Boundary Layer Laden with Microbubbles," J. Fluid Mech., **503**, pp. 345–355.

[9] Ferrante, A., and Elghobashi, S., 2005, "Reynolds Number Effects on Drag Reduction in a Bubble-Laden Spatially Developing Turbulent Boundary Layer Over a Flat Plate," *Proceedings of the 2nd International Symposium on Seawater Drag Reduction*, Busan, Korea, May.

[10] Tryggvason, G., and Lu, J., 2005, "DNS of Drag Reduction Due to Bubble Injection Into Turbulent Flow," *Proceedings of the 2nd International Symposium on Seawater Drag Reduction*, Busan, Korea, May, US Office of Naval Research, Arlington, VA.

[11] Kunz, R. F., Deutsch, S., and Lindau, J. W., 2003, "Two Fluid Modeling Of Microbubble Turbulent Drag Reduction," ASME Paper No. FED2003-45640, *Proceedings of FEDSM'03: 4TH ASME-JSME Joint Fluids Engineering Conference*, Honolulu, Hawaii, July 6–11, ASME, New York.

[12] Dong, S., Xu, J., Maxey, M. R., and Karniadakis, G. E., 2005, "Microbubble Dynamics in Turbulent Channel Flow," *Proceedings of the 2nd International Symposium on Seawater Drag Reduction*, Busan, Korea, May, US Office of Naval Research, Arlington, VA.

[13] Sanders, W. C., Dowling, D. R., Perlin, M., and Ceccio, S. L., 2006, "Bubble Friction Drag Reduction in a High Reynolds Number Flat Plate Turbulent Boundary Layer," J. Fluid Mech., **552**, pp. 353–380.

[14] Fontaine, A. A., Petrie, H. L., DeVilbiss, D. W., Money, M. J., and Deutsch, S., 2005, "Void Fraction and Velocity Probe for Micro-bubble Flow Studies," *Proceedings of the 2nd International Symposium on Seawater Drag Reduction*, Busan, Korea, May, US Office of Naval Research, Arlington, VA.

[15] Hibiki, T., Takamasa, T., and Ishii, M., 2001, "Interfacial Area Transport of Bubbly Flow in a Small Diameter Pipe," J. Nucl. Sci. Technol., **38**(8), 614–620.

[16] Loth, E., 2000, "Numerical Approaches for Motion of Dispersed Particles, Droplets and Bubbles," Prog. Energy Combust. Sci., **26**, 161–223.

[17] Richardson, J. F., and Zaki, W. N., 1954, "Sedimentation and Fluidization: Part I," Trans. Inst. Chem. Eng., **32**, pp. 35–53.

[18] Johansen, S. T., and Boysan, F., 1988, "Fluid Dynamics in Bubble Stirred Ladles: Part II. Mathematical Modeling," Metall. Trans. B, **19b**, pp. 755–764.

[19] Lahey, R. T., and Drew, D. A., 2000, "An Analysis of Two-Phase Flow and Heat Transfer Using a Multidimensional, Multi-field, Two-Fluid Computational Fluid Dynamics (CFD) Model," *Japan/US Seminar on Two-Phase Flow Dynamics*, Santa Barbara, California.

[20] Kawamura, T., and Yoshiba, H., 2004, "Numerical Modelng of Bubble Distributions in Horizontal Bubbly Channel Flow," *Proceedings of the 5th International Conference on Multiphase Flow*, Yokohama, Japan, Paper No. 354.

[21] Lopez de Bertodano, M., 1998, "Two-fluid Model for Two-phase Turbulent Jets," Nucl. Eng. Des., **179**, pp. 65–74.

[22] Moraga, F. J., Larreteguy, A. E., Drew, D. A., and Lahey, R. T., Jr., 2003, "Assessment of Turbulent Dispersion Models for Bubbly Flows in the Low Stokes Number Limit," Int. J. Multiphase Flow, **29**, pp. 655–673.

[23] Carrica, P. M., Drew, D., Bonetto, F., and Lahey, R. T., Jr., 1999, "A Polydisperse Model for Bubbly Two-phase Flow around a Surface Ship," Int. J. Multiphase Flow, **25**, pp. 257–305.

[24] Prince, M. J., and Blanch, H. W., 1990, "Bubble Coalescence and Breakup in Air-Sparged Bubble Columns," AIChE J., **36**(10), pp. 1485–1499.

[25] Batchelor, G. K., 1988, "A New Theory of the Instability of a Uniform Fluidized Bed," J. Fluid Mech., **193**, pp. 75–110.

[26] Martinez-Bazan, C., Montanes, J. L., and Lasheras, J. C., 1999, "On the Breakup of an Air Bubble Injected into a Fully Developed Turbulent Flow. Part 1. Breakup Frequency," J. Fluid Mech., **401**, pp. 157–182.

[27] Levich, V. G., 1962, *Physicochemical Hydrodynamics*, Prentice-Hall, Englewood Cliffs, N.J..

[28] Chesters, A. K., and Hofman, G., 1982, "Bubble Coalescence in Pure Liquids," Appl. Sci. Res., **38**, pp. 353–361.

[29] Lehr, F., and Mewes, D., 2001, "A Transport Equation for the Interfacial Area Density Applied to Bubble Columns," Chem. Eng. Sci., **56**, pp. 1159–1166.

[30] Durbin, P. A., 1991, "Near-Wall Turbulence Closure Modeling Without Damping Functions," Theor. Comput. Fluid Dyn., **3**, pp. 1–13.

[31] Van Doormal, J. P., and Raithby, G. D., 1984, "Enhancements of the SIMPLE Method for Predicting Incompressible Fluid Flows," Numer. Heat Transfer, **7**, pp. 147–163.

[32] Kunz, R. F., and Venkateswaran, S., 2000, "On the Roles of Implicitness, Realizability, Boundary Conditions and Artificial Dissipation in Multidimensional Two-Fluid Simulations with Interfacial Forces," *AMIF-ESF Workshop on Computing Methods for Two-Phase Flow*, Centre Paul Langevin, Aussois, France, January 12–14.

[33] Kunz, R. F., Yu, W. S., Antal, S. P., and Ettorre, S. M., 2001, "An Unstructured Two-fluid Method Based on the Coupled Phasic Exchange Algorithm," AIAA Paper No. 2001–2672.

[34] Lomholt, S., and Maxey, M. R., 2003, "Force-coupling Method for Particulate Two-phase Flow: Stokes Flow," J. Comput. Phys., **184**, pp. 381–405.

Alternate Scales for Turbulent Flow in Transitional Rough Pipes: Universal Log Laws

Noor Afzal
Professor
e-mail: prof_noor_afzal@yahoo.com

Abu Seena

Department of Mechanical Engineering,
Aligarh University,
Aligarh 202002,
India

In transitional rough pipes, the present work deals with alternate four new scales, the inner wall transitional roughness variable $\zeta = Z_+/\phi$*, associated with a particular roughness level, defined by roughness scale* ϕ *connected with roughness function* $\triangle U_+$*, the roughness friction Reynolds number* R_ϕ *(based on roughness friction velocity), and roughness Reynolds number* Re_ϕ *(based on roughness average velocity) where the mean turbulent flow, little above the roughness sublayer, does not depend on pipes transitional roughness. In these alternate variables, a two layer mean momentum theory is analyzed by the method of matched asymptotic expansions for large Reynolds numbers. The matching of the velocity profile and friction factor by Izakson-Millikan-Kolmogorov hypothesis gives universal log laws that are explicitly independent of pipe roughness. The data of the velocity profile and friction factor on transitional rough pipes provide strong support to universal log laws, having the same constants as for smooth walls. There is no universality of scalings in traditional variables and different expressions are needed for various types of roughness, as suggested, for example, with inflectional-type roughness, monotonic Colebrook-Moody roughness, etc. In traditional variables, the roughness scale, velocity profile, and friction factor prediction for inflectional pipes roughness are supported very well by experimental data.* [DOI: 10.1115/1.2375129]

1 Introduction

The rough wall flows are of great importance, but they are much more poorly understood than flows over smooth walls. The technological importance of rough wall bounded turbulent flows is also well known. In many situations a turbulent flow develops over surfaces that are hydrodynamically rough over some portion of their length. The major impact of wall roughness is to perturb the wall layer which, in general, leads to an increase in wall shear stress. The increase in wall shear stress is almost invariably accompanied by an increase in the wall heat and mass transfer rate.

Millikan [1] proposed a two layer theory for three cases of transitional, fully smooth, and fully rough pipes to obtain the log laws, where the slope k, the Karman's constant, is a universal number, but the additive constant depends on roughness. All traditional theories of transitionally rough wall are based on fully smooth wall variable $Z_+ = Zu_\tau/\nu$ or fully rough wall variable Z/h, which strongly depends on roughness effects (Millikan [1], Raupach et al. [2], and Jimenez [3]). Clauser [4] and Hama [5] simplified the matter by introducing the roughness function $\triangle U_+$, as an additional term to smooth wall log law, in transitional rough wall region, as

$$\triangle U_+ = \left(\frac{u}{u_\tau}\right)_S - \frac{u}{u_\tau} \tag{1}$$

where suffix S refers to fully smooth wall. The shift in the overlap region remains the same, if expression (1) is estimated at the boundary layer edge $y = \delta$ and $u = U_c$, to yield

$$\triangle U_+ = \left(\frac{U_c}{u_\tau}\right)_S - \frac{U_c}{u_\tau} = \left(\frac{2}{C_f}\right)_S^{1/2} - \left(\frac{2}{C_f}\right)^{1/2} \tag{2}$$

where $C_f = 2\tau_w/\rho U_c^2$ is the local skin friction coefficient. The roughness function $\triangle U_+$ is a useful descriptor of the surface roughness effects on mean velocity distribution in the inner region. It physically represents the roughness dominated shift in the velocity profile from log law of smooth wall. For $\triangle U_+ > 0$ the shift is downwards due to increase of the drag and $\triangle U_+ < 0$ the shift is upwards due to reduction of the drag of the rough surface. The shift is generally downwards causing increase in drag due to wall roughness, but in certain surfaces, i.e., longitudinal roughness can under certain conditions produce an upward shift causing reduction of drag (Abe et al. [6]). Likewise, the friction factor also contains roughness function $\triangle U_+$ as an additive term over the smooth wall value. The roughness function $\triangle U_+$ data for various types of roughness may be found in the reviews by Raupach, Antonia and Rajagopalan [2], Jimenez [3], Schlichting [7], Grigson [8], Patel [9] and Antonia et al. [10,11]. The three methods of determination of the roughness function $\triangle U_+$ are described in Granville [12] and Schultz and Myers [13]. The normal coordinate $Z = y + \epsilon_r$, where ϵ_r is the origin of the normal coordinate on the rough surface, is caused by irregular protrusions of the hydraulic roughness of height h. It is a particular level between the protrusion bases and heads which automatically satisfies the constraints $0 < \epsilon_r < h$ and $\epsilon_r = 0$ for smooth surface. Clauser [4] proposed a method of determining the effective surface roughness origin ϵ_r and skin friction u_τ.

The transitional behavior for a particular surface depends critically on the geometric nature of the roughness and its connection with hydraulic roughness regarding the onset of rough wall behavior, and relationship between root mean square (rms) roughness h_{rms} and hydraulic sand grain roughness h_s, which is surface dependent. Nikuradse [14] measurements of rough pipes, rightly celebrated for their care and completeness, have become a sort of crucial test for the experimental verification of any proposed law for velocity profile. The homogeneous roughness was obtained by gluing sand grain with various assigned diameters h to the walls of steel pipes with different diameters. The measurements were conducted using a series of tiny Pitot probes (internal diameter ranging from 0.21 and 0.3 mm and length 30 mm) placed in a section 1–2 mm downstream end of the pipe and obtained detailed and careful measurements up to the near wall proximity, for various values of roughness δ/h and Reynolds number Re. The

---

Contributed by the Fluids Engineering Division of ASME for publication in the Journal of Fluids Engineering. Manuscript received February 6, 2006; final manuscript received June 22, 2006. Review conducted by Joseph Katz.

inflectional-type roughness has also been observed by Streeter [15] in artificially roughened with spherically cut grooves for $100 \leq D/h \leq 400$, Perry and Abell [16] in a pipe covered with nylon mesh $D/h=400$.

Shockling [17], Shockling et al. [18], and Smits et al. [19] presented the machine roughness data for a fabricated pipe of diameter $D_p=128$ mm; the optical image of the "rough" surface, shows that the mean roughness height of this new surface is 1.6 μm. The root mean square roughness was $h_{\mathrm{rms}}/D_p=19.4 \times 10^6$ (about 17 times larger than the original superpipe surface), over a range of Reynolds numbers from 57×10^3 to 21.2×10^6, where h_+ varies from 0.17 to 44.4 (h is the equivalent sand grain roughness). All measurements were made at a location 191D downstream from the inlet contraction. The equivalent sand grain roughness for this surface on the basis of the friction factor data required $h \approx 3\ h_{\mathrm{rms}}$. However, in the rough regime $h=7.4$ m required $h=5.78\ h_{\mathrm{rms}}$, and earlier Hama [5] proposed $h=5\ h_{\mathrm{rms}}$. It was found that the roughness function and friction factor on machined hones roughness in superpipe shows inflectional-type roughness of Nikuradse [14], rather than Colebrook [20] and Moody [21] monotonic roughness. Allen et al. [22] for a given roughness h_+ estimated $\triangle U_+$ from $(h, \triangle U_+)$ diagram from one experiment to another, and considered $h=3\ h_{\mathrm{rms}}$ for Nikuradse data and $h=3\ h_{\mathrm{rms}}$ and $h=5.78\ h_{\mathrm{rms}}$ for their own data, to predict the friction factor results, but, as shown later, the results predicted in the present work are better than predictions of Allen et al. [22].

Direct numerical simulation (DNS) of fully developed turbulent flow in a smooth pipe has been reported by Eggels et al. [23] and smooth pipe annulus by Quadrio and Luchini [24]. In channel flow, the effects of roughness on DNS solutions have been studied by Abe et al. [25], Leonardi et al. [26], Nagano et al. [27], Ashrafian et al. [28], Krogstad et al. [29]. The comparison of data with experiments has been reported by Djendi et al. [30] and Bakken et al. [31].

The present work deals with a more appropriate alternate variable, the inner rough wall variable $\zeta=Z_+/\phi$, based on transitional roughness scale ϕ, such that all mean relative motions and energy-containing components of the turbulent motion do not depend on surface roughness. Further, based on roughness velocity, two new numbers termed as roughness friction Reynolds number R_ϕ and roughness Reynolds number Re_ϕ are identified. An alternate, two layer theory for transitionally rough pipes is formulated in terms of alternating more appropriate inner wall variables by the method of matched asymptotic expansions. The matching by Izakson-Millikan-Kolmogorov hypothesis in the overlap region gives the universal log law and universal friction factor law, for all types of roughness. The extensive data on transitional rough wall velocity profile and friction factor are the universal relations. The data for various types of roughness, in transitional regime, provide good support to the predictions of alternate universal log law velocity profile based on single parameter, the roughness friction Reynolds number. In addition to log laws, the matching condition in the overlap region, also admits the power law solutions as shown by Afzal [32–35]. It is shown that the power law velocity profile is equivalent to the log law velocity profile, for very large Reynolds numbers, when constants k and B are universal numbers independent of the Reynolds numbers. But at moderately large Reynolds numbers the power law relations predict k and B as a function of Reynolds number and the power law theory is not equivalent to the log law theory. The power law theory, in transitional rough pipes, has been compared with experimental data and also provides strong support to the theory.

2 Momentum Equation

The Reynolds equation of mean motion in fully developed pipe flow is

$$\nu \frac{du}{dy} + \frac{\tau}{\rho} = u_\tau^2 \left(1 - \frac{y}{\delta}\right) \tag{3}$$

Here $u(y)$ is the axial velocity, y is the normal coordinate, $\tau = -\rho\langle u'v'\rangle$ is the appropriate Reynolds shear stress, $u_\tau = \sqrt{\tau_w/\rho}$ is the friction velocity, τ_w is the skin friction, ρ is the fluid density, and ν is the molecular kinematic viscosity of fluid. In fully developed channel (or pipe) flow U_c is independent of x, representing the velocity at pipe axis $y=\delta$, where δ is pipe radius. The boundary conditions on the wall require velocity u and Reynolds shear stress τ to vanish there, and on the axis are those of symmetry as given below

$$y=0, \quad u=0, \quad \tau=0 \tag{4}$$

$$y=\delta, \quad u=U_c, \quad \tau=0 \tag{5}$$

The present work is defining the roughness velocity u_ϕ and roughness coordinate y_ϕ in terms of axial velocity u at normal distance y, as given below

$$y_\phi = \frac{y}{\phi}, \quad u_\phi = \frac{u}{\phi} \tag{6}$$

Here ϕ is the transitional roughness wall scale, defined by relation (12), such that all mean velocity and energy-containing components of the turbulent Reynolds stress do not depend on surface roughness. Based on alternate rough wall variables (6), the inner variables are defined as

$$\zeta = \frac{Z u_{\tau\phi}}{\nu} = \frac{Z_+}{\phi}, \quad Z_+ = \frac{Z u_\tau}{\nu}, \quad Z = y + \epsilon_r \tag{7}$$

$$u_+ = \frac{u_\phi}{u_{\tau\phi}} = \frac{u}{u_\tau}, \quad u_{\tau\phi} = \frac{u_\tau}{\phi} \tag{8}$$

where ϵ_r is the virtual origin, located below the top of the roughness element. Two roughness friction Reynolds number new parameters R_ϕ is defined by the relation

$$R_\phi = \frac{u_{\tau\phi}\delta}{\nu} = \frac{R_\tau}{\phi}, \quad R_\tau = \frac{U_\tau \delta}{\nu} \tag{9}$$

and roughness Reynolds number Re_ϕ based on pipe diameter $d_p = 2\delta$ and average velocity U_b is

$$\mathrm{Re}_\phi = \frac{U_{b\phi} d_p}{\nu} = \frac{\mathrm{Re}}{\phi}, \quad \mathrm{Re} = \frac{U_b d_p}{\nu} \quad U_{b\phi} = \frac{U_b}{\phi} \tag{10}$$

The two Reynolds numbers are connected by the relation

$$R_\phi = \mathrm{Re}_\phi \sqrt{\frac{\lambda}{8}} \tag{11a}$$

$$\lambda = 8\left(\frac{u_\tau}{U_b}\right)^2 \tag{11b}$$

$$\lambda = -\frac{dp}{dx}\frac{2d_p}{\rho U_b^2} \tag{11c}$$

where λ is the friction factor. Extensive analysis of data shows that the roughness scale ϕ is connected with roughness function $\triangle U_+$, as given below

$$\triangle U_+ = \frac{1}{k} \ln \phi \tag{12}$$

The appropriate parameter R_ϕ is the roughness friction Reynolds number. The overall description of turbulent flows is in terms of two length scales of the inner and outer layers. The dimensional analysis based on the inner region scaling (ν and $u_{\tau\phi}$) and the outer wake region scaling (δ, u_τ and ϕ) are considered.

2.1 Inner Wall Layer. The inner region scales (ν and $u_{\tau\phi}$) give the inner length scale $\nu/u_{\tau\phi}$ and the inner limit is ζ fixed for $R_\phi \to \infty$. The velocity profile and Reynolds shear stress in the inner wall layer variables are

$$u_\phi = \frac{u}{\phi} = \phi u_{\tau\phi} f(\zeta, R_\phi), \quad \tau = \rho\phi^2 u_{\tau\phi}^2 g(\zeta, R_\phi), \quad \zeta = \frac{Z u_{\tau\phi}}{\nu} \tag{13}$$

and Eq. (3) in the inner layer becomes

$$\frac{df}{d\zeta} + g = 1 - R_\phi^{-1}\zeta \tag{14}$$

2.2 Outer Layer. The outer layer length scale is δ and outer limit is $Y = Z/\delta$ fixed for $R_\phi \to \infty$. The velocity profile and Reynolds shear stress in the outer layer variables are

$$u = U_c - u_\tau F(Y, R_\phi), \quad \tau = \rho u_\tau^2 G(Y, R_\phi), \quad Y = \frac{Z}{\delta} \tag{15}$$

and Eq. (3) in outer layer becomes

$$G = 1 - Y + R_\phi^{-1}\frac{dF}{\phi dY} \tag{16}$$

2.3 Matching. The matching of inner and outer layers velocity profile and Reynolds shear stress profiles for large Reynolds numbers $R_\phi \to \infty$ requires

$$u_+(\zeta) = \frac{U_c}{u_\tau} - F(Y) \tag{17a}$$

$$g(\zeta) = G(Y) \tag{17b}$$

where $u_+(\zeta) = u/u_\tau$. Following, Millikan [1] and Afzal [35], we differentiate Eq. (17a) to get

$$\zeta\frac{du_+}{d\zeta} = -Y\frac{dF}{dY} \tag{18}$$

for $\zeta \to \infty$ and $Y \to 0$. The matching relations (17a) and (18) provide both the log law and power law solutions (Afzal et al. [32–35]). The integrations of Eq. (18) give the log laws velocity profiles in the overlap region and the matching relation (17a) gives the skin friction log laws as given below

$$\frac{u}{u_\tau} = \frac{1}{k}\ln\zeta + B \tag{19a}$$

$$\frac{U_c - u}{u_\tau} = -\frac{1}{k}\ln Y + D \tag{19b}$$

$$\frac{U_c}{u_\tau} = \frac{1}{k}\ln R_\phi + B + D \tag{20}$$

The composite velocity profile solutions are given below

$$\frac{u}{u_\tau} = \frac{1}{k}\ln\zeta + B + \frac{\Pi}{k}W(Y) \tag{21}$$

$$\frac{U_c - u}{u_\tau} = -\frac{1}{k}\ln Y + \frac{\Pi}{k}[W(1) - W(Y)] \tag{22}$$

Here Π is the wake parameter and $W(Y)$ is the wake function (Coles [36]), defined by the relation (23), with the boundary conditions $W(0)=0$ and $W(1)=1$ or 2 as desired and $D = W(1)\ \Pi/k$.

The Reynolds shear stress in the inner and outer variables becomes

$$\frac{\tau}{\tau_w} = 1 - \frac{1}{k\phi\zeta} - R_\phi^{-1}\left(\zeta + \frac{\Pi}{k\phi}\frac{dW}{dY}\right) \tag{23a}$$

$$\frac{\tau}{\tau_w} = 1 - Y - R_\phi^{-1}\left(\frac{1}{k\phi Y} + \frac{\Pi}{k\phi}\frac{dW}{dY}\right) \tag{23b}$$

In the overlap region, the wake component is neglected and the expressions become

$$\frac{\tau}{\tau_w} = 1 - \frac{1}{k\phi\zeta} - \zeta R_\phi^{-1} \tag{24a}$$

$$\frac{\tau}{\tau_w} = 1 - Y - \frac{1}{k\phi Y}R_\phi^{-1} \tag{24b}$$

The relation (24a) gives maxima in Reynolds stress $\zeta_{+\max}$ and maximum value $\tau_{\max}$ given below

$$\zeta_{+\max} = \sqrt{\frac{R_\phi}{k\phi}} \tag{25a}$$

$$\frac{\tau_{\max}}{\tau_w} = 1 - \frac{2}{\sqrt{k\phi R_\phi}} \tag{25b}$$

2.4 Friction Factor. The integration of logarithmic expression for the velocity profile (22) over the cross section of pipe gives a relationship between friction factor $\lambda = 8(u_\tau/U_b)^2$ and frictional rougness Reynolds number as

$$\frac{U_b}{u_\tau} = 2\int_0^1 \frac{u}{u_\tau}(1 - Y)dY = \frac{1}{k}\ln R_\phi + B + D - D_b \tag{26}$$

$$\frac{1}{\sqrt{\lambda}} = A_1\log R_\phi + B_1 \tag{27}$$

$$A_1 = \frac{1}{k\sqrt{8}\ln 10}, \quad B_1 = \left(B + \frac{\Pi}{k}W(1) - D_b\right) \Big/ \sqrt{8}, \quad D = \frac{\Pi}{k}W(1) \tag{28}$$

$$U_b = U_c - u_\tau D_b, \quad D_b = \frac{3}{2k} + \frac{\Pi}{k}\left[W(1) - 2\int_0^1 (1 - Y)W(Y)dY\right] \tag{29}$$

Using Coles [32] Wake function $W(Y)$, the constant D_b becomes

$$W(Y) = \frac{W(1)}{2}[1 - \cos(\pi Y)], \quad D_b = \frac{3}{2k} + \frac{2\Pi}{k}\frac{W(1)}{\pi^3} \tag{30}$$

and adopt $W(1)=1$ or 2 as appropriate. For fully smooth pipes ($\phi=1$), the constants proposed by Prandtl [37] are $A_1=2$ and $B_1 = -0.8 + 2\log\sqrt{32} = 0.705$, MeKeon et al. [38], $A_1 = 1.93$ and $B_1 = -0.537 + 1.93\log\sqrt{32} = 0.915$, Zagarola and Smits [39] $A_1 = 1.89$ and $B_1 = -0.3577 + 1.89\log\sqrt{32} = 1.065$. The constants, slightly adjusted (following Prandtl [37] for smooth pipe) and relation (27) yield

$$\frac{1}{\sqrt{\lambda}} = 2\log_{10}(\mathrm{Re}_\phi\sqrt{\lambda}) - 0.8 \tag{31a}$$

$$\frac{1}{\sqrt{\lambda}} = 2\log_{10}(R_\phi\sqrt{32}) - 0.8 \tag{31b}$$

For smooth flow $\phi=1$, $\mathrm{Re}_\phi = \mathrm{Re}$ and relations (31a) and (31b) give Prandtl universal log law relation. The constants, of McKeon et al. [38] (for smooth pipe) yields relation (27) as

$$\frac{1}{\sqrt{\lambda}} = 1.93\log_{10}(\mathrm{Re}_\phi\sqrt{\lambda}) - 0.537 \tag{32a}$$

$$\frac{1}{\sqrt{\lambda}} = 1.93\log_{10}(R_\phi\sqrt{32}) - 0.537 \tag{32b}$$

3 Reduction to Traditional Picture

The uniformly valid velocity profile (21) may be expressed in traditional variables of smooth wall variable Z_+ and roughness function $\triangle U_+$, with the help of expressions (9) and (12), as

$$\frac{u}{u_\tau} = \frac{1}{k}\ln Z_+ + B - \triangle U_+ + \frac{\Pi}{k}W(Y) \tag{33}$$

Likewise, the skin friction relation (20) yields

$$\frac{U_c}{u_\tau} = \frac{1}{k}\ln R_\tau + B - \triangle U_+ + \frac{\Pi}{k}W(1) \tag{34}$$

The velocity profile (33) may also be expressed as

$$\frac{u}{u_\tau} = \frac{1}{k}\ln Z_+ + B_t + \frac{\Pi}{k}W(Y) \tag{35a}$$

$$\triangle U_+ = B - B_t \tag{35b}$$

In meteorological approach the atmosphere data of velocity profile (33) in terms of rough wall variable Z/h becomes

$$\frac{u}{u_\tau} = \frac{1}{k}\ln\frac{Z}{h} + B_T + \frac{\Pi}{k}W(Y) \tag{36}$$

where B and B_T are the intercepts of log laws in fully smooth wall and transitional roughness flows. The roughness function $\triangle U_+$ and roughness scale ϕ from relations (35) and (38) yield

$$\triangle U_+ = \frac{1}{k}\ln h_+ + B - B_T \tag{37}$$

$$\phi = \exp(k\triangle U_+) = h_+\exp[k(B - B_T)] \tag{38}$$

When h_+ is sufficiently small (less than about 5 for sand roughness) the flow is hydraulically smooth where $B=5.5$, $\triangle U_+=0$, and $\phi=1$. When h_+ is sufficiently large (more than about 70 for sand roughness) the flow is fully rough $B_T=B_R=8.5$, the roughness functions $\triangle U_+$ and roughness potential ϕ become large.

4 Commercial and Sand Grain Roughness

It has been pointed out by Bendrict [40] that one of the amazing fortuitous happenings in engineering, and a tribute to Colebrook's [20] insight that the simple addition of two limiting expressions, associated with the log terms in the friction factors for fully smooth and fully rough pipes, predicted a transitional friction factor that increases monotonically with h_+. The roughness scale ϕ for Colebrook [20] commercial pipes roughness corresponds to

$$\triangle U_+ = \frac{1}{k}\ln(1 + \chi h_+) \tag{39a}$$

$$\phi = 1 + \chi h_+ \tag{39b}$$

$$\chi = \exp[k(B - B_F)] \tag{39c}$$

where $B=5.5$ and $B_F=8.5$ and $\chi=\exp[k(B-B_F)]=0.306$. Colebrook [20] monotonic roughness (39) for friction factor leads to the well known Moody [21] plot (see page 528, Fig. 20.25 Schlichting [7]), of friction factor. Colebrook-type roughness function (39) has been used for random roughness by Grigson [8] and his Table 1 gives values of χ for the finishes of the hull surfaces.

The inflectional roughness data of Nikuradse [14] has been analyzed by Loselevich and Pilipenko (see Cebeci [41]) to suggest the following correlation

$$\triangle U_+ = (B - 8.5 + k^{-1}\ln h_+)\sin(\pi q) = \frac{1}{k}\ln\phi, \quad q = \frac{\ln(h_+/2.25)}{\ln(90/2.25)} \tag{40}$$

for $2.25 \le h_+ < 90$ with $B=5.2$ and $k=0.42$. In present work dealing with inflectional pipes roughness, a simple expression for roughness scale ϕ is proposed by introducing an exponential function $\exp(-j/h_+)$ in Colebrook [20] relations (39*a*) and (39*b*) for $\phi=1+\chi h_+$ yields

$$\phi = 1 + \chi h_+\exp\left(-\frac{j}{h_+}\right) \tag{41a}$$

$$\triangle U_+ = \frac{1}{k}\ln\phi \tag{41b}$$

$$\chi = \exp[k(B - B_F)] \tag{41c}$$

where $j=0$ corresponds to Colebrook [20] monotonic commercial roughness and $j\neq 0$ is a free parameter. The roughness scale ϕ relation (41*a*) for parameter $j\neq 0$ has a point of inflection at origin $h_+=0$. Further, the exponential function in the relation (41*a*) approaches unity for $h_+\to\infty$ and zero for $h_+\to 0$, that maintain, respectively, the traditional friction factor relations of Nikuradse [14] for fully rough pipes and Prandtl [37] for fully smooth pipes. Consequently, for inflectional-type roughness the choice $j=11$ has been obtained by curve fitting to the data of Nikuradse [14] and Shockling [17].

The roughness friction Reynolds number R_ϕ and roughness Reynolds number Re_ϕ becomes

$$R_\phi = R_\tau \bigg/ \left[1 + \chi h_+\exp\left(-\frac{j}{h_+}\right)\right] \tag{42a}$$

$$\mathrm{Re}_\phi = \mathrm{Re} \bigg/ \left[1 + \chi h_+\exp\left(-\frac{j}{h_+}\right)\right] \tag{42b}$$

The constants B_T and B_t from relations (39*a*), (39*b*), and (37) based on roughness functions (41*a*), (41*b*) become

$$B_T = B - \frac{1}{k}\ln\left[\frac{1}{h_+} + \chi\exp\left(-\frac{j}{h_+}\right)\right] \tag{43a}$$

$$B_t = B - \frac{1}{k}\ln\left[1 + \chi h_+\exp\left(-\frac{j}{h_+}\right)\right] \tag{43b}$$

The velocity profile log law (22) and the skin friction log law (21) become

$$\frac{u}{u_\tau} = \frac{1}{k}\ln\left\{Z_+ \bigg/ \left[1 + \chi h_+\exp\left(-\frac{j}{h_+}\right)\right]\right\} + B + \frac{\Pi}{k}W(Y) \tag{44}$$

$$\frac{U_c}{u_\tau} = \frac{1}{k}\ln\left\{R_\tau \bigg/ \left[1 + \chi h_+\exp\left(-\frac{j}{h_+}\right)\right]\right\} + B + D \tag{45}$$

The friction factor log law (45) may also be expressed as

$$\frac{U_c}{u_\tau} = -\frac{1}{k}\ln\left[\frac{1}{R_\tau}\exp[-k(B+D)] + \frac{h}{\delta}\exp[-k(B_F+D)] \times\exp\left(-\frac{j}{h_+}\right)\right] \tag{46}$$

The friction factor log law relation (46) holds for the turbulent boundary layer as well as fully developed pipe in the transition region of the technical commercial roughness. In terms of average velocity U_b from relation (29), the friction factor (46) gives

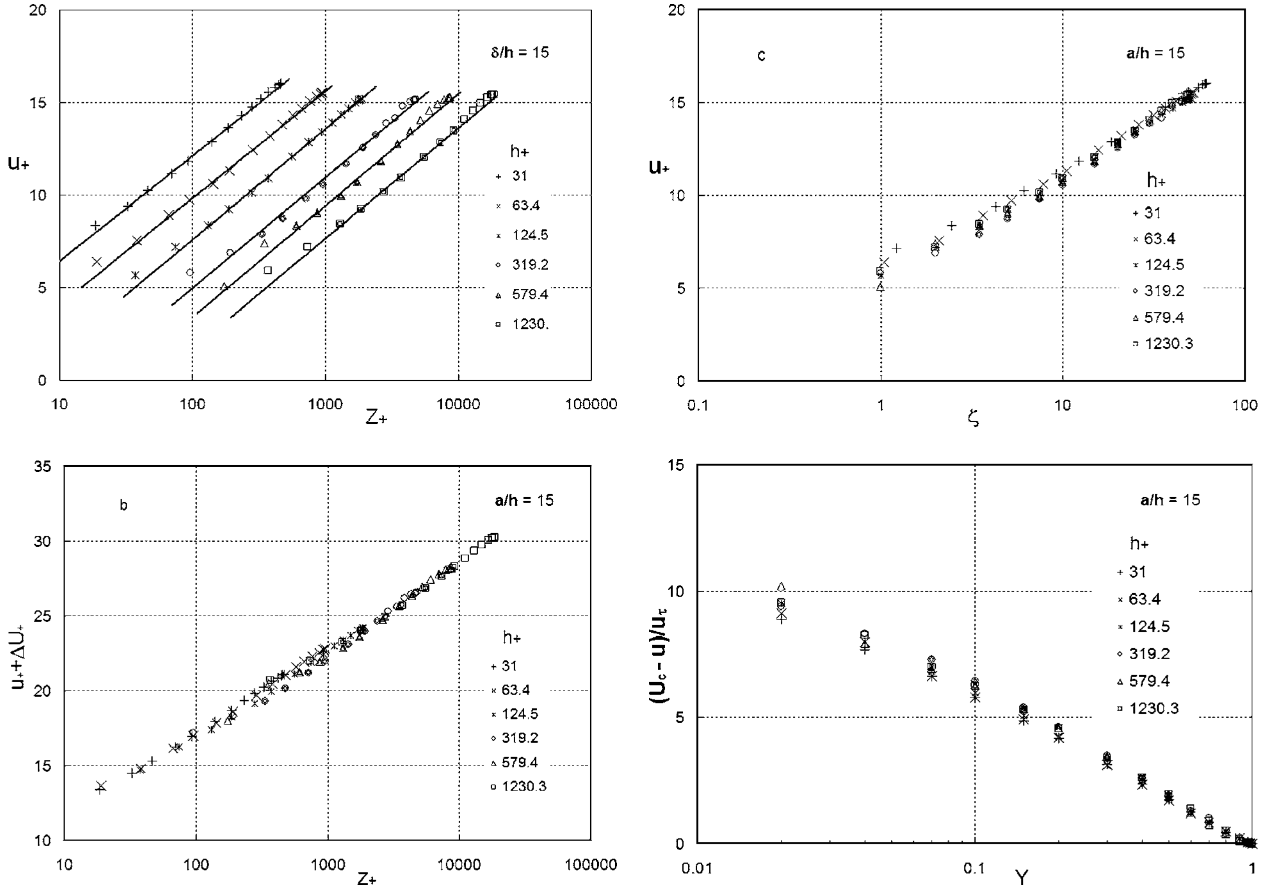

Fig. 1 The log law velocity profile for transitional roughness $\delta/h=60$ for various values of h_+ in the range $31 \le h_+ \le 1230.3$ from sand grain data of Nikuradse (1933): (*a*) Traditional inner wall law in smooth wall variables (u_+, Z_+). (*b*) Velocity profile shifted by the roughness function $u_+ + \triangle U_+$ with smooth wall variable Z_+. (*c*) Proposed inner transitional rough wall in universal variables (u_+, ζ). (*d*) Outer velocity defect variables $(U_{c+} - u_+, Y)$.

$$\sqrt{\frac{8}{\lambda}} = -\frac{1}{k}\ln\left[\frac{1}{R_\tau}\exp[-k(B+D+D_b)] + \frac{h}{\delta}\exp[-k(B_F+D+D_b)]\exp\left(-\frac{j}{R_\tau}\frac{\delta}{h}\right)\right] \tag{47}$$

$$\sqrt{\frac{8}{\lambda}} = -\frac{1}{k}\ln\left\{\left[\exp[-k(B+D+D_b)]\right]\left[\frac{1}{R_\tau} + \chi\frac{h}{\delta}\exp\left(-\frac{j}{R_\tau}\frac{\delta}{h}\right)\right]\right\} \tag{48}$$

The relation (48) expressed in terms of Reynolds number $\mathrm{Re} = U_b d/\nu$ is given below

$$\sqrt{\frac{8}{\lambda}} = -\frac{1}{k}\ln\left\{\left[\exp[-k(B+D+D_b)]\right] \times \left[\frac{1}{\mathrm{Re}}\sqrt{\frac{32}{\lambda}} + \chi\frac{h}{\delta}\exp\left(-\frac{j}{\mathrm{Re}}\sqrt{\frac{32}{\lambda}}\frac{\delta}{h}\right)\right]\right\} \tag{49}$$

The friction factor expression (31*a*) and roughness scale ϕ relations (39*a*), (39*b*) in terms of friction Reynolds number R_τ and Reynolds number Re yield

$$\frac{1}{\sqrt{\lambda}} = 1.74 - 2\log_{10}\left[\frac{3.288}{R_\tau} + \frac{h}{\delta}\exp\left(-\frac{j}{R_\tau}\frac{\delta}{h}\right)\right] \tag{50}$$

$$\frac{1}{\sqrt{\lambda}} = 1.74 - 2\log_{10}\left[\frac{18.6}{\mathrm{Re}\sqrt{\lambda}} + \frac{h}{\delta}\exp\left(-j\frac{5.66}{\mathrm{Re}\sqrt{\lambda}}\frac{\delta}{h}\right)\right] \tag{51}$$

The friction factor relations (50) and (51) may also be expressed as

$$\frac{1}{\sqrt{\lambda}} = -2\log_{10}\left[\frac{0.444}{R_\tau} + \frac{h}{3.7\delta}\exp\left(-\frac{j}{R_\tau}\frac{\delta}{h}\right)\right] \tag{52}$$

$$\frac{1}{\sqrt{\lambda}} = -2\log_{10}\left[\frac{2.51}{\mathrm{Re}\sqrt{\lambda}} + \frac{h}{3.7\delta}\exp\left(-j\frac{5.66}{\mathrm{Re}\sqrt{\lambda}}\frac{\delta}{h}\right)\right] \tag{53}$$

where $j=11$ for inflectional roughness of Nikuradse and $j=0$ for Colebrook monotonic roughness.

5 Results and Discussion

The velocity profile and friction factor for transitional pipes roughness are the universal log laws in inner variable ζ and roughness friction Reynolds number R_ϕ, that are explicitly independent of pipe roughness. But, these variables involve the roughness scale ϕ, and dependence on wall roughness is implicit.

The velocity distribution for sand grain roughness pipes data of Nikuradse [14] for $\delta/h=15$ and $31 \le h_+ \le 1230.3$ is shown in Fig. 1 and for $\delta/h=60$ and $8 \le h_+ \le 369.8$ is shown in Fig. 2. The velocity distribution for machine surface transitional super pipe data of Shockling [17] for roughness $\delta/h=7190$ and $0.1 \le h_+ \le 45$ are shown in Fig. 3. In traditional smooth wall variables (u_+, Z_+), the velocity profile data of Nikuradse [14] and Shockling

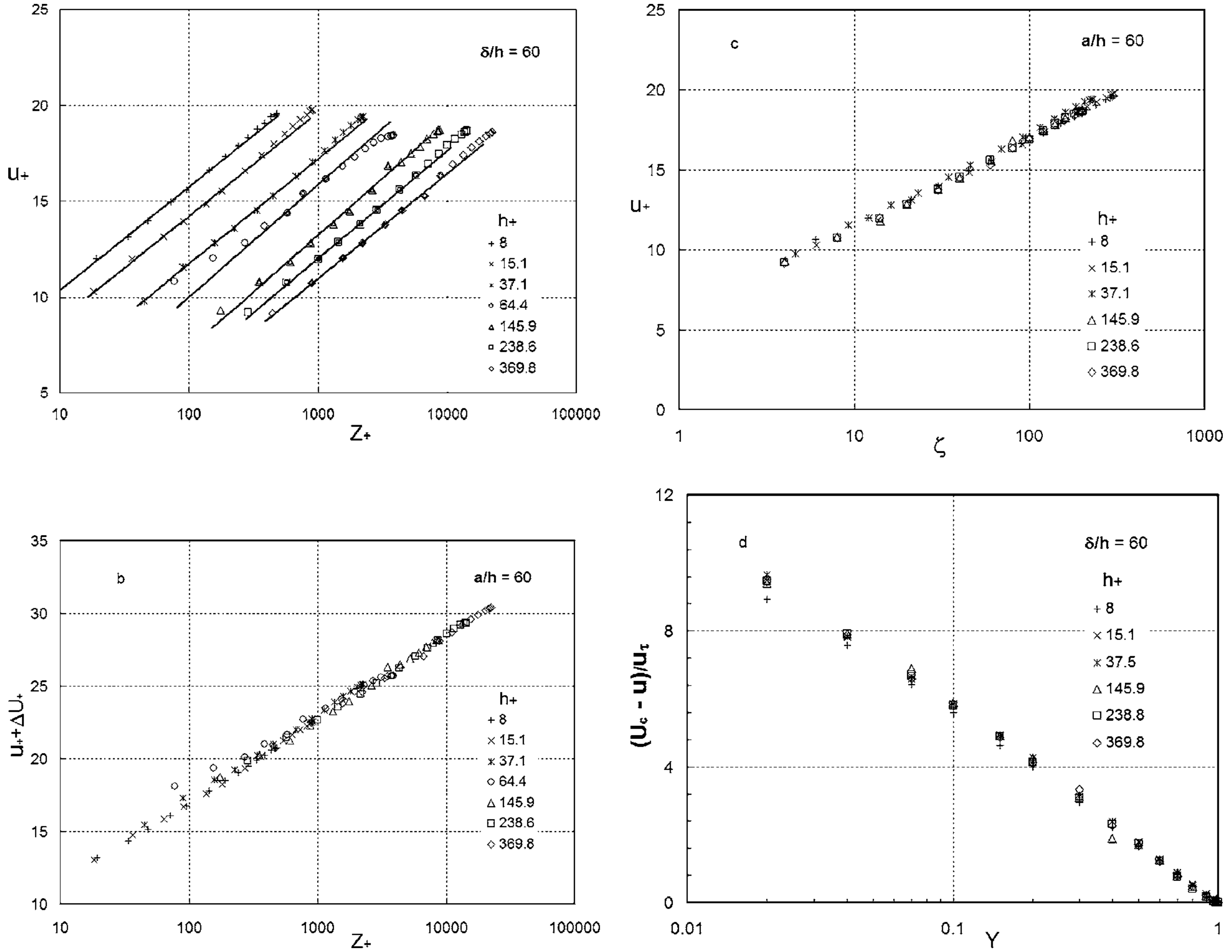

Fig. 2 The log law velocity profile for transitional roughness $\delta/h=60$ for various values of h_+ in the range $8 \le h_+ \le 369.8$ from sand grain data of Nikuradse (1933): (*a*) Traditional inner wall law in smooth wall variables (u_+, Z_+). (*b*) Velocity profile shifted by the roughness function $u_+ + \triangle U_+$ with smooth wall variable Z_+. (*c*) Proposed inner transitional rough wall in universal variables (u_+, ζ). (*d*) Outer velocity defect variables $(U_{c+} - u_+, Y)$.

[17] are shown in the Figs. 1(*a*), 2(*a*), and 3(*a*). The data shift their locations with change of roughness parameter h_+ or δ/h. The data represented by traditional log law (33), in the overlap region, determines the roughness function $\triangle U_+$ from shift of data in the overlap region as a funcion of roughness parameter h_+ or δ/h.

In transitional rough wall variables (u_+, ζ) the velocity profile log law (19*a*) in inner variable ζ is a universal function, which contains two constants, the slope k and additive term B, the same as in smooth wall. The velocity distribution shifted by roughness function $u_+ + \triangle U_+$ against traditional smooth wall variable Z_+ is shown in Figs. 1(*b*), 2(*b*), and 3(*b*) on semi-log plot for log law profile $u_+ + \triangle U_+ = k^{-1} \ln Z_+ + B$, that does not show dependance on wall roughness. In transitional wall roughness new variable ζ proposed in this paper, the sand grain roughness data of Nikuradse [14] and machine surface transitional super pipe data of Shockling [17], shown in Figs. 1(*c*), 2(*c*), and 3(*c*), collapse on this single line $u_+ = k^{-1} \ln \zeta + B$, described by Eq. (19), showing that it does not explicitly depend on wall roughness h_+ or δ/h. However, the relation (19) implicitly depends on roughness scale ϕ involved in definition of inner variable ζ. The velocity profiles in outer layer defect variables $(U_{c+} - u_+, Y)$ predicted by relation (19*b*) contain two constants, the slope k and additive constant D are universal numbers, same as for smooth walls constants. The data shown in Figs. 1(*d*), 2(*d*), and 3(*d*) collapse on single line (19*b*), irrespective of roughness scale h_+. The present work of Flack et al. [42] and Connelly et al. [43] support the Townsend similarity hypothesis, which states that the turbulence outside of the roughness sublayer, a layer extending out approximately five roughness heights from the wall, is independent of the surface condition at sufficiently high Reynolds numbers. However, some recent research (see Antonia and Krogstadt [11]) casts doubts on the wall similarity hypothesis, stating that roughness effects can be observed well into the outer layer, but Flack et al. [42] and Connelly et al. [43] in turbulent boundary layer flows have shown excellent agreement among the smooth and rough surfaces for Reynolds stresses for $y > 5h$ and the higher-order turbulence statistics up to the fourth moment also showed good agreement for $y > 8h$. Moreover, in fully developed pipe flow, the outer layer is weak and its influence on inner wall layer is not significant.

The roughness function $\triangle U_+$ with roughness variable h_+ is shown in Fig. 4(*a*) for sand grain roughness data of Nikuradse [14] and machine surface transitional super pipe data of Shockling [17]. The present prediction (41*b*) based on (41*a*) for inflectional roughness ($j=11$), also shown in the same figure, compares well with all data. The roughness scale ϕ is connected with roughness function $\triangle U_+$ by relation (12). The roughness scale ϕ with roughness variable h_+ is also shown in Fig. 4(*b*) for sand grain roughness data of Nikuradse [14] and machine surface transitional super pipe data of Shockling [17]. The present prediction (41*a*) for $j=11$ also shown in same figure compares well with the data. The

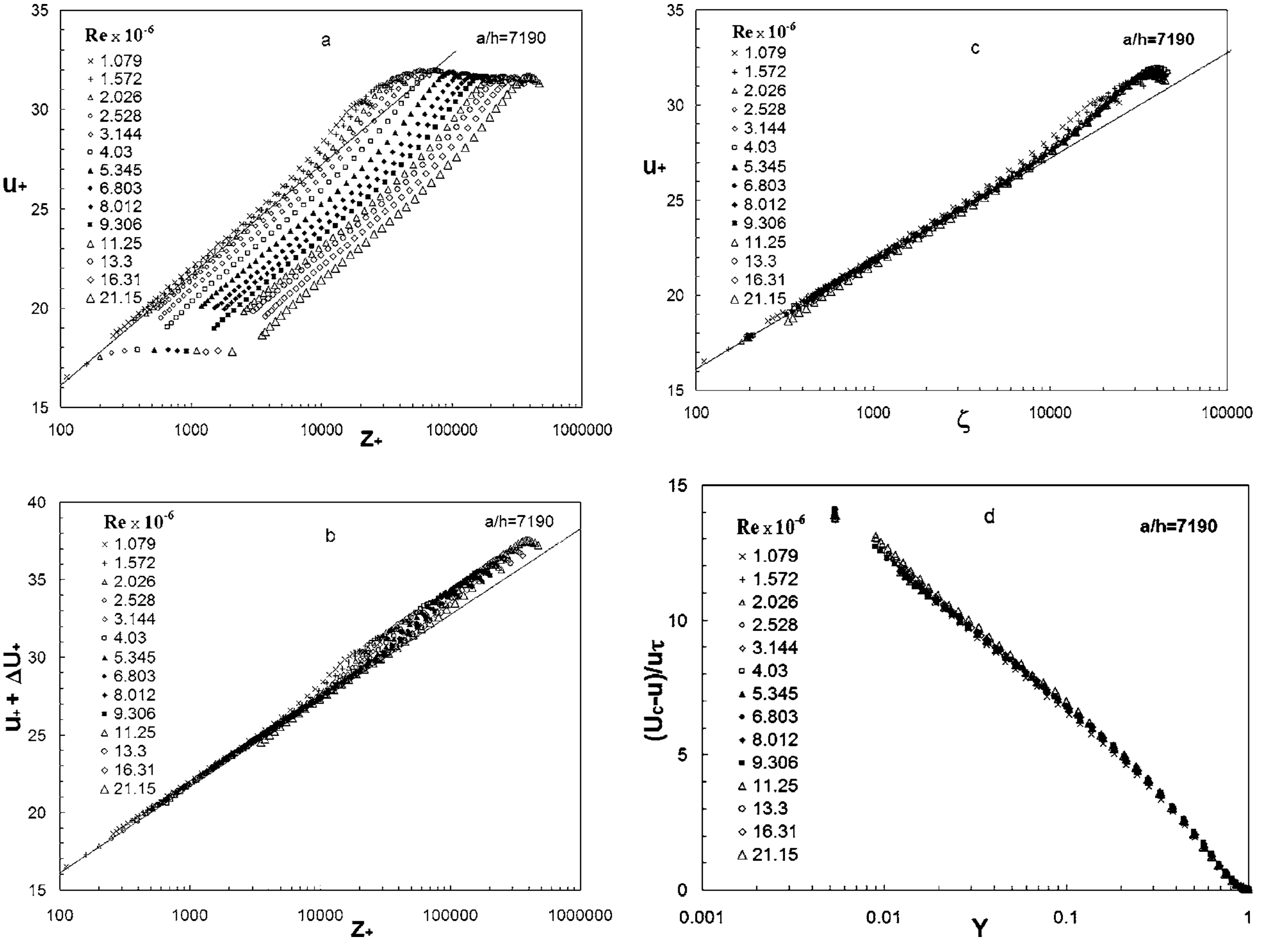

Fig. 3 The log law velocity profile for transitional roughness $\delta/h=7190$ for various values of h_+ in the range $0.1\le h_+ \le 44.46$ from machine surface roughness super pipe data of Shockling (2005): (*a*) Traditional inner wall law in smooth wall variables (u_+, Z_+). (*b*) Velocity profile shifted by the roughness function $u_+ + \triangle U_+$ with smooth wall variable Z_+. (*c*) Proposed inner transitional rough wall in universal variables (u_+, ζ). (*d*) Outer velocity defect variables $(U_{c+}-u_+, Y)$.

predictions for Colebrook commercial roughness are also shown in these figures 4(*a*) and 4(*b*) for appreciation of monotonic roughness effects.

The traditional log law (36) containing the additive intercept B_T (in fully rough wall variable Z/h) and log law (35) with intercept B_t (in fully smooth wall variable Z_+) from sand grain roughness data of Nikuradse [14] is compared with present predictions (43*a*), (43*b*). The additive constant B_T for sand grain roughness, shown in Fig. 5(*a*), compares well with the prediction (43*a*). Further, the additive constant B_t for sand grain roughness, shown in Fig. 5(*b*), also compares well with the prediction (43*b*) for inflectional roughness ($j=11$). For comparison, the predictions of B_T and B_t with $j=0$ for Colebrook commercial roughness are also shown in same figures for appreciation on Colebrook commercial technical roughness. The constant B_T from Shockling [17] machine surface roughness data $0.185<h_+<44.45$ and $B_t=B_T-\triangle U_+$ are also shown in these figures that depart for $h_+>6$ from Nikuradse data. The point of view of Shockling [17] that the surface elevation due to honed roughness has a nearly Gaussian roughness distribution, whereas the roughness elements used by Nikuradse [14] sandgrain roughness had an extremely narrow bandwidth and would not necessarily possess a Gaussian distribution, may be of interest and further investigation is needed. An attempt is made to check the consistency of Shockling [17] tabulated data for B_T and $\triangle U_+$ for various values of pipe roughness parameter h_+. Based on data $(\triangle U_+, h_+)$ of Shockling the constant B_T and B_t are estimated from fundamental relation (37) with $k=0.4$ and $B=5.5$ and relation (35*b*) are marked *Sh-R* in Figs. 5(*a*) and 5(*b*). The data *Sh-R* marked by solid triangles is quite close to Nikuradse data, as well as present prediction (43*a*), (43*b*) of inflectional-type roughness ($j=11$).

The friction factor predictions (31*a*), (31*b*) are universal for all kinds of roughness, based on the same universal constants as in Prandtl universal friction factor of smooth pipes, are tested with sand grain roughness data of Nikuradse and machine surface roughness data of Shockling [17]. The friction factor, in alternate transitional rough pipe variables $(\lambda, \mathrm{Re}_\phi)$ from the data of Nikuradse [14] and Shockling [17] shown in Fig. 6(*a*), collapse on a universal prediction (31*b*). Likewise, the friction factor in alternate transitional rough pipe variables $(\lambda, \mathrm{Re}_\phi)$ from data of Nikuradse [14] and Shockling [17], shown in Fig. 6(*b*), also collapse on universal relation (31*a*). The data for various types of roughness, in transitional and fully rough regime, provide good support to the predictions of the universal log laws for velocity profile and friction factor, based on single parameter Re_ϕ or R_ϕ as appropriate.

The friction factor relations (31*a*) and (31*b*) by using roughness function (41*a*) and (41*b*) have been expressed in terms of traditional Reynolds number, yielding the relations (50) and (51) for inflectional roughness as well as Colbrook monotonic roughness. The friction factor relations with $j=0$ corresponds to Colebrook [20] monotonic wall roughness, which represent the well known Moody [21] diagram. Our predictions (50) and (51) for inflectional roughness fit well with data of Nikuradse [14] and Shock-

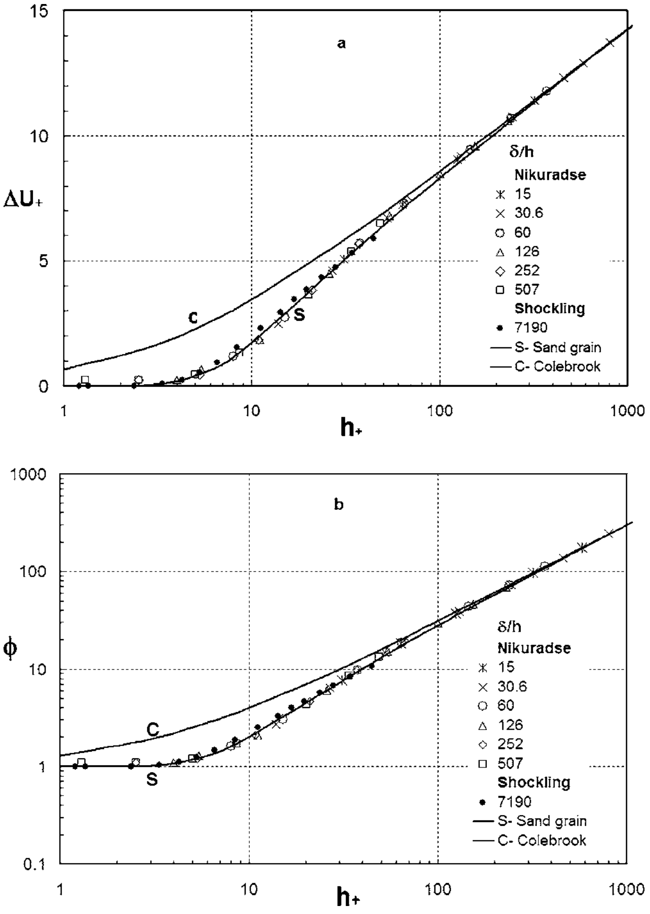

Fig. 4 The transitional roughness characteristics from Nikuradse data of sand grain pipes roughness and Shockling data of machined honed surface roughness in Princeton's superpipe: (*a*) Roughness function $\triangle U_+$ against h_+. (*b*) Roughness scale ϕ against h_+. Prediction lines (41) and (39) marked *S* is for inflectional roughness and marked *C* is for Colebrook commercial roughness.

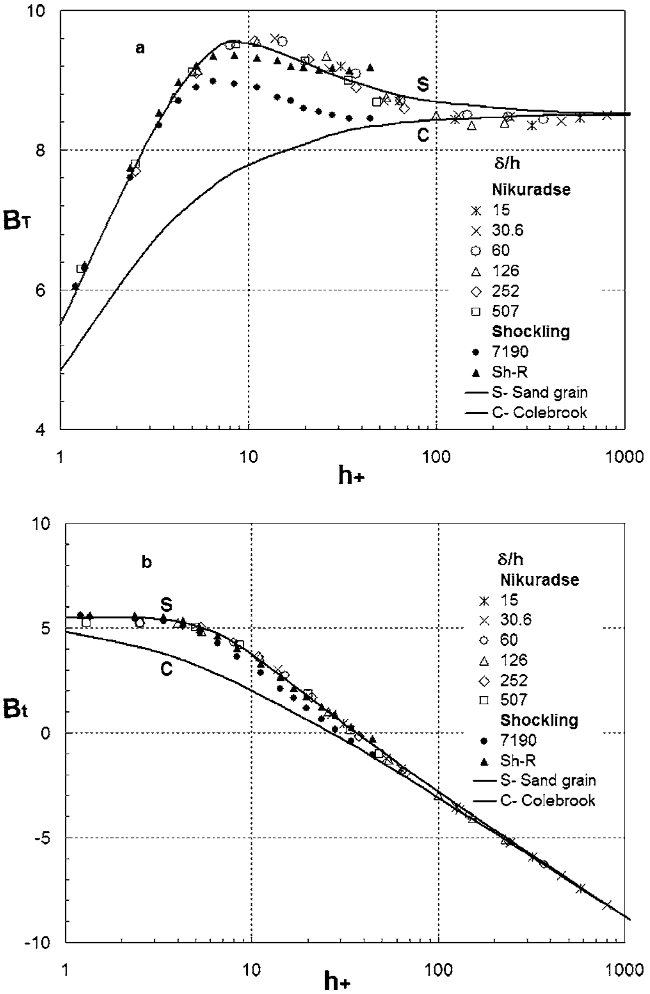

Fig. 5 The log law intercepts B_T and B_t from Nikuradse data of sand grain roughness and Shockling data of machined honed surface roughness for various values of h_+ and δ/h. Sh-R denotes the predictions of B_T and B_t from Shocking roughness function and roughness ($\triangle U_+$, $h+$) data and constants $k=0.4$ and $B=5.5$. Prediction lines (43*a*) and (43*b*) marked *S* is for inflectional roughness and marked *C* is for Colebrook commercial roughness.

ling [17] for ($j=11$). The predictions of friction factor for inflectional roughness ($j=11$) are compared with the data of Nikuradse [14] and Shockling [17] in Fig. 7(*a*) against R_τ and Fig. 7(*b*) against Re. For each value of δ/h the prediction is represented by the line, which for large R_τ approaches to fully rough wall values and for small R_τ it merges with smooth wall skin friction law. Nikuradse [14] and Shockling [17] data shown in Fig. 7(*a*) and Fig. 7(*b*) provide very good support to the proposed prediction in the turbulent flow existing beyond the upper critical Reynolds number Re=3000, where $\lambda=0.0213$ and $R_\tau=77.16$. Allen et al. [22] for a given roughness h_+ estimated $\triangle U_+$ from $(h, \triangle U_+)$ diagram from one experiment to another, and considered $h=3\ h_{\mathrm{rms}}$ for Nikuradse data and $h=3\ h_{\mathrm{rms}}$ and $h=5.78\ h_{\mathrm{rms}}$ for data, for prediction of the friction factor results. But our closed form predictions (52) and (53) for inflectional roughness ($j=11$) are more accurate when compared with numerical predictions of Allen et al. [22].

The additional friction factor data, for which velocity profiles are not given in Nikuradse [14], are also shown in Figs. 7(*a*) and 7(*b*). For $\delta/h=15$ and $\mathrm{Re}<10^4$, the data begin to depart from present predictions, and the relaminarization begins, tending to merge with transition region ($2000\leq\mathrm{Re}\leq 3000$) data; see also Fig. 9 of Nikuradse [14] and Fig. 20.18, page 580 of Schlichting [7], that also show relaminarization. As roughness increases $\delta/h \leq 15$, the relaminarization would begin at further higher Reynolds numbers $\mathrm{Re}\geq 10^4$.

The friction factor λ in the scale $R_\phi\sqrt{\lambda}$, shown in Fig. 8(*a*), is universal behavior, supported by extensive data of Nikuradse [14] for sand grain roughness data, Shockling [17] for machined honed surface roughness of Princeton's superpipe and smooth pipe data of McKeon [44], Oregon data (McKeon et al. [45]), Patel and Head [46] and Blasius law [47]. The data compare very well with predicted universal friction factor (31*a*), that is explicitly independent, but implicitly depends on surface roughness scale ϕ connected with roughness function $\triangle U_+$. The friction factor λ in the traditional scale $\mathrm{Re}\sqrt{\lambda}$ shown in Fig. 8(*b*) the each roughness data is described by a particular line that is predicted well by proposed relation (53). The higher order effects in the present work on transitional rough pipes may also considered (see Afzal [48]) from extension of smooth pipe relations of Afzal [49,50].

The Reynolds shear stress relations (23*a*), (23*b*) in the inner and outer variables, expressed in terms of friction Reynolds number R_τ, become

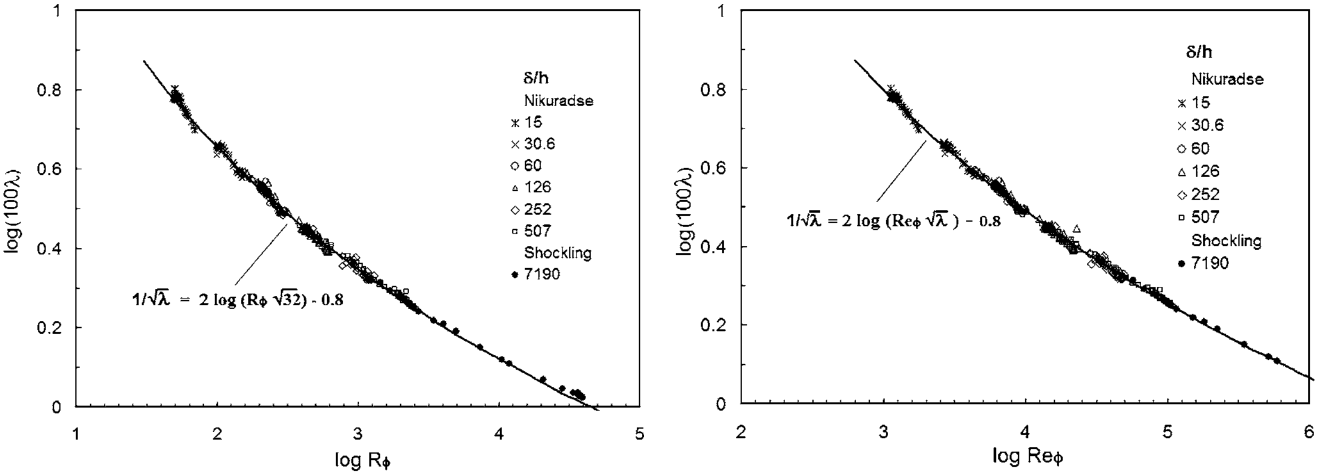

Fig. 6 Comparison of the universal friction factor λ of transitional rough pipes data of Nikuradse and Shockling and present predictions: (*a*) Friction factor λ vs roughness friction Reynolds number $R_\phi=R_\tau/\phi$ data and relation (34)——$1/\sqrt{\lambda}=2\log_{10}(R_\phi\sqrt{32})-0.8$. (*b*) Friction factor λ vs roughness Reynolds number $\mathrm{Re}_\phi=\mathrm{Re}/\phi$ data and relation (33)——$1/\sqrt{\lambda}=2\log_{10}(\mathrm{Re}_\phi\sqrt{\lambda})-0.8$.

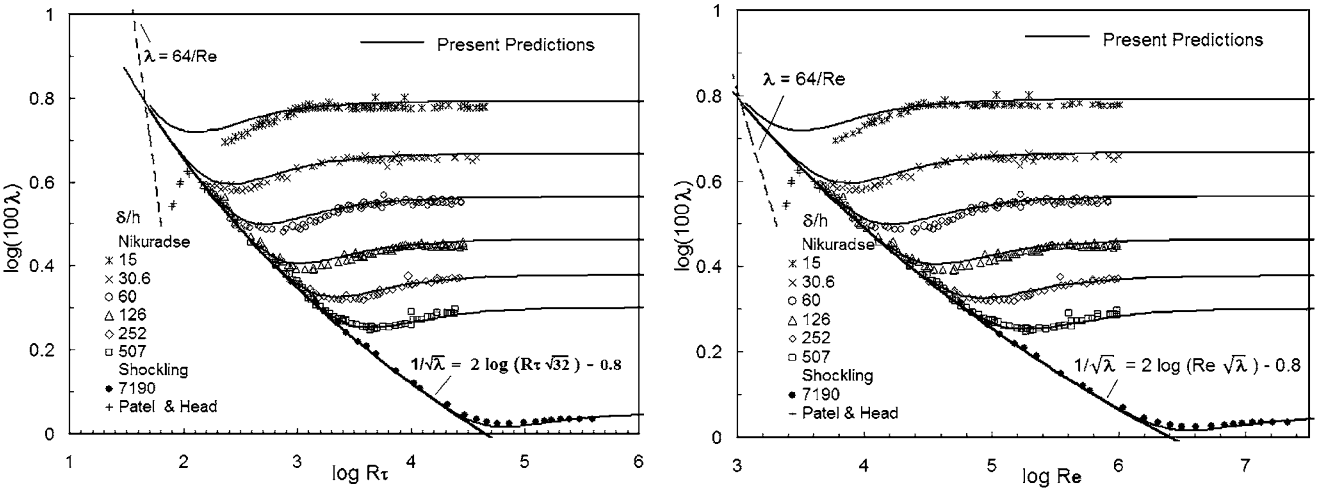

Fig. 7 Comparison of the friction factor λ of transitional rough pipes data of Nikuradse and Shockling and present predictions: (*a*) Friction factor λ vs friction Reynolds number R_τ data and relation (69). (*b*) Friction factor λ vs Reynolds number Re data and relation (70).

$$\frac{\tau}{\tau_w}=1-\frac{1}{kZ_+}-R_\tau^{-1}\left(Z_+ +\frac{\Pi}{k}\frac{dW}{dY}\right) \qquad (54a)$$

$$\frac{\tau}{\tau_w}=1-Y-R_\tau^{-1}\left(\frac{1}{kY}+\frac{\Pi}{k}\frac{dW}{dY}\right) \qquad (54b)$$

and location of maxima $Z_{+\max}$ and maximum value $\tau_{\max}$ expressions (25*a*), (25*b*) become

$$Z_{+\max}=\sqrt{\frac{R_\tau}{k}} \qquad (55a)$$

$$\frac{\tau_{\max}}{\tau_w}=1-\frac{2}{\sqrt{kR_\tau}} \qquad (55b)$$

The above results show that the Reynolds shear stress, just above the roughness level, does not explicitly depend on pipe roughness. In a wall bounded turbulent shear flow, the role played by surface roughness is to shift the origin of normal coordinate for proper estimation of the Reynolds shear stress (see Fig. 5(*a*) in Rupach et al. [2]). Further, the velocity distribution needs two shifts, the origin of normal coordinate as well as the velocity by an amount equal to the roughness function.These relations for smooth pipes were first given by Afzal [50] and with $k=0.4$ the Reynolds shear stress maxima location yields $y_{+\max}/\sqrt{R_\tau}=1.58$, whereas the experimental data predicted 1.85. Based on recent experimental data of Zanoun [51] in smooth pipes and channels and smooth channel DNS data of Abe, Kawamura, and Matsuo [52], the location of maxima $y_{+\max}$ is shown in Fig. 9(*a*) and maxima of Reynolds stress $\tau_{+\max}/\tau_w$ is shown in Fig. 9(*b*). The predictions (55*a*), (55*b*) of Afzal [50] shown in Figs. 9(*a*) and 9(*b*), compare very well with the data of Zanoun [51] and Abe et al. [52].

6 Conclusions

(1) Four new roughness scales have been introduced, roughness scale ϕ connected with roughness function $\triangle U_+$, the inner wall transitional roughness variable $\zeta=Z_+/\phi$, the roughness friction Reynolds number R_ϕ (based on roughness friction velocity) and roughness Reynolds number Re_ϕ (based on roughness average velocity) where the mean turbulent flow, little above the roughness sublayer, does not depend on pipes transitional roughness.

(2) The velocity profile, in transitional wall roughness inner variable $\zeta=Z_+/\phi$, is universal for all types of wall roughness, in contrast to traditional wall variable Z_+ or Z/h. Of course, velocity, profile relation (19) is explicitly independent of wall roughness,

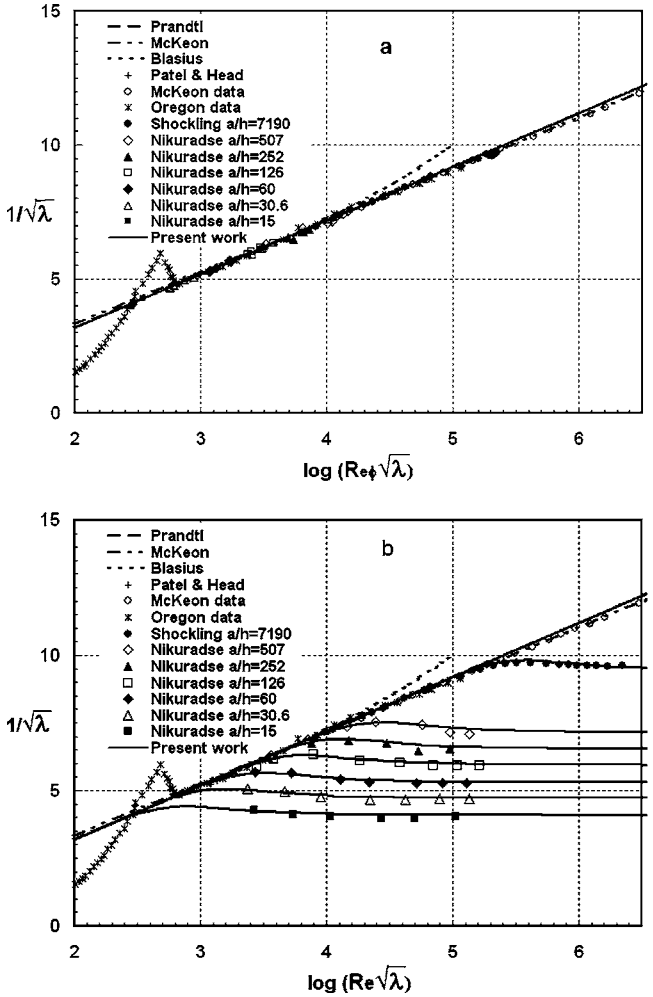

Fig. 8 Comparison of proposed predictions of the friction factor λ with experimental data. (*a*) Fiction factor λ with roughness Reynolds number function $Re_\phi\sqrt{\lambda}$ showing the universal relationship. (*b*) Fiction factor λ with traditional Reynolds number function $Re\sqrt{\lambda}$. Smooth pipes data: McKeon et al. (2003), Oregon data (McKeon et al. 2004), Patel and Head (1968), Blasius (1912) relation. Transitional pipe roughness data: Shockling (2005) for machine honed surface roughness and Nikuradse (1933) sand grain roughness data.

but it implicitly depends on roughness scale ϕ through inner variable ζ. The outer velocity profiles (20) are also universal, which supports Townsend's similarity hypothesis.

(3) The roughness scale ϕ and roughness function $\triangle U_+$ from the Nikuradse and Shockling data compare very well with the prediction relation (46) and (47) for sand grain roughness ($j = 11$). The prediction of traditional log law intercepts B_T and B_t also compare well with the proposed predictions.

(4) The friction factor (31*a*) based on roughness Reynolds number $Re_\phi = Re/\phi$ and relation (31*b*) based on roughness Reynolds number $R_\phi = R_\tau/\phi$ are also universal relations, explicitly independent of wall roughness. Here constants are the same as in Prandtl's universal friction factor of smooth pipes. In traditional variables the single relation (50) and (51) describe the friction factor for inflectional roughness of Nikuradse and Shockling for $j = 11$ and Colebrook monotonic roughness for $j = 0$. The predictions of skin friction for inflectional-type roughness of Nikuradse for each value of δ/h represents a line which for large R_τ (or Re) approaches to fully rough wall limit and for small R_τ (or Re) it merges with smooth wall skin friction law.

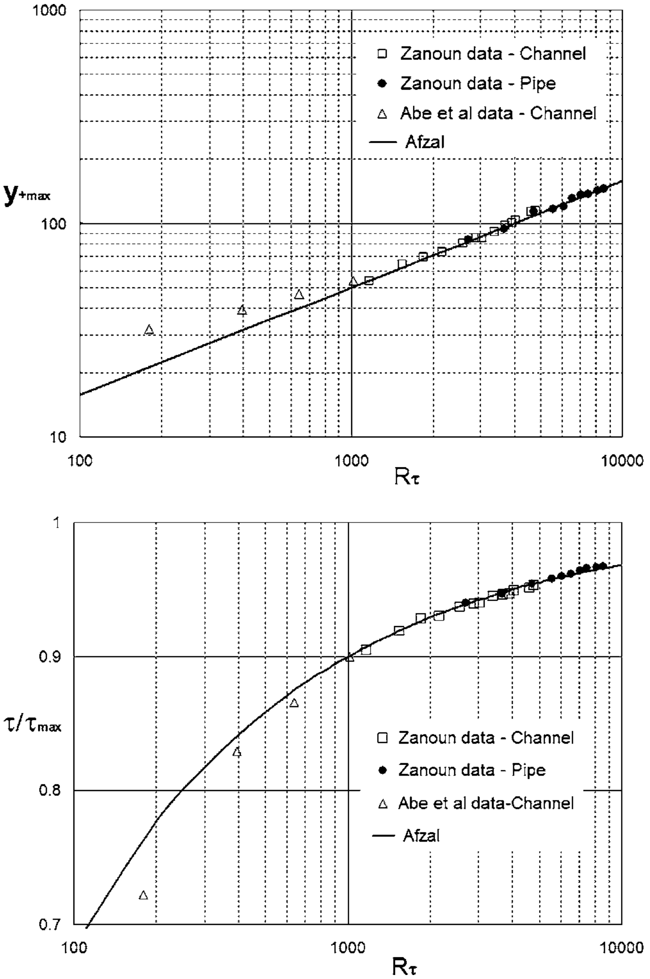

Fig. 9 Comparison of maxima in Reynolds shear stress prediction of Afzal (1982) with the experimental data of Zanoun (2003) for smooth pipe and smooth channel and DNS data of Abe et al. (2004) for channel. (*a*) The prediction (55*a*) for location of the maxima shear stress. (*b*) The prediction (55*b*) for magnitude of maximum shear stress.

(5) The present work, in traditional Reynolds number Re, provides better predictions of the friction factor when compared with predictions of Allen et al. [22] based for given roughness h_+ and the knowledge of $\triangle U_+$ vs h_+ from one experiment to another, in the situations of machined honed superpipe roughness data and Nikuradse sand grain roughness data.

(6) The friction factor data of Nikuradse [14] for $\delta/h = 15$ and for $Re < 10^4$, begins to depart from the prediction, and the relaminarization begins. The data of friction factor monotonically decreases, and tend to merge wish transition region ($2000 \leq Re \leq 3000$) data. If roughness is increased beyond $\delta/h \leq 15$, the relaminarization would begin at further higher Reynolds numbers $Re \geq 10^4$. For $\delta/h = 15$, and $Re \leq 10^4$, if the turbulent flow in pipe is maintained, then the present prediction of friction factor would remain valid.

References

[1] Millikan, C. B., 1938, "A Critical Discussion of Turbulent Flow in Channels and Circular Tubes," *Proc. 5th Int. Cong. Appl. Mech.* (Cambridge), J. P. den Hartog and H. Peters, eds., Wiley/Chapman and Hall, New York-London, pp. 386–392.

[2] Raupach, M. R., Antonia, R. A., and Rajagopalan, S., 1991, "Rough-Wall Turbulent Boundary Layer," Adv. Appl. Mech., **44**, pp. 1–25.

[3] Jimenez, J., 2004, "Turbulent Flow Over Rough Walls," Annu. Rev. Fluid Mech., **36**, pp. 173–196.

[4] Clauser, F. H., 1954, "Turbulent Boundary Layers in Adverse Pressure Gradients," J. Aeronaut. Sci., **21**, pp. 91–108.

[5] Hama, F. R., 1954, "Boundary-Layer Characteristics for Rough and Smooth Surfaces," Trans Society of Naval Architecture and Marine Engineers, **62**, pp. 333–351.

[6] Abe, K., Matsumoto, A., Munakata, H., and Tani, I., 1990, "Drag Reduction by Sang Grain Roughness," In *Structure of Turbulence and Drag Reduction*, A. Gyr, ed., Springer-Verlag, Berlin, pp. 341–348.

[7] Schlichting, H., 1968, *Boundary Layer Theory*, McGraw–Hill, New York, p. 505.

[8] Grigson, C., 1992, "Drag Losses of New Ships Caused by Hull Finish," J. Ship Res., **36**(2), pp. 182–196.

[9] Patel, V. C., 1998, "Perspective: Flow at High Reynolds Number and Over Rough Surfaces: Achilles Heel of CFD," J. Fluids Eng., **120**, pp. 434–444.

[10] Krogstad, P.-A., Antonia, R. A., and Browne, L. W. B., 1992, "Comparison Between Rough- and Smooth-Wall Turbulent Boundary Layers," J. Fluid Mech., **245**, pp. 599–617.

[11] Antonia, R. A., and Krogstad, P.-A., 2001, "Turbulence Structure in Boundary Layer Over Different Types of Surface Roughness," Fluid Dyn. Res., **28**, pp. 139–157.

[12] Granville, P. S., 1987, "Three Indirect Methods for Drag Characterization of Arbitrary Rough Surfaces on Flat Plate," J. Ship Res., **31**, pp. 70–77.

[13] Schultz, M. P., and Myers, A., 2003, "Comparison of Three Roughness Function Determination Methods," Exp. Fluids, **35**(4), pp. 372–379.

[14] Nikuradse, J., 1933, "Laws of Flow in Rough Pipe," *VI, Forchungsheft N-361*, (English translation NACA TM 1292, 1950).

[15] Streeter, V. L., 1936, "Frictional Resistance in Artificially Roughened Pipes," Trans. ASCE, **61**, pp. 163–186.

[16] Perry, A. E., and Abell, C. K., 1977, "Asymptotic Similarity of Turbulence Structures in Smooth and Rough Walled Pipes," J. Fluid Mech., **79**, pp. 785–799.

[17] Shockling, M. A., 2005, "Turbulent Flow in Rough Pipe," MSE thesis, Princeton University.

[18] Shockling, M. A., Allen, J. J., and Smits, A. J., 2006, "Roughness Effects in Turbulent Pipe Flow," J. Fluid Mech., **564**, pp. 267–285.

[19] Smits, A. J., Shockling, M. A., and Allen, J. J., 2005, "Turbulent Flow in Smooth and Rough Pipes," *Paper AIAA-2005-4807, 35th AIAA Fluid Dynamics Conference*, June 6–9, Toronto, p. 9.

[20] Colebrook, C. F., 1939, "Turbulent Flow in Pipes With Particular Reference to the Transition Region Between the Smooth and Rough Pipe Laws," J. Inst. Civ. Eng, **11**, pp. 133–156.

[21] Moody, L. F., 1944, "Friction Factors for Pipe Flow," Trans. ASME, **66**, pp. 671–684.

[22] Allen, J. J., Shockling, M. A., and Smits, A. J., 2005, "Evaluation of a Universal Transitional Resistance Diagram for Pipes With Honed Surfaces," Phys. Fluids, **17**, pp. 121–702.

[23] Eggels, J. G. M., Unger, F., Wiess, M. H., Westerweel, J., Adrian, R. J., Friedrich, R., and Nieuwstadt, F. T. M., 1994, "Fully Developed Turbulent Pipe Flow: A Comparison Between Direct Numerical Simulation and Experiments," J. Fluid Mech., **268**, pp. 175–209.

[24] Quadrio, M., and Luchini, P., 2004, "Direct Numerical Simulation of the Turbulent Flow in a Pipe With Annular Cross Section," Eur. J. Mech. B/Fluids, **21**, pp. 413–427.

[25] Abe, H., Kawamura, H., and Matsuo, Y., 2001, "Direct Numerical Simulation of a Fully Developed Turbulent Channel Flow With Respect to Reynolds Number," J. Fluids Eng., **123**, pp. 382–393.

[26] Leonardi, S., Orlandi, P., Smalley, R. J., Djenidi, L., and Antonia, R. A., 2003, "Direct Numerical Simulations of Turbulent Channel Flow With Transverse Square Bars on One Wall," J. Fluid Mech., **491**, pp. 229–238.

[27] Nagano, Y., Hattori, H., and Houra, T., 2004, "DNS of Velocity and Thermal Fields in Turbulent Channel Flow With Transverse Rib Roughness," Int. J. Heat Fluid Flow, **25**, pp. 393–403.

[28] Ashrafian, A., Andersson, H. I., and Manhart, M., 2004, "DNS of Turbulent Flow in a Rod-Roughened Channel," Int. J. Heat Fluid Flow, **25**, pp. 373–383.

[29] Krogstadt, P.-A., Anderson, H. I., Bakken, O. M., and Ashrafian, A., 2005, "An Experimental and Numerical Study of Channel Flow With Rough Walls," J. Fluid Mech., **530**, pp. 327–352.

[30] Djendi, L., Elavarasan, R., and Antonoa, R. A., 1999, "The Turbulent Boundary Layer Over Transverse Square Cavities," J. Fluid Mech., **395**, pp. 271–294.

[31] Bakken, O. M., Krogstad, P. A., Ashrafian, A., and Andersson, H. I., 2005, "Reynolds Number Effects in the Outer Layer of the Turbulent Flow in a Channel With Rough Walls," Phys. Fluids, **17**, pp. 1–16.

[32] Afzal, N., Seena, A., and Bushra, A., 2006, "Power Law Turbulent Velocity Profile in Transitional Rough Pipes," J. Fluids Eng., **128**, pp. 548–558.

[33] Afzal, N., 2005, "Scaling of Power Law Velocity Profile in Wall-bounded Turbulent Shear Flows." Paper No. AIAA-2005-0109, *43rd AIAA Aerospace Sciences Meeting and Exhibit*, Jan. 10–13, Reno, NV, p. 11.

[34] Afzal, N., 2005, "Analysis of Power Law and Log Law Velocity Profiles in Overlap Region of a Turbulent Wall Jet," Proc. R. Soc. London, Ser. A, **46**, pp. 1889–1910.

[35] Afzal, N., 1976, "Millikan Argument at Moderately Large Reynolds Numbers," Phys. Fluids, **19**, pp. 600–602.

[36] Coles, D., 1969, "The Young Person Guide to the Data," In *Proc. Computations of Turbulent Boundary Layer, 1968-AFOSR-IFP-Stanford Conference*, II, pp. 1–46.

[37] Prandtl, L., 1935, "The Mechanics of Viscous Fluids," *Aerodynamic Theory*, **III**, W. F. Durand, ed., Springer Verlag, Berlin, pp. 34–208.

[38] McKeon, B. J., Zagarola, M. V., and Smits, A. J., 2005, "A New Friction Factor Relationship for Fully Developed Pipe Flow," J. Fluid Mech., **538**, pp. 429–443.

[39] Zagarola, M. V., and Smits, A. J., 1998, "Mean Flow Scaling in Turbulent Pipe Flow," J. Fluid Mech., **373**, pp. 33–79.

[40] Bendrict, R., *Fundamentals of Pipe Flow*, Wiley, New York, p. 240.

[41] Cebeci, T., 2004, *Analysis of Turbulent Flows*, Elsevier, New York, p. 114.

[42] Flack, K. A., Schultz, M. P., and Shapiro, T. A., 2005, "Experimental Support for Townsend's Reynolds Number Similarity Hypothesis on Rough Walls," Phys. Fluids, **17**, pp. 035102-1–035102-12.

[43] Connelly, J. S., Schultz, M. P., and Flack, K. A., 2006, "Velocity-Defect Scaling for Turbulent Boundary Layers With a Range of Relative Roughness," Exp. Fluids, **40**, pp. 188–195.

[44] McKeon, B. J., 2003, "High Reynolds Number Turbulent Pipe Flow," Ph.D. thesis, Princeton University.

[45] McKeon, B. J., Swanson, C. J., Zagarola, M. V., Donnelly, R. J., and Smits, A. J., 2004, "Friction Factor for Smooth Pipe Flow," J. Fluid Mech., **511**, pp. 41–44.

[46] Patel, V. C., and Head, M. R., 1969, "Some Observations on Skin Friction and Velocity Profile in Fully Developed Pipe and Channel Flow," J. Fluid Mech., **38**, pp. 181–201.

[47] Blasius, H., 1912, "Das Aehnlichkeitsgesetz bei Reibungsvorgngen," Z. Ver. Dtsch. Ing., **56**(16), pp. 639–643.

[48] Afzal, N., 2006, "Friction Factor for Transitional Rough Pipes." (unpublished).

[49] Afzal, N., and Yajnik, K., 1973, "Analysis of Turbulent Pipe and Channel Flows at Moderately Large Reynolds Number," J. Fluid Mech., **61**, pp. 23–31.

[50] Afzal, N., 1982, "Fully Developed Turbulent Flow in a Pipe: An Intermediate Layer," Ing.-Arch., **53**, pp. 355–377.

[51] Zanoun, E. S., 2003, "Answer to Some Open Questions in Wall-Bounded Laminar and Turbulent Flows," Doctor-Ingeniur, University of Erlangen-Nurnberg.

[52] Abe, H., Kawamura, H., and Matsuo, Y., 2004, "Surface Heat-Flux Fluctuations in a Turbulent Channel up to $R_\tau=1020$ with $\mathrm{Pr}=0.025$ and 0.71," Int. J. Heat Fluid Flow, **25**, pp. 404–419.

On the Mechanisms Affecting Fluidic Vectoring Using Suction

R. D. Gillgrist[1]
D. J. Forliti[2]
P. J. Strykowski

Mechanical Engineering Department,
University of Minnesota,
111 Church St. SE,
Minneapolis, MN 55455

Suction was applied asymmetrically to the exhaust of a rectangular subsonic jet creating a pressure field capable of vectoring the primary flow at angles up to 15 deg. *The suction simultaneously creates low pressures near the jet exhaust and conditions capable of drawing a secondary flow along the jet shear layer in the direction opposite to the primary jet. This countercurrent shear layer is affected both by the magnitude of the suction source as well as the proximity of an adjacent surface onto which the pressure forces act to achieve vectoring. This confined countercurrent flow gives rise to elevated turbulence levels in the jet shear layer as well as considerable increases in the gradients of the turbulent stresses. The turbulent stresses are responsible for producing a pressure field conducive for vectoring the jet at considerably reduced levels of secondary mass flow than would be possible in their absence.* [DOI: 10.1115/1.2375125]

Introduction

The desire for enhanced aircraft, missile, and torpedo maneuverability has motivated the search for useful methods of vectoring jet exhaust in the harsh environments found in typical propulsion systems. Initial control efforts led to the development of mechanical-based approaches that redirect the jet exhaust using deflector plates, fins, or the like, to produce the necessary side forces for altitude control, enhanced pitch, yaw, and roll rates, emergency deceleration, the redirection of noxious gases, and operation on damaged airfields. At the present time, weight, reliability, drag penalties, and complexity remain the chief concerns regarding the implementation of these mechanical strategies. Furthermore, the relatively low dynamic response rates of mechanical systems make their employment equally problematic.

In principle, the simplicity of fluidic approaches provides numerous advantages relative to mechanically actuated scenarios, though fluidic control can be plagued by hysteretic effects and substantial penalties in terms of the mass flow required for actuation [1,2]. Fluidic strategies are not new, having appeared through lateral fluid injection, so-called boundary layer control, as well as the confined use of jet injection [3–7]. More recent approaches to fluidic vectoring include methods that rely on synthetic jet forcing of the jet shear layer [8], asymmetric suction [9], fluidic injection to achieve throat skewing [10], nozzle interior separation control [11], Coanda effect attachment control using blowing [12], and periodic excitation of the shear layer in the presence of confinement [13].

The focus of the present study is to examine the physical mechanisms responsible for achieving fluidic vectoring using a vacuum source located in the jet exit plane. This configuration is shown schematically in Fig. 1. The primary jet nozzle is positioned symmetrically between curved surfaces, hereinafter called *collars*, extending downstream of the primary jet exit plane. When a vacuum source is connected to the gap between the nozzle and the upper collar as shown in Fig. 1, but not to the lower gap, an asymmetric pressure field is created sufficient to vector the primary flow upward as shown in the figure. The feasibility of this approach has been established for flows ranging between low subsonic to at least Mach two [14,15] and in a variety of geometries including rectangular, diamond, and axisymmetric jet cross sections [16]. An important difference between the approach taken here and the use of actuators [8] or the suction approach of Lim and Redekopp [9] is the introduction of an adjacent surface used to manipulate the entrainment field. While this surface is not required, per se, to achieve vectoring with suction, it provides flow guidance which is otherwise difficult due to the sink-like nature of the imposed vacuum conditions.

While numerous studies have examined the nature of this flow field [14–17] and reflect the basic understanding that alterations in the entrained flow are responsible for the jet's behavior, relatively little is known about the physical mechanisms causing the flow turning. In the present study, detailed velocity-field measurements are described using PIV, which provide new insight into the relationship between the velocity changes created by vacuum and the pressure field necessary to vector the primary jet. Specifically, the data presented below explain why enhanced turbulence plays a role in the vectoring process. Earlier supersonic PIV measurements [15] only showed the presence of enhanced turbulence, though it was not possible to study the mechanisms at play due to the accuracy and resolution of the data, as well as complications due to compressibility effects.

Strykowski and Krothapalli [18] were the first to study the configuration in Fig. 1, where the jet response was shown to be proportional to the vacuum pressure in the gap between the jet nozzle and adjacent collar. Subsequent work [14,15] provided detailed measurements of the jet behavior at subsonic and supersonic conditions. Van der Veer and Strykowski [14] studied the vectoring of a rectangular jet turned about its long axis at an operating Mach number of 0.5 and identified both continuous and bistable regimes of operation. Strykowski et al. [15] examined the flow response at Mach 2 and outlined key operational parameters governing the vectoring process; in particular, it was observed that the Mach 2 flow could be continuously vectored up to nearly twenty degrees. Comparisons made between the subsonic and supersonic studies were also valuable in illustrating that the vectoring phenomenon was not dependent upon the presence of shocks in the primary flow.

More recent studies [19–21] have corroborated the above findings and have provided useful scaling relationships upon which to base performance. However, these studies have also shown that the asymmetric introduction of subatmospheric pressure in the jet exit plane can produce both coflowing and counterflowing secondary streams between the jet and the collar surface. Strykowski et al. [17] opined that the presence of coflow or counterflow would depend on the performance characteristics of the vacuum pump relative to the pumping action of the ejecting shear layer itself. In

---

[1] Present address: Pastor, Wit's End Church, 925 N. 130th Street, Seattle, WA 98133.

[2] Present address: Assistant Professor, Department of Mechanical and Aerospace Engineering, State University of New York at Buffalo, Buffalo, NY 14260.

Contributed by the Fluids Engineering Division of ASME for publication in the JOURNAL OF FLUIDS ENGINEERING. Manuscript received November 15, 2005; final manuscript received June 2, 2006. Assoc. Editor: Timothy J. O'Hern.

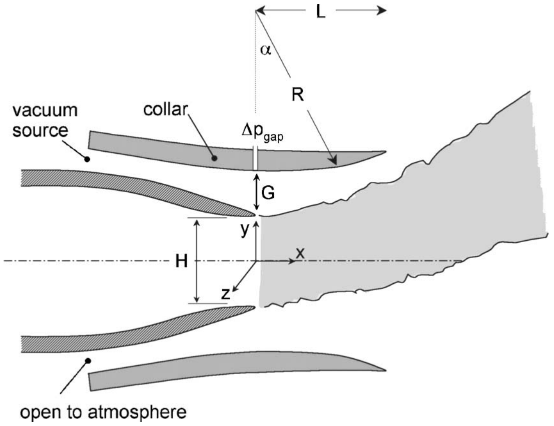

Fig. 1 Nozzle-collar configuration illustrating jet response when vacuum is applied asymmetrically to the jet exhaust

a computational study, Hunter and Deere [21] found that local velocity profiles between the jet shear layer and the collar surface may display counterflow over a significant portion of the collar length, even though the net flow from the vacuum system is in the direction of the primary jet, i.e., a net coflow through the gap at the nozzle exit plane.

The objective of the present study was to conduct detailed velocity and pressure field measurements in the neighborhood of the jet exit and collar surface and thereby begin to unravel the physical connection between the shear layer dynamics and the jet response. In the section to follow we begin by describing the experimental facilities used to study the fluidic vectoring of a Mach 0.5 rectangular jet. The basic approach was to obtain detailed pressure measurements on the collar surface using surface-mounted static taps and document the mean and fluctuating velocity field using particle image velocimetry, necessary both because of the reverse velocity in the laboratory reference frame as well as the high local turbulence intensities observed in this region.

Facilities and Instrumentation

The fundamental configuration studied was shown previously in Fig. 1. Air is supplied to the primary nozzle at a stagnation temperature and pressure of nominally 120 kPa and 315 K, respectively, providing steady flow at Mach 0.5 at the primary nozzle exit plane; the Reynolds number of the jet based on the short dimension of the nozzle was 1.1×10^5 at a representative exhaust velocity of 175 m/s. The primary flow was delivered to the fifth-order polynomial two-dimensional nozzle from a regenerative blower after having passed through a water-cooled heat exchanger and flow conditioning elements. The characteristics of the baseline flow were documented by removing the collars from the long dimension of the 4:1 aspect ratio rectangular primary nozzle, thereby allowing unrestricted entrainment of ambient air. The jet exhausts from the rectangular nozzle having a short dimension $H=1$ cm and a long dimension of $W=4$ cm. Side walls, or end caps, were positioned at the end span of the nozzle-collar configuration to confine the fluid motion to the two-dimensional pathway between the jet shear layer and collar surface; these end walls were transparent to accommodate the optical access needed for PIV. Total pressure surveys taken across the jet centerplane for the baseline case in the y- and z-directions indicated uniformity in Mach number distributions to better than 1% outside the sidewall boundary layers.

Symmetrically placed collars could be variably positioned aft of the primary nozzle, through a set of parameters including offset distance G and extension length L; the collar geometry could also be tailored through its radius of curvature R, where the variables are coupled through the expression $L=R\cdot\sin(\alpha)$. The selection of parameters in the present study were not made with performance optimization in mind, but rather to choose a representative geometry having sufficient scale that pressure and velocity field measurements could be reasonably made in the confined environment. The collar selected for study was defined by $L/H=2.0$, $R/H=2.3$, and $G/H=0.5$.

A ring compressor configured for vacuum was connected to the nozzle-collar gap through a manifold distributing the subatmospheric pressure boundary condition uniformly across the long dimension of the jet exit. To further assure that the boundary conditions were uniform, a dense porous insert was used upstream of the nozzle-collar gap. Gas drawn into the vacuum system passed through a laminar-flow element for metering purposes. This provided accurate volumetric flow rate information at minimal loss in delivered vacuum pressure. The vacuum boundary condition established in the secondary flow gap G, was captured in the jet exit plane $(x=0)$ with a flush-mounted static pressure tap, as seen in Fig. 1, and is denoted by the symbol Δp_{gap} reflecting the fact that gage pressures were measured throughout. Collar gage pressures were normalized by the primary jet momentum $\rho_j U_j^2$. The study described in detail below was conducted under three different flow conditions: The baseline condition or unvectored flow; flow vectoring corresponding to approximately 6 deg of flow turning where $\Delta p_{\text{gap}}/\rho_j U_j^2=-0.057$; and flow vectoring at 14 deg at a dimensionless gap pressure of $\Delta p_{\text{gap}}/\rho_j U_j^2=-0.12$.

Measurements of laboratory temperature, primary jet stagnation temperature and dynamic pressure, secondary mass flow drawn into the vacuum system, and collar static pressures were obtained under each set of operating conditions. The jet temperature was measured using type-K thermocouples sampled in the primary jet plenum. The temperature was monitored continuously to assure steady state conditions were maintained during each test run. Precision mercury thermometers safely mounted in the laboratory were used to record the laboratory ambient conditions. Streamwise collar pressure distributions were acquired with fourteen static pressure ports flush mounted along the centerline of the collar in arc increments of 4 deg. To minimize interference effects between ports, the taps were alternately staggered in the spanwise direction.

Particle image velocimetry (PIV) was used to capture the instantaneous and time-averaged velocity fields in the jet near field at the three conditions discussed above, focusing on the details of the velocity characteristics in the shear layer region between the jet edge and collar surface. A Continuum Surelite II dual head Nd:YAG laser was employed to illuminate the center plane of the z-span of the exhausting rectangular jet, capturing the velocity in the x-y plane. The approach taken is based on the autocorrelation technique, namely where a single 1.4 Megapixel digital array (1340×1037 pixels; each pixel was 6.8 μm squared) stores the double-exposed image of the flow made visible by the introduction of fine particulate that accurately follows the flow. Biasing is required to remove directional ambiguity using autocorrelation techniques, and this was accomplished using a balanced spinning mirror. During post processing, the peak location in the autocorrelation function is identified (excluding the self correlation peak); furthermore subpixel accuracy is achieved using a Gaussian curve-fit algorithm. Image capture and processing was accomplished using the TSI Insight Software System.

The interrogation spot size of a PIV measurement was carefully determined. Mean velocities between the primary jet and collar wall were expected in the range of 220 to −110 m/s, requiring the rotating mirror. The effect of the mirror (set to 70 Hz) is to offset this range to entirely positive values, hence increasing each displacement vector magnitude. The available CCD image area, coupled with the findings of Prasad et al. [22], suggest that a 64-pixel resolution sufficiently reduced bias error and was chosen for this reason. A downside of this choice is some sacrifice in terms of spatial resolution, though as the results will show, the general trends of the data indicate that the observations made are sufficiently robust to be elucidated from the data sets.

Convergence studies were conducted to assess measurement uncertainty using the autocorrelation technique. The largest uncertainties were found in the shear layer itself, as this flow region is highly three-dimensional and dropouts occur due to out-of-plane particle motion. Statistics were taken when processing N instantaneous velocity fields, where N varied up to 500 images. While convergence in the primary jet and secondary flow path achieved errors less than 1% after 150 field averages, similar levels of accuracy required nearly 350 images for convergence in the shear layer; accuracies at this level could not be achieved in the region immediately downstream of the nozzle trailing edge and hence data were not reported in this region. It must be remembered that even if 350 images are captured, it is typical that some vector dropouts will occur. To assure that each measurement point had a minimum of 350 valid vectors, total record lengths of 500 images were used throughout the study. A more detailed discussion of the bias and precision errors associated with this approach is given by Gillgrist [23].

The tracer particles used to follow the flow were generated using a Laskin nozzle. The nozzle is driven by house compressed air and creates a fine oil mist that was introduced into the main jet plenum as well as a reservoir supplying the ambient neighborhood surrounding the jet. Droplet size distributions produced using this type of generator are in the submicron range, and can be shown to accurately follow the flow under the conditions examined here [24].

Flow Response to Suction

Experiments were conducted to examine the response of the rectangular jet when the vacuum system was connected to the upper gap in Fig. 1. We begin by describing the global response of the jet to the applied vacuum, and follow the discussion with a detailed look at the instantaneous and mean velocity-vector fields established between the jet and collar surfaces. During the experiments, the lower gap was left open to atmosphere to allow relatively free entrainment of ambient gas into the lower jet shear layer. The effective thrust vector angle of the jet was determined as a function of the suction level developed in the gap using a momentum balance. A control volume was taken coincident with the jet exit plane and the two collar surfaces, incorporating the momentum flows of the primary and secondary streams as well as the pressures measured on the collar surfaces. The jet deflection δ_v was determined as $\tan^{-1}(R_y/R_x)$, where R_x and R_y are the net axial and side forces acting on the nozzle-collar hardware. At each setting of the gap pressure, Δp_{gap}, the mass drawn into the vacuum pump was metered and is denoted as $\dot{m}_s$ (secondary mass flow) and was compared to the primary jet mass flow rate $\dot{m}_p$. For all operating conditions the secondary mass flow through the vacuum pump originated in the ambient and was drawn in the direction opposite to the primary jet, namely the secondary mass flows represent countercurrent flow between the primary jet and collar surface.

Figure 2 illustrates the flow behavior for primary jet deflection angles up to approximately 15 deg. As the magnitude of the vacuum source is increased relative to the primary jet momentum, the jet increases its deflection and produces a concomitant increase in the secondary mass flow drawn through the vacuum system. Due to the relatively large gap between the jet and collar ($G/H=0.5$) the secondary mass flow rates are significant. For example, for the two primary vectoring cases considered here, corresponding to angles of 6 and 14 deg, the secondary mass flow rates were 7.3% and 8.6%, respectively. As reported in earlier studies using vacuum [15,16] the secondary mass flow requirements are proportional to the gap height and hence can be decreased considerably by employing a more compact geometry; these studies also revealed that the secondary flow can be decreased as the Mach number is increased. The impact on secondary flow can be appreciated at the larger deflection angles, where the secondary mass flow requirement appears to asymptote as a consequence of the proximity of the jet to the collar at higher values of δ_v, namely a doubling of the jet deflection requires only a modest (20%) increase in mass flow. However, for the purposes of the present investigation the relatively large gap was chosen to facilitate the study of the velocity field between the jet and collar using PIV.

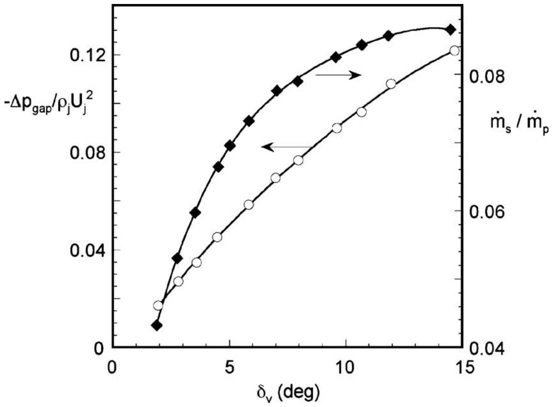

Fig. 2 Normalized gap pressure and secondary mass flow requirement as a function of primary jet turning angle

We begin the discussion of the detailed velocity field by focusing on the upper jet shear layer for the unvectored baseflow. These baseline conditions were achieved by disconnecting the vacuum source from the upper shear layer and matching the nominally free entrainment conditions in the upper and lower shear layers. Instantaneous velocity-vector fields are shown in Fig. 3 with emphasis on the region between the jet and collar. The images provide a sense of the temporal variations of the velocity field at a particular flow condition and will be compared shortly to the flow response during vectoring. Note that interrogation spots are left empty at locations where the autocorrelation peak could not be detected above the noise, i.e., no smoothing or interpolation was performed on the data. These dropout points were minimized to the extent possible by the appropriate selection of seed and PIV parameters, but are fairly common in autocorrelation mode PIV.

Turbulent structure is resolved in the downstream half of the domain. The direction of the velocity vectors in the shear layer indicates counter-clockwise rotating fluid, illustrating the nature of entrained secondary flow into the primary jet shear layer. The variation in size and location of shear layer structures shown in Fig. 3 are indicative of many images examined at these flow conditions, and correspond to integral length scales on the order of 0.2–0.3 H. A close examination of instantaneous vectors in the secondary stream suggest that a considerable fraction of the entrained gas originates from ambient fluid entering the collar space from downstream, as opposed to that originating via the path which is ultimately connected to the vacuum source. This balance will be shown next by examining the time-averaged flow field.

The mean velocity field and corresponding streamline pattern is provided in Fig. 4 for the baseline conditions. These fields may be thought of as containing three regions: a lower region of the jet's potential core, an upper region of comparatively stagnant fluid, and the shear layer. In each of these regions the vectors were obtained by ensemble averaging 500 instantaneous fields; while the detection rate was as high as 98% in the potential core, rates closer to 70% were typical in the shear layer.

Figure 4(*a*) provides a zoomed out view of the baseline mean velocity field and Fig. 4(*b*) is the corresponding streamlines focusing on the region outside the jet potential core (streamlines were removed from the potential core for clarity). The streamline pattern indicates that the presence of the collar manipulates the

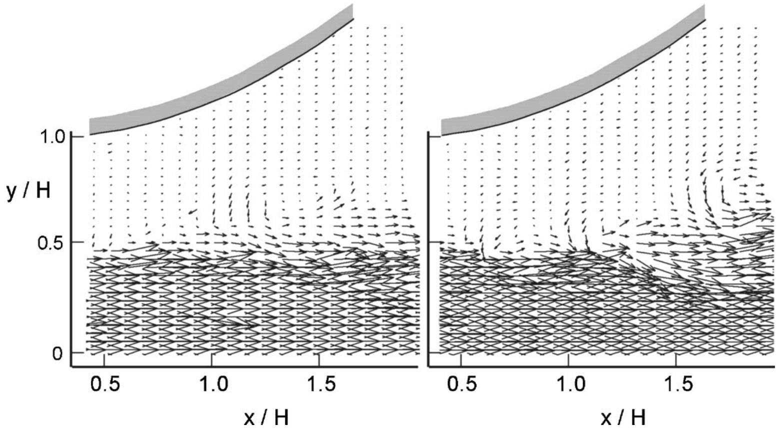

Fig. 3 Instantaneous velocity-vector fields in the upper shear layer of the jet taken for the unvectored baseflow

otherwise free entrainment process that would be present. Integration of the velocity profile in the secondary flow path suggests that the net flow entering the jet shear layer from the suction gap results in a *coflow* of less than 1% of the primary jet mass. Entrainment also originates from downstream of the collar, seen flowing counter to the primary jet along the collar and eventually being ingested by the primary flow and ejected downstream with it. The pumping action of the shear layer leads to a slight reduction of the pressure in the jet near field as indicated by a normalized gap pressure of $\Delta p_{\mathrm{gap}}/\rho_j U_j^2 = -0.0018$.

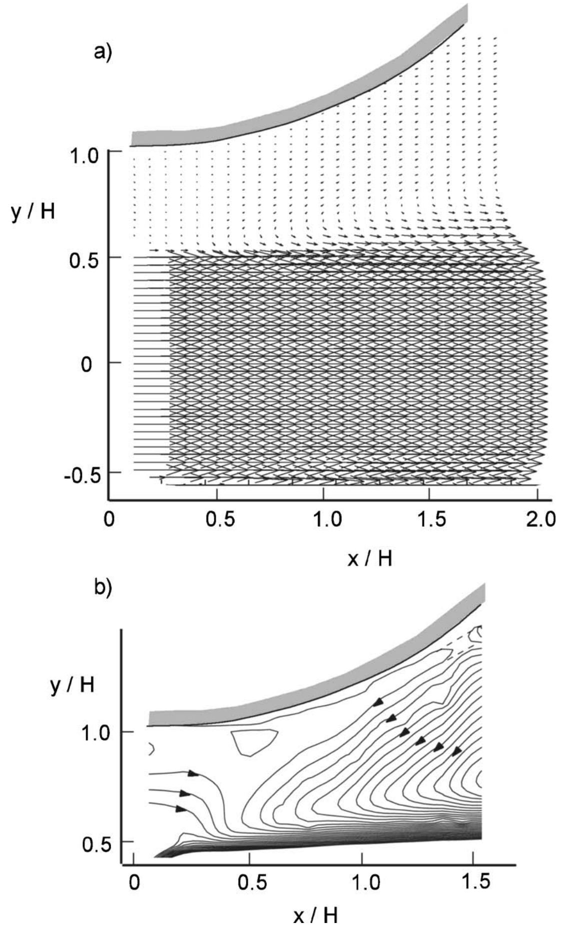

Fig. 4 Time-averaged velocity fields and streamlines for the unvectored baseflow. Dashed lines in (*b*) appear where the streamline does not represent the actual flow field

As discussed previously, two flow conditions corresponding to vector angles of approximately 6 and 14 deg were examined in detail, and will be referred to as the moderately and highly vectored cases, respectively. The first case to be discussed is when the primary jet experiences moderate vectoring and occurs when the vacuum system is connected to the upper collar gap at a level of $\Delta p_{\mathrm{gap}}/\rho_j U_j^2 = -0.057$. Instantaneous velocity fields depicting the central portion of the upper shear layer are presented in Fig. 5. These representative images illustrate the considerable temporal variation observed in the instantaneous fields required to turn the primary jet. The disturbance level as indicated by the integral scale of the shear layer structures is considerable when compared to the unvectored base flow seen in Fig. 3. Rough estimates indicate that the largest scales of turbulence are of the order of 0.5–0.75 H. Also notice that the qualitative behavior of the counterflowing secondary stream appears uniform and regular in certain regions and quite disturbed in others, though large numbers of images consistently indicate that the large structures are concentrated in the shear layer and typically do not penetrate all the way to the collar surface. Finally, there appears to be enhanced cross-stream turbulent transport of momentum insofar that structures are of sufficient energy to penetrate substantially into the high momentum gas of the primary Mach 0.5 stream.

The average flow characteristics during moderate vectoring are shown in Fig. 6. Mean flow vectoring can be assessed from the velocity-vector field by averaging the deflection of the flow within the jet potential core. This was accomplished by considering vectors whose magnitude was within 90% of the centerline value, thus excluding the flow in the shear layers and beyond. This is a reasonable approach due to the momentum flux scaling with the square of the velocity magnitude. The core experiences very little deflection up to $x/H \sim 0.4$, after which the jet turns continuously, eventually achieving a mean angle of 5.7 deg at $x/H \sim 1.8$ at the end of the PIV domain. The pressure field to be presented below indicates nearly atmospheric pressure at the downstream most extent of the collar $(x/H = 2)$ suggesting that flow turning will cease at that location as well.

The other interesting feature of the mean velocity-vector field is the significant magnitude of the reverse velocity observed in the neighborhood of the collar, where a nearly potential flow is established with negative velocities as high as 60 m/s, or 34% of the velocity of the primary jet in the nozzle exit plane. Vectors throughout the secondary flow path show counterflow levels consistently from 20% to 30% of the primary jet velocity, which should be compared to levels less than 3% in the unvectored baseflow. The counterflow velocity profiles outside the shear layer are

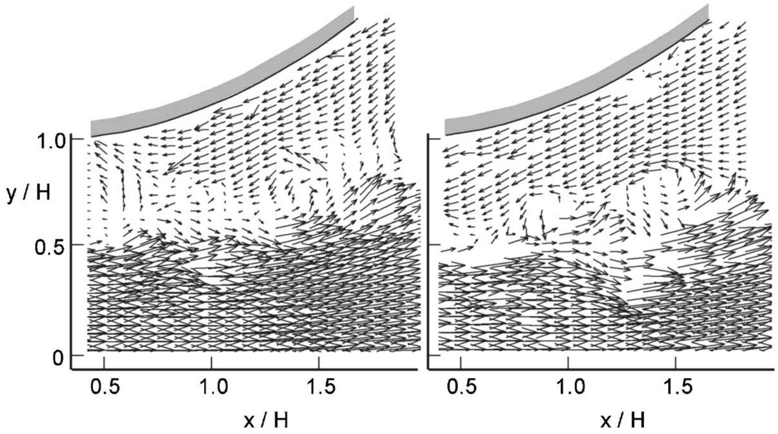

Fig. 5 Instantaneous velocity-vector fields in the upper shear layer of the jet taken for moderate vectoring; $\Delta p_{gap}/\rho_j U_j^2 = -0.057$

generally uniform in the cross-stream direction, though the width of the flow path is considerably smaller than observed in Fig. 4. This is naturally a result of the movement of the primary jet toward the collar, but is also due to the turbulent diffusion accompanying the flow structures seen in the instantaneous fields. The accompanying mean flow streamlines in Fig. 6(*b*) illustrate that much of the secondary flow drawn past the collar is ultimately ingested by the primary jet resulting in a net secondary mass flow drawn into the vacuum system of 7.3% the primary jet mass. Finally, a close observation of the primary jet velocity profile near the nozzle exit appears to have a small cross-stream gradient, namely a skewness, associated with the nonsymmetric pressure boundary condition imposed across the nozzle exit. The control volume used to compute the resultant forces on the nozzle-collar assembly incorporated this skewness into the momentum balance.

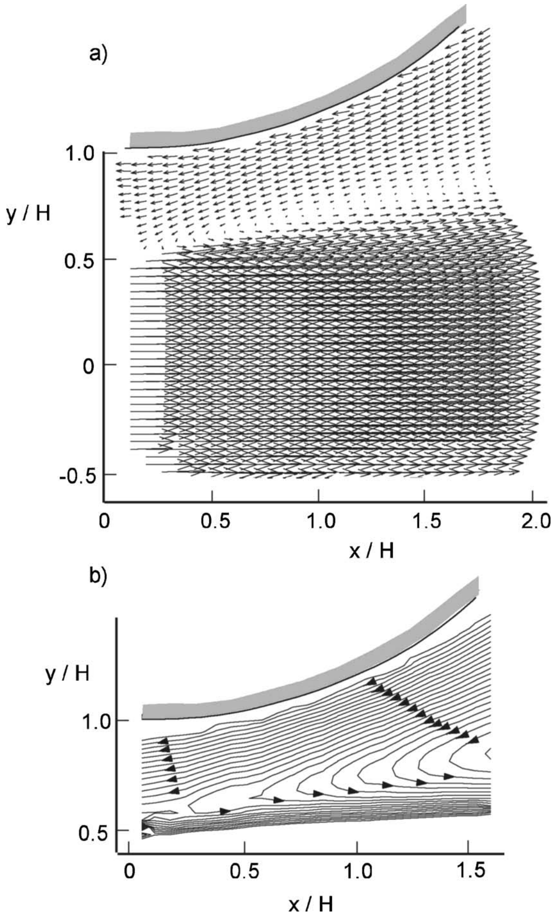

Fig. 6 (*a*) Time-averaged velocity field and (*b*) streamlines for moderate flow vectoring; $\Delta p_{gap}/\rho_j U_j^2 = -0.057$

Measurements made at the highest vector angle, corresponding to a gap pressure of $\Delta p_{gap}/\rho_j U_j^2 = -0.12$, are summarized in Fig. 7. The instantaneous vector images reveal the rather violent nature of the flowfield between the primary jet and collar. The turbulent structures scale on the order of H and are consistently observed to penetrate well into the jet potential core as well as to the collar surface; seldom was potential fluid motion observed in the secondary flow path in contrast to the case for moderate vectoring seen in Fig. 5. The absence of secondary potential flow is confirmed in the mean vector field as well, where the magnitude of the reverse velocity is seen to increase continuously toward the collar. (The PIV approach taken did not allow for accurate interrogation of the velocity field within the boundary layer developed on the collar itself.) The flow in the secondary flow path no longer appears irrotational, hence the role of a Bernoulli-type pressure drop may not play a significant role under these conditions. The movement of the jet towards the collar causes a reduction in available flow cross-sectional area for the secondary stream. Using the streamlines as a guide, the reduced flow path may lead to additional flow acceleration in the secondary stream. This in part could explain the lower pressures needed to vector the flow from 6 to 14 deg, although *significant* acceleration is not observed in the velocity fields as compared to the moderately vectored flow suggesting that a different mechanism is at work at the highest angle of flow deflection.

Interpreting Velocity and Pressure Fields

To further evaluate the physical source of the pressure drop along the secondary flow path, collar surface pressure distributions were examined together with averaged velocity field data. The static pressure distribution along the collar is shown as solid symbols in Fig. 8 for the moderately vectored jet. (The value of the ordinate at $x/H=0$ corresponds to the gap pressure, Δp_{gap}.) The integrated collar pressures provide the net force per unit depth applied to the collar assembly. The pressure approaches zero gage near the end of the collar; the slightly negative static gage pressure at the downstream collar extent is expected since the flow from the ambient to the collar has accelerated from stagnation conditions as it enters the secondary flow path. As the flow travels farther along the collar toward the nozzle it accelerates giving rise to a reversible pressure drop, however, there will also be irreversible pressure loss since the fluid must work against the lateral turbulent diffusion of the shear layer.

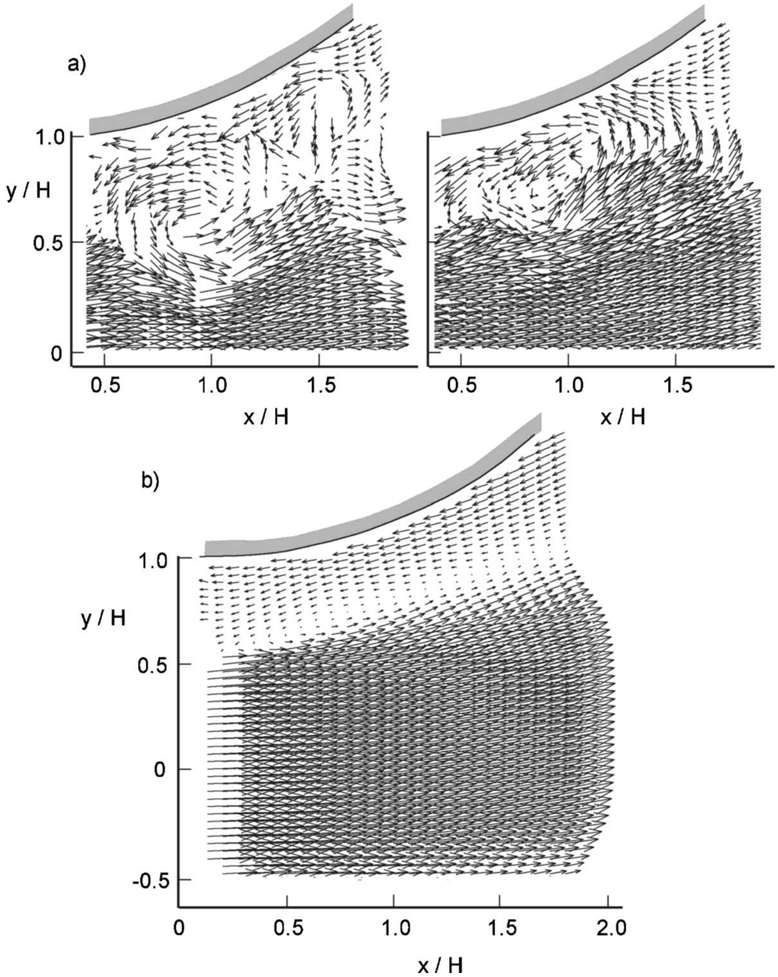

Fig. 7 (*a*) Instantaneous velocity-vector fields and (*b*) mean velocity field for the highly vectored primary jet; $\Delta p_{\mathrm{gap}}/\rho_j U_j^2 = -0.12$

The origin of these pressure changes was assessed by computing the frictionless pressure drop along the secondary flow path. This was accomplished by selecting a representative streamline approximately coincident with the maximum secondary velocity, though the results were not highly sensitive to this selection due to the nearly uniform velocity distribution in the secondary stream; see for example Fig. 6(*a*). The computed isentropic pressure profile is obtained from a compressible form of the Bernoulli equation using the measured peak velocities in the secondary flow path and is included in Fig. 8; it is seen to agree reasonably well with the measured surface pressure distribution, particularly away from the nozzle. However, the curves display deviations exceeding the uncertainty estimates for streamwise positions less than $x/H \sim 1$, indicating that the measured pressure losses in that region exceed the predictions for isentropic flow.

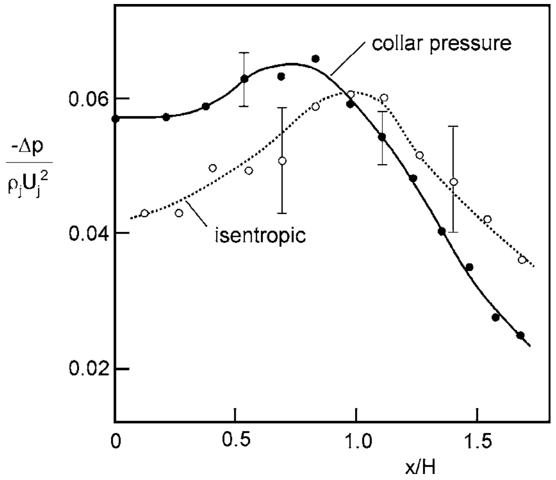

Fig. 8 Collar static pressure distribution and theoretical pressures computed assuming isentropic acceleration along the secondary flow path; moderate flow vectoring

To place these trends in context, a similar analysis was conducted for the measured collar pressure distribution for the highly vectored jet; these results are shown in Fig. 9. The collar pressure distribution achieves vacuum levels nearly twice the value measured in Fig. 8, but this should be expected since the lateral collar force should more than double to achieve an increase in flow vectoring from 6 to 14 deg. As fluid enters the restricted secondary flow path near the end of the collar, its reversible acceleration accurately predicts the measured pressures. However, as the flow propagates further along the path, the ideal flow analysis drastically under predicts the collar static pressures. The absence of a well-defined potential core in the highly vectored jet would dispel the expectation that reversible flow mechanisms would be at play. The irreversible pressure losses are clearly associated with the highly turbulent nature of the flow field in the curved shear layer. For example, the magnitude of the secondary flow velocities in the moderately and highly vectored cases, shown in Fig. 6(*a*) and 7(*b*), respectively, are quite comparable yet the pressures are con-

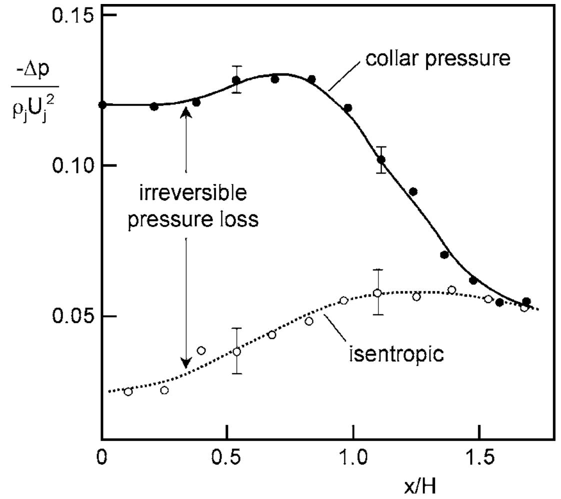

Fig. 9 Collar static pressure distribution and theoretical pressures computed assuming isentropic acceleration along the secondary flow path; highly vectored flow

siderably lower in the latter case. This is to be expected for a friction dominated process and is advantageous in the present situation, producing high flow turning at modest secondary flow penalties. As shown in earlier studies [16], the thrust loss coefficient is relatively insensitive to counterflow level, indicating that the irreversible mechanism does not sacrifice vectoring performance, yet achieves the control at a considerably lower mass flow penalty.

It is clear that vectoring is a response of the jet to a cross-stream pressure gradient. A *free* jet issuing into an ambient environment will create a slightly negative pressure at the jet boundary; the slight negative pressure generates the entrainment flow. Engulfment of ambient air by turbulence near the jet boundary is the driving mechanism for this slightly reduced pressure. Turbulence control impacting the entrainment will also affect the local sub-atmospheric pressure near the jet. For example, the asymmetrical forcing of the jet periphery may lead to flow turning under unconfined conditions as shown by Smith and Glezer [8] and Lim and Redekopp [9]. The partial confinement created by the collar magnifies the effect of mixing control on the cross-stream pressure gradient, in other words, at transmitting the vectoring effect to the nozzle through the potential fluid. Confinement restricts the freedom of entrainment, leading to lower pressures near the jet.

Consider a planar free jet with collars placed symmetrically as illustrated in Fig. 1, but with both suction gaps open to atmosphere. As natural entrainment causes a subtle pressure reduction in the jet near field, the proximity of the collar causes the entrainment flow to accelerate into that region, lowering the local static pressure on both sides of the jet. Under these circumstances the pressure reduction causes ambient air to be drawn through the suction gap in a coflowing manner as in a common ejector pump, albeit inefficiently due to the outwardly curving collar design. No vectoring is observed since the cross-stream pressure gradient is nominally zero due to symmetry. Under strong confinement, unsteadiness in the jet can lead to temporal cross-stream pressure gradients sufficient to cause attachment to the either collar. This is a bistable hysteretic operating regime that is undesirable [14].

Consider now the moderately vectored jet that has been shown to produce substantially low collar pressures through essentially reversible flow acceleration. In this situation, the upper gap is connected to a suction system and a modest amount of pumping is applied. The pumping causes a reduction in the pressure in the region between the collar and the primary jet, inducing ambient air flow into the collar region due to the pressure difference. As long as potential flow can be maintained in the secondary stream the mixing characteristics of the shear layer will play a minor role in the global response of the jet. However, if the shear layer can be manipulated to augment its entrainment—for example, using external forcing from microjets, vortex generators, MEMS, etc.—then any increase in entrainment will reduce the pumping requirements of the vacuum system. In the present geometry the countercurrent shear is the mechanism by which the mixing is being controlled, however, under the conditions of the moderately vectored jet this mechanism is not particularly efficient.

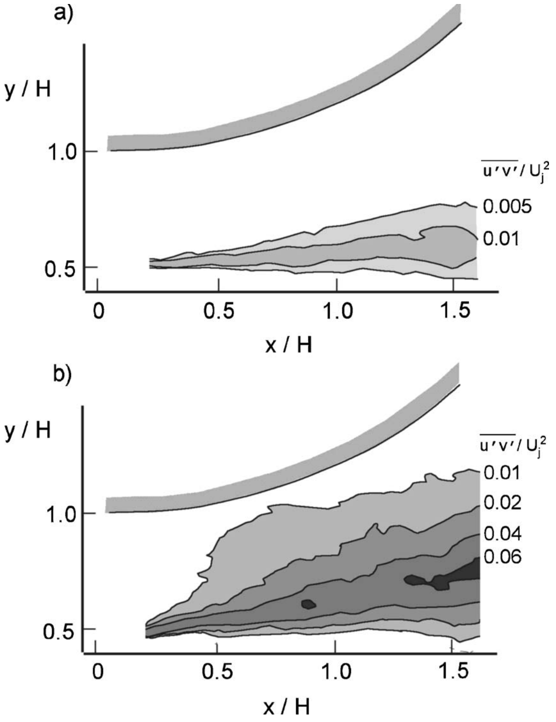

Fig. 10 Distributions of Reynolds stress for (*a*) unvectored and (*b*) highly vectored flow conditions

Now consider the situation that occurs for the highly vectored jet. As the suction is increased, irreversible pressure gradients begin to play a significant role in the vectoring process (Fig. 9). The basic physical mechanism at work here is the interplay between the vacuum source and the resistance to the secondary flow created by the primary jet. The equilibrium that is reached depends on the resistance elements in the flow path, of which the dynamic nature of the turbulent stress field is a critical element. Recent studies indicate that the stresses in a turbulent planar shear layer increase dramatically when counterflow is present at levels exceeding approximately 13% of the primary flow velocity [25]. The connection between the stress and pressure fields can be seen in the Reynolds-averaged Navier-Stokes equations, which when curvature effects are neglected, take the form (x-momentum)

$$\rho\bar{u}\frac{\partial\bar{u}}{\partial x}+\rho\bar{v}\frac{\partial\bar{u}}{\partial y}=-\frac{\partial\bar{p}}{\partial x}+\mu\nabla^2\bar{u}-\rho\frac{\partial\overline{u'^2}}{\partial x}-\rho\frac{\partial\overline{u'v'}}{\partial y}$$

Note that the gradients in the z-direction are considered negligible relative to x and y, and have been removed.

Although the cross-stream pressure difference is the driving force for the vectoring effect, the low pressure along the collar must be sustained in the streamwise direction. In principle, the streamwise pressure gradients can be achieved through appropriate modifications of the turbulence leading to gradients in the Reynolds stresses, as indicated by the equation of momentum conservation shown above. Figure 10 shows the cross-stream turbulent transport term $\overline{u'v'}/U_j^2$ for the baseline and highly vectored cases. The difference between the two distributions is quite dra-

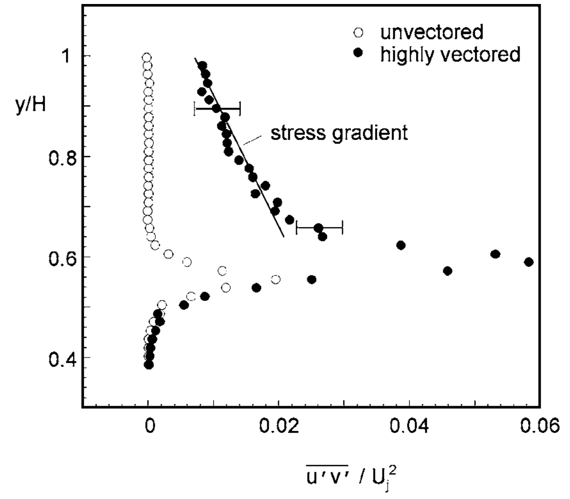

Fig. 11 Reynolds stress profiles taken at *x*/*H*=1 for the baseline and highly vectored flow conditions

matic. While the accuracy of the second order turbulent statistics is limited by the sample size and is approximately 12%, the differences in the two distributions is considerably larger than this uncertainty. Peak levels increase by a factor of approximately three to five for the case with suction. The increase in shear (ΔU across the shear layer) for the countercurrent shear layer is about 30%, thus the increase in turbulent stresses is primarily due to enhanced turbulent production mechanisms. Peak turbulence levels are greater than that found by Forliti et al. [25] for fully developed planar countercurrent shear layers at comparable mean flow conditions. The enhanced turbulent energy observed for the vectoring application may be attributed to limitations in the diffusion of turbulent energy caused by the confinement.

As indicated in the Reynolds averaged transport equation, the gradients in the turbulent stresses are more important in developing streamwise pressure gradients than the peak levels in the shear layer itself. Furthermore in the present application the cross-stream gradients are much larger than those in the streamwise direction indicating the importance of the term $\overline{u'v'}$ relative to u'^2. Cross-stream Reynolds stress profiles are shown in Fig. 11 for the unvectored and highly vectored flow conditions taken at the mid-plane of the collar ($x/H=1$). Reynolds stresses in the shear layer of the highly vectored flow are not only significantly larger in magnitude than the base flow, but are sustained across the secondary stream toward the collar. (Reynolds stresses were not computed beyond $y/H \sim 1$ due to measurement uncertainty in the region very close to the collar.) A comparison between the turbulent shear stress gradient and the observed pressure gradient along the collar surface shows agreement within approximately 30%, with the difference likely caused by the nominally large uncertainty in the spatial gradient of the Reynolds stress as well as other effects including streamline curvature. A similar RANS-based approach has been used to explain the streamwise pressure gradient characteristics of reattaching shear layers [26].

The shear layer of the vectored flow is in close enough proximity to the collar that stress gradients remain finite to the collar surface. The efficiency of the countercurrent shear layer in producing energetic turbulence over a large spatial domain benefits flow control in this application. Presumably the lower secondary mass flow rates observed in other studies [15,16] to achieve comparable flow turning, benefit from the smaller cross-stream distance G/H of the collars used in those investigations. Certainly the presence of turbulent stresses allows for the development of larger pressure differences by irreversible means at reduced mass flow levels as compared to reversible mechanisms alone.

Concluding Remarks

Intuition might suggest that reversible mechanisms such as seen in the moderately vectored flow reported here would be desirable for optimal fluidic vectoring, however the irreversibility caused by the turbulent stress field is advantageous for several reasons. First, we can expect that the secondary mass flow required to achieve a higher streamwise pressure gradient will be less when that field is created through irreversible mechanisms. This would support a system design to create vacuum at relatively low volumetric flow rates, e.g., an ejector pump. It also suggests that seeking ways to further enhance the head loss, such as additional high-loss restrictive elements, may also be beneficial. Second, if we restrict ourselves to reversible secondary streams, we are limited to pressure ratios on the order of one-half to avoid choking in isentropic flow. The choking requirement has no such constraint when turbulent stress gradients create the pressure field (e.g., as in classic Fanno flow [27]). Finally, to minimize external drag it is essential to reduce the cross-stream extent of the collar hardware, leading to small secondary flow gaps, *G*, and the need to design systems that will be dominated by the turbulent stresses.

While many other mechanisms have been proposed to locally alter the pressure field sufficient to vector the flow (e.g., Coanda effect, wall suction, blowing, etc.), few have been shown to provide the desired proportional control at low actuation penalties. It is the countercurrent shear layer interaction with the collar surface that causes the observed irreversible pressure drop. In practice, any means of facilitating such a stress field could be used to vector the flow, but generating such turbulence levels with other flow control strategies may be very difficult to realize and highlights a unique benefit of countercurrent shear.

Acknowledgment

The authors would like to thank the generous financial support of the Office of Naval Research, and the continued guidance we receive from Dr. Gabriel D. Roy.

References

[1] Wing, D. J., 1994, "Static Investigation of Two Fluidic Thrust-Vectoring Concepts on a Two-Dimensional Convergent Divergent Nozzle," NASA TM-4574.
[2] Chiarelli, C., Johnsen, R. K., and Shieh, C. F., 1993, "Fluidic Scale Model Multi-Plane Thrust Vector Control Test Results," AIAA 93-2433.
[3] Fitzgerald, R. E., and Kampe, R. F., 1983, "Boundary Layer TVC for Missile Applications," AIAA Paper 83-1153.
[4] Carrol, G. R., and Cox, H., 1983, "A Missile Flight Control System Using Boundary Layer Thrust Vector Control," AIAA Paper 83-1149.
[5] Snow, B. H., 1990, "Thrust Vectoring Control Concepts and Issues," SAE Trans., **99**, pp. 1488–1499.
[6] Gilbert, B., 1991, "Directional Control of Large Mass Flows by Fluidics," ASME 3rd International Symposium on Fluid Control, Measurement and Visualization, FLUCOME.
[7] Porzio, A. J., and Franke, M. E., 1989, "Experimental Study of a Confined Jet Thrust Vector Control Nozzle," J. Propul. Power, **5**(5), pp. 596–601.
[8] Smith, B. L., and Glezer, A., 2002, "Jet vectoring using synthetic jets," J. Fluid Mech., **458**, pp. 1–34.
[9] Lim, D. M., and Redekopp, L. G., 2002, "Aerodynamic Flow-Vectoring for a Planar Jet in a Coflowing Stream," J. Fluid Mech., **450**, pp. 343–375.
[10] Miller, D. N., Yagle, P. J., and Hamstra, J. W., 1999, "Fluidic Throat Skewing for Thrust Vectoring in Fixed-Geometry Nozzles," AIAA 99-0365.
[11] Deere, K. A., Berrier, B. L., Flamm, J. D., and Johnson, S. K., 2003, "Computational Study of Fluidic Thrust Vectoring Using Separation Control in a Nozzle," AIAA-03-3803.
[12] Mason, S. M., and Crowther, W. J., 2002, "Fluidic Thrust Vectoring of Low Observable Aircraft," CEAS Aerospace Aerodynamics Research Conference. Cambridge, UK.
[13] Pack, L. G., and Seifert, A., 2001, "Periodic Excitation for Jet Vectoring and Enhanced Spreading," J. Aircr., **38**(3), pp. 486–495.
[14] Van der Veer, M. R., and Strykowski, P. J., 1997, "Counterflow Thrust Vector Control of Subsonic Jets: Continuous and Bistable Regimes," J. Propul. Power, **13**(3), pp. 412–420.
[15] Strykowski, P. J., Krothapalli, A., and Forliti, D. J., 1996, "Counterflow Thrust Vectoring of Supersonic Jets," AIAA J., **34**(11), pp. 2306–2314.
[16] Alvi, F. S., Strykowski, P. J., Krothapalli, A., and Forliti, D. J., 2000, "Vectoring Thrust in Multiaxes using Confined Shear Layers," ASME J. Fluids Eng., **122**, pp. 3–13.
[17] Strykowski, P. J., Schmid, G. F., Alvi, F. S., and Krothapalli, A., 1997, "Vectoring Thrust Using Confined Shear Layers," AIAA 97-1997.

[18] Strykowski, P. J., and Krothapalli, A., 1993, “The Countercurrent Mixing Layer: Strategies for Shear-Layer Control,” AIAA 93-3260.
[19] Washington, D. M., Alvi, F. S., Strykowski, P. J., and Krothapalli, A., 1996, “Multiaxis Fluidic Thrust Vector Control of a Supersonic Jet Using Counterflow,” AIAA J., **34**(8), pp. 1734–1736.
[20] Flamm, J. D., 1998, “Experimental Study of a Nozzle Using Fluidic Counterflow for Thrust Vectoring,” AIAA 98-3255.
[21] Hunter, C. A., and Deere, K. A., 1999, “Computational Investigation of Fluidic Counterflow Thrust Vectoring,” AIAA 99-2669.
[22] Prasad, A. K., Adrian, R. J., Landreth, C. C., and Offutt, P. W., 1992, “Effect of Resolution on the Speed and Accuracy of Particle Image Velocimetry Interrogation,” Exp. Fluids, **13**, pp. 105–116.
[23] Gillgrist, R. D., 1999, “A Fundamental Study of Thrust Vector Control Using Counterflow,” M.S. thesis, University of Minnesota, Minneapolis, MN.
[24] Rabe, D., and Sabroske, K., 1994, “Laskin Nozzle Performance for Laser Flow Measurement Seeding,” 32nd Aerospace Sciences Meeting, AIAA 94-0044.
[25] Forliti, D. J., Tang, B. A., and Strykowski, P. J., 2005, “An Experimental Investigation of Planar Countercurrent Turbulent Shear Layers,” J. Fluid Mech., **530**, pp. 241–264.
[26] Adams, E. W., and Johnston, J. P., 1988, “Effects of the Separated Shear Layer on the Reattachment Flow Structure Part 1: Pressure and Turbulence Quantities,” Exp. Fluids, **6**, pp. 400–408.
[27] Shapiro, A. H., 1953, “*The Dynamics and Thermodynamics of Compressible Fluid Flow*,” Wiley, New York, Chap. 6, Vol. I, pp. 159–186.

Ali M. Jawarneh[1]
Assistant Professor
Department of Mechanical Engineering,
The Hashemite University,
Zarqa 13115,
Jordan
e-mail: alijaw@yahoo.com

P. Sakaris
Research Assistant

Georgios H. Vatistas
Professor

Department of Mechanical and Industrial Engineering,
Concordia University,
1455 de-Maisonneuve Blvd. West,
Montreal H3G 1M8,
Canada

Experimental and Analytical Study of the Pressure Drop Across a Double-Outlet Vortex Chamber

This paper presents experimental and analytical results concerning the pressure drop and the core size in vortex chambers. The new formulation is based on the conservation of mass and energy integral equations and takes into account the presence of two outlet ports. The diminishing vortex strength is introduced through the vortex decay factor. The influence of vortex chamber geometry, such as diameter ratio, aspect ratio, and Reynolds number, on the flow field have been examined and compared with the present experimental data. It is shown that the presence of the swirl velocity component makes the pressure drop across a vortex chamber significantly different than the familiar unidirectional pipe flow. When the chamber length is increased, the vortex diminishes under the action of friction, producing a weaker centrifugal force which leads to a further pressure drop. It is revealed that by increasing the Reynolds number, the cores expand resulting into a larger pressure coefficient. For a double-outlet chamber where the flow is divided into two streams, the last parameter is found to be less than that of a single-outlet.
[DOI: 10.1115/1.2375131]

1 Introduction

Swirling flows occur in many engineering applications, such as vortex separators, pumps, gas turbine combustors, furnaces, spray dryers, vortex combustors, and gas-core nuclear rockets. In modern combustors, swirl is used to produce good mixing and to improve the flame stability. In furnaces and incinerators, swirl keeps the solid fuel in suspension, increases its residence time, and compels even the most difficult (low calorific value) fuel to burn completely. In all confined vortex applications, it is important to adequately understand the overall flow field evolution as a function of both the geometrical and flow parameters. Knowledge of these flows will improve the design and performance of a variety of vortex devices.

Two interesting features of the flow of practical importance are the pressure drop of the fluid as it flows through the chamber and the dimensions of the viscous core region. The pressure drop across a vortex chamber with a single-outlet has been the subject of several papers. Shakespear and Levy [1] reported on experimental findings with respect to the pressure drop and the core size in a vortex chamber with a rotating permeable inlet assuming a potential flow. Vyas and Majdalani [2] have shown analytically that the pressure drop and the core size are a function of the aspect ratio and Reynolds number. Yang [3] has studied the vortex throttles, and has found that the pressure drop across the vortex throttles occurs through the axial throttling port by the dissipation of the high tangential velocity. Escudier et al. [4] demonstrated experimentally the axial and swirl velocity distributions using LDA measurements. The experiments revealed a remarkable change in the vortex core structure as the exit diameter hole is reduced. Kreith and Sonju [5] studied the decay of swirl in a long pipe. The swirl was induced by tangential jets along the periphery of the pipe. The experiments indicated that the vortex decay increases as the Reynolds number decreases. Osami [6] has shown experimentally that the swirl intensity decays downstream as a result of wall friction, and that the core size is dependent upon the upstream conditions. Steenbergen and Voskamp [7] have shown that the vortex decay appears to vary with the Reynolds number in the same way as the friction factor in a pipe flow. The core size structure inside a vortex chamber has a wavy variation; see Darmofal et al. [8]. Meanwhile, the core structure based on the laser doppler anemometry (LDA) measurements of Escudier [9] confirm that the variations are very small. In addition, the experimental visualization results of Lam [10] and Alekseenko et al. [11] showed that the core of the vortex remains approximately the same throughout the chamber, and the amplitude of the oscillations was found to be small in comparison with the size of the vortex core.

Previous literature dealt with a chamber with a single outlet port, but some of the important industrial vortex devices deal with double-outlet ports, such as the dust separator, the vortex pump, and the cyclone which is used in the fluid catalytic cracking (FCC) unit. Good understanding of the pressure drop leads to an improvemant of the cyclone efficiency and minimizes the pollutions like SOX, NOX, and particulate emissions. Also, the double-outlet configuration is used in the heat exchanger to enhance the heat transfer in vortex tubes, where the air flow splits into two parts—cold air at one end and hot air at the other.

The experimental and analytical work by Vatistas and Sakaris [12] dealt with a double-outlet chamber configuration. The analytical model gives satisfactory results for very high Reynolds number and an aspect ratio equal to one, while it is inadequate for low Reynolds numbers and an aspect ratio of greater than one.

The purpose of this paper is to study the pressure drop and the core size both experimentally and analytically in double-outlet chambers at different lengths, exit holes, and Reynolds numbers. The experimental results will be shown to correlate well with the theortical findings.

2 Experiments

The present experiments have been conducted using a jet-driven vortex chamber similar to the one utilized by Vatistas et al. [13]. The main difference between the two is that in the latest version, shown schematically in Fig. 1, two vortex chambers made of Plexiglas with two lengths (L_1, L_2) are used. They have a cylindrical configuration with constant cross-sectional area ($A_o = 153.86\ \text{cm}^2$), and the two axes of the chambers are horizontal with respect to the ground. Swirl is imparted to the fluid via the

---

[1] Corresponding author.

Contributed by the Fluids Engineering Division of ASME for publication in the JOURNAL OF FLUIDS ENGINEERING. Manuscript received March 9, 2005; final manuscript received June 8, 2006. Review conducted by Joseph Katz.

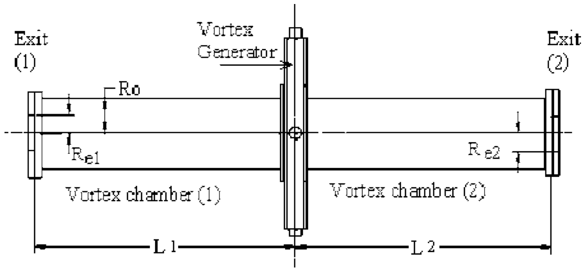

Fig. 1 Experimental setup

vortex generator shown in Fig. 2. It has four perpendicular air inlets where the compressed air is introduced. The required set of inlet conditions is obtained by the insertion of the appropriate vortex generator block (swirler) into the vortex generator assembly along the periphery of the vortex generator (the vortex generator was made from aluminum and mounted between the two chambers). A number of inclined inlet holes (16 holes) with inlet diameter $d_{\text{in}}=1.267$ cm are drilled at a specified angle $\varphi=30$ deg. When the air flow passes through the swirler holes, it is guided and enters both vortex chambers in the tangential ($V_{\varphi\text{in}}$) and radial ($V_{r\text{in}}$) directions so that swirl is formed inside the chambers. For the experiments reported here, the first chamber length was fixed at $L_1=42$ cm, and its exit hole diameter was fixed at $2R_{e1}=1.879$ cm. Three lengths were used for the second chamber, and they were varied from $L_2=42$, 61, and 122 cm. Their exit hole diameters ($2R_{e2}$) were also varied from 1.879, 1.976, 2.164, 2.413, 2.649, 2.794 and 3.175 cm. The static pressure is measured by a series of taps located ahead of the tangential ports (see Fig. 2) and is averaged by connecting in parallel all the pressure pick-up tubes into a common tube. The measurements of the mean gauge pressure ($P_{\text{in}}-P_a$) were obtained using a U-tube filled with Meriam oil, having a specific gravity equal to 1.00. The estimated uncertainty is less than ±8% for the pressure drop measurements. The measurements were made at three inlet air flow rates (Q_{in}): 0.0117, 0.014, and 0.0187 m^3/s, which correspond to three Reynolds numbers (R_{eo}): 7245, 8694, and 11,592, respectivelly. This is defined based on the average axial velocity as

$$R_{eo}=\frac{4Q_{\text{in}}}{\nu\pi D_o}$$

A rotameter is used to measure the volumetric flow rate of the inlet air. This was carefully calibrated in standard conditions (1 atmosphere and 20±0.5% °C). For the flow rate used, the uncertainty was estimated to be ±2%.

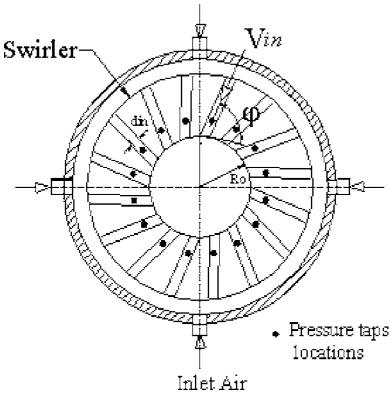

Fig. 2 Vortex generator

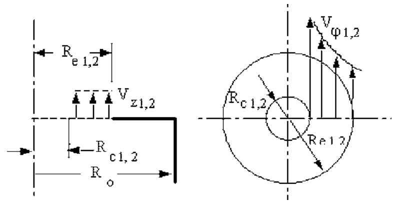

Fig. 3 Outlet flow boundary conditions

3 Analysis

The energy equation is considered for strong swirl, steady, constant viscosity, axisymmetric, and incompressible flow. In order to simplify the problem several assumptions are made. These are: The pressure and the total velocity at the inlet are both uniform; the radial velocity at the exit is neglected since it does not have the space to develop; and at the double-outlet exit the pressure is ambient. The energy balance over the control volume enclosing the chambers yields

$$\left(\frac{P_{\text{in}}}{\rho}+\frac{1}{2}V_{\text{in}}^2\right)Q_{\text{in}}=\int_{R_{c1}}^{R_{e1}}\left\{\frac{P_a}{\rho}+\frac{1}{2}V_{\varphi 1}^2+\frac{1}{2}V_{z1}^2\right\}V_{z1}2\pi r\,dr+\int_{R_{c2}}^{R_{e2}}\left\{\frac{P_a}{\rho}+\frac{1}{2}V_{\varphi 2}^2+\frac{1}{2}V_{z2}^2\right\}V_{z2}2\pi r\,dr \tag{1}$$

The swirl velocities at the vortex chamber exits (shown in Fig. 3) are based on the free vortex model and given by

$$V_{\varphi 1}=\frac{\delta_1\Gamma}{2\pi r}$$

$$V_{\varphi 2}=\frac{\delta_2\Gamma}{2\pi r}$$

Γ is the vortex circulation and is given by

$$\Gamma=2\pi R_o V_{\varphi\text{in}}$$

and the inlet tangential velocity (shown in Fig. 4) is defined as

$$V_{\varphi\text{in}}=V_{\text{in}}\cos(\varphi)$$

The bulk of the energy loss is assumed to occur across the vortex chamber and it is mainly associated with the decay of the swirl velocity. The vortex decay factors δ_1 and δ_2 defined here are similar to Jawarneh et al. [14] as

$$\delta_1=\frac{\Omega_1}{\Omega_{\text{in}}}$$

$$\delta_2=\frac{\Omega_2}{\Omega_{\text{in}}}$$

where the vortex strength at the inlet is given by

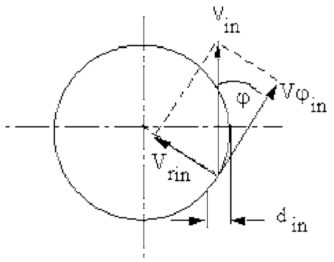

Fig. 4 Inlet flow boundary condition

$$\Omega_{\text{in}} = \frac{\Gamma}{2\pi}$$

Average axial velocities are assumed at the exit ports of the chamber (see Fig. 3) and are given by

$$V_{z1} = \frac{Q_1}{\pi(R_{e1}^2 - R_{c1}^2)}$$

$$V_{z2} = \frac{Q_2}{\pi(R_{e2}^2 - R_{c2}^2)}$$

From the continuity equation

$$Q_{\text{in}} = Q_1 + Q_2$$

$$\text{or} \quad 1 = \gamma_1 + \gamma_2$$

where

$$\gamma_1 = \frac{Q_1}{Q_{\text{in}}}, \quad \gamma_2 = \frac{Q_2}{Q_{\text{in}}}, \quad \text{and} \quad Q_{\text{in}} = V_{\text{in}} A_{\text{in}}$$

Energy Eq. (1) becomes

$$\left(\frac{P_{\text{in}}}{\rho} + \frac{1}{2}V_{\text{in}}^2\right)Q_{\text{in}} = \frac{P_a}{\rho}Q_{\text{in}} + (\delta_1\Omega_{\text{in}})^2 Q_1 \frac{\text{Ln}\left(\frac{R_{e1}}{R_{c1}}\right)}{(R_{e1}^2 - R_{c1}^2)} + \frac{1}{2}V_{z1}^2 Q_1 + (\delta_2\Omega_{\text{in}})^2 Q_2 \frac{\text{Ln}\left(\frac{R_{e2}}{R_{c2}}\right)}{(R_{e2}^2 - R_{c2}^2)} + \frac{1}{2}V_{z2}^2 Q_2 \tag{2}$$

If the dimensionless parameters are defined as follows:

$$C_p = \frac{2\Delta P}{\rho V_{\text{in}}^2}, \quad \Delta P = P_{\text{in}} - P_{\text{out}}$$

$$\beta = \frac{L_2}{L_1}, \quad \alpha = \frac{A_{\text{in}}}{A_o}$$

$$\chi_1 = \frac{R_{c1}}{R_{e1}}, \quad \chi_2 = \frac{R_{c2}}{R_{e2}}$$

$$\xi_1 = \frac{R_o}{R_{e1}}, \quad \xi_2 = \frac{R_o}{R_{e2}}$$

where C_p is the pressure drop coefficient. The rest of the parameters

$$\Delta P, \beta, \alpha, \chi_1, \chi_2, \xi_1, \xi_2$$

are the static pressure difference between the inlet and outlet pressure, aspect ratio, area ratio, the dimensionless core size at exit (1), the dimensionless core size at exit (2), the diameter ratio at exit (1), and the diameter ratio at exit (2), respectively. Then the energy (Eq. (2)) becomes

$$C_p = \underbrace{\alpha^2\xi_1^4\gamma_1^3\frac{1}{(1-\chi_1^2)^2} - 2\cos^2(\varphi)\xi_1^2\gamma_1\delta_1^2\frac{\text{Ln}[\chi_1]}{(1-\chi_1^2)}}_{C_{p1}} + \underbrace{\alpha^2\xi_2^4\gamma_2^3\frac{1}{(1-\chi_2^2)^2} - 2\cos^2(\varphi)\xi_2^2\gamma_2\delta_2^2\frac{\text{Ln}[\chi_2]}{(1-\chi_2^2)}}_{C_{p2}} - 1 \tag{3}$$

Since $\gamma_2 = 1 - \gamma_1$ at given design geometry parameters $(\xi_1, \xi_2, \varphi, \alpha, \beta)$, then

$$C_p = f_n(\chi_1, \chi_2, \delta_1, \delta_2, \gamma_1) \tag{4}$$

There are five unknown variables, so five equations are required. The first equation comes from the comparability of the pressure. Since the two chambers share the same inlet static pressure, and the outlet pressure for both chambers is ambient, then

$$C_{p1} = C_{p2}$$

or

$$\underbrace{\alpha^2\xi_1^4\gamma_1^3\frac{1}{(1-\chi_1^2)^2} - 2\cos^2(\varphi)\xi_1^2\gamma_1\delta_1^2\frac{\text{Ln}[\chi_1]}{(1-\chi_1^2)}}_{C_{p1}} = \underbrace{\alpha^2\xi_2^4\gamma_2^3\frac{1}{(1-\chi_2^2)^2} - 2\cos^2(\varphi)\xi_2^2\gamma_2\delta_2^2\frac{\text{Ln}[\chi_2]}{(1-\chi_2^2)}}_{C_{p2}} \tag{5}$$

Equation (3) reveals that C_p is unbounded when χ_1 and χ_2 tend to zero or one, therefore, there must exist $0 < \chi_1 < 1$ and $0 < \chi_2 < 1$ such that C_p is the minimum. The latter required that

$$\frac{\partial C_{p1}}{\partial \chi_1} = 0.0$$

or

$$4a_1\alpha^2\chi_1^2 - b_1\{(1-\chi_1^2)^2 + 2\chi_1^2(1-\chi_1^2)\text{Ln}[\chi_1]\} = 0.0 \tag{6}$$

and

$$\frac{\partial C_{p2}}{\partial \chi_2} = 0.0$$

or

$$4a_2\alpha^2\chi_2^2 - b_2\{(1-\chi_2^2)^2 + 2\chi_2^2(1-\chi_2^2)\text{Ln}[\chi_2]\} = 0.0 \tag{7}$$

where a_1, b_1, a_2, b_2 are defined as

$$a_1 = \alpha^2\xi_1^2\gamma_1^3$$

$$b_1 = 2\gamma_1\delta_1^2\cos^2(\varphi)$$

$$a_2 = \alpha^2\xi_2^2\gamma_2^3$$

$$b_2 = 2\gamma_2\delta_2^2\cos^2(\varphi)$$

Based on the experimental results of C_p, the least squares technique error will be implemented according to the formula

$$E = \sum_{i=1}^{N}[C_{p\,\exp\,i} - C_{p\,\text{theor}\,i}]^2 \tag{8}$$

where N is the total number of measurements, $C_{p\,\exp}$ is the measured pressure drop coefficient, and $C_{p\,\text{theor}}$ is the theortical pressure drop coefficient as given in Eq. (3).

The necessary last equation to close the system comes from the fact that the chamber length L_1 was kept constant, while the vortex decay factor δ_1 has to remain constant at a given Reynolds number. In this case the solution to the set of Eqs. (5)–(8) begins at the aspect ratio $\beta = 1.00$ $(L_1 = L_2)$, where the vortex decay factor δ_1 is equal to δ_2. Then the pressure drop coefficient is a function of four parameters

$$C_p = f_n(\chi_1, \chi_2, \delta_1, \gamma_1) \tag{9}$$

The last equation is solvable since it has four variables with four equations. Now, if the aspect ratio $\beta(L_1 < L_2)$ is increased while keeping the same Reynolds number, the vortex decay factor δ_1 is known from the previous step, and the pressure drop coefficient is given by

$$C_p = f_n(\chi_1, \chi_2, \delta_2, \gamma_1) \tag{10}$$

The last equation is solvable since there are four unknowns and four equations.

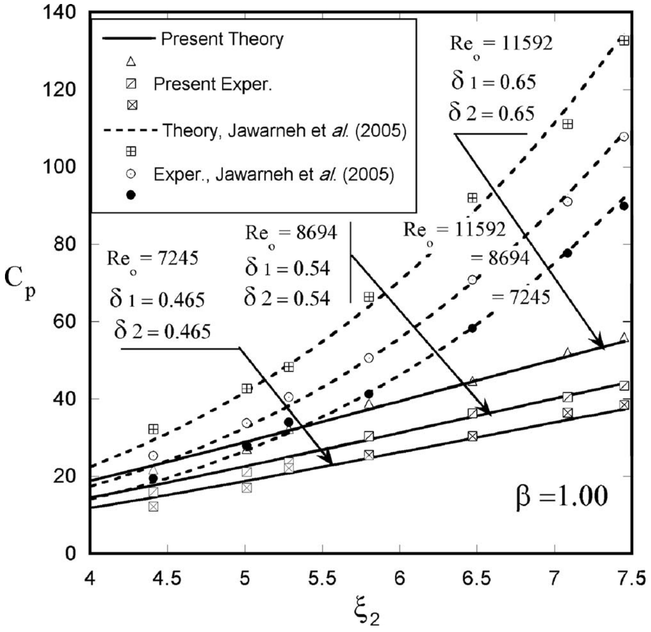

Fig. 5 Pressure drop coefficient at aspect ratio $\beta = 1.00$ for different Reynolds numbers (11,592, 8694, 7245). The solid lines represent a double-outlet chamber while the dashed lines represent a single-outlet chamber.

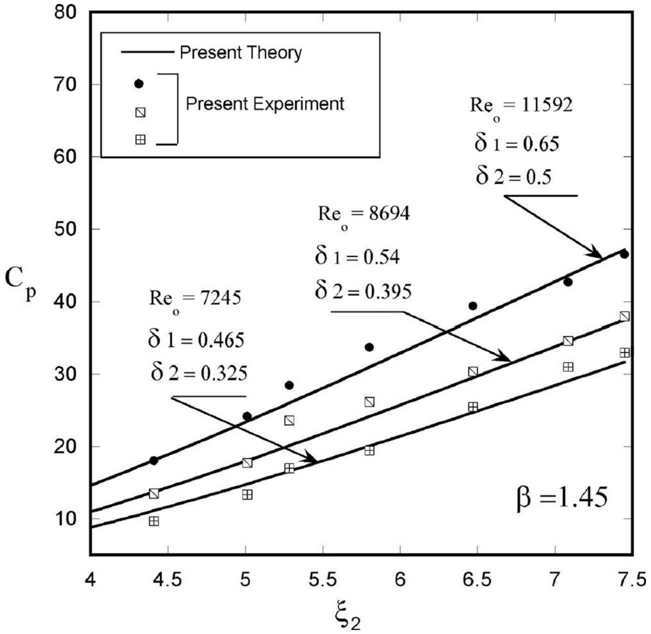

Fig. 6 Pressure drop coefficient for aspect ratio $\beta = 1.45$ for different Reynolds numbers (11,592, 8694, 7245)

4 Discussion of Results

The present model has two limiting factors: (i) For low contraction ratios (i.e., $\xi_2 < 4.0$), the intense swirl condition is reduced resulting in more than 8% error; and (ii) for high contraction ratios (i.e., $\xi_2 > 7.5$), the compressibility effects are evident (see Jawarneh et al. [14]).

In this study, the flow is dominated by an intense confined vortex where the tangential velocity is several orders of magnitude larger than the radial and axial velocity components. So, there is a strong centrifugal force which decays with the length, thus shaping the development of the overall flow-field. Some of the kinetic energy is dissipated as thermal energy by the viscous action due to friction at the toroidal recirculation flow area and the contraction joint (the exit hole). The head losses do not appear as explicit in the energy equation as the pipe flow. It can be taken into account if the detailed flow field inside the chamber is known. Since the latter is presently not available, an attempt will be made here to include it through the reduction of the swirl kinetic energy. It is implicitly included through the vortex decay factor, which represents the bulk of the energy loss across the vortex chamber.

The estimated uncertainty for the pressure drop coefficient C_p has appeared at a maximum of ±8%. Figures 5 and 6 compare the present experimental data with the present theory of the pressure drop coefficient C_p for aspect ratios $\beta = 1.00$ and 1.45. The error between the experiment and the present theory is found to be less than 8%. It is clear that as the diameter ratio ξ_2 and the Reynolds number R_{eo} increase, the pressure coefficient C_p rises. Stronger vortices are created by a higher diameter ratio and/or Reynolds number leading to a rise in tangential velocity and hence a higher pressure drop. In the case where the Reynolds number is increased, the total inlet velocity V_{in}, the inlet tangential velocity $V_{\varphi\text{in}}$, and the circulation Γ will increased; hence, the vortex strength will be stronger and, therefore, a higher pressure drop will result. The vortex decay factors δ_1, δ_2 are directly related to the Reynolds number R_{eo}, so the inertia effects dominate the viscous effects leading to a strong generated vortex with higher tangential velocity and a greater pressure drop. For aspect ratio $\beta = 1.00$, the vortex decay factors δ_1, δ_2 are equal for the same Reynolds number. This means the tangential velocities start to decay at the same rate for equal chamber lengths. However, for the aspect ratio $\beta = 1.45$ shown in Fig. 6, the vortex decay factor δ_1 is higher than δ_2 as expected because the tangential velocity decay rate in the longer chamber is greater than the shorter one due to friction. The experiments and the theortical model of Jawarneh et al. [14] were constructed for a chamber with a single outlet. The comparison between single-outlet and double-outlet chambers is shown in Fig. 5. As expected, the pressure drop coefficient for a single-outlet is higher than that of a double-outlet chamber because the flow is diverted to two outlets, thus reducing the vortex strength and the pressure drop.

The behavior of the vortex dimensionless core sizes χ_1, χ_2 for aspect ratio $\beta = 1.00$ are shown in Fig. 7. Both cores are equal for the same diameter ratio $\xi_1 = \xi_2 = 7.448$ and increase as the diameter ratio ξ_2 decreases. Since the diameter ratio ξ_1 was kept constant, the expansion rate of χ_1 is higher than that of χ_2. Therefore, the dimensionless core size χ_1 will have to expand in size more than χ_2 in order to achieve the mass conservation principle which leads to an increase in axial velocity. A greater Reynolds number leads to larger core sizes (χ_1, χ_2) as shown in Fig. 7.

Figure 8 shows the exit volumetric fractions γ_1, γ_2 for two aspect ratios $(\beta = 1.00, 1.45)$. Volumetric fractions clearly show a strong dependence with the aspect and diameter ratios, while the Reynolds number is independent.

The observations show that the pressure drop decreases with the length. The pressure drop across the vortex chamber differs from that in the pipe flow, due to the mechanism of swirl flow. It depends mainly on the intensity of the tangential velocity. If the chamber length is increased, the vortex decay factor decreases, lowering the tangential velocity, producing a weaker vortex at the exit plane for longer chambers, which leads to less pressure drop.

The pressure drop coefficient for various aspect ratios β is given in Fig. 9. It shows a decrease in the pressure drop with increasing length. This appears to be counterintuitive since one habitually expects the pressure drop to be larger for longer lengths. However, a closer examination reveals that in addition to the radial-axial plane flow, there is also a substantial centrifugal force which decays with the length, thus shaping the development of the overall flow-field. The pressure drop across the vortex

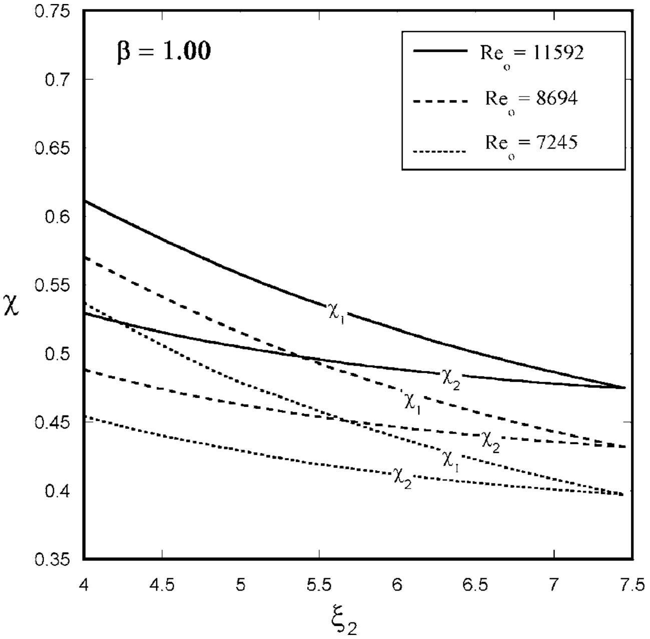

Fig. 7 Dimensionless core size at aspect ratio β=1.00 for different Reynolds numbers (11,592, 8694, 7245)

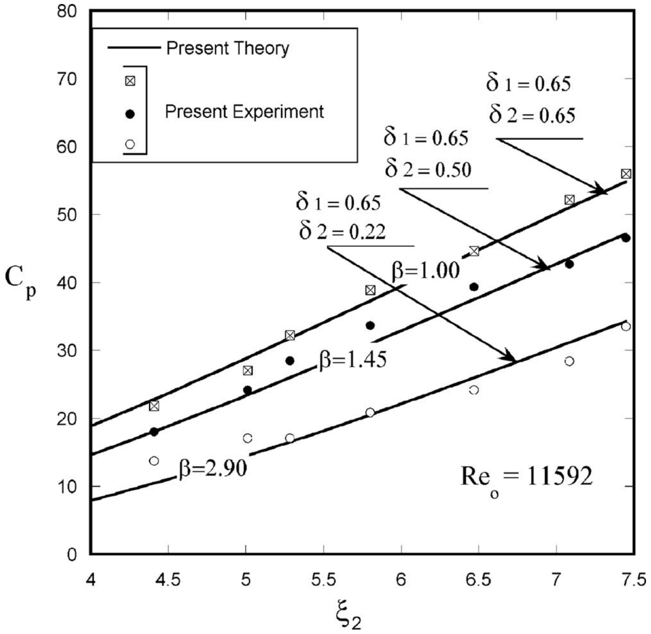

Fig. 9 Pressure drop coefficient for different aspect ratios (1, 1.45, 2.9) for Reynolds number R_{eo}=11,592

chamber differs from that in the pipe flow due to the nature of swirl flow. It depends mainly on the intensity of the tangential velocity. Longer chamber lengths lead to a reduction of the vortex decay factor, thus producing a weaker vortex and a smaller pressure drop.

Figure 10 shows the core sizes for different aspect ratios ($\beta = 1.00, 1.45, 2.90$) at a specific Reynolds number (R_{eo}=11,592). As the diameter ratio increases, the core size (the radius of peak tangential velocity profile) contracts. The vortex strength inside the forced-vortex region is focused and the free-vortex region is expanded. When the dimensionless core size χ_1 contracts, the exit volumetric fraction γ_1 increases as shown in Fig. 11. The effective outlet area (the area between the wall and the core size) at the exit (1) expands, leading into an increased axial velocity (to compensate for the increase of the effective outlet area). While the dimensionless core size χ_2 reduces, the exit volumetric fraction γ_2 decreases as seen from Fig. 11, causing the effective outlet area at exit (2) to contract and, in order to conserve the mass, causes an increase in the axial velocity at exit (2).

When the aspect ratio is increased the dimensionless core size χ_1 expands and χ_2 contracts. Similarly, the exit volumetric fraction γ_1 increases and γ_2 decreases. The effective outlet area at exit (1) shrinks while the other exit enlarges. The overall result is a reduction in axial velocity at both exits.

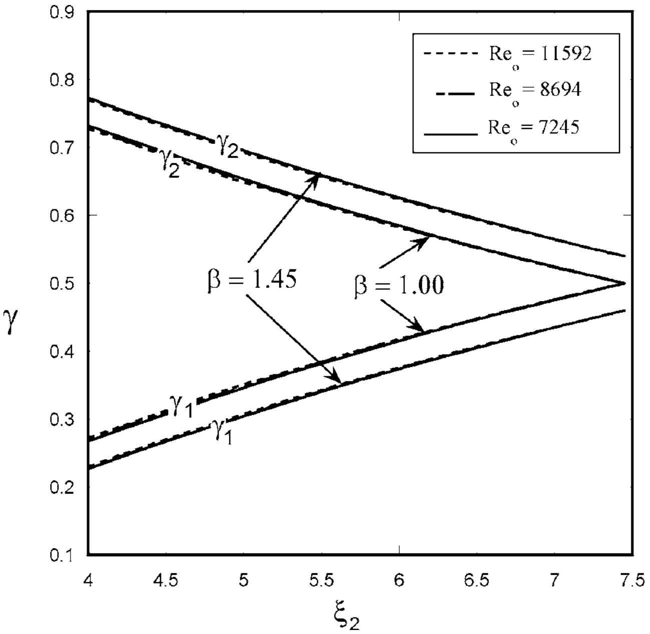

Fig. 8 Exit volumetric fractions at different aspect ratios (1, 1.45) and Reynolds numbers (11,592, 8694, 7245)

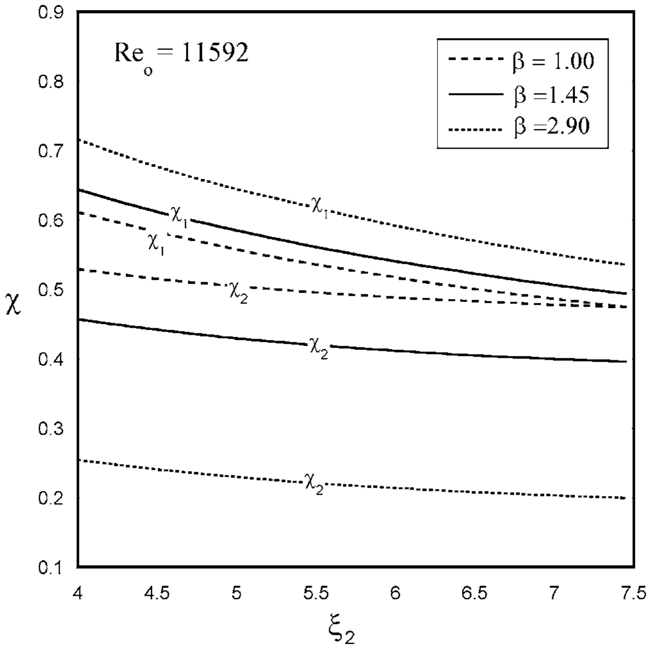

Fig. 10 Dimensionless core size for different aspect ratios (1, 1.45, 2.9) for Reynolds number R_{eo}=11,592

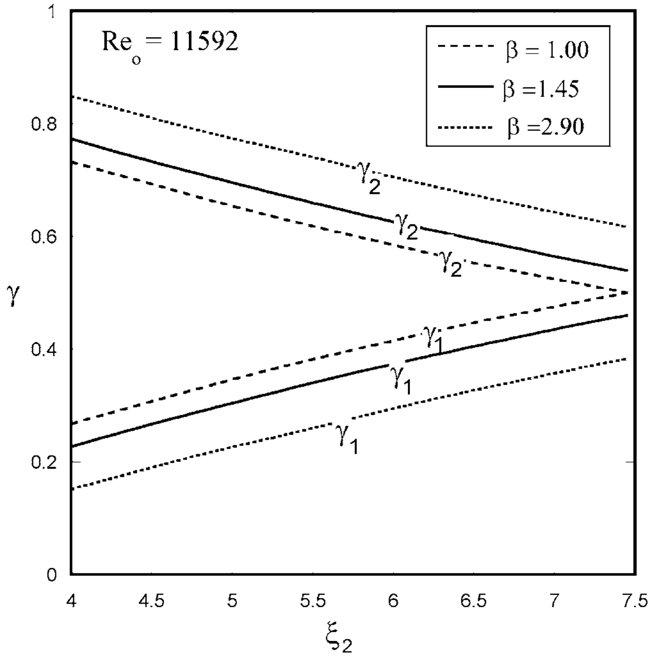

Fig. 11 Exit volumetric fraction for different aspect ratios (1, 1.45, 2.9) for Reynolds number R_{eo}=11,592

5 Conclusions

The present study explored the effects of vortex chamber geometry with a double-outlet. It has been found that higher Reynolds numbers cause the core sizes to expand and will increase the pressure drop. Larger diameter ratios made the core sizes smaller and also increased the pressure. A stronger vortex will be produced by increasing the diameter ratio and/or Reynolds number, resulting in a higher tangential velocity and hence a higher pressure difference. On the other hand, the pressure drop decreased with the aspect ratio. The exit volumetric fractions are shown to be independent of the Reynolds number; meanwhile, they are strongly dependent on the aspect and the diameter ratios.

Nomenclature

A_o = cross sectional area of the vortex chamber (πR_o^2)
A_{in} = total inlet area ($n\pi r_{\text{in}}^2$)
C_p = pressure coefficient ($2\Delta P/\rho V_{\text{in}}^2$)
D_e = diameter of the exit port ($2R_e$)
D_o = chamber diameter ($2R_o$)
d_{in} = diameter of the inlet port ($2r_{\text{in}}$)
$L_{1,2}$ = chamber lengths
n = numbers of the inlet holes
P = static pressure
P_a = ambient static pressure
P_{in} = static pressure at the inlet
Q_{in} = inlet volumetric flow rate
Q_1 = outlet volumetric flow rate at exit (1)
Q_2 = outlet volumetric flow rate at exit (2)
r, θ, z = radial, tangential, and axial coordinate, respectively
R_{c1} = core radius at exit (1)
R_{c2} = core radius at exit (2)
R_{e1} = radius of exit port (1)
R_{e2} = radius of exit port (2)
R_{eo} = Reynolds number ($R_{eo}=4Q_{\text{in}}/\nu\pi D_o$)
R_o = radius of the chamber
V_{z1} = axial velocity component at exit (1)
V_{z2} = axial velocity component at exit (2)
V_{in} = total average velocity vector through the inlets
$V_{r\text{in}}$ = inlet radial velocity component
$V_{\varphi\text{in}}$ = inlet tangential velocity component

Greek Symbols

α = area ratio (A_{in}/A_o)
γ_1 = volumetric fraction at exit (1)
γ_2 = volumetric fraction at exit (2)
Γ = vortex circulation
ΔP = static pressure difference ($P_{\text{in}}-P_a$)
δ_1 = vortex decay factor for chamber (1)
δ_2 = vortex decay factor for chamber (2)
Ω_{in} = vortex strength at the inlet ($\Gamma/2\pi$)
Ω_1 = vortex strength at exit (1) ($\delta_1\Gamma/2\pi$)
Ω_2 = vortex strength at exit (2) ($\delta_2\Gamma/2\pi$)
υ = kinematics viscosity
ρ = density of the fluid
φ = angle between the total velocity vector and the tangential velocity component at the inlet (inlet angle)
χ_1 = dimensionless core size at exit (1) (R_{c1}/R_{e1})
χ_2 = dimensionless core size at exit (2) (R_{c2}/R_{e2})
β = aspect ratio (L_2/L_1)
ξ_1 = diameter ratio (R_o/R_{e1})
ξ_2 = diameter ratio (R_o/R_{e2})

References

[1] Shakespeare, W. J., and Levy, E. K., 1980, "Pressure Drop in a Confined Vortex With High Flow Rate," paper presented at the ASME Winter Annual Meeting, Chicago, IL, November.

[2] Vyas, B, and Majdalani, J., 2003, "The Bidirectional Vortex. Part 2: Viscous Core Corrections," 39th AIAA Conference and Exhibit, July 20–23.

[3] Yang, Z. Y., and Priestman, G. H., 1991, "Internal Flow Modelling of Vortex Throttles," Proc. Inst. Mech. Eng., **205**, pp. 405–413.

[4] Escudier, M. P., Bornstein, J., and Zehender, N., 1980, "Obsevations and LDA Measurements of Confined Turbulent Vortex Flow," J. Fluid Mech., **98**(1), pp. 49–63.

[5] Kreith, F., and Sonju, O. K., 1965, "The Decay of a Turbulent Swirl in a Pipe," J. Fluid Mech., **22**(2), pp. 257–271.

[6] Osami, K., 1991, "Experimental Study of Turbulent Swirling Flow in a Straight Pipe," J. Fluid Mech., **225**, pp. 445–479.

[7] Steenbergen, W., and Voskamp, J., 1998, "The Rate of Decay of Swirl in Turbulent Flow," Flow Meas. Instrum., **9**, pp. 67–78.

[8] Darmofal, D. L., Khan, R., Greitzer, E. M., and Tan, C. S., 2001, "Vortex Core Behaviour in Confined and Unconfined Geometries: A Quasi-One-Dimensional Model," J. Fluid Mech., **449**, pp. 61–84.

[9] Escudier, M., 1979, "Estimation of Pressure Loss in Ring-Type Exit Chamber," ASME J. Fluids Eng., **101**, pp. 511–516.

[10] Lam, H. C., 1993, "An Experimental Investigation and Dimensional Analysis of Confined Vortex Flows," Ph.D. thesis, Department of Mechanical Engineering, Concordia University, Montreal, Canada.

[11] Alekseenko, S. V., Kuibin, P. A., Okulov, V. L., and Shtork, S. I., 1999, "Helical Vortices in Swirl Flow," J. Fluid Mech., **382**, pp. 195–243.

[12] Vatistas, G. H., and Sakaris, P., 2000, "Pressure Drop Across a Double-Oulet Vortex Chamber," AIAA J., **17**(3), pp. 711–716.

[13] Vatistas, G. H., Lam, C., and Lin, S., 1989, "Similarity Relationship for the Core Radius and the Pressure Drop in Vortex Chambers," Can. J. Chem. Eng., **67**, pp. 540–544.

[14] Jawarneh, A., Vatistas, G. H., and Hong, H., 2005, "On the Flow Development in Jet-Driven Vortex Chambers," J. Propul. Power, **21**(3), pp. 564–570.

Axisymmetric Stagnation—Point Flow and Heat Transfer of a Viscous Fluid on a Rotating Cylinder With Time-Dependent Angular Velocity and Uniform Transpiration

A. B. Rahimi
Professor
P. O. Box No. 91775-1111,
Faculty of Engineering,
Ferdowsi University of Mashhad,
Mashhad, Iran
e-mail: rahimiab@yahoo.com

R. Saleh
Assistant Professor
Azad University of Mashhad,
P.O. Box No. 91735-413,
Mashhad, Iran

The unsteady viscous flow and heat transfer in the vicinity of an axisymmetric stagnation point of an infinite rotating circular cylinder with transpiration U_0 *are investigated when the angular velocity and wall temperature or wall heat flux all vary arbitrarily with time. The free stream is steady and with a strain rate of* Γ. *An exact solution of the Navier-Stokes equations and energy equation is derived in this problem. A reduction of these equations is obtained by the use of appropriate transformations for the most general case when the transpiration rate is also time-dependent but results are presented only for uniform values of this quantity. The general self-similar solution is obtained when the angular velocity of the cylinder and its wall temperature or its wall heat flux vary as specified time-dependent functions. In particular, the cylinder may rotate with constant speed, with exponentially increasing/decreasing angular velocity, with harmonically varying rotation speed, or with accelerating/decelerating oscillatory angular speed. For self-similar flow, the surface temperature or its surface heat flux must have the same types of behavior as the cylinder motion. For completeness, sample semi-similar solutions of the unsteady Navier-Stokes equations have been obtained numerically using a finite-difference scheme. Some of these solutions are presented for special cases when the time-dependent rotation velocity of the cylinder is, for example, a step-function. All the solutions above are presented for Reynolds numbers,* $\mathrm{Re}=\Gamma a^2/2\upsilon$, *ranging from 0.1 to 1000 for different values of Prandtl number and for selected values of dimensionless transpiration rate,* $S=U_0/\Gamma a$, *where* a *is cylinder radius and* υ *is kinematic viscosity of the fluid. Dimensionless shear stresses corresponding to all the cases increase with the increase of Reynolds number and suction rate. The maximum value of the shear stress increases with increasing oscillation frequency and amplitude. An interesting result is obtained in which a cylinder rotating with certain exponential angular velocity function and at particular value of Reynolds number is azimuthally stress-free. Heat transfer is independent of cylinder rotation and its coefficient increases with the increasing suction rate, Reynolds number, and Prandtl number. Interesting means of cooling and heating processes of cylinder surface are obtained using different rates of transpiration.*
[DOI: 10.1115/1.2375132]

Keywords: stagnation flow, time-dependent rotation, time-dependent heat transfer, transpiration, exact solution

1 Introduction

The problem of finding exact solutions of the Navier-Stokes equations is a very difficult task. This is primarily due to the fact that these equations are nonlinear. An exact solution of these equations governing the problem of two-dimensional stagnation flow against a flat plate has been given by Hiemenz [1]. Homann [2] derived an exact solution of the Navier-Stokes equations for the three-dimensional case of the axisymmetric stagnation flow against a plate. Howarth [3] and Davey [4] presented results for asymmetric cases of stagnation flow against a flat plate. The first exact solution of the problem of axisymmetric stagnation flow on an infinite circular cylinder was obtained by Wang [5]. Gorla [6–10], in a series of papers, studied the steady and unsteady flows and heat transfer over a circular cylinder in the vicinity of the stagnation-point for the cases of constant axial movement, and the special case of axial harmonic motion of a nonrotating cylinder. In more recent years, Cunning, Davis, and Weidman [11] have considered the stagnation flow problem on a rotating circular cylinder with constant angular velocity. They have also included the effects of suction and blowing in their study. Takhar, Chamkha, and Nath [12] have investigated the unsteady viscous flow in the vicinity of an axisymmetric stagnation point of an infinite circular cylinder for the particular case when both the cylinder and the free stream velocity vary inversely as a linear function of time. The study considered by Saleh and Rahimi [13] presents results for the study of axisymmetric stagnation-point

---

Contributed by the Fluids Engineering Division of ASME for publication in the JOURNAL OF FLUIDS ENGINEERING. Manuscript received April 7, 2005; final manuscript received June 9, 2006. Assoc. Editor: Malcolm J. Andrews.

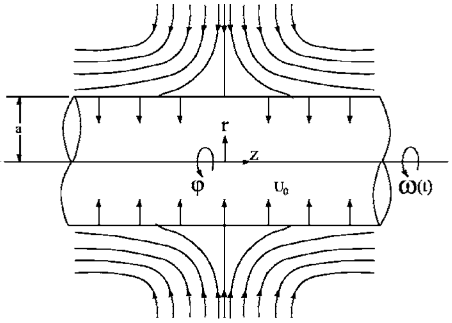

Fig. 1 Schematic diagram of a rotating cylinder under radial stagnation flow in the fixed cylindrical coordinate system $(\boldsymbol{r},\boldsymbol{\varphi},\boldsymbol{z})$

flow and heat transfer of a viscous fluid on a moving cylinder with time-dependent axial velocity and uniform transpiration.

The effects of cylinder rotation with time-dependent angular velocity and time-dependent heat transfer along with transpiration, perhaps of interest in cooling and centrifugal processes in industry, concerned with accelerating phases of rocket motors, and calcination of cement, etc. have not yet been investigated. Our motivation is originally to produce friction-less situations in fluids and insulated surfaces in heat transfer by means of certain types of movements and temperature difference. Besides, our study generalizes the problem of stagnation-point flow and heat transfer of a fluid on a rotating cylinder.

In the present analysis, the unsteady viscous flow and heat transfer in the vicinity of an axisymmetric stagnation point of an infinite rotating cylinder with uniform transpiration is considered when the angular velocity varies arbitrarily with time, though the reduction of the Navier-Stokes equations and the energy equation is obtained for the more general case of time-dependent transpiration rate. An exact solution of the Navier-stokes equations and the energy equation is obtained. The general self-similar solution is obtained when the angular velocity of the cylinder and its surface temperature or heat flux vary in a prescribed manner. The cylinder may perform different types of motion: It may rotate with constant speed (i.e., steady state cooling processes in industry, etc.), with exponentially increasing/decreasing angular velocity (i.e., start up and stopping stages of centrifugal processes in industry, etc.), with harmonically varying rotation speed, or with accelerating/decelerating oscillatory angular speed (sinusoidal blenders in industry, etc.). The cylinder surface temperature and its surface heat flux may have the same behavior as the cylinder motion.

For different forms of azimuthal component of velocity, sample distribution of shear stresses, and temperature fields are presented for Reynolds numbers ranging from 0.1 to 1000, and different values of Prandtl numbers, Pr, and selected values of uniform suction and blowing rates. Particular cases of these results are compared with existing results of Wang [5], Gorla [6], and Cunning, Davis, and Weidman [11], correspondingly. For completeness, some semi-similar solutions of the Navier-Stokes equations are obtained and result, for example, of cylinder rotation in the form of a step-function is presented for selected values of flow parameters.

2 Problem Formulation

We consider the laminar unsteady incompressible flow and heat transfer of a viscous fluid in the neighborhood of an axisymmetric stagnation-point of an infinite rotating circular cylinder with uniform normal transpiration U_0 at its surface, where $U_0>0$ corresponds to suction into the cylinder, though the formulation of the problem is for the more general case of time-dependent transpiration rate. The flow configuration is shown in Fig. 1 in cylindrical coordinates (r,φ,z) with corresponding velocity components (u,v,w). The cylinder rotates with time-dependent angular velocity ω and the wall temperature or the wall heat flux is also a function of time. A radial external flow of strain rate (strength) Γ impinges on the cylinder of radius a, centered at r=0. The unsteady Navier-Stokes and energy equations in cylindrical polar coordinates governing the axisymmetric flow and heat transfer are given by [6,8,10,5]:

Mass

$$\frac{\partial}{\partial r}(ru)+r\frac{\partial w}{\partial z}=0 \tag{1}$$

Momentum

$$\frac{\partial u}{\partial t}+u\frac{\partial u}{\partial r}-\frac{v^2}{r}+w\frac{\partial u}{\partial z}=-\frac{1}{\rho}\frac{\partial p}{\partial r}+\upsilon\left(\frac{\partial^2 u}{\partial r^2}+\frac{1}{r}\frac{\partial u}{\partial r}-\frac{u}{r^2}+\frac{\partial^2 u}{\partial z^2}\right) \tag{2}$$

$$\frac{\partial v}{\partial t}+u\frac{\partial v}{\partial r}+\frac{uv}{r}+w\frac{\partial v}{\partial z}=\upsilon\left(\frac{\partial^2 v}{\partial r^2}+\frac{1}{r}\frac{\partial v}{\partial r}-\frac{v}{r^2}+\frac{\partial^2 v}{\partial z^2}\right) \tag{3}$$

$$\frac{\partial w}{\partial t}+u\frac{\partial w}{\partial r}+w\frac{\partial w}{\partial z}=-\frac{1}{\rho}\frac{\partial p}{\partial z}+\upsilon\left(\frac{\partial^2 w}{\partial r^2}+\frac{1}{r}\frac{\partial w}{\partial r}+\frac{\partial^2 w}{\partial z^2}\right) \tag{4}$$

Energy

$$\frac{\partial T}{\partial t}+u\frac{\partial T}{\partial r}+w\frac{\partial T}{\partial z}=\alpha\left[\frac{1}{r}\frac{\partial}{\partial r}\left(r\frac{\partial T}{\partial r}\right)+\frac{\partial^2 T}{\partial z^2}\right] \tag{5}$$

where p, ρ, υ, and α are the fluid pressure, density, kinematic viscosity, and thermal diffusivity. The boundary conditions and the initial conditions for the velocity field are

$$r=a:\quad u=-U_0(t),\quad v=a\,.\,\omega(t),\quad w=0 \tag{6}$$

$$r\rightarrow\infty:\frac{\partial u}{\partial r}=-\Gamma,\quad \lim_{r\rightarrow\infty} rv=0,\quad w=2\Gamma z \tag{7}$$

$$t=0:\quad u(r,t)=u(r)_{\text{steady-state}},\quad v(r,t)=v(r)_{\text{steady-state}},$$

$$w(r,t)=w(r)_{\text{steady-state}} \tag{8}$$

Here, relations (6) are transpiration and no-slip boundary conditions on the cylinder wall, where $U_0(t)$ is the transpiration rate and $\omega(t)$ is the angular velocity of the cylinder. Relations (7) show that the viscous flow solution approaches, in a manner analogous to the Hiemenz flow, the potential stagnation field as $r\rightarrow\infty$, Ref. [11]. This is imposing the condition of zero circulation at infinity on the swirl velocity of the stagnation flow.

For the temperature field we have

$$r=a:\quad (i)T=T_w(t)\qquad \text{for defined wall temperature}$$

$$(ii)\frac{\partial T}{\partial r}=-\frac{q_w(t)}{k}\quad \text{for defined wall heat flux}$$

$$r\rightarrow\infty:T\rightarrow T_\infty$$

$$t=0:T(r,t)=T(r)_{\text{steady-state}} \tag{9}$$

where k is the thermal conductivity of the fluid and $T_w(t)$ and $q_w(t)$ are temperature and heat flux at the wall cylinder, respectively.

A reduction of the Navier-Stokes equations is obtained by applying the following transformations:

$$u=-\Gamma\frac{a}{\sqrt{\eta}}f(\eta,\tau),\quad v=+\Gamma\frac{a}{\sqrt{\eta}}G(\eta,\tau),\quad w=2\Gamma z\frac{\partial f(\eta,\tau)}{\partial\eta},$$

$$p=\rho\Gamma^2a^2P \tag{10}$$

where $\tau=2\Gamma t$ and $\eta=(r/a)^2$ are dimensionless time and radial variables. Transformations (10) satisfy (1) automatically and their insertion into Eq. (2) yields a differential equation in terms of $f(\eta,\tau)$ as following:

$$\eta\frac{\partial^3 f}{\partial\eta^3}+\frac{\partial^2 f}{\partial\eta^2}+\mathrm{Re}\left[1-\left(\frac{\partial f}{\partial\eta}\right)^2+f\frac{\partial^2 f}{\partial\eta^2}-\frac{\partial^2 f}{\partial\eta\,\partial\tau}\right]=0 \tag{11}$$

where $\mathrm{Re}=\Gamma a^2/2\nu$ is the Reynolds number. From conditions (6) and (7), the boundary conditions for (11) are

$$\eta=1{:}f=S(\tau),\quad \frac{\partial f}{\partial\eta}=0$$

$$\eta\to\infty:\frac{\partial f}{\partial\eta}=1 \tag{12}$$

in which, $S=U_0/\Gamma a$ is the dimensionless wall-transpiration rate.

For the sake of brevity, only results for $S(\tau)$=constant are shown in this paper. For $S(\tau)$=constant, none of the boundary conditions of Eq. (11) are function of time and assuming steady-state initial conditions for this equation, we have

$$\tau=0\to\frac{\partial^2 f}{\partial\eta\,\partial\tau}=0$$

Therefore in this case $f(\eta,\tau)=f(\eta)$ and Eq. (11) is reduced to the following form:

$$\eta f'''+f''+\mathrm{Re}[1-(f')^2+ff'']=0 \tag{13}$$

where prime denotes differentiation with respect to η.

Insertion of transformations (10) into (3) and (4) yields a differential equation in terms of $f(\eta)$ and $G(\eta,\tau)$ and an expression for the pressure

$$\eta\frac{\partial^2 G}{\partial\eta^2}+\mathrm{Re}\left[f\frac{\partial G}{\partial\eta}-\frac{\partial G}{\partial\tau}\right]=0 \tag{14}$$

$$P-P_o=-\left[\frac{f^2}{2\eta}+\frac{1}{Re}f'+2\left(\frac{z}{a}\right)^2-\frac{1}{2\Gamma^2}\int_1^\eta\frac{G^2(\xi)}{\xi^2}d\xi\right] \tag{15}$$

From conditions (6)–(8), the boundary and initial conditions for (14) are as following:

$$\eta=1:\quad G=\omega(\tau)/\Gamma=\Omega(\tau)$$

$$\eta\to\infty:\quad G=0$$

$$t=0:\quad G(\eta,\tau)=G(\eta)_{\text{steady-state}} \tag{16}$$

To transform the energy equation into a nondimensional form for the case of defined wall temperature, we introduce

$$\Theta=\frac{T(\eta,\tau)-T_\infty}{T_w(\tau)-T_\infty} \tag{17}$$

Making use of (10) and (17), the energy equation may be written as

$$\eta\frac{\partial^2\Theta}{\partial\eta^2}+\frac{\partial\Theta}{\partial\eta}+\mathrm{Re}\,\mathrm{Pr}\left(f\frac{\partial\Theta}{\partial\eta}-\frac{\partial\Theta}{\partial\tau}-\frac{dT_w/d\tau}{T_w-T_\infty}\Theta\right)=0 \tag{18}$$

with the boundary and initial conditions as

$$\Theta(1,\tau)=1,\quad \Theta(\infty,\tau)=0$$

$$\Theta(\eta,0)=\Theta(\eta)_{\text{steady-state}} \tag{19}$$

For the case of defined wall heat flux, we introduce

$$\Theta=\frac{T(\eta,\tau)-T_\infty}{aq_w(\tau)/2k} \tag{20}$$

Now making use of (10) and (20), the energy equation can be written as

$$\eta\frac{\partial^2\Theta}{\partial\eta^2}+\frac{\partial\Theta}{\partial\eta}+\mathrm{Re}\,\mathrm{Pr}\left(f\frac{\partial\Theta}{\partial\eta}-\frac{\partial\Theta}{\partial\tau}-\frac{dq_w/d\tau}{q_w}\Theta\right)=0 \tag{21}$$

with the boundary and initial conditions as

$$\frac{\partial\Theta(1,\tau)}{\partial\eta}=-1,\quad \Theta(\infty,\tau)=0$$

$$\Theta(\eta,0)=\Theta(\eta)_{\text{staedy-state}} \tag{22}$$

Here, Equations (13), (14), and (18) or (21) are for different forms of S, $\omega(\tau)$, $T_w(\tau)$, or $q_w(\tau)$ functions and have been solved numerically with Re and Pr as parameters.

In what follows, first the self-similar equations and the exact solutions of some particular $\omega(\tau)$, $T_w(\tau)$, or $q_w(\tau)$ functions are presented and then, for completeness, the semi-similar equations of $\omega(\tau)$, $T_w(\tau)$, or $q_w(\tau)$ functions are obtained and one example of numerical solution for a given value of $\Omega(\tau)$is presented.

3 Self-Similar Equations

Equations (14) and (18) or (21) can be reduced to ordinary differential equations if we assume that the function $G(\eta,\tau)$ in (14) and $\Theta(\eta,\tau)$ in (18) or (21) are separable as

$$G(\eta,\tau)=g(\eta)\,.\,\psi(\tau)$$

$$\Theta(\eta,\tau)=\theta(\eta)\,.\,Q(\tau) \tag{23}$$

Substituting these separation of variables into (14) and (18) or (21), correspondingly gives

$$\eta\frac{g''}{g}+\mathrm{Re}\,f\frac{g'}{g}=\mathrm{Re}\frac{d\psi(\tau)/d\tau}{\psi(\tau)} \tag{24}$$

$$\eta\frac{\theta''}{\theta}+\frac{\theta'}{\theta}+\mathrm{Re}\,\mathrm{Pr}(f\theta'/\theta)=\mathrm{Re}\,\mathrm{Pr}\left(\frac{dQ/d\tau}{Q}+\frac{dT_w/d\tau}{T_w-T_\infty}\right) \tag{25}$$

or for defined wall heat flux

$$\eta\frac{\theta''}{\theta}+\frac{\theta'}{\theta}+\mathrm{Re}\,\mathrm{Pr}(f\theta'/\theta)=\mathrm{Re}\,\mathrm{Pr}\left(\frac{dQ/d\tau}{Q}+\frac{dq_w/d\tau}{q_w}\right) \tag{26}$$

where again prime denotes differentiation with respect to η. Solutions to the differential equations in (24) and (25) or (26)) with τ as an independent variable are as the following:

$$\psi(\tau)=b\exp[(\lambda+i\beta)\tau] \tag{27}$$

$$Q(\tau)=\frac{c\exp[(\gamma+i\delta)\tau]}{T_w(\tau)-T_\infty} \tag{28}$$

or for defined wall heat flux

$$Q(\tau)=\frac{c\exp[(\gamma+i\delta)\tau]}{q_w(\tau)} \tag{29}$$

Here, $i=\sqrt{-1}$ and b, λ, and β and also c, γ, and δ are constants. The boundary conditions are

$$G(1,\tau)=\Omega(\tau)=\psi(\tau)g(1)\to\psi(\tau)=\Omega(\tau)\text{ and }g(1)=1,\text{ gives}$$

$$\Omega(\tau)=b\exp[(\lambda+i\beta)\tau] \tag{30}$$

$$G(\infty,\tau)=0=\psi(\tau)g(\infty)\to g(\infty)=0 \tag{31}$$

For the above-defined wall temperature and wall heat flux, respectively, one obtains

$$\Theta(1,\tau) = 1 = \theta(1)Q(\tau) \rightarrow \theta(1) = 1, Q(\tau) = 1 \rightarrow T_w(\tau) - T_\infty = c\,\exp[(\gamma + i\delta)\tau]$$

$$\frac{\partial\Theta(1,\tau)}{\partial\eta} = -1 = \theta'(1)Q(\tau) \rightarrow \theta'(1) = -1, Q(\tau) = 1 \rightarrow q_w(\tau) = c\,\exp[(\gamma + i\delta)\tau] \tag{32}$$

$$\Theta(\infty,\tau) = 0 = \theta(\infty)Q(\tau) \rightarrow \theta(\infty) = 0 \tag{33}$$

Substituting the solutions (27), (28), or (29) into the differential equations in (24) and (25) or (26) with η as independent variable results in

$$\eta g'' + \mathrm{Re}[fg' - \lambda g - i\beta g] = 0 \tag{34}$$

$$\eta\theta'' + \theta' + \mathrm{Re}\,\mathrm{Pr}(f\theta' - \gamma\theta - i\delta\theta) = 0 \tag{35}$$

Note that, in (30) $b=0$ corresponds to the case of nonrotating cylinder, as of Wang [5]. If $b \neq 0$ and $\lambda=\beta=0$, (30) gives the case of a uniformly rotating cylinder with constant angular velocity, Cunning et al. [11]. $b \neq 0$, $\lambda \neq 0$ and $\beta=0$, corresponds to the case of rotating cylinder with an exponential angular velocity. $b \neq 0$, $\beta \neq 0$, and $\lambda=0$, corresponds to the case of pure harmonic rotation of the cylinder. The case of nonzero b, λ, and β is the most general case which is considered in this paper. If $b=0$ and $c \neq 0$, $\gamma=\delta=0$, Eq. (32) correspond to the result of Gorla [6] which is for a nonrotating cylinder. Since the heat transfer is axisymmetric in φ direction, it is independent of cylinder rotation and therefore this result would be the same as Cunning et al. [11] problem in which the cylinder rotates with a constant angular rotation. Other combinations of values of c, γ, and δ in Eqs. (32) give the different time-dependent wall temperature and wall heat flux functions.

To obtain solutions of Eqs. (34) and (35), it is assumed that the functions $g(\eta)$ and $\theta(\eta)$ are complex functions as

$$g(\eta) = g_1(\eta) + ig_2(\eta) \tag{36}$$

$$\theta(\eta) = \theta_1(\eta) + i\theta_2(\eta) \tag{37}$$

Substituting (36) and (37) into (34) and (35), the following coupled systems of differential equations are obtained:

$$\begin{aligned} &\eta g_1'' + \mathrm{Re}(fg_1' - \lambda g_1 + \beta g_2) = 0 \\ &\eta g_2'' + \mathrm{Re}(fg_2' - \lambda g_2 - \beta g_1) = 0 \end{aligned} \tag{38}$$

$$\begin{aligned} &\eta\theta_1'' + \theta_1' + \mathrm{Re}\,\mathrm{Pr}(f\theta_1' - \gamma\theta_1 + \delta\theta_2) = 0 \\ &\eta\theta_2'' + \theta_2' + \mathrm{Re}\,\mathrm{Pr}(f\theta_2' - \gamma\theta_2 - \delta\theta_1) = 0 \end{aligned} \tag{39}$$

Considering the boundary conditions (6), (7), and (9), the boundary conditions for functions f, g, and θ become

$$\eta = 1: \quad f = 0, \quad f' = 0, \quad g = 1, \quad \theta = 1 (or\ \theta' = -1) \tag{40}$$

$$\eta \rightarrow \infty : f' = 1, \quad g = 0, \quad \theta = 0 \tag{41}$$

Hence, the boundary conditions on functions g_1, g_2 and θ_1, θ_2 are

$$\eta = 1: \quad g_1 = 1, \quad g_2 = 0, \quad \theta_1 = 1 (or\ \theta_1' = -1), \quad \theta_2 = 0 \tag{42}$$

$$\eta \rightarrow \infty : g_1 = 0, \quad g_2 = 0, \quad \theta_1 = 0, \quad \theta_2 = 0 \tag{43}$$

The coupled system of Eqs. (38) and (39) along with boundary conditions (42) and (43) have been solved by using the fourth-order Runge-Kutta method of numerical integration along with a shooting method, Presss et al. [14]. Using this method, the initial values of $g_1'(1)$, $g_2'(1)$, θ_1' (or $\theta_1(1)$) and $\theta_2'(1)$ were guessed and the integration was repeated until convergence was obtained. The values of $g_2(\eta)=0$ and $\theta_2(\eta)=0$ were assumed initially and then by repeating the integration of these two systems of equations, final values of $g_1(\eta)$, $g_2(\eta)$, $\theta_1(\eta)$, and $\theta_2(\eta)$ were obtained.

The angular velocity is

$$\omega(\tau) = b\,\exp(\lambda\tau)[\cos(\beta\tau) + i\,\sin(\beta\tau)] \tag{44}$$

and thus, the azimuthal component of velocity from definition (10) becomes

$$v(\eta,\tau) = \frac{ab}{\sqrt{\eta}}\exp(\lambda\tau)[\{g_1(\eta)\cos(\beta\tau) - g_2(\eta)\sin(\beta\tau)\} + i\{g_1(\eta)\sin(\beta\tau) + g_2(\eta)\cos(\beta\tau)\}] \tag{45}$$

4 Semi-Similar Equations

Equation (12) has been solved by Gorla but it is repeated here for different values of Re and S. Equations (14), (18), and (21) can be solved directly for any chosen $\Omega(\tau)$, $T_w(\tau)$, and $q_w(\tau)$ functions. The solutions obtained this way, are called semi-similar solutions. These equations along with boundary conditions (16), (19), and (22) were solved by using a central finite difference method which lead to a tri-diagonal matrix. Assuming steady-state for $\tau \leqslant 0$, the solution starts from $\Omega(0)$, $T_w(0)$, or $q_w(0)$ and marching through time, time-dependent solutions for $\tau > 0$ were obtained. Sample angular velocity profiles will be presented in later sections.

5 Shear Stress and Heat Transfer Coefficient

The shear stress at the cylinder surface is calculated from [11]

$$\sigma = \mu\left[r\frac{\partial}{\partial r}\left(\frac{v}{r}\right)\hat{e}_\varphi + \frac{\partial w}{\partial r}\hat{e}_z\right] \tag{46}$$

where μ is the fluid viscosity. Using definition (10), the shear stress at the cylinder surface for semisimilar solutions becomes

$$\sigma = 2\Gamma\mu\left[\frac{\partial G(1,\tau)}{\partial\eta} - \Omega(\tau)\right]\hat{e}_\varphi + 4\mu\frac{\Gamma z}{a}f''(1)\hat{e}_z \tag{47}$$

Thus the axial and azimuthal shear stress components are proportional to $f''(1)$, which has been presented in Ref. [11], and $(\partial G(1,\tau)/\partial\eta - \Omega(\tau))$, respectively. Azimuthal surface shear stress for self-similar solutions is presented by the following relation:

$$\sigma_\varphi = \sigma_{\varphi_1} + i\sigma_{\varphi_2} = 2\mu b\,\exp(\lambda\tau)[\{\cos(\beta\tau)(g_1'(1) - 1) - \sin(\beta\tau)g_2'(1)\} + i\{\sin(\beta\tau)(g_1'(1) - 1) + \cos(\beta\tau)g_2'(1)\}] \tag{48}$$

Some numerical values of real part of σ_φ will be presented later for few examples of angular velocities. Of course, it is noted that the real and imaginary parts of this quantity are actually the same but with a phase difference of $\pi/2$.

The local heat transfer coefficient and rate of heat transfer for defined wall temperature case are given by

$$h = \frac{q_w}{T_w - T_\infty} = \frac{-k\left(\frac{\partial T}{\partial r}\right)_{r=a}}{T_w - T_\infty} = -\frac{2k}{a}\frac{\partial\Theta(1,\tau)}{\partial\eta} \text{ for semi-similar case}$$

$$h = -\frac{2k}{a}[\theta_1'(1) + i\theta_2'(1)] \text{ for self-similar case} \tag{49}$$

or in terms of Nusselt number

$$Nu = \frac{ha}{2k} = Nu_r + iNu_i = -[\theta_1'(1) + i\theta_2'(1)]$$

$$q_w = -\frac{2k}{a}\frac{\partial\Theta(1,\tau)}{\partial\eta}(T_w - T_\infty) \text{ for semi-similar case}$$

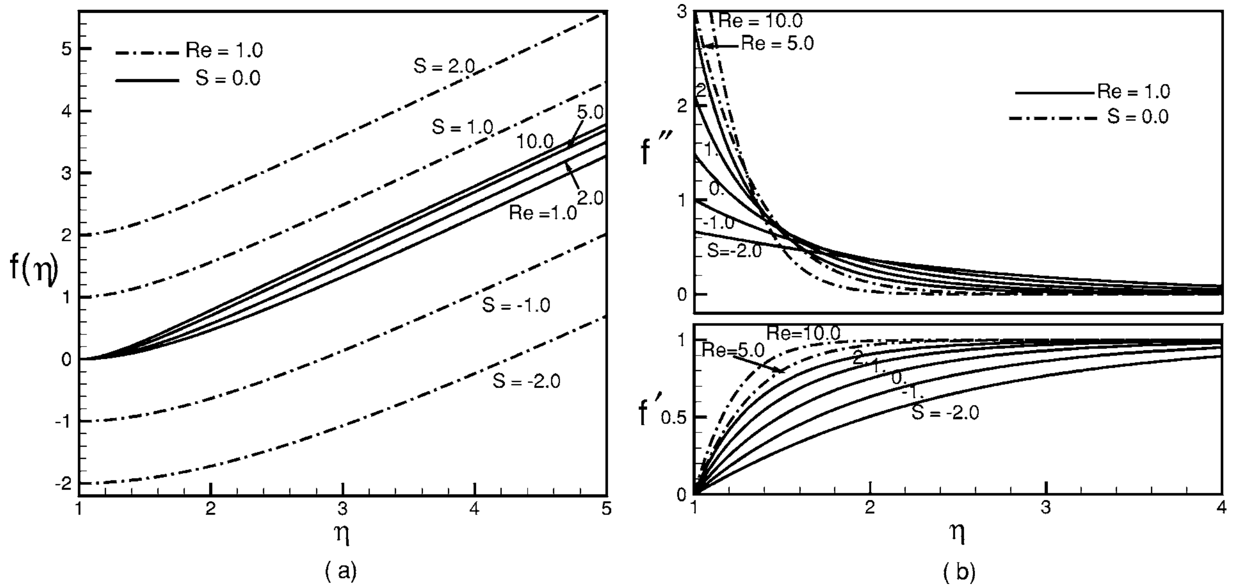

Fig. 2 Sample profiles of (*a*) *f*(*η*) function, (*b*) *f*′ and *f*′ functions for selected values of suction rate and Reynolds number

$$q_w = -\frac{2k}{a} c \exp(\gamma\tau)[\{\theta_1'(1)\cos(\delta\tau) - \theta_2'(1)\sin(\delta\tau)\} + i\{\theta_1'(1)\sin(\delta\tau) + \theta_2'(1)\cos(\delta\tau)\}] \text{ for self-similar case} \tag{50}$$

And for defined wall heat flux case

$$h = \frac{q_w}{T_w - T_\infty} = \frac{2k}{a}\frac{1}{\Theta(1,\tau)} \text{ for semi-similar case}$$

$$h = \frac{2k}{a}\left(\frac{1}{\theta_1(1) + i\theta_2(1)}\right) \text{ for self-similar case} \tag{51}$$

or in terms of Nusselt number

$$\mathrm{Nu} = \frac{ha}{2k} = \mathrm{Nu}_r + i\mathrm{Nu}_i = \left(\frac{1}{\theta_1(1) + i\theta_2(1)}\right)$$

$$(T_w - T_\infty) = \frac{a}{2k}\Theta(1,\tau)q_w \text{ for semi-similar}$$

$$(T_w - T_\infty) = \frac{a}{2k} c \exp(\gamma\tau)[\{\theta_1(1)\cos(\delta\tau) - \theta_2(1)\sin(\delta\tau)\} + i\{\theta_1(1)\sin(\delta\tau) + \theta_2(1)\cos(\delta\tau)\}] \text{ for self-similar case} \tag{52}$$

From (49) and (51), it is seen clearly that for self-similar cases, the local heat transfer coefficient is not a function of time contrary to the fact that wall temperature and wall heat flux are time-dependent.

6 Presentation of Results

6.1 Fluid Flow Results. In this section, only the real part of the solution of the self-similar Eqs. (34) and (35) and the semi-similar Eq. (14) along with surface shear-stresses and heat transfer coefficient for different functions of angular velocity and prescribed values of wall temperature or wall heat flux, and selected values of suction and blowing rates are presented. Also, the real part of azimuthal component of velocity, $v(\eta,\tau)$, for self-similar case is given.

Sample profiles of the f function in terms of η are shown in Fig. 2, for selected values of transpiration rate and Reynolds number. This function, for the first time, was solved by Wang [5] for the case of $S=0$ and later was presented by Cunning [11] for selected values of suction rate. It is evident from this figure that as Reynolds number increases the f function increases a little and approaches the inviscid solution in the limit. In this figure the dash-dot curves present the variations of f function in terms of transpiration rate in which negative S is blowing rate and positive S is the suction rate. Sample profiles of the f' and f'' functions in terms of η are depicted in Fig. 2(*b*), for selected values of transpiration rate and Reynolds number. From this figure, the initial slope of the f function ($f''(1)$) increases with increasing Reynolds number and transpiration rate and this causes the solution to approach faster to one in the limit. From relations (10) and (47), f' presents the velocity profile in z direction and $f''(1)$ is the value of wall shear stress in this direction. Therefore, the increase of suction rate and Reynolds number increases the wall shear stress in z direction and on the other hand causes that the value of fluid velocity in this direction approaches its value in inviscid flow, rapidly. In fact the increase of suction rate and Reynolds number decrease the thickness of the boundary layer.

Sample profiles of the $g(\eta)$ function for $\Omega(\tau)$ in exponential form for accelerating and decelerating case at $\mathrm{Re}=1.0$ are presented in Fig. 3(*a*), for selected values of transpiration rate. It is interesting to note that as λ or suction rate increases, the depth of the diffusion of the fluid velocity field decreases, and it increases as λ or suction rate decreases. For $\lambda<0$, at any rate of suction and for the absolute value of λ greater than a certain value, the fluid velocity in the vicinity of the cylinder cannot decrease with the same rate as the cylinder rotation velocity and, therefore, in this region the fluid velocity is greater than the cylinder velocity. Note, $\lambda=0$ indicates the case of a rotating cylinder with constant angular velocity, Ref. [11]. Sample profiles of $g_1(\eta)$ function for $\Omega(\tau)$ for accelerating and decelerating oscillatory motion and pure harmonic motion of the cylinder at $\mathrm{Re}=1000$ displayed in Fig. 3(*b*) for transpiration rate of $S=0$ show that like the exponential angular velocity case, the depth of the diffusion of the fluid velocity field for $\lambda>0$ is less and for $\lambda<0$ is more than that for the case of $\lambda=0$. Further, it is concluded that the case of $\lambda=\beta=0$ is the same as in Ref. [11] and clearly the imaginary part of $g(\eta)$ is zero. As in the foregoing discussion, we observe that the thinning of the difussion of the velocity field with increasing values of β is

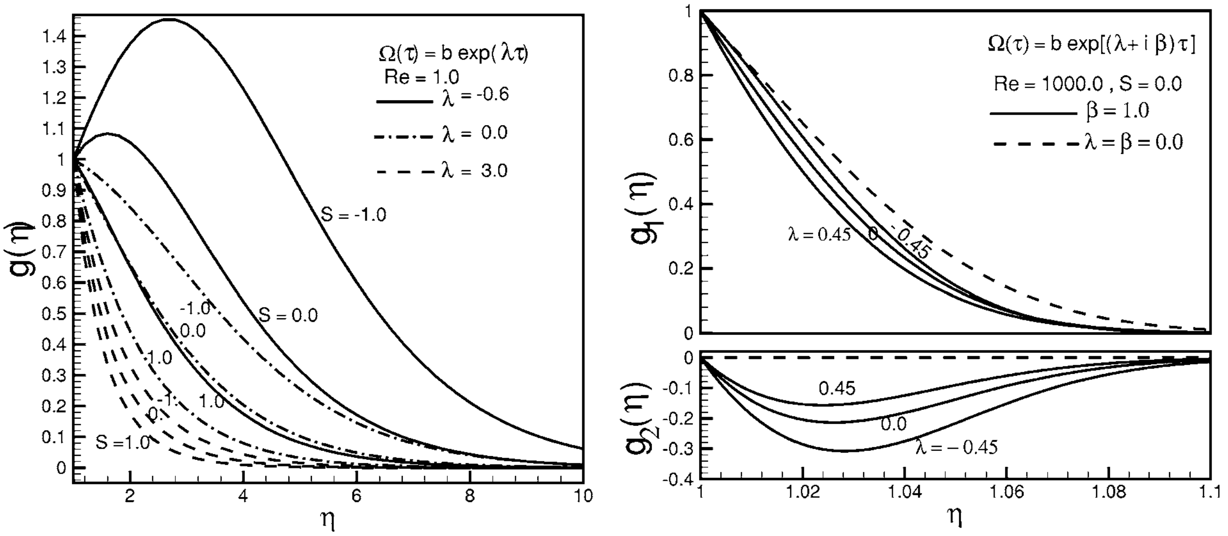

(a)

(b)

Fig. 3 Sample profiles of $g(\eta)$ for cylinder with (*a*) exponential angular velocity for Re=1 and selected values of suction and λ, (*b*) accelerating and decelerating oscillatory motion for Re=1000, S=0 and selected values of λ and β

evident.

Sample profiles of the real part of azimuthal component of velocity for pure harmonic motion of the cylinder for selected time variation ($\beta\tau$) are given in Fig. 4(*a*), at Re=1000 and S=0. Here, the real azimuthal velocity component is shown for a complete period of oscillation. Figure 4(*b*) presents the semi-similar solutions for step-function angular velocity in which the function $G(\eta,\tau)$ is shown in terms of η and for different nondimensional time values at Re=0.1 and transpiration rate S=0. Here, the solution of two step-functions is shown simultaneously. In the first one the angular velocity of the cylinder at $\tau<0$ is equal to zero and at $\tau\geqslant 0$ its value becomes one suddenly. But in the second function the angular velocity of the cylinder at $\tau<0$ is one and at $\tau\geqslant 0$ becomes zero, suddenly. These results are given here for the sake of completeness.

The azimuthal shear stress on the surface of the cylinder for exponential angular velocity in terms of acceleration rate at Re =0.1 and 1000 is displayed in Figure 5(*a*) for selected values of transpiration rate. Results for Re=0.1 and for Re=1000 are read from the left and right coordinates, correspondingly. Note that the slope of the curves decreases with increasing λ, meaning that the sensitivity of shear stress with respect to variation of λ decreases as λ increases. Further, λ=0 corresponds to the same shear stress value as the case in Ref. [11]. Comparing results for Re=0.1 and Re=1000, the absolute value of the azimuthal shear stress increases with increasing Reynolds number. Also from this figure, the absolute value of the azimuthal shear stress increases with increasing suction rate. The practical application of this interesting result is that by providing blowing on the surface of a cylinder, reduction of resistance against its rotation inside a fluid can be achieved. It is also interesting to note that at any Reynolds number and suction rate, there is a particular value of negative λ, (for example λ=−0.4,Re=1000) for which the value of shear stress is zero. This interesting result opens the way for an analysis into

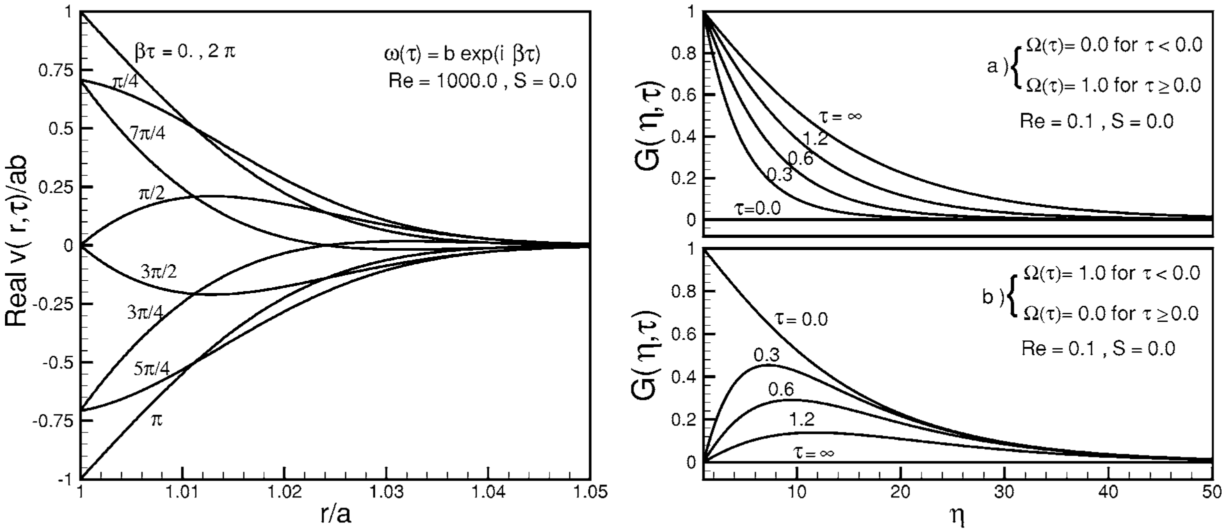

(a)

(b)

Fig. 4 (*a*) Real part of azimuthal velocity in terms of time for cylinder with harmonic rotation, for Re=1000, s=0. (*b*) Sample profiles of $G(\eta,\tau)$ for step-function angular velocity for selected values of time at Re=0.1, s=0.

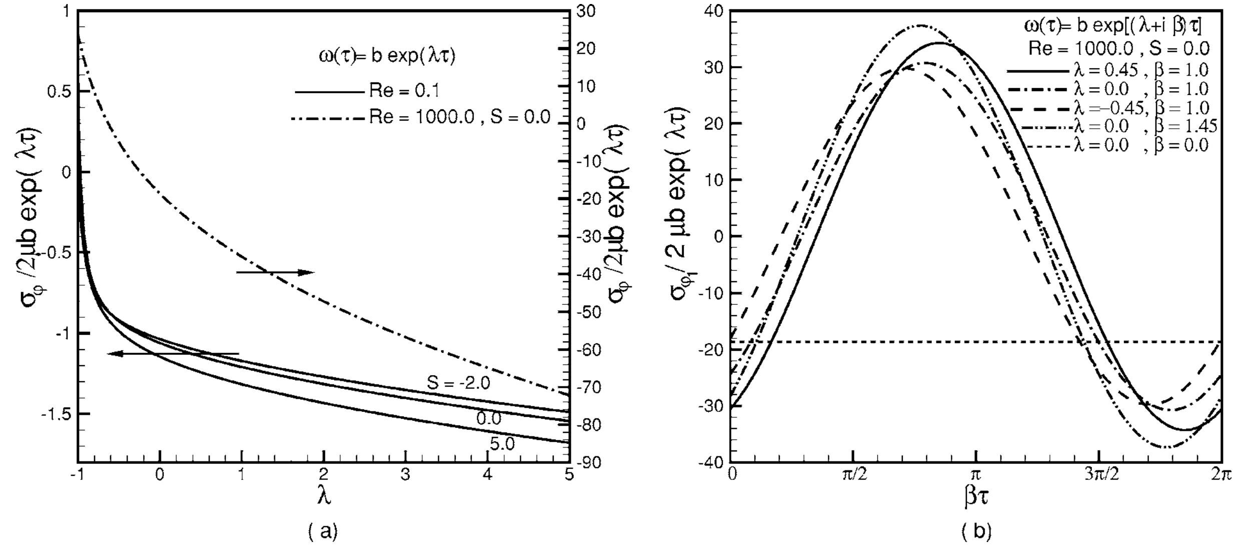

Fig. 5 (***a***) **Azimuthal shear stress component for cylinder with exponential angular velocity.** (***b***) **Real part of azimuthal shear stress component for cylinder with accelerating and decelerating oscillatory motion, for Re=1000 and** ***s*****=0.**

flows for which a cylinder spinning with a decreasing velocity in an exponential manner is azimuthally stress-free for certain combinations of Reynolds number, λ, and suction rate. The real part of azimuthal shear stress component on the surface of the cylinder with harmonic rotation and with accelerating and decelerating oscillatory motions at Re=1000 is presented in Figure 5(*b*), for transpiration rate $S=0$. This shear stress is for a complete period between 0 and 2π. It can be seen that as the frequency of the oscillation increases, the maximum of the absolute value of the shear stress increases, and $\beta=0$ corresponds to the case of constant angular velocity in which the imaginary part of the azimuthal shear-stress is zero and its real part is a constant, as in Ref. [11]. Comparing Figs. 4(*a*) and 5(*b*), it is concluded that the real part of azimuthal shear-stress and azimuthal velocity are in different phases. This figure also shows that the maximum of the absolute value of the real part of azimuthal shear-stress for $\lambda > 0$ is more and for $\lambda < 0$ is less than the case of pure oscillation. Also note that the phase-difference of shear-stress and azimuthal velocity decreases with increasing λ.

6.2 Heat Transfer Results. Sample profiles of the $\theta(\eta)$ function for wall temperature and wall heat flux, both varying exponentially with time are presented in Fig. 6, for selected values of Reynolds number, Prandtl number, and transpiration rate. From Fig. 6(*a*), it is seen that as the rate of exponential function or suction rate increases, the depth of diffusion of the temperature field decreases and thus the heat transfer coefficient increases. From Fig. 6(*b*), it is noted that as the rate of exponential function increases, wall temperature and its depth of diffusion decreases. In Fig. 6(*a*) for $\gamma < 0$, as the absolute value of γ increases, the fluid in the vicinity of the cylinder is not cooled as fast as the cylinder wall and, therefore, the fluid temperature here is greater than the

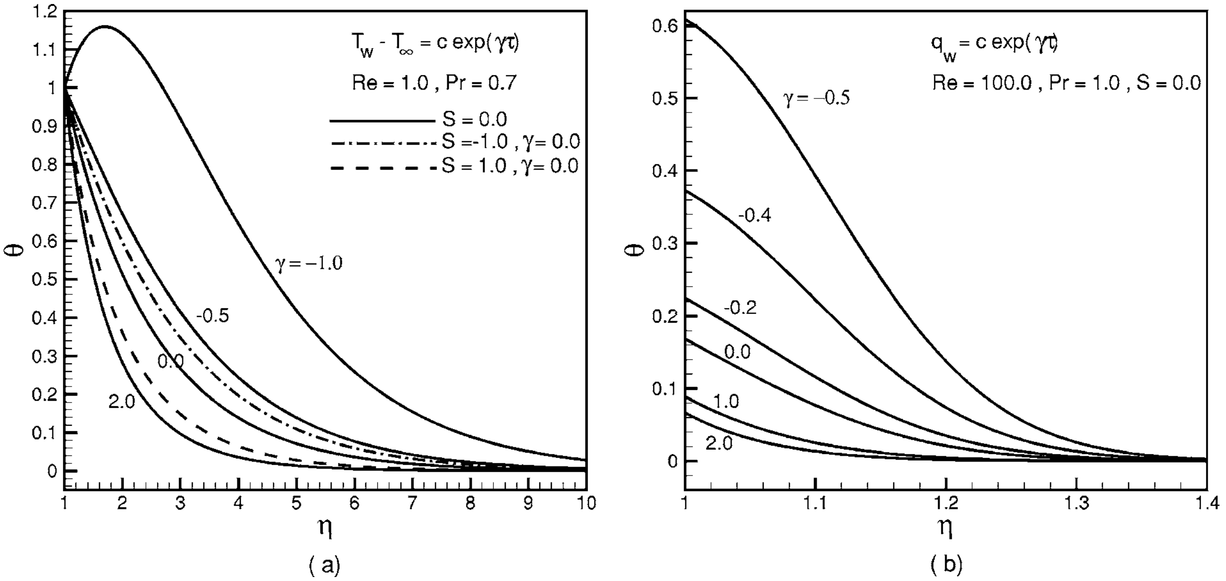

Fig. 6 Sample profiles of $\theta(\eta)$ **for,** (***a***) **wall temperature,** (***b***) **wall heat flux, varying exponentially with time for selected values of Re, Pr, and suction rate**

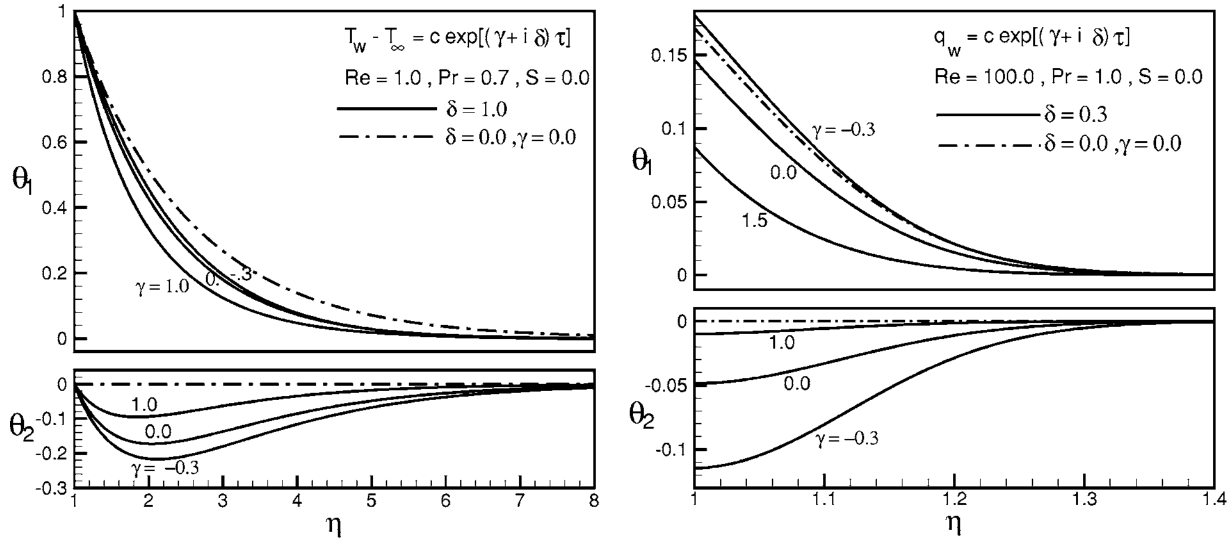

(a) (b)

Fig. 7 Sample profiles of $\theta_1(\eta)$ for, (*a*) wall temperature, (*b*) wall heat flux, varying with accelerating and decelerating oscillatory function of time for $s=0$ and selected values of Re, Pr, γ, and δ

wall temperature. It is interesting to note that for a particular negative value of γ, the slope of temperature on the surface is zero and, therefore, there is no heat transfer. From both of these figures and $\gamma=0$, the results of Ref. [6] are obtained.

Sample profiles of $\theta_1(\eta)$ function for wall temperature and wall heat flux, both varying with accelerating and decelerating oscillatory functions of time with different rates for transpiration rate $S=0$ are given in Fig. 7 for selected values of Reynolds number and Prandtl number. It is noted in Fig. 7(*a*) that as the oscillation frequency increases, the initial slope of $\theta_1(\eta)$ increases. Further, as γ increases, the depth of the $\theta_1(\eta)$ decreases. From Fig. 7(*b*), as oscillation frequency increases, $\theta_1(\eta)$ and its depth of diffusion decrease. Also, as γ increases, the absolute value of $\theta_1(\eta)$ and its depth of diffusion decrease. From both of these figures and for $\delta=0$, the results of Ref. [6] are obtained.

Sample profiles of the $\theta_1(\eta)$ function for wall temperature and wall heat flux varying with an accelerating oscillatory function of time, and for selected values of Prandtl number and Reynolds number are depicted in Fig. 8, for transpiration rate $S=0$. From Fig. 8(*a*), it is noted that as Prandtl number or Reynolds number increases, the depth of diffusion of the temperature field decreases rapidly and, therefore, the heat transfer coefficient increases. In Fig. 8(*b*), the absolute value of $\theta_1(\eta)$ function and its depth of diffusion decrease with increasing Prandtl number or Reynolds number.

Sample profiles of the real part of local heat transfer coefficient (Nusselt number) for Fig. 9(*a*) wall temperature and Fig. 9(*b*) wall heat flux varying with accelerating oscillatory functions for selected values of γ and δ in terms of Prandtl number at Re $=1000$ are depicted in Fig. 9 for $S=0$. In both cases, Nusselt number increases as Prandtl number increases. Besides, as γ and δ increase, the real part of Nusselt number increases.

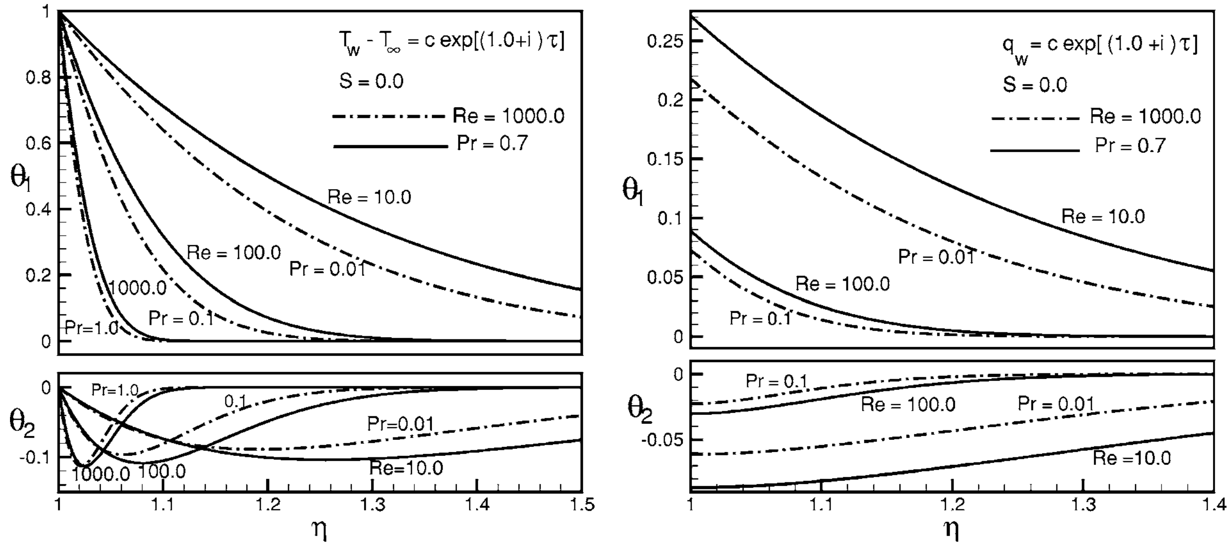

(a) (b)

Fig. 8 Sample profiles of $\theta_1(\eta)$ for (*a*) wall temperature, (*b*) wall heat flux, varying with accelerating oscillatory function of time for selected values of Pr and Re, and $s=0$

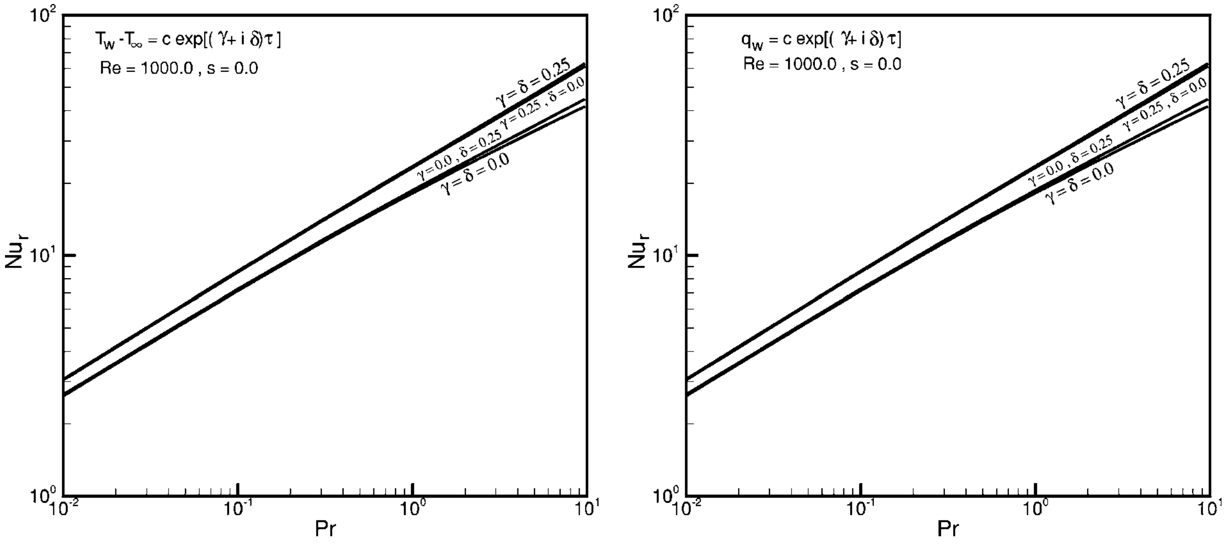

(a) (b)

Fig. 9 Sample profiles of real part of Nusselt number in terms of Pr for (*a*) wall temperature, (*b*) wall heat flux for accelerating oscillatory function of time, for selected values of γ, δ and Re=1000, *s*=0

Sample profiles of the real part of local heat transfer coefficient (Nusselt number) for wall temperature varying with accelerating oscillatory functions for selected values of γ and δ at Re=1.0 to 1000 and Pr=0.7 are presented in Fig. 10(*a*), for $S=0$. Here, the Nusselt number increases as Reynolds number increases. From Figs. 9 and 10(*a*) and Eqs. (49) and (51), it is noted again that the local coefficient of heat transfer (Nusselt number) is not a function of time, though the temperature field is time-dependent. Sample profiles of the $\theta(\eta)$ function for constant wall heat flux at Re =1.0 and Pr=0.7 are given in Fig. 10(*b*), for selected values of transpiration rate. It is seen that as the suction rate increases, wall temperature and its depth of diffusion decreases rapidly. So higher suction rates provide a means for cooling the surface, and higher blowing rates provide a means for heating the surface of the cylinder. Therefore, in a constant wall heat flux case, to prevent high wall temperature, higher rates of suction can be provided and vice versa. Again from both Figs. 6(*a*) and 10(*b*) and for $S=0$, the results in Ref. [6] are obtained.

7 Conclusions

An exact solution of the Navier-Stokes equations and energy equation is obtained for the problem of stagnation-point flow on a circular cylinder with uniform transpiration rate. The formulation of the problem, though, is for the more general case of time-dependent transpiration rate. A general self-similar solution is obtained when the cylinder has different forms of rotational motions including: Constant angular velocity rotation, exponential angular velocity rotation, pure harmonic rotation, both accelerating, and decelerating oscillatory rotations. Since the heat transfer is axi-

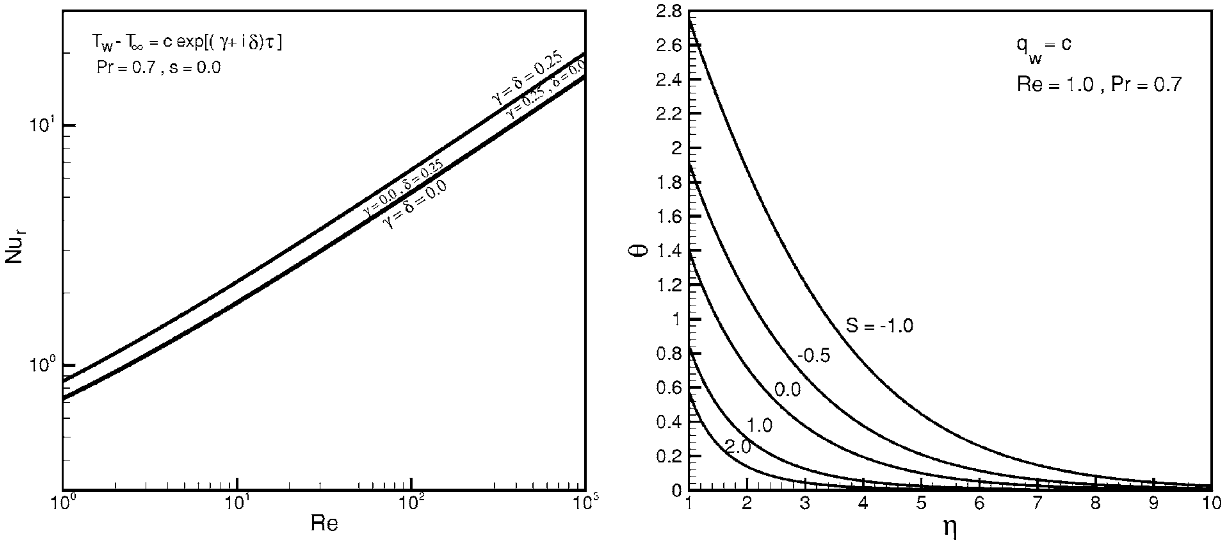

(a) (b)

Fig. 10 (*a*) Sample profiles of real part of Nusselt number for wall temperature with accelerating oscillatory function of time, for Pr=0.7, and *s*=0. (*b*) Sample profiles of $\theta(\eta)$ for constant wall heat flux and selected values of suction and blowing rate, for Re=1 and Pr=0.7.

symmetric in the φ direction, the cylinder rotation has no effect on the temperature field. Results for different time-dependent wall temperature and heat flux functions including: Constant wall temperature or heat flux, exponential and oscillatory form of wall temperature or wall heat flux are presented. Also, one sample semi-similar solution for the same problem has been considered when the circular cylinder is rotating with particulare type of time-dependent angular velocity. The azimuthal component of fluid velocity and surface azimuthal shear stress on the cylinder are obtained in all the above situations, and for different values of Reynolds number and transpiration rates. The dimensionless azimuthal shear stress corresponding to all the cases increases with increasing Reynolds number and suction rate. Also, the maximum value of shear stress increases with increasing oscillation frequency and accelerating and decelerating parameter λ in the exponential amplitude function. In the defined wall temperature case, heat transfer increases with the increase of Reynolds number, Prandtl number, and suction rate, whereas the depth of the diffusion of temperature field decreases. In the case of defined wall heat flux, the wall nondimensional temperature, $\theta(\eta)$, and its depth of diffusion decrease with increase of Reynolds number, Prandtl number, and suction rate. So, an increase of suction rate can be used as means of cooling the surface and increase of blowing can be used as means of heating the surface. It is shown that by providing blowing on the surface of a cylinder, a reduction of resistance against its rotation inside a fluid can be achieved. It is also shown that a cylinder spinning with a decreasing velocity in an exponential manner is azimuthaly stress-free for certain combinations of Reynolds number and rate of this exponential function. Further, it is found that higher suction rates are means for cooling the surface and higher blowing rates are means of heating the surface of the cylinder. An interesting result is also obtained showing that a cylinder with certain type of exponential wall temperature exposed to a temperature difference has no heat transfer. The local coefficient of heat transfer is found to be independent of time, though the temperature field is time-dependent.

References

[1] Hiemenz, K., 1911, "Die Grenzchicht an Einem in den Gleichformingen Flussigkeitsstrom Eingetauchten Geraden Kreiszylinder," Dinglers Polytechnic J., **326**, pp. 321–410.

[2] Homann, F. Z., 1936, "Der Einfluss Grosser Zahighkeit bei der Strmung um den Zylinder und um die Kugel," Z. Angew. Math. Mech., **16**, pp. 153–164.

[3] Howarth, L., 1951, "The Boundary Layer in Three Dimensional Flow. Part II. The Flow Near a Stagnation Point," Philos. Mag., **42**, pp. 1433–1440.

[4] Davey, A., 1951, "Boundary Layer Flow at a Saddle Point of Attachment," J. Fluid Mech., **10**, pp. 593–610.

[5] Wang, C., 1974, "Axisymmetric Stagnation Flow on a Cylinder," Q. Appl. Math., **32**, pp. 207–213.

[6] Gorla, R. S. R., 1976, "Heat Transfer in an Axisymmetric Stagnation Flow on a Cylinder," Appl. Sci. Res., **32**, pp. 541–553.

[7] Gorla, R. S. R, 1977, "Unsteady Laminar Axisymmetric Stagnation Flow Over a Circular Cylinder," Dev. Mech., **9**, pp. 286–288.

[8] Gorla, R. S. R., 1978, "Nonsimilar Axisymmetric Stagnation Flow on a Moving Cylinder," Int. J. Eng. Sci., **16**, pp. 392–400.

[9] Gorla, R. S. R., 1978, "Transient Response Behavior of an Axisymmetric Stagnation Flow on a Circular Cylinder due to a Time Dependent Free Stream Velocity," Lett. Appl. Eng. Sci., **16**, pp. 493–502.

[10] Gorla, R. S. R., 1979, Unsteady Viscous Flow in the Vicinity of an Axisymmetric Stagnation-Point on a Cylinder," Int. J. Eng. Sci., **17**, pp. 87–93.

[11] Cunning, G. M., Davis, A. M. J., and Weidman, P. D., 1998, "Radial Stagnation Flow on a Rotating Cylinder With Uniform Transpiration," J. Eng. Math., **33**, pp. 113–128.

[12] Takhar, H. S., Chamkha, A. J., and Nath, G., 1999, "Unsteady Axisymmetric Stagnation-Point Flow of a Viscous Fluid on a Cylinder," Int. J. Eng. Sci., **37**, pp. 1943–1957.

[13] Saleh, R., and Rahimi, A. B., 2004, "Axisymmetric Stagnation-Point Flow and Heat Transfer of a Viscous Fluid on a Moving Cylinder With Time-Dependent Axial Velocity and Uniform Transpiration," J. Fluids Eng., **126**, pp. 997–1005.

[14] Press, W. H., Flannery, B. P., Teukolsky, S. A., and Vetterling, W. T., 1997, *Numerical Recipes, The Art of Scientific Computing*, Cambridge University Press, Cambridge.

Journal of
Fluids
Engineering

Technical Brief

On the Stability of Two Superposed Viscous-Viscoelastic (Walters B′) Fluids

Pardeep Kumar

Roshan Lal

Department of Mathematics,
ICDEOL,
Himachal Pradesh University,
Summer-Hill,
Shimla-171005, India

The Rayleigh-Taylor instability of a Newtonian viscous fluid overlying Walters B′ viscoelastic fluid is considered. For the stable configuration, the system is found to be stable or unstable under certain conditions. However, the system is found to be unstable for the potentially unstable configuration. Further it is found numerically that kinematic viscosity has a destabilizing effect, whereas kinematic viscoelasticity has a stabilizing effect on the system. [DOI: 10.1115/1.2375135]

Keywords: Rayleigh-Taylor instability, Walters B′ viscoelastic fluid

1 Introduction

When two fluids of different densities are superposed one over the other (or accelerated toward each other), the instability of the plane interface between the two fluids, when it occurs, is called Rayleigh-Taylor instability. Chandrasekhar [1] has given a detailed account of the instability of the plane interface between two incompressible and viscous fluids of different densities when the lighter fluid is accelerated into the heavier. A good account of hydrodynamic stability problems have been given by Drazin and Reid [2] and Joseph [3]. The fluids have been considered to be Newtonian in all the above studies.

With the growing importance of non-Newtonian fluids in modern technology and industries, further investigations on such fluids are desirable. Molten plastics, petroleum oil additives, and whipped cream are examples of incompressible viscoelastic fluids. Walters [4] reported that the mixture of polymethyl methacrylate and pyridine at 25 °C containing 30.5 g of polymer per l with a density of 0.98 g per l behaves very nearly as a Walters B′ elastico-viscous fluid [5]. Sharma and Kumar [6] studied the stability of the plane interface separating two viscoelastic (Walters B′) superposed fluids of uniform densities and found that for the stable configuration, the system is stable or unstable under a condition depending only on kinematic viscoelasticity. Kumar [7] has studied the effect of rotation on thermal instability in a Walters elastico-viscous fluid and found that the rotation has a stabilizing effect and the presence of each rotation and viscoelasticity introduces oscillatory modes which were nonexistent in their absence. It is this class of elastico-viscous fluids we are interested in, particularly to study the stability of the plane interface between viscous and viscoelastic (Walters B′) fluids.

The stability of the plane interface between viscous (Newtonian) and viscoelastic (Walters B′) fluids may find applications in geophysics, chemical technology, and biomechanics and is therefore, studied in the present paper.

2 Formulation of the Problem and Perturbation Equations

Let T_{ij}, τ_{ij}, e_{ij}, δ_{ij}, v_i, x_i, p, μ, and μ' denote the stress tensor, shear stress tensor, rate-of-strain tensor, Kronecker delta, velocity vector, position vector, isotropic pressure, viscosity, and viscoelasticity, respectively. The constitutive relations for the Walters B′ viscoelastic fluid are

$$T_{ij} = -p\delta_{ij} + \tau_{ij}$$

$$\tau_{ij} = 2\left[\mu - \mu'\frac{\partial}{\partial t}\right]e_{ij}$$

$$e_{ij} = \frac{1}{2}\left[\frac{\partial v_i}{\partial x_j} + \frac{\partial v_j}{\partial x_i}\right] \tag{1}$$

Consider a static state, in which an incompressible Walters B′ viscoelastic fluid is arranged in a horizontal strata and the pressure p and the density ρ are functions of the vertical coordinate z only. The character of the equilibrium of this initial static state is determined, as usual, by supposing that the system is slightly disturbed and then by following its further evolution.

Let $\boldsymbol{v}(u,v,w),\rho$ and p denote the velocity of the fluid, the density, and the pressure, respectively. Then the momentum balance and mass balance equations for Walters B′ incompressible viscoelastic fluid are

$$\rho\left[\frac{\partial \boldsymbol{v}}{\partial t} + (\boldsymbol{v}\cdot\nabla)\boldsymbol{v}\right] = -\nabla p + \rho\boldsymbol{g} + \rho\left(\nu - \nu'\frac{\partial}{\partial t}\right)\nabla^2\boldsymbol{v} + \left[\frac{d\mu}{dz} - \frac{\partial}{\partial t}\frac{d\mu'}{dz}\right]\left(\frac{\partial w}{\partial \bar{x}} + \frac{\partial \boldsymbol{v}}{\partial z}\right) \tag{2}$$

$$\nabla\cdot\boldsymbol{v} = 0 \tag{3}$$

where $\nu(=\mu/\rho)$ and $\nu'(=\mu'/\rho)$ denote the kinematic viscosity and the kinematic viscoelasticity of the fluid, $\boldsymbol{g}=(0,0,-g)$ is the acceleration due to gravity, and $\bar{x}=(x,y,z)$.

Contributed by the Fluids Engineering Division of ASME for publication in the JOURNAL OF FLUIDS ENGINEERING. Manuscript received June 22, 2005; final manuscript received June 2, 2006. Assoc. Editor: Dennis Siginer.

Since the density of a fluid particle remains unchanged as we follow it with its motion, we have

$$\frac{\partial \rho}{\partial t} + (\boldsymbol{v} \cdot \nabla)\rho = 0 \tag{4}$$

Let $\boldsymbol{v}(u,v,w)$, $\delta\rho$ and δp denote the perturbation in fluid velocity $(0,0,0)$, density ρ, and pressure p, respectively. Then the linearized perturbation equations appropriate to the problem are

$$\rho\frac{\partial \boldsymbol{v}}{\partial t} = -\nabla\delta p + \boldsymbol{g}\,\delta\rho + \rho\left(\nu - \nu'\frac{\partial}{\partial t}\right)\nabla^2\boldsymbol{v} + \left[\frac{d\mu}{dz} - \frac{\partial}{\partial t}\frac{d\mu'}{dz}\right]\left(\frac{\partial w}{\partial \bar{x}} + \frac{\partial \boldsymbol{v}}{\partial z}\right) \tag{5}$$

$$\nabla \cdot \boldsymbol{v} = 0 \tag{6}$$

$$\frac{\partial}{\partial t}\delta\rho = -wD\rho \tag{7}$$

where $D=d/dz$.

Analyzing the disturbances into normal modes, we assume that the perturbation quantities have the space and time dependence of the form

$$\exp(ik_x x + ik_y y + nt) \tag{8}$$

where k_x, k_y are horizontal wave numbers, $k^2=k_x^2+k_y^2$, and n is a complex constant.

For perturbations of the form (8), Eqs. (5)–(7) give

$$\rho n u = -ik_x\delta p + \rho(\nu - \nu' n)(D^2 - k^2)u + (ik_x w + Du)(D\mu - nD\mu') \tag{9}$$

$$\rho n v = -ik_y\delta p + \rho(\nu - \nu' n)(D^2 - k^2)v + (ik_y w + Dv)(D\mu - nD\mu') \tag{10}$$

$$\rho n w = -D\delta p - g\,\delta\rho + \rho(\nu - \nu' n)(D^2 - k^2)w + 2Dw(D\mu - nD\mu') \tag{11}$$

$$ik_x u + ik_y v + Dw = 0 \tag{12}$$

$$n\,\delta\rho = -wD\rho \tag{13}$$

Eliminating δp between Eqs. (9)–(11) with the help of (12) and (13), we obtain

$$n[D(\rho Dw) - k^2\rho w] - [D\{\rho(\nu - \nu' n)(D^2 - k^2)Dw\} - k^2\rho(\nu - \nu' n) \times (D^2 - k^2)w] + \frac{gk^2}{n}(D\rho)w - [D\{(D\mu - nD\mu')(D^2 + k^2)w\} - 2k^2(D\mu - nD\mu')(Dw)] = 0 \tag{14}$$

3 Two Uniform Viscous and Viscoelastic (Walters B′) Fluids Separated by a Horizontal Boundary

Consider the case of two homogeneous fluids of densities, viscosities; ρ_2, μ_2 (upper Newtonian fluid) and ρ_1, μ_1 (lower, Walters B′ viscoelastic fluid) separated by a horizontal boundary at $z=0$. Then, in each region of constant ρ and constant μ, μ', Eq. (14) becomes

$$(D^2 - k^2)(D^2 - q^2)w = 0 \tag{15}$$

where

$$q^2 = k^2 + \frac{n}{\nu - \nu' n}$$

Since w must vanish both when $z \to +\infty$ (in the upper fluid) and $z \to -\infty$ (in the lower fluid), the general solution of Eq. (15) can be written as

$$w_1 = A_1 e^{+kz} + A_2 e^{+q_1 z} \quad (z < 0) \tag{16}$$

$$w_2 = A_3 e^{-kz} + A_4 e^{-q_2 z} \quad (z > 0) \tag{17}$$

where A_1, A_2, A_3, A_4 are constants of integration,

$$q_1 = \sqrt{k^2 + \frac{n}{\nu_1 - \nu_1' n}} \quad \text{and} \quad q_2 = \sqrt{k^2 + \frac{n}{\nu_2}} \tag{18}$$

In writing the solutions (16) and (17), it is assumed that q_1 and q_2 are so defined that their real parts are positive.

3.1 Boundary Conditions.

The solutions (16) and (17) must satisfy certain boundary conditions. Clearly, all three components of velocity and tangential viscous stresses must be continuous. The continuity of Dw follows from (12) and the continuity of u and v. Since

$$\tau_{xz} = \left(2\mu - 2\mu'\frac{\partial}{\partial t}\right)e_{xz} = (\mu - \mu' n)(Du + ik_x w)$$

and

$$\tau_{yz} = \left(2\mu - 2\mu'\frac{\partial}{\partial t}\right)e_{yz} = (\mu - \mu' n)(Dv + ik_y w)$$

are continuous,

$$ik_x\tau_{xz} + ik_y\tau_{yz} = -(\mu - \mu' n)(D^2 + k^2)w$$

is continuous across an interface between the two fluids. Hence, the interface conditions to be satisfied are

$$w \tag{19}$$

$$Dw \tag{20}$$

$$(\mu - \mu' n)(D^2 + k^2)w \tag{21}$$

must be continuous. Integrating (14) across the interface $z=0$, we obtain another condition

$$[\rho_2 Dw_2 - \rho_1 Dw_1]_{z=0} - \left[\frac{1}{n}\mu_2(D^2 - k^2)Dw_2 - \frac{1}{n}(\mu_1 - \mu_1' n) \times (D^2 - k^2)Dw_1\right]_{z=0} = -\frac{gk^2}{n^2}[\rho_2 - \rho_1]w_0 - \frac{2k^2}{n}[\mu_2 - \mu_1 + n\mu_1'](Dw)_0 \tag{22}$$

where w_0, $(Dw)_0$ are the common values of w_1, w_2 and Dw_1, Dw_2, respectively at $z=0$.

4 Dispersion Relation and Discussion

Applying the boundary conditions (19)–(22) to the solutions (16) and (17), and eliminating the constants A_1, A_2, A_3, A_4 from resulting equations, we obtain

$$\det(a_{ij}) = 0 \tag{23}$$

where $i,j=1,2,3,4$ and

$$a_{11} = a_{12} = 1,\ a_{13} = a_{14} = -1,\ a_{21} = a_{23} = k,\ a_{22} = q_1,\ a_{24} = q_2,$$
$$a_{31} = 2k^2(\mu_1 - \mu_1' n)$$

$$a_{32} = (\mu_1 - \mu_1' n)(q_1^2 + k^2),\ a_{33} = -2k^2\mu_2,\ a_{34} = -\mu_2(q_2^2 + k^2)$$

$$a_{41} = -\alpha_1 + \frac{R}{2} + \frac{k^2}{n}(\nu_2\alpha_2 - \nu_1\alpha_1 + n\nu_1'\alpha_1)$$

$$a_{42} = \frac{R}{2} + \frac{k}{n}(\nu_2\alpha_2 - \nu_1\alpha_1 + n\nu_1'\alpha_1)q_1$$

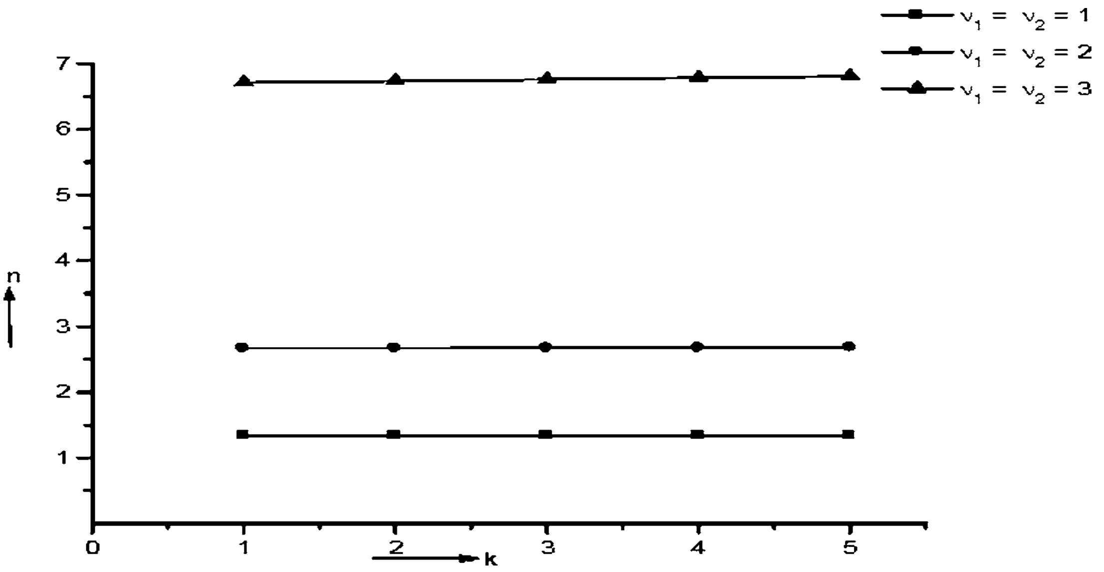

Fig. 1 The variation of the growth rate *n* (positive real value) with the wave number *k* for the kinematic viscosities $\nu_1=\nu_2=1,2,5$ when $\alpha_1=0.38$, $\alpha_2=0.62$, and $\nu_1'=2$

$$a_{43} = -\alpha_2 + \frac{R}{2} - \frac{k^2}{n}(\nu_2\alpha_2 - \nu_1\alpha_1 + n\nu_1'\alpha_1)$$

$$a_{44} = \frac{R}{2} - \frac{k}{n}(\nu_2\alpha_2 - \nu_1\alpha_1 + n\nu_1'\alpha_1)q_2$$

$$\alpha_{1,2} = \frac{\rho_{1,2}}{\rho_1+\rho_2} \quad \text{and} \quad R = \frac{gk}{n^2}(\alpha_2-\alpha_1) \tag{24}$$

Equation (23) yields the following characteristic equation:

$$\begin{aligned}(q_1-k)\Bigg\{&-2k^2(\nu_2\alpha_2-\nu_1\alpha_1+n\nu_1'\alpha_1)\bigg[-\frac{k}{n}(\nu_2\alpha_2-\nu_1\alpha_1+n\nu_1'\alpha_1)\\ &\times(q_2-k)+\alpha_2\bigg]+(R-1)(\nu_2\alpha_2)(q_2^2-k^2)\Bigg\}-2k\Bigg\{(\nu_1\alpha_1\\ &-n\nu_1'\alpha_1)(q_1^2-k^2)\bigg[-\frac{k}{n}(\nu_2\alpha_2-\nu_1\alpha_1+n\nu_1'\alpha_1)(q_2-k)+\alpha_2\bigg]\\ &+(\nu_2\alpha_2)(q_2^2-k^2)\bigg[\frac{k}{n}(\nu_2\alpha_2-\nu_1\alpha_1+n\nu_1'\alpha_1)(q_1-k)+\alpha_1\bigg]\Bigg\}\\ &+(q_2-k)\Bigg\{(\nu_1\alpha_1-n\nu_1'\alpha_1)(q_1^2-k^2)(R-1)+2k^2(\nu_2\alpha_2-\nu_1\alpha_1\\ &+n\nu_1'\alpha_1)\bigg[\frac{k}{n}(\nu_2\alpha_2-\nu_1\alpha_1+n\nu_1'\alpha_1)(q_1-k)+\alpha_1\bigg]\Bigg\}=0\end{aligned} \tag{25}$$

The dispersion relation (25) is quite complicated, as the values of q_1 and q_2 involve square roots. We, therefore, make the assumption that the fluids are highly viscous and high viscoelastic. Under this assumption, we have

$$q = k\sqrt{1+\frac{n}{k^2(\nu-\nu'n)}} = k\left[1+\frac{1}{2}\frac{n}{k^2(\nu-\nu'n)}\right] = k + \frac{n}{2k(\nu-\nu'n)} \tag{26}$$

so that

$$q_1 - k = \frac{n}{2k(\nu_1-\nu_1'n)} \quad \text{and} \quad q_2 - k = \frac{n}{2k\nu_2} \tag{27}$$

Substituting the values of q_1-k and q_2-k from (26) and (27) in Eq. (25), we obtain the dispersion relation

$$\begin{aligned}&\alpha_1\nu_1'[2k^2\alpha_1\nu_1'-1]n^3+[(\alpha_1\nu_1+\alpha_2\nu_2)(1-4k^2\alpha_1\nu_1')]n^2\\ &+[\alpha_1\alpha_2k(4k\nu_1\nu_2+g\nu_1')+k^2(\alpha_1^2\nu_1^2+2\alpha_2^2\nu_2^2)+\alpha_1^2k(k\nu_1^2-g\nu_1')]n\\ &-gk(\alpha_2-\alpha_1)(\alpha_1\nu_1+\alpha_2\nu_2)=0\end{aligned} \tag{28}$$

4.1 Stable Case. For the **potentially stable arrangement** $(\alpha_2<\alpha_1)$, if

$$\frac{1}{\sqrt{2\alpha_1\nu_1'}} < k < \frac{1}{2\sqrt{\alpha_1\nu_1'}} \tag{29}$$

and

$$k > \frac{g\nu_1'}{\nu_1^2} \tag{30}$$

all the coefficients of Eq. (28) are positive. So, all the roots of Eq. (28) are either real and negative or there are complex roots (which occur in pairs) with negative real parts and the rest negative real roots. The system is, therefore, stable in each case. Hence the potentially stable arrangement remains stable if (29) and (30) are satisfied, otherwise, the system is unstable for stable configuration. This is in contrast to the stability of two Newtonian fluids where the system is stable for stable arrangement (Chandrasekhar [1]).

4.2 Unstable Case. For the **potentially unstable arrangement** $(\alpha_2>\alpha_1)$, the constant term in Eq. (28) is negative. Equation (28), therefore, allows at least one change of sign and so has at least one positive real root. The occurrence of a positive root implies that the system is unstable for disturbances of all wave numbers. The system is, therefore, unstable for the potentially unstable case.

We now examine the behavior of the growth rates with respect to kinematic viscosity and kinematic viscoelasticity numerically. We have plotted the growth rate n (positive real value) versus the wave number k for several values of the kinematic viscosity ν and the kinematic viscoelasticity ν_1' in Fig. 1 and 2, respectively.

In Fig. 1, the growth rate n is plotted against wave number k, for fixed value of $\nu_1'=2$, $\alpha_1=0.38$, $\alpha_2=0.62$, and for $\nu_1=\nu_2=1,2,5$. The growth rate increases with an increase in kinematic viscosity showing its destabilizing effect on the system. In Fig. 2, growth rate n is plotted against wave number for fixed $\nu_1=\nu_2=2$,

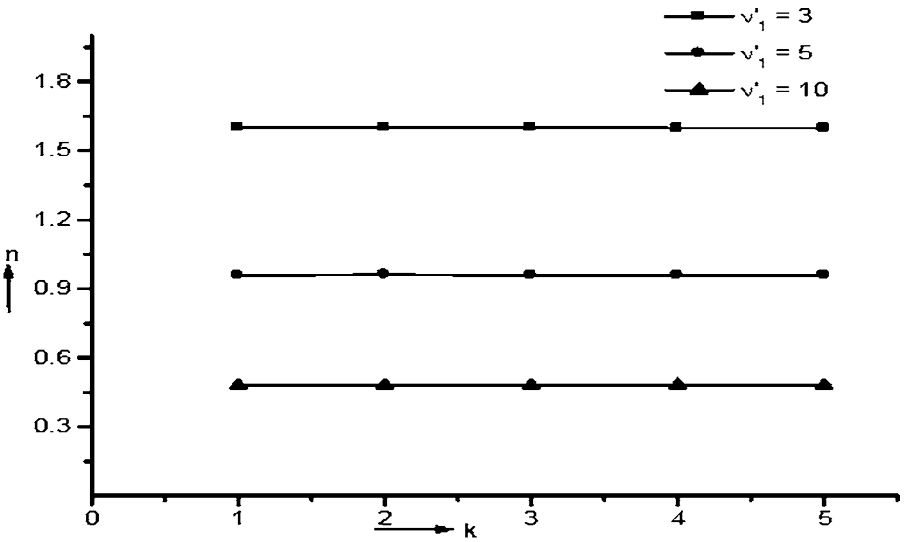

Fig. 2 The variation of the growth rate *n* (positive real value) with the wave number *k* for the kinematic viscoelasticities $\nu_1'=3,5,10$ when $\alpha_1=0.38$, $\alpha_2=0.62$, and $\nu_1=\nu_2=2$

$\alpha_1=0.38$, $\alpha_2=0.62$, and for $\nu_1'=3$, 5, 10. It is seen that for the same wave number *k*, the growth rate *n* decreases as the kinematic viscoelasticity ν_1' increases, showing the stabilizing character of the kinematic viscoelasticity. However, it is interesting to note that the curves are not affected by the wave numbers.

5 Conclusions

A detailed account of stability of superposed Newtonian fluids, under varying assumptions of hydrodynamics and hydromagnetics, was given by Chandrasekhar [1]. With the growing importance of non-Newtonian fluids in chemical engineering, modern technology, and industry, the investigations on such fluids are desirable. The Walters B′ fluid is one such important non-Newtonian (viscoelastic) fluid. Walters [4] reported that the mixture of polymethylmethacrylate and pyridine at 25 °C containing 30.5 g of polymer per l with a density of 0.98 g per l behaves very nearly as the Walters B′ viscoelastic fluid.

Viscoelastic fluids may have a different effect as compared to Newtonian fluids, on the stability problems. For example, the effect of a uniform rotation on the thermal instability of a Maxwellian viscoelastic fluid is destabilizing (Bhatia and Steiner [8]), whereas the uniform rotation has a stabilizing effect on the thermal instability of a Newtonian fluid.

The Rayleigh-Taylor instability of a Newtonian fluid overlying Walters B′ viscoelastic fluid has been studied. For the potentially stable arrangement (lesser density fluid overlies the heavier one), the system is found to be stable or unstable under certain conditions. This is in contrast to the stability of two superposed Newtonian fluids where the system is stable for a stable arrangement. However, the system is unstable for the potentially unstable arrangement (heavier fluid overlying the lighter one). The dispersion relation is also solved numerically and it is found that the kinematic viscosity has a destabilizing effect, whereas the kinematic viscoelasticity has a stabilizing effect on the system.

Acknowledgment

The authors are grateful to Professor Dennis Siginer and the learned referees for their critical and technical comments that led to a significant improvement of the paper.

References

[1] Chandrasekhar, S., 1981, *Hydrodynamic and Hydromagnetic Stability*, Dover, New York.

[2] Drazin, P. G., and Reid, W. H., 1981, *Hydrodynamic Stability*, Cambridge University Press.

[3] Joseph, D. D., 1976, *Stability of Fluid Motions II*, Springer-Verlag, New York, Chap. XIII.

[4] Walters, K., 1962, "The Solution of Flow Problems in the Case of Materials With Memory," J. Mec., **1**, pp. 469–479.

[5] Walters, K., 1960, "The Motion of an Elastico-Viscous Liquid Contained Between Coaxial Cylinders," Q. J. Mech. Appl. Math., **13**, pp. 444–453.

[6] Sharma, R. C., and Kumar, P., 1997, "On the Stability of Two Superposed Walters *B′* Viscoelastic Liquids," Czech. J. Phys., **47**, pp. 197–204.

[7] Kumar, P., 2001, "Effect of Rotation on Thermal Instability in Walters Elastico-Viscous Fluid," Proc. Nat. Acad. Sci. India, **71**, pp. 33–41.

[8] Bhatia, P. K., and Steiner, J. M., 1972, "Convective Instability in a Rotating Viscoelastic Fluid Layer," Z. Angew. Math. Mech., **52**, pp. 321–324.